Thèse n° 9049

Material Development for Perovskite/Silicon Tandem Photovoltaics

Présentée le 18 mai 2022

Faculté des sciences et techniques de l'ingénieur
Laboratoire de photovoltaïque et couches minces électroniques
Programme doctoral en science et génie des matériaux

pour l'obtention du grade de Docteur ès Sciences

par

Peter Joseph FIALA

Acceptée sur proposition du jury

Prof. F. Nüesch, président du jury
Prof. C. Ballif, Dr Q. T. Jeangros, directeurs de thèse
Prof. A. Tiwari, rapporteur
Dr M. Ledinský, rapporteur
Prof. M. K. Nazeeruddin, rapporteur

École
polytechnique
fédérale
de Lausanne

2022

I'm not going to rest
until this world we share
is a better place to live in.

We owe this to eachother.

To my parents.
To everyone I meet.

Acknowledgments

Creation is the greatest of human acts.
Creating with others is only better.

Few efforts in the modern world are as collaborative as the scientific community. The spirit of curiosity, teaching eachother, and setting aside ego to do what is best for the expansion of human knowledge is the foundation of what we do; and this spirit is as strong at PV-Lab as it is anywhere on earth. This thesis work is a collaborative effort as much as any other. None of what I write here could be possible without those who taught me, guided me, and supported me through the last four years. The culture at PV-Lab is truly special, and this all starts from the source. I extend my thanks first and foremost to Professor Christophe Ballif, who gave me the chance to pursue my thesis in his group. His guidance throughout this work has been crucial, and his passion for photovoltaics is both inspiring and unmatched. I also must thank my co-director, Dr. Quentin Jeangros. The road to get here was often difficult, but I never lacked for experienced advice, friendly motivation, a good example, or a clever idea of what to try next. His role in making this thesis a reality cannot be understated.

Thank you to the jury president Prof. Frank Nüesch and the jury members Dr. Martin Ledinský, Prof. Mohammad K. Nazeeruddin, and Prof. Ayodhya N. Tiwari for generously giving their time to asses this thesis.

Thank you so much to the perovskite team in Neuchâtel. Florent, Daniel, Xin-Yu, Saeid, Christian, Quentin G., Jérémie, Matthias, Terry, Fan, Björn, Marion, Soo-Jin, Arnaud, Brett, Adrianna, Ricardo, and Patricia, I've learned something from all of you. Thank you for sharing a lab with me all these years and making it as enjoyble as it has been. Particularly, Jérémie, Matthias, and Florent for teaching me so much about perovskites when I first arrived; Quentin J. and Björn for believing in me at the very beginning and all the way through; and again Florent, Saeid, and Xin-Yu for sharing with me all the secrets of tandems.

Thank you to my office-mates, Mario, Luca, Olatz, and Terry. It was a pleasure to share our space over the last four years. That was really four whole years? Well the camaraderie of experiencing the struggles, frustration, and occasional joys of being a Ph.D. student with you guys really made the whole thing bearable. I wish you all success.

To all the other members of the PV-Lab who helped me along the way and made my work possible, thank you. Particularly the technical staff, Cédric, Aymeric, and Nicolas, your saving work could not be more appreciated. Thank you to Céline, Moustafa, Ludovic, Gab, and Laura for cleaning, depositions, and measurements. Thank you to the SHJ and HTPC teams for your advice and help understanding the weird IR-active substrates that we use in tandems. Particularly thank you to Vincent and Deniz for the tireless production (and improvement!) of bottom-cells. Thank you to Karine, Hassan, and Mary-Claude for making every administrative part of my time here simple and smooth. Thank you to Dr. Mounir Mensi and Dr. Julian A. Steele for performing measurements and aiding in interpretation of the results. You both provided data that was important in the story of this thesis.

Last but not least, thank you to my family and my friends in Neuchâtel and beyond. Really this thesis was one of the most difficult things that i've done in my life, and i needed every bit of support i received. Mom and Dad, i would never have started a Ph.D., or had the strength to get through it, or the educational basis to qualify for this post, or the curiosity that motivated me, or the work ethic to get it done, had you two not raised me the way that you did and provided for me the whole way through. Thank you. To my friends in Switzerland, Ryan, Maria, Maëlis, Fanny, Alex, Alice, and so many more, i have had a wonderful time here and it pains me to leave. Neuchâtel will always be home to me. To Kelly, Audrey, and Alex, who are struggling through their own Ph.D.s back in the US, though we were far away your support was felt and it meant a lot. Good luck with yours and stay strong. Thank you to Franz and Stephanie for teaching me alpinism and bringing me up my first peaks. I'm going to keep this up as long as i'm able. I should probably also thank the SuisseMobile team. I hiked over 1,500 km in canton Neuchâtel alone, and i never got lost. This was one of my greatest pleasures in Switzerland.

No great achievement was ever done alone, and this thesis in particular is on the low end of greatness and on the high end of collaboration. But now it is done, and my appreciation goes out to each and every one of you that helped me get here and attain this degree. Thank you.

Neuchâtel, 20 Décembre 2021

Abstract

The developed world is built on the fact that energy is readily available and functionally infinite. The electricity from the wall, the gas at the station, and the heat in our homes are reliable and low-cost. But this comfort is so far only possible through the combustion of fossilized carbon sources. This is not a sustainable system. Not only are these sources finite, but the long-term effects of this much combustion are catastrophic for our planet and species. Transitioning from current energy production to sustainable sources will require the development and deployment of a diverse group of technologies. Chief among these is the generation of electricity from sunlight, or photovoltaics (PV).

Most modern PV is based on crystalline silicon. Silicon PV alone could be scaled to provide the necessary energy production, but this could be realized more quickly and efficiently if more advanced technologies are used. The defining metric is the cost per generated electricity. In the case of silicon, the current cost breakdown of materials, manufacturing, installation, and system costs leaves little room for further price reduction; and light-to-electricity efficiencies are near their practical limit. Of the proposed alternatives, the pairing of silicon with a thin film of lead-halide perovskite in a multijunction or "tandem" architecture is one of the most promising. This splits the solar spectrum in two, and raises the theoretical maximum efficiency from 33.3% to 45.1% based on each material better using its segment than any one material could use the full spectrum. The central goal of this thesis was therefore to advance the capability of this type of solar cell while remaining within the constraints of industrially-plausible production methods.

Towards this goal, we first isolated perovskite layers to study what limits their performance. This led to improvements in the bulk material quality, the interfaces with adjacent materials, and the layer morphology. We reduced bulk disorder via balancing the annealing temperature, time, and environment. The interfaces were improved by selecting passivating materials which were compatible with our deposition methods. We further observed a complex interplay between the materials used and the environment of the annealing, which illuminated critical dependencies of device performance and gave us a more complete understanding of our material. Finally the morphology was improved via high-temperature annealing. This was

enabled by a surface-binding additive which reduced the detrimental effects of such an anneal while preserving the benefits, resulting in a perovskite with less internal resistance. From there, we moved outside of the perovskite layer and developed a light scattering ZnO layer which increased the optical performance and absorption of our cells. Returning to the main goal of the thesis, the lessons learned from work on isolated perovskites were applied in tandems on textured silicon. We additionally increased the perovskite layer thickness and made the bottom-cell more robust to processing damages. Together, the result was a stabilized efficiency of 27.3%. This is better than any silicon cell to date, but work remains to achieve 30% and beyond, extend material stability, scale up the deposition area, and transfer these capabilities to industry. Together, the work done as a part of this thesis represents a step forward in the journey towards carbon-neutral energy production.

Key words:
Photovoltaics, Renewable Energy, Perovskite, Silicon, Multijunction, Tandem
Textured Absorber, Thin Films, Materials Science

Résumé

Une majorité de l'énergie consommée sur la planète provient de combustibles fossiles. Ces sources d'énergie sont disponibles en quantités limitées et leur utilisation à une telle échelle promet une véritable catastrophe écologique. Il apparaît ainsi essentiel d'accélérer la transition énergétique vers des sources renouvelables telles que l'énergie photovoltaïque (PV).

Le marché du PV est actuellement largement dominé par une famille de dispositifs qui se basent sur des cellules à base de silicium cristallin. Bien que ce type de cellules solaires pourrait fournir toute l'électricité PV nécessaire à la transition énergétique, des technologies plus avancées permettraient d'accélérer cette transition en baissant le prix de l'électricité générée. Le prix d'une installation PV est actuellement dominé par les coûts du système autres que ceux du module et des cellules qui le composent. Ainsi, la meilleure approche pour faire baisser le prix de l'électricité consiste à augmenter l'efficacité des cellules et du module PV afin de produire plus de W par m^2 et ainsi baisser les couts d'installation par W de capacité de production électrique. L'option la plus prometteuse pour augmenter l'efficacité des cellules solaires au-delà de la limite d'efficacité théorique d'un matériau unique (33.3%) consiste à créer une cellule multi-jonction, notamment en combinant deux cellules solaires en un seul dispositif appelé « tandem ». Cette architecture en tandem permet une meilleure utilisation du spectre solaire comparé à un matériau unique et ainsi d'augmenter l'efficacité maximale théorique à 45.1%. Afin de maintenir des coûts de production raisonnables, le type de tandem le plus prometteur actuellement consiste à ajouter une cellule couche mince à base d'un matériau pérovskite sur la face avant d'une cellule solaire industrielle en silicium. Le but central de cette thèse est de développer cette nouvelle technologie afin d'en augmenter l'efficacité.

En combinant plusieurs méthodes d'analyse, nous avons d'abord étudié la couche mince pérovskite afin d'identifier les mécanismes menant à des pertes de sa performance. Cette stratégie a permis d'améliorer les propriétés intrinsèques du matériau en optimisant notamment l'étape de recuit menant à la cristallisation de la pérovskite, ceci en trouvant un équilibre entre conditions de dépôt, température, et atmosphère du recuit. Plus particulièrement, un additif ajouté au mélange de précurseurs en phase liquide a permis de recuire la pérovskite à plus haute température sans l'endommager, et ainsi d'augmenter la taille des grains qui la

composent et ainsi améliorer sa capacité à transporter les charges électriques. La qualité des interfaces de la pérovskite a ensuite été optimisée en sélectionnant des couches de contacts permettant de passiver les défauts présents en surface et d'extraire sélectivement les porteurs de charge. De plus, il a été révélé que l'atmosphère du recuit influence fortement la qualité de ces interfaces. Afin d'améliorer les propriétés optiques de la cellule solaire pérovskite, nous avons aussi développé une couche de ZnO qui permet de disperser la lumière en amont de la couche pérovskite et ainsi d'augmenter le nombre de photons absorbés. Nous nous sommes ensuite concentrés sur les tandems pérovskite/silicium, où nous avons appliqué les leçons apprises lors du développement des cellules pérovskite à simple jonction. Pour optimiser la distribution de courant entre les deux sous-cellules de la tandem, nous avons augmenté l'épaisseur de la couche pérovskite et avons modifié la cellule en silicium pour améliorer sa résistance aux dégâts introduits lors de la fabrication. Combinés, ces efforts ont permis de produire une cellule tandem avec une efficacité stabilisée de 27.3% et un courant >20 mA/cm^2 grâce à l'utilisation d'un wafer silicium texturés sur ses deux faces. Cette performance est supérieure au record obtenu avec une cellule silicium (26.7%), mais, comme discuté dans ce document, il reste cependant du chemin à parcourir avant que la technologie perce industriellement : l'efficacité doit être augmentée >30%, la taille de la cellule augmentée du cm^2 actuel à >200 cm^2, la stabilité améliorée pour atteindre >20 ans comme le silicium, et les processus de fabrication rendus industriellement compatibles. Cette thèse a néanmoins contribué au développement de cette nouvelle technologie prometteuse en vue d'une société neutre en carbone.

Mots clés :
photovoltaïque, énergie renouvelable, pérovskite, silicium, multijonction, tandem
absorbeur texturé, couches minces, science des matériaux

Contents

Acknowledgments **i**

Abstract **iii**

1 Introduction and Literature Review **1**

1.1 Background and Motivations 1

1.1.1 Energy on Earth 1

1.1.2 State of the Solar Industry 3

1.1.3 Objectives of Thesis 11

1.1.4 Contribution to the Field 11

1.2 Literature Review 13

1.2.1 Perovskite Background 13

1.2.2 Stages of PSC Development 14

1.2.3 Tandem Research 23

2 Material and Interface Development in Single Junction PSC **31**

2.1 Introduction and Motivations 32

2.1.1 The Standard Cell Architecture and Perovskite Composition 34

2.1.2 Fabrication and Characterization Tools 35

2.2 Bulk Material Quality of Perovskites from the Hybrid Method 37

2.2.1 Bilayer Interdiffusion 37

2.2.2 Humidity and Solvent Effects 39

2.2.3 Bulk Disorder 43

2.2.4 Conclusion 50

2.3 Interface Passivation in Hybrid-Method PSC 51

2.3.1 Passivation via Material Selection 51

2.3.2 Passivation via Processing Conditions 55

2.3.3 Conclusion 71

2.4 Perovskite Morphology and Charge Transport 72

2.4.1 Modifying Perovskite Crystallization 72

2.4.2 Effect on Charge Transport 78

2.5 Conclusion 83

3 ZnO Texture for Improved Optics in Single Junction PSC 85
3.1 Introduction 86
3.2 Zinc Oxide as a Source of Texture 88
3.2.1 History of Textured ZnO Use for Thin Film Photovoltaics 88
3.2.2 Optical Simulations 89
3.3 Zinc Oxide Layer Development 92
3.3.1 Controlling ZnO Morphology and Optical Performance 92
3.3.2 Fine Tuning the ZnO Recipe for Cell Application 98
3.4 Perovskite Solar Cells with ZnO-Textured Active Layer 103
3.4.1 Cells Made with the Hybrid PVD/SP Method 103
3.4.2 Cells Made with Solution-Processed Perovskite 116
3.5 Conclusion 119

4 Development of Monolithic Perovskite/c-Si Tandem Solar Cells 121
4.1 Tandem Cell Architecture 122
4.2 Increasing Tandem J_{SC} via Top-Cell Design 126
4.2.1 Manufacturing Thicker Perovskite Layers 128
4.2.2 Tuning of the IZO Front Contact 130
4.3 Increasing Tandem V_{OC} via Interface Tuning 134
4.4 Improving Tandem Fill-Factors Through Sub-Cell Optimization 140
4.4.1 Eliminating Processing Damages in c-Si Bottom-Cells 142
4.4.2 Applying Single Junction Improvements to Tandem Top-Cells 149
4.5 Conclusion 157
4.6 Remaining Losses and Oulook 158

Concluding Remarks 161

Outlook for Perovskite/Silicon Tandem Photovoltaics 163

A List of Abbreviations 165

B Supplementary Tests and Figures 169

Bibliography 213

Curriculum Vitae 239

1 Introduction and Literature Review

1.1 Background and Motivations

Before discussing the research done in this thesis work, we will outline the context in which the work was performed. This context is what drives the decisions to develop the specific type of solar cell which we use, and further motivates certain restrictions which we place on ourselves. We want to do work with a realistic chance of having an impact. We cannot know what type of solar panel will be the key piece of energy production in 30 years, but we can predict what it is likely to be, and design our work to reach that goal as quickly as possible. For this, we must first understand the context of the world around us, its energy use, and how solar fits into this.

1.1.1 Energy on Earth

The world's energy consumption is ever increasing. As the world population grows, becomes more urbanized, and increases in quality of life, the demand for energy will increase in parallel. This isn't necessarily a bad thing, but it will be as long as energy production continues to be based on combustion of fossil fuels. Consumption of carbon-based fuels is directly linked to increasing of global temperatures, and the long-term effects are expected to be disastrous if this warming is not mitigated [1]. The extent of our society's reliance on these fossil fuels for energy can be seen in figure 1.1. Quantified, over 80% of the world's energy in 2019 came from coal, oil, or natural gas. The segment for renewables is the most rapidly increasing, having gone up more than 2.5x from 2010 to 2019, but this remains insignificant next to the fossil fuel segments, which together remain 15x greater than hydro and renewables [2]. In order to reach net-zero emissions by 2050 and have a hope of withstanding climate change, the International Energy Agency estimates that fossil fuels would need to drop to 20% of total production, while the remaining supply come from a diverse mix of solar, wind, biofuels, nuclear, and others [3]. Among these, the International Energy Agency projects solar photovoltaics (PV) as the single largest contributor, with over 30,000 TWh (20% global supply in 2050).

This is a lot of energy, but relatively small compared to the resources available. Total proven reserves of coal, oil, and natural gas amount to 8.4 million, 2.9 million, and 2.1 million TWh of expected extractable energy [4]. Ignoring the disastrous ecological consequences of burning that much carbon based fuel, this is still not enough for even 100 years of energy when consuming at the 2019 pace. By comparison, the sun irradiates 2.9 million TWh daily onto the earth's surface [5]. 24 hours of sunlight on earth's surface is roughly equivalent to the energy we could make from all the known oil reserves on earth (244 G tonnes = 2.84 million TWh [4]). Notably, much of this energy is already put to use. It grows plants, heats the atmosphere, and causes weather. Regardless, reaching 30,000 TWh per year is extremely feasible in perspective of the magnitude of the resource. Only 0.003% of solar energy would need to be captured as electricity to meet this goal.

30,000 TWh is small compared to the total solar energy available, but large compared to our current capability to collect, convert, and use solar energy. In terms of modules that exist on the market currently, we would need roughly 100 000 km^2 of modules (with 20% efficiency and 1500 hours of sunlight per year). Whether or not this is realistic to achieve depends on how many modules can be produced per year, and what efficiency those modules have. These can be combined in a single metric as the total production capacity, measured in Watts-peak (Wp, Watts outputted at standard irradiation conditions). Seen in figure 1.2a, the global annual PV production is currently around 150 GWp. The current growth rate translates to roughly 50 years to produce the expected 30,000 TWh, even when ignoring the need to replace modules at the end of their lifetimes. Considering replacement every 30 years on average, we should target 1 TWp production per year in order to sustain a 30,000 TWh per year generation rate. Thus the current production of 150 GWp is insufficient, and highlights the main challenge of PV: How can we produce more Wp per year? For now, the production is steadily rising at an increasing pace. This is encouraging, but even if the production continues increasing linearly

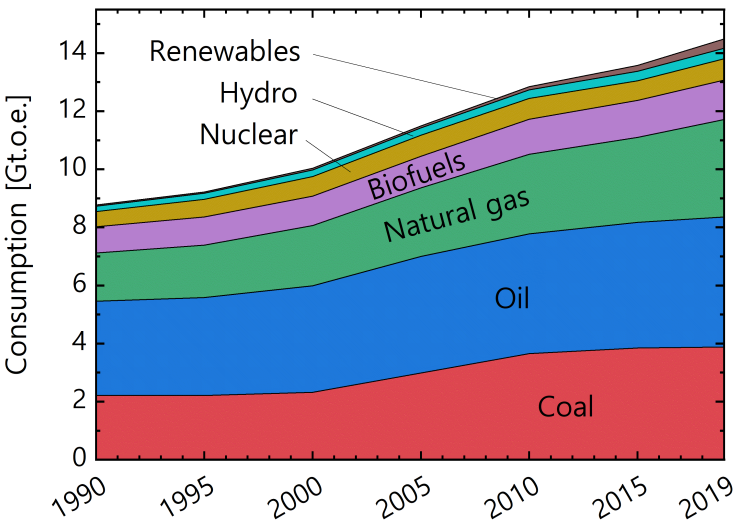

Figure 1.1 – World energy use over time, divided by source. Units are Tonnes of Oil Equivalent (t.o.e.), and one t.o.e. is equivalent to 11.63 MWh. In 2019 the world consumption neared 1.69×10^5 TWh (14.5 Gt.o.e.). Data from IEA World Energy Balances 2021 [2].

at the rate of the last five years, it will be the 2070's before we reach a TWp per year production rate. Increasing production at this pace year after year is a challenge on it's own, but reaching 2050 net-zero emission goals will demand even faster increases [3]. This is possible, but the solutions for how to achieve this goal are complicated and require a deeper look at the current state of the PV industry.

1.1.2 State of the Solar Industry

The global PV industry is a complex network of material extraction, refinement, and production. It is already growing at an impressive rate, with cumulative PV installations increasing at 35% compound annual growth rate from 2010 to 2020 [6]. But to increase this rate and achieve the production rates necessary to decarbonize world energy, we must look into the complexities of what drives production and what limits further improvements.

What Limitations Remain to be Broken?

Many of the challenges facing PV uptake are related to how it differs from traditional energy sources. PV production cannot be turned up and down in the way that combustion-based systems can be, and thus supply cannot be tailored to follow demand. Similarly, PV is constrained to the weather, day/night, and summer/winter cycles. Together, these force PV to partner with energy storage systems or the grid. Energy storage, such as batteries, increases the initial capital expenditure (capex) for consumers. Systems can instead be connected to the extant electricity grid. This allows for buying/selling energy to the grid operator as a form of storage. This lowers the barrier to entry, but forces reliance on a system built and maintained by established power companies. This comes without any guarantee that the grid will be able or willing to continue the partnership, and devalues PV electricity via unequal buy/sell pricing. Finally, solar on the level of residential or commercial consumers requires high initial capex, followed by years or decades of near-free electricity production. This is a major contrast to traditional centralized power plants/grids which are cheap for users to connect to and charge as electricity is used. This amounts to a meaningful difference in the barrier to entry for PV relative to traditional energy systems. The consequence of all these consumer-end differences is that companies selling PV often have to operate at the lowest possible price points in order to attract customers, which obliges extremely thin profit margins. This puts a hard limit on the materials and methods available for use in production, and emphasizes cost reduction at all levels.

Despite all of these challenges and an economic environment hostile to newcomers, PV installations have steadily increased and prices have similarly gone down. These trends can be seen in figures 1.2b and 1.3, respectively. Over 700 GWp have been installed cumulatively, and costs are converging on 1 €/Wp. This corresponds to roughly 700 TWh of yearly production and 4 €cts/kWh (assuming 1000 hours per year with standard 1000 W/m^2 solar intensity and

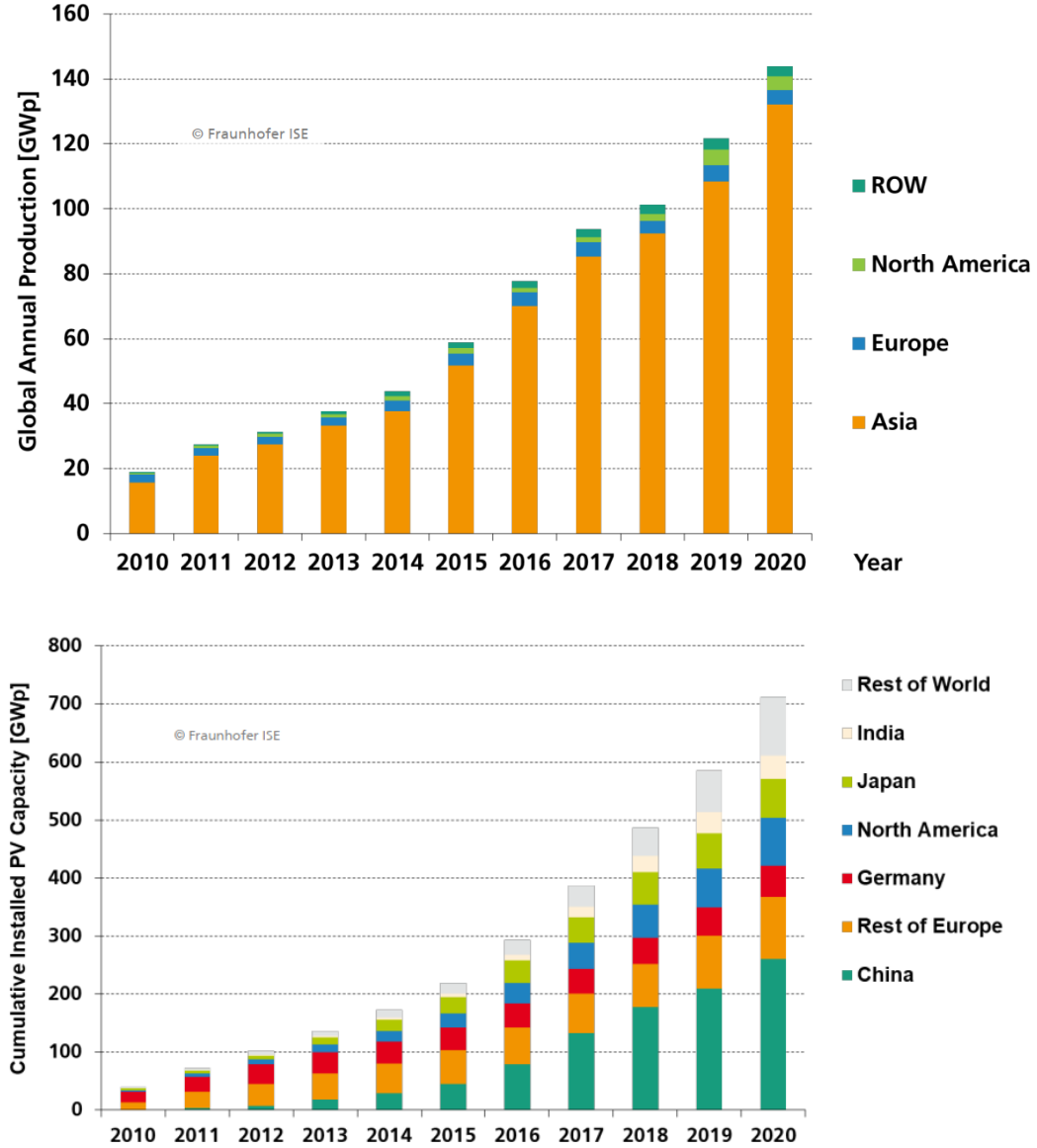

Figure 1.2 – Solar production and installation global totals by region. Production is measured in Watts-peak, which is the Watt rating of each module at standard 1000 W/m^2 intensity, summed over all modules produced. Source: Fraunhofer ISE Photovoltaics report 2021 [6].

a 30 year PV system lifetime). Compared to the 30,000 TWh per year target, this is far short. But the price already is favorable when compared to the 10-20 $cts/kWh typical end-user electricity costs (in the US, 2021 [8]).

Accelerating uptake will require even more attractive costs, in order to overcome the barrier of high initial capex and expand northward the geographical region in which this price is reasonable. We can break down the price of PV based on source. Costs are contributed either from the modules themselves, or the "balance of systems" (BOS). This entails the inverter,

installation, mounting fixtures, and manpower necessary to install and connect the modules. The BOS cost is relatively stable over time, while the module cost has dropped dramatically over the last 15 years [6] due to improvements in manufacturing and cheapening of raw materials[1]. In the current market, the BOS represents a majority of the installation cost, and neither component has much remaining potential for improvement [6]. The consequence of this is that the price per installation is unlikely to dramatically change. However, the cost is not rated by the end price of a system, but rather the price per electricity generated. Thus, the price can be further lowered regardless of the materials and manufacturing, by increasing the efficiency of the modules.

Module efficiencies have been consistently increasing, at nearly 0.5% absolute per year, and currently average about 20.0% [6]. But there is an upper limit set by the fundamental limitations on energy conversion and the material properties of crystalline silicon (c-Si)[2]. The maximum theoretical efficiency limit for terrestrial PV with the bandgap of c-Si is 33.3% [10], but drops to roughly 29% when including other losses such as Auger recombination, depending on how the calculation is performed [11]. The best c-Si cells made with laboratory-scale methods have been approaching this limit for years (26.7% from Kaneka) [12], and there is little room left for improvement. Due to the optical and electronic consequences of connecting and encapsulating cells, module efficiencies are slightly behind. The best being 24.4%

[1] It is worthwhile to note that the price of raw materials is likely to increase, depending on the morality of those in charge of supply chain management. This is due to recent revelations that much of the world's poly-silicon supply relies on forced labor [9].

[2] c-Si technologies dominate industry, and are the case considered when discussing the PV industry as a whole [6].

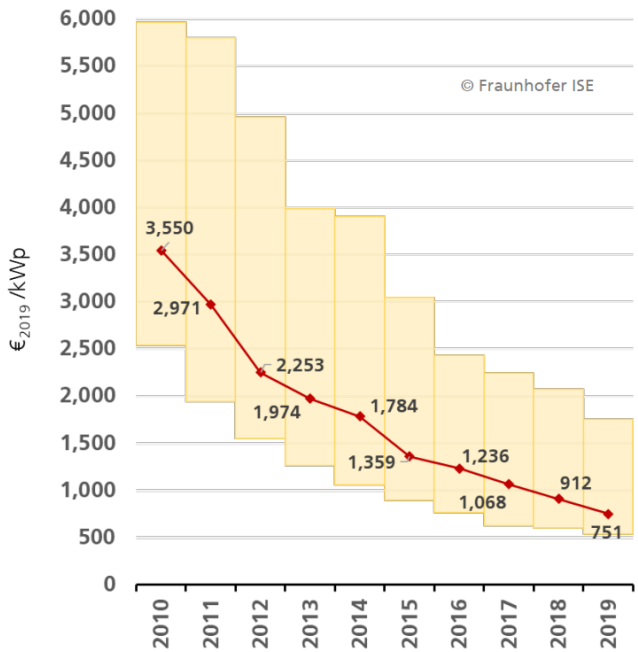

Figure 1.3 – Global weighted average price for large PV installations over time. Price includes total installation costs for utility-scale (>1 MWp) systems. The bars give the 5th and 95th percentile. Graph: Fraunhofer ISE Photovoltaics report 2021 [6]. Data: International Renewable Energy Agency [7].

from a 108-cell module (Kaneka) [13]. There are still gains to be made on the module level as lab technology migrates to larger scale production and eventual deployment, but overall, commercial c-Si module efficiencies are already too close to their limits to dramatically change. The change in total GWp production upon increasing module efficiency from 20% to 24% will be significant on its own, but achieving the goal of 30,000 TWh per year will require that no improvement be left unexploited. Thus, we look past c-Si alone and onto more advanced technologies with higher efficiency potentials.

The Role of Multijunction Solar

Higher efficiency modules promise lower $/Wp, reduced space usage, and higher Wp production per year. Multijunction cell architectures (also called "tandem") are one of the main avenues pursued en route to higher commercial module efficiencies. They are based on combining two absorber materials into one solar cell, which will split the absorption of the solar spectrum into two pieces. This way each material can better "use" its segment than one material could ever do for the whole spectrum. Furthermore, this halves the current produced by the cell and more than doubles the voltage, leading to a higher overall power output and less need for expensive current-collection elements. A promising route to industrializing this idea is to pair the already mass-produced c-Si with a second material which is cheap relative to the c-Si cost. Given utility scale electricity prices in the range of 10 - 20 $cts/kWh (in the US [8]), a tandem-cell module that gives 28% efficiency would produce enough electricity (over 10 years with 1000h/sun/year) relative to a 23% module to justify a 75 $/m^2 production cost increase. This is industrially feasible given current thin film solar costs in the range of 40 - 50 $/m^2 [14]. Thus the strategy of forming multijunction solar cells with c-Si is a realistic path towards high efficiency and economic PV, provided the existence of a suitable material. It is then a matter of identifying the correct material, developing its performance, and engineering large-scale production capability.

Before discussing possible candidates, we first give a better explanation of what makes multijunction PV work. The general concept is illustrated in figure 1.4. As the bandgap energy (E_g) of the absorber material increases, the number of solar photons which it absorbs decreases. The maximum possible power out is simply the total photons absorbed times the energy of the resulting electron-hole pairs, illustrated by the dark rectangle. For any material, a significant part of the energy available is lost either to transmission (below E_g loss) or by relaxation of high-energy photons down to the E_g (thermalization loss). These losses can be reduced by simply including more materials which cut into the two loss mechanisms. One material will absorb the high energy photons and extract a similar voltage from them, while transmitting the lower energy photons to be absorbed in the second material. Increasing from one to two junctions improves the maximum theoretical efficiency for any E_g from 30.4% to 42.3%, and infinite junctions under one sun could theoretically reach 68.2% [15]. There is still a gap between the ideal case and 100% efficiency cells due to other fundamental losses besides transmission and thermalization (figure 1.5). These are: emission losses, which reduce the

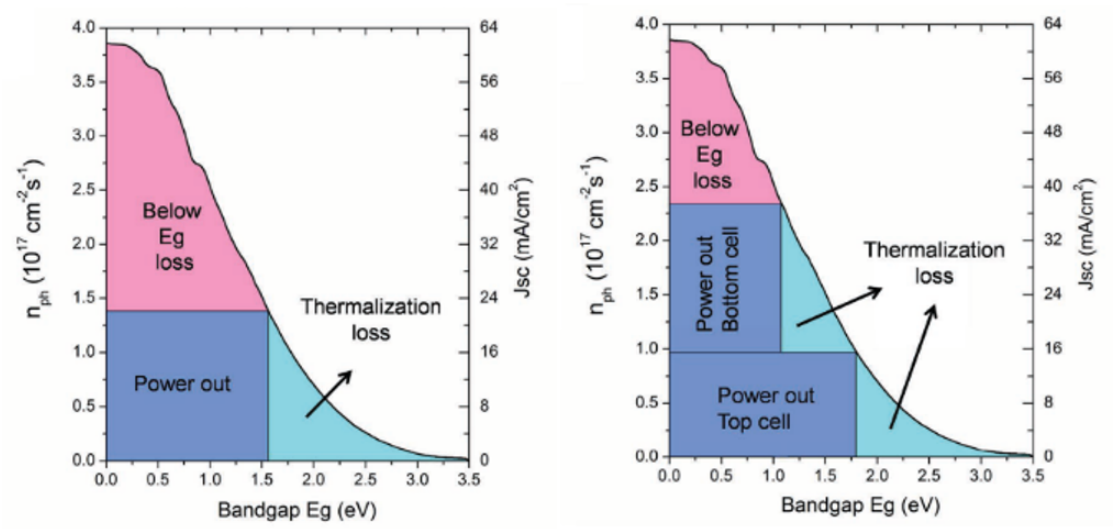

Figure 1.4 – Basic principle of multi-junction PV. The curved line shows the total photon flux in the terrestrial solar spectrum above a given energy, as a function of that energy. A semiconductor of a given E_g can only use the quantity of photons at or above that energy, and can only use an amount of energy from those photons equivalent to the E_g. Data from: [17]. Figure from: [18], reprinted with permission from John Wiley & Sons, Inc.

number of photons/electrons a cell can use due to the natural blackbody radiation of any material above 0 K; Boltzmann losses, which come from the entropy of having a larger solid angle of emission than illumination; and Carnot losses, which are due to the temperature difference between the solar cell and the sun. While multijunction designs reduce the transmission and thermalization losses, the other losses increase. Nonetheless, the overall theoretical efficiency only improves with added junctions [16]. More junctions may give higher theoretical efficiencies, but in practice the complexity of combining multiple materials together makes this type of cell challenging and expensive to produce. Thus, we focus on just adding a second material before considering >2 junction cases.

Modern research into multijunction solar is split into different areas which pursue different goals for different applications. There is significant research and production of multijunction PV based on stacked III-V semiconductors for space and terrestrial concentrator use. This technology is well developed and shows high efficiencies (38.8% for 1-sun, 5-junction, by Spectrolab and 47.1% at 143-suns, 6-junctions, by NREL [13]). But due to expensive deposition procedures and low material abundance, this type of solar cell remains in the range of 50 - 200 $/Wp [19] (recall the 1 €/Wp for rooftop systems in the German market). This blocks large-scale industrial uptake and III-V cells are mostly limited to special applications where cost and large area are not a priority, such as powering spacecraft and concentrator PV [20]. In contrast to this, a tandem based on c-Si could in theory combine the low cost and industrial scale of c-Si PV with the high efficiency of multijunction PV, provided the matching material exists. This could be achieved by using c-Si as the "bottom-cell" and another material as the "top-cell" in the tandem stack. It is expected that the optimal partner for c-Si will be a

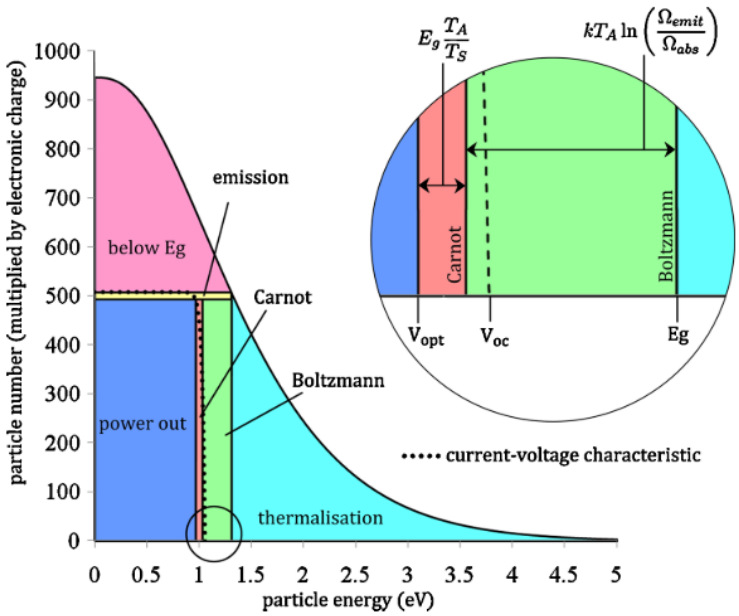

Figure 1.5 – Fundamental losses in single junction PV. Beyond thermalization and transmission losses, all solar cells lose some current to emission losses, and some voltage to Boltzmann and Carnot losses. Figure from: [16], reprinted with permission from John Wiley & Sons, Inc.

thin-film based technology, due to low material use and therefore potentially low additional production cost. Among the materials proposed for this role are more III-V materials, hybrid organic/inorganic lead-halide perovskites, and many chalcogenide materials. III-V top-cells are well developed and show high efficiencies when paired with c-Si (35.9%, 1-sun, 3-junction, by NREL/CSEM/EPFL [13], [21]), but again these rely on expensive and industrially impractical methods such as epitaxial growth and mechanical stacking, keeping cost estimates in the range of 5 - 10 $/Wp [21].

Notably, thin films based on perovskites have seen a boom in research relative to other top cell options. This is due to perovskite cells' low potential material costs, low processing costs, low-temperature processing, E_g tunability (to ideally match with c-Si), high performance, and ease of lab-scale research, which together make perovskites both highly suitable for pairing with c-Si and ideal for rapid lab-scale development. Particularly, monolithic perovskite/c-Si tandems are of interest. Monolithic structures are advantageous over stacked sub-cells when looking to industrial use, since the economic viability of a tandem as compared to single junction c-Si is strongly dependent on the number of additional processing steps [22]. Direct integration of the two sub-cells into a single device stack with a single electronic circuit minimizes the total layer count and cuts in half the material and deposition costs for the electronic contacts. The details of why the material behaves in such a desirable way are discussed in the following chapter.

Current State of the Art

Perovskite/silicon multijunction PV is not yet at the point of commercially available modules. But still the research level results can be compared to that of c-Si to give an idea of the relative development of the fields. As an example, record cell and module efficiencies for various technologies are plotted in figure 1.6. Single junction silicon modules are classified by whether the silicon is single- or multi-crystalline. Single-crystal Si is more efficient, with a record cell efficiency of 26.7% and module efficiency of 24.4% (79.0 cm^2 and 13,177 cm^2, by Kaneka, [13]). Multi-crystalline Si uses a cheaper base material, but its cell and module records are also lower, at 24.4%[3] and 20.4%, respectively (by Hanwha and Jinko, [13]). Perovskites have quickly come into a similar range with cells, but at impracticably small areas. The current record of 25.5% was achieved at 0.0954 cm^2, and the best efficiency of a cell with over 1 cm^2 area is only 21.6% (by UNIST Ulsan and ANU, [13]).

Reproducibility of perovskites over large area is a known issue for the field, and efficiencies drop off quickly with device area [23]. Perovskite modules have attained 21.4% over smaller scales of 26 cm^2 [24] and 17.9% with an area still less than 10% of the Si record modules' areas (804 cm^2 by Panasonic, [13]). Achieving reasonable device stability is also a key factor for perovskite PV. Commercial c-Si modules offer warranties or typically 25 years, often guaranteeing performance of 80% the original power output after this time. Perovskites are far from this point, but quantification remains difficult [25]. This is due to the significantly different physical degradation mechanisms of the two material classes, and standardized "accelerated aging" tests that are designed to probe those of c-Si. Thus in total, there remains no agreed-upon testing procedure for perovskite cell or module degradation [25], and reliable reporting on expected lifetimes is currently complex.

Overall, perovskites alone have been developed enough to surpass multi-crystalline Si and nearly match mono-crystalline Si in terms of efficiency (figure 1.6). But this is only one metric. Perovskites remain far behind c-Si in device area and stability. This is understandable for such a young technology, as high efficiencies are easier used to justify the research costs of upscaling, rather than the inverse. But still, in order for perovskites to exist on an industrial scale parallel to c-Si, they will need to improve in these areas[4]. Each of these subjects receives meaningful research attention, and is believed solvable, but this remains to be demonstrated [27], [28]. Confidence in the eventual success of research and development efforts is high enough for perovskite technology to garner the interest of industry. We already stated that the record for the highest perovskite module efficiency belongs to a private company (Panasonic). As monolithic perovskite/c-Si tandems are such an attractive technology, they naturally draw enthusiasm from industry as well. The highest demonstrated efficiencies for monolithic perovskite/c-Si tandems already come from private industrial research. This record, from the

[3] This result used a "directionally solidified" wafer, sometimes called a "cast mono". This is not strictly multi-crystalline, but is also definitively not a float-zone or Czochralski wafer as is used in mono-crystalline records.

[4] It is estimated that perovskite/c-Si tandems would need a module efficiency of 28.7% and at maximum 2% degradation rate per year to achieve economic viability relative to c-Si alone [26]. But this calculation relies on many assumptions related to degradation rate and production cost, and is therefore not considered a hard limit.

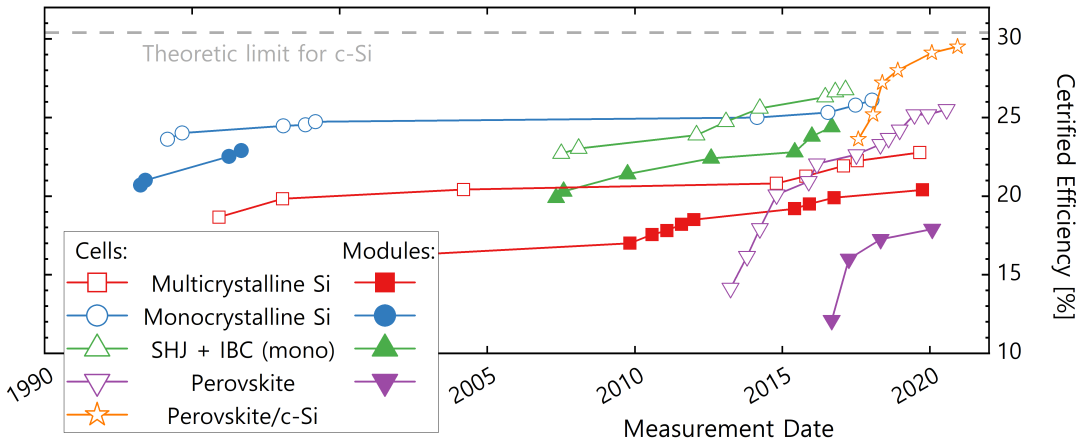

Figure 1.6 – Cell and module efficiency records for various PV technologies. All data comes from the NREL efficiency charts: [12], [30]. Monocrystalline Si module records continue to advance, but since the late 1990's none have been without IBC or SHJ technology. No perovskite/c-Si modules have been certified to date.

company Oxford PV, is an efficiency of 29.5% [29], which already surpasses all other single junction non-concentrator technologies. Again, this is at a cell size of roughly 1 cm^2, but it again shows the potential for efficiencies far beyond what c-Si can do alone. It is also not the end of the road. The best c-Si cell is 26.7% compared to its theoretical limit of 30.4% [15], while the best perovskite/c-Si tandem is only 29.5% compared to its theoretical limit of 42.3% [15]. It is reasonable to expect that, over the course of this technology's maturation, lab-scale devices will reach the mid-30's in efficiency.

Conclusion

The PV industry as a whole is moving fast. It has already reached a point of economic competitiveness with traditional energy sources. But to achieve worldwide net-zero emissions and avoid catastrophic effects of climate change, the PV industry needs to produce more, faster, cheaper. This can be achieved by scaling up production of current module technologies, but the rate can be further increased if the modules themselves are more efficient. This is best realized by moving beyond single-material solar cells and on to multi-junction technologies. Various prospects have already been demonstrates, but in their current state are either not developed enough or too expensive to justify the additional power output. Among these, the most promising to break these barriers is perovskite thin films integrated monolithically on top of standard wafer-based c-Si cells. This type of device has already surpassed c-Si in terms of efficiency, but is still limited by cell area and stability. Research is ongoing into these efforts, while in parallel the efficiency of lab-scale perovskite/c-Si tandems continues to be pushed. The record perovskite/c-Si tandem efficiency is still more than 10% absolute below the theoretical limit, while the more mature c-Si technology has closed the gap to less than 4%.

Attaining higher efficiencies for perovskite/c-Si tandems is realistic, and will in turn incentivize research into stability and upscaling, potentially enabling a market entry and increased PV production.

1.1.3 Objectives of Thesis

The goal of this thesis work was to develop monolithic perovskite/c-Si tandem solar cells. This was to be achieved through characterization-based understanding of the device limitations and scientific approach to resolving them.

More specifically, we sought to:

1. Characterize state of the art perovskite top cells to determine and quantify the physical mechanisms that limit their device performance.

2. Discern the causes of these limitations and understand their sources

3. Prescribe solutions to these limitations based on taking strategies from the literature and modifying them to our material composition and deposition mechanisms.

4. Develop methods for texturing single junction perovskite solar cells, so as to improve their optical performance and advance the understanding of perovskite formation on non-flat surfaces.

5. Combine all lessons learned and apply them in perovskite/c-Si tandem solar cells to achieve high efficiencies.

1.1.4 Contribution to the Field

This work brought several developments to the field of perovskite/c-Si tandem cell research. In general, these advancements pertain to perovskites deposited with a hybrid evaporation/spin-coating method compatible with direct deposition on textured c-Si substrates, which should facilitate industrial transfer. We first characterized the effects of each step in this method. The interdependencies of different variables was described and the overlapping effects were unified by measuring the bulk disorder. This was minimized to obtain an optimal recipe for thin, flat perovskite layers.

We showed a multifunctional method for material improvement based on a molecular additive (fluorinated benzene phosphonic acid). This reduced non-radiative charge recombination and boosted cell voltage. It also improved the perovskite's robustness to chemical degradation during annealing, allowing higher temperatures to be used. This brought the benefit of improved layer morphology and charge extraction, evidenced by lower series resistance and higher fill-factors (8.5% absolute). This result is in preparation for publication.

We proposed and demonstrated the use of active-layer texturing for improving cell optics. Texture was achieved via gas-phase deposition of ZnO thin films. These achieved a natural texture, and the deposition parameters were tuned to balance absorption and optical scattering. The hybrid deposition method from flat single junctions was transposed to these textured substrates. This produced working cells, but multiple problems were found related to the specifics of the deposition method and how it interacts with textured substrates. Thus we switched to a solution-based deposition method which was able to cover the pyramids and fill the valleys effectively. The improved optics of texturing gave 1.0 mA/cm^2 of improvement to short-circuit current. This result is in preparation for publication.

The lessons learned via tuning of the hybrid evaporation/spin-coating method process steps were applied to top-cells of perovskite/silicon tandem solar cells. This resulted in a 50% thicker top-cell which satisfied the current-matching condition with a larger bandgap perovskite. The hole-transport layer was further modified to give a better interface and device voltage, and the same high-temperature annealing developed on single junctions was applied. All together, these lessons were combined and resulting devices showed short-circuit current over 20.2 mA/cm^2 and a maximum stabilized efficiency of 27.3%, up from 25.1% before this work.

1.2 Literature Review

1.2.1 Perovskite Background

The name perovskite does not refer to any specific material, but rather to a class of materials defined by a common crystal structure. This is the structure ABX_3, where A is a +1 ion, B is a +2 ion, and X is a -1 ion (figure 1.7). This does not necessarily give a photoactive material, and in fact was first described as an inert mineral [31]. Over time, more variations on this base structure were discovered, and some of them were identified as semiconductors [32]. This eventually led to their application in PV, called perovskite solar cells (PSC), only now in organic-lead-halide compositions. This refers to the specific compositional space in which the A site is occupied by various small organic or alkaline ions such as methylammonium (MA), formamidinium (FA), or Cs. The B site is occupied by a transition metal such as Pb, but can also sometimes be substituted for Sn. The X site is occupied by halide ions, such as I, Br, or Cl. For the sake of brevity, "perovskite" will be used to refer exclusively to this sub-class of materials for the remainder of this work. Importantly, the A, B, and X groups do not need to be homogeneous. Anywhere from one to three or potentially more types of ion can be mixed together, from the prototypical $MAPbI_3$ to cation and anion varied compositions such as $(CsFAMA)PbI_3$ or $FAMAPb(IBr)_3$ [33]–[35]. This flexibility of constituent ions is reflected in perovskite material properties. By varying the different ion ratios, the bandgap, morphology, phase stability, defect densities, etc. change as well. This enables perovskites to tailor their properties to different applications, and optimize for one parameter while holding another constant.

In general, perovskite research has advanced at an impressive pace. From the first report of a perovskite-based solar cell in 2009 at 3.8% [37], device efficiencies have topped 25% already in just the 11 years since [12]. This success was driven by a combination of factors that are unique to perovskites. The first is the high semiconductor quality of the material, due largely to their defect tolerance. In general, the energy levels of many crystallographic defects of perovskites are not within the bandgap [38]. Thus, they can tolerate the rather

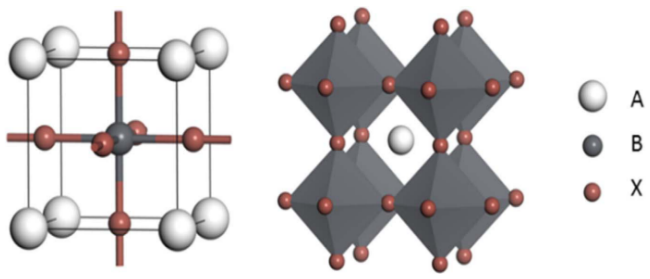

Figure 1.7 – Diagram of perovskite unit cell and crystal structure. The unit cell (left) and a conventionally stylized crystal structure (right) of the perovskite ABX_3 structure. Hybrid organic-inorganic lead halide perovskites, as used in this thesis, use a typically organic monovalent cation in the A-site, a divalent metal cation in the B-site, and a monovalent halide anion in the X-site. Reprinted from [36], with permission from Elsevier.

high defect concentrations that come with low processing temperatures and facile solution-based deposition methods, without experiencing severe recombination and performance reduction. This leads to impressive material properties and device performance for perovskites, despite low-tech fabrication methods which many labs can implement. Next, the tunability of perovskites (discussed above) is an important part of their success. Perovskites' versatility allows them to be applied in many ways. This has led to a diverse research field covering many types of PV architectures [39], lasers [40], LEDs [41], memory devices [42], [43], and more [44], [45]. Finally, the high performance and diverse applications of perovskites combine with potentially low material and productions costs to form a subject primed for rapid lab-driven progress. Most perovskite materials use mainly earth-abundant elements such as lead, iodide, and bromide, along with simple organics (MA, FA). Likewise, useful perovskites can be deposited with from simple, low-temperature, solution-based methods such as spin coating. Normally this type of deposition results in a high defect density and performance too poor for use in semiconductor research, which is why III-V semiconductor research uses high-temperature and expensive epitaxial growth [20].

Most importantly to this thesis work, perovskites were identified early on as a potential partner with c-Si to form multi-junction cells. Aside from the reasons discussed above that made perovskites alone an attractive research topic, there are additional aspects of perovskites that particularly suit them to the role of top-cells in multijunction configurations. Notably, they have a E_g tunable within the range relevant for pairing with c-Si [33], [46], [47] and low absorption below the E_g [48]. The different tandem structures and the constraints that they each apply to the materials used are detailed in section 1.2.3. For now, these constraints are much more easily satisfied if one material has a tunable E_g. This grants an additional degree of freedom in the cell design, allowing for more flexibility to pair perovskite top-cells with different bottom-cell materials. Whether it is c-Si or something else, such as another lower-E_g perovskite or copper-indium-gallium-selenide (Cu(InGa)Se_2, or CIGS), perovskites can be made to have the ideal E_g, and thus are an attractive partner. Beyond that, the sharp absorption edge of perovskites combined with the low sub-E_g absorption, means that nearly all of the light that is not used by the perovskite can be transmitted to the bottom-cell. Overall, the high-potential application of perovskites as top-cell in a tandem configuration is an important part of why this material has received so much research attention.

1.2.2 Stages of PSC Development

Initial work with perovskite PV was more of a transition than a starting point. PV based on sensitizing organic dye molecules had been researched since the 1990's, but had remained stagnant for more than a decade [12]. These cells relied on a mesoporous metal oxide layer that allowed for a high surface-area contact between the dye molecules (sensitizing the meso-porous surface) and the liquid electrolyte [49]. Initially perovskites were used as a direct replacement of these dye molecules [37]. But soon after, it was discovered that the perovskite structure had sufficient capability for bulk charge transfer, and thus didn't require the meso-

porous framework of organic dye-sensitized cells [50]. Further, new production methods were developed, such as the anti-solvent method, which allowed for facile and quick formation of high-quality materials [51], [52]. This allowed perovskites to depart from the structures, materials, and methods it inherited from its predecessor, and be treated as a thin film material and class of solar cells all its own. The following is an segmented history of different strategies and sub-topics that were prominent before and during my thesis work, and their current status. There is significant temporal overlap between certain sections, and thus the developments achieved in each section are not fully independent, as methods and cell structures were shared.

We will quantify the success of the presented methods using the voltage loss of the material (W_{OC}). This refers to the difference between the E_g and the open-circuit voltage (V_{OC}) of the cell ($W_{OC} = E_g/q - V_{OC}$), and can be used to compare the passivation quality of materials with different E_g. In some cases, the W_{OC} which we report is different from that claimed in the literature. This comes from differences in how the E_g is determined from measurement. For this analysis, we used the method recommended by Krückemeier et al. [53], which takes the energy at which the external quantum efficiency (EQE) curve has its maximum inflection point. This measurement is reported for all cited cases, and is thus used to standardize W_{OC} calculation. For example, at the beginning of this thesis, our lab was using a 1.64 eV perovskite and achieving V_{OC} values in the range of 1.00 - 1.05 V. Thus our minimum W_{OC} was 0.59 V. For comparison, the best III-V cells have W_{OC} in the range of 0.3 - 0.4 V, and champion c-Si cells reach 0.36 V of W_{OC} [13]. Thus, perovskite cells are comparatively underdeveloped, but this gap has shrunk over time as more research has been done. A comparison of W_{OC} values for perovskites achieved using different strategies is shown in figure 1.12. Each of these strategies is discussed in the following sub-sections.

Compositional and Structural Optimization

The earliest strategy to gain prominence in perovskite research was compositional optimization. This refers to the compositional space described above, in which primarily the A and X site ions are varied between different species [33]. Early reports of perovskite materials used in photovoltaics often used compositions with one ion species per site, such as $MAPbI_3$ or $MAPbBr_3$ [37]. However, it was quickly discovered that these could be mixed, in that the A, B, or X site would be occupied by a mix of viable ions [46], [54]. The viability of different ions is determined by a tolerance factor defined by Goldschmidt which relies on the ionic radii of each species [31]. Examples of tolerance factor values for common A-site ions is shown in figure 1.8. The effect of varying the A- and X-site ions between MA/FA and I/Br on the perovskite layer color is shown in figure 1.9. These colors come about from changes in E_g. It was found that the same E_g could be achieved with different compositions, and therefore different levels of material quality, performance, and stability. The best W_{OC} values demonstrated from this method were in the range of 0.44 - 0.52 V [55]–[57] (figure 1.12).

Relevant to this thesis is the instability of perovskites based primarily on the MA cation, particularly thermal stability above the realistic operating temperature of 80°C [59]. This was solved by replacing MA with an alloy of FA and Cs [54], [60], [61]. The alloying of two cations was important for the stabilization of the photoactive α phase of $FAPbI_3$, which is normally unstable at room temperature [54]. This resulted in improved heat/moisture stability, and was used as the standard cation makeup for the entirety of this thesis work. As the compositional space for varying both the A and X sites between three options is quite large, this was the subject of many publications, and a significant part of the previous theses in our lab [62], [63].

Throughout this process, other aspects of PSC performance other than just efficiency emerged as research priorities. The first is the effect of the overall chemical balance of the perovskite material. During the process of compositional optimization, it was discovered that a small molar excess of PbI_2 in the bulk material was advantageous to PSC efficiency [64], [65]. This came with side-effects, though, as PbI_2-rich samples experienced faster degradation and lower JV stability in general [66], with unreacted PbI_2 eventually being identified as both a product and cause of material degradation [59], [67]. Still, a certain amount of PbI_2 excess (roughly 5-10%) became standard in the field. This was a relevant parameter to this thesis, and the balance of PbI_2 to the other perovskite components is discussed throughout chapter 2.

The second notable discovery was that of halide segregation. It was found during characterization of mixed-halide perovskite films that the observed E_g was often unstable during photoluminescence (PL) measurement [68] (figure 1.10). Particularly, the halide ions and their vacancy states were shown to be mobile within the crystal lattice, with very low activation energies which were easily obtained under operating conditions [69]. The mobility of these ions led them to reshuffle within the layer, and arrange themselves into distinct regions rich

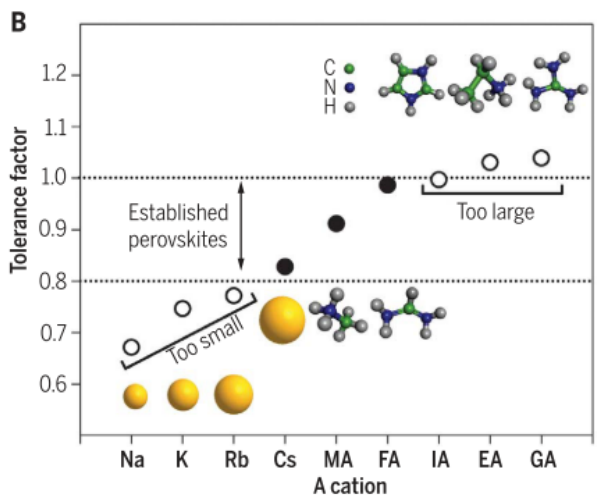

Figure 1.8 – Tolerance factors of various A-site ions in an $APbI_3$ perovskite structure. The tolerance factor as established by Goldschmidt [31] can be used to determine if an A-site ion will form a cubic structure within ABX_3, according to that ion's radius and the fixed radii of the other two species. Values between 0.8 and 1 are considered feasible, and values outside of this range mean the ions are either too small or too large. This case shows calculations for A-site ions in $APbI_3$. These thresholds can be bent by the mixing of differently sized ions within each site. Other popular "large" ammonium cations include butylammonium and phenethylammonium. Figure from [58], reprinted with permission from AAAS.

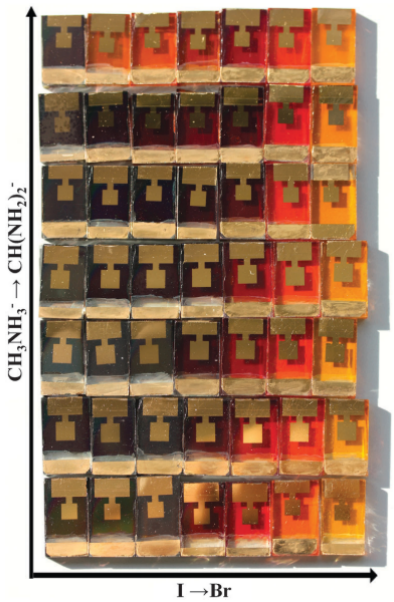

Figure 1.9 – Image of perovskite cells made with varied A- and X-site ions. Perovskite layers were made with a matrix of ion mixes spanning MA to FA and I to Br. The molar ratios of the A- and X-site species are spaced linearly between pure $MAPbI_3$ in the bottom left, to pure $FAPbBr_3$ in the top left. Figure from [33], reprinted with permission from the Royal Society of Chemistry.

in one halide species over the other [69]. This therefore gave regions within the perovskite with different E_g values. The activation of this process was tied to the concentration of excited charge carriers [70]. This could be supplied by illumination or electrical bias, meaning that the measurement technique itself often influenced the material behavior [70]. For example, simply illuminating the perovskite at open-circuit conditions induces a higher carrier concentration than is present during operation, accelerating the segregation. In any case, having this ionic mobility and the segregation that came with it was shown to be detrimental to device performance [71]–[73]. Furthermore, mobile charges within the layer could accumulate at different interfaces, leading to localized doping and unusual electronic performance including incorrect efficiency measurements [74]–[76], and be pushed into adjacent layers where they reduce performance [77].

Over time, the effects of ion migration within mixed-halide perovskites were further distinguished based on the physical mechanisms at play. Notable effects that were eventually linked to ion migration include the hysteresis in JV measurements depending on measurement conditions, E_g instability, non-diode behavior under reverse bias, and eventual long-term irreversible degradation [74], [75], [77]. Numerous characterization techniques were applied to untangle these effects, explain their causes, and discover solutions. Prevailing theories were based on the idea that polaronic effects and vacancy defects drove migration due to lattice strain, and that these were created naturally due to gradients in excitation or bias [69], [70], [78]. It followed that the migration could be arrested by passivating these defects. Many methods were proposed and realized, such as: simple compositional tuning within the established space (balancing I, Br, and Cl [55], using CsFA without MA at the A-site [61]); expanding the compositional space with small alkaline ions (using Rb [79] or K [80], [81]); passivation with exposure to O_2 versus N_2 [82]; charge-blocking to reduce the potential drop across the

perovskite [83]; and interfacial passivation [84]. Over the same time period, other theories were proposed and later disproved with new evidence. Notably, the idea that segregation into low-E_g regions pinned the device voltage based on this reduced charge separation [71], [72]. This theory was wide-spread, and various teams attributed high or record efficiencies to stopping halide segregation [85], [86]. However, these gains were more likely due to various treatments' reduction of defect states, which reduced trap-assisted recombination and ion mobility together. Eventually this theory was dropped, as the problem of halide segregation was revealed to be less significant to device voltage than trap-assisted recombination losses [87].

In parallel with the work done on compositional optimization was research into structural optimization of perovskite layers. Primarily, the focus of this channel of research was to use ammonium-based cations with a size too large to fit into the normal perovskite lattice (according to a tolerance factor outlined by Goldschmidt [31], and shown in figure 1.8). The idea behind these cations was that they were too big to fit into the lattice, and thus would sit at the surface of perovskite crystal grains, where the ammonium moiety would terminate the crystal lattice in a way that did not leave dangling bonds or vacancies, nor allow for a next layer of crystal growth [72]. With optimized deposition conditions, they could be made to form 2D sheets of perovskite, with parallel faces terminated with the large cations. These perovskites showed increased environmental stability and had larger E_g than standard 3D perovskites with the same A, B, and X mixtures. In cells, these cations were either intermixed throughout the bulk 3D material to terminate surfaces, post-deposited on top to form a thin 2D layer on top of the main 3D absorber, or used so that the entire absorber layer was made of stacked 2D perovskite layers. The results showed improvements to performance [24], [88]–[94],

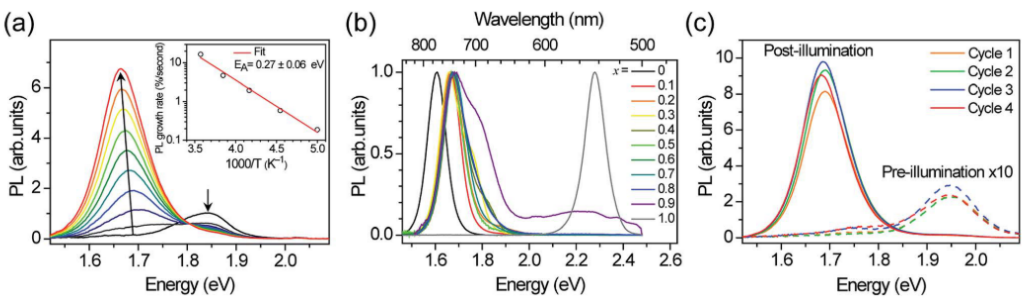

Figure 1.10 – Characterization of PL emission instability due to halide migration. PL was measured with a 457 nm source at 10-100 mW/cm^2, with samples at 300 K. The perovskite was MAPb(Br$_X$I$_{1-X}$)$_3$. (a) shows the PL evolution of a single X = 0.4 film illuminated over 45 seconds, with 5 second intervals. The peak starts at about 1.85 eV and quickly evolves to a much larger peak around 1.65 eV. The inset shows a fit used to extract the process activation energy of 0.27 ± 0.06 eV. (b) shows a single PL peak, normalized, for multiple compositions denoted by their X value. While the pure iodide and bromide phases remain stable, all the mixed compositions settle to a similar E_g value near 1.7 eV. (c) shows a single X = 0.6 film over four cycles of 2 minutes illumination followed by five minutes of relaxation in the dark. The sample is observed to return to its initial state, before again following the evolution shown in (a), when again illuminated. Figure from [68], used with permission from the Royal Society of Chemistry.

environmental stability [24], [88], [92]–[94], E_g segregation [89], [94], passivation [24], [90], [95], and halide contamination of adjacent layers [91]. These strategies were popular, and we briefly pursued this route as well. The results are shown in section B.2. For layered 2D/3D perovskites, the high E_g of the 2D materials functioned as an electron-blocking layer [92], [93]. This made it ideal on top of the bulk perovskite in cells with n-i-p polarity, as it would aid in selectivity of holes. Some groups used the same concept in p-i-n cells, with the electron-blocking 2D perovskite in between the bulk absorber and the electron extraction layer, and claimed that it did not harm extraction [91], [95]. Other research groups achieved the p-i-n polarity via intermixing the large cations with the main perovskite in a single solution deposition [96], [97]. Still, groups that are not constrained in such ways continued with this strategy. This has led to multiple results at the forefront of the efficiency race [96]–[101], and W_{OC} values as low as 0.33 V [98].

Chemical Passivation

During the time of my thesis work, a new strategy emerged for making higher-quality perovskites. From the research on compositional optimization, which sought to create a naturally defect-free perovskite crystals via incorporation of alkaline elements or ammonium-based lattice termination, researchers instead chose to use additives in the perovskite to chemically passivate defective states that were treated as inevitable. This followed from early investigations that while K-doping did modify the crystal lattice up to about 10% molar relative to Pb [80]. But going far beyond this (up to 40% molar relative to Pb) yielded extremely well passivated materials [81], achieving a photoluminescence quantum yield of 66% and a W_{OC} of 0.43 V (the photoconductance dropped at these high doping rates, leaving an optimum at 10%). Thus it was inferred that the role of the K ions was not only to enter the crystal and improve its quality, but to actively passivate via ionic bonding to the inevitable defective states. Expanding on this, research groups sought out ions or molecules to add to their perovskite based on their ability to chemically bond to the expected detrimental defect states without negative side effects. Research was particularly focused on perovskite surfaces and interfaces. After the early research on the chemical composition, bulk defects and disorder were considered minor problems [38], and multiple groups identified that the surfaces and interfaces were the primary loss sources [36], [84], [102]–[104].

Sorting through the crowd of passivation approaches, certain groups can be defined based on the chemical nature of the passivation agent. Additives and treatments were considered either a Lewis acid or a Lewis base, depending on their electron-accepting or electron-donating nature, respectively [105]. These are each useful for a different type of defect, as illustrated in figure 1.11. The theory uniting all of these is that in an ionic material like perovskites, all crystalline imperfections will have a charge associated with them [103]. Thus one must choose a treatment option which matches to the dominant defect type, and the material can be passivated as such [106]. Of course, it is not truly so simple. Determining the dominant defect type can be difficult, and likely there is more than one type of imperfection in the crystal.

Though, as discussed above, many groups use an intentional excess of PbI_2 in their perovskite. In this case of excess PbI_2 there would be an expected dominance of iodide lattice termination (fixed negative charge), which would lend itself to passivation with positively-charged chemical moieties (such as K^+ or Lewis acids) [81]. Alternatively, the known evaporation of MA, FA, and I_2, at elevated temperatures [59], [107] would likely leave a Pb terminated surface (fixed positive charge), which would then lend itself to passivation with negatively-charges chemical moieties (such as Cl^- or Lewis bases) [108]. Furthermore, extensive characterization across the research field has led to the general conclusion that crystal grain surfaces were the primary locations for defects, and that the interfacial electronic states formed between these defective surfaces and the adjacent materials were the dominant loss pathway for most perovskite systems [103], [109], [110]. This allowed for more specific tailoring of passivation mechanisms, in that they could be targeted to these interfaces. This was accomplished either by depositing the passivating agent onto an already-complete perovskite layer, or by choosing a molecule sufficiently large as to not enter the lattice and rather sit on grain surfaces (as the large ammonium cations of the previous section did).

Examples of these methods include oxygen-based methods for binding Pb and I defects [118], [121]–[124]; inorganic Pb-salts[5] [112]–[114]; a few Lewis acids [119], [125]; and many Lewis bases [106], [115], [116], [126]–[128]. In terms of W_{OC}, the best of the oxygen based methods reached 0.69 V for an inorganic perovskite [121] and 0.47 V for a hybrid organic/inorganic perovskite [118], the Pb-salts achieved 0.34 V [114], Lewis acids reached 0.48 V [119], and Lewis

[5] Such as $PbSO_4$, PbSCN, or $PbCH_3CO_2$

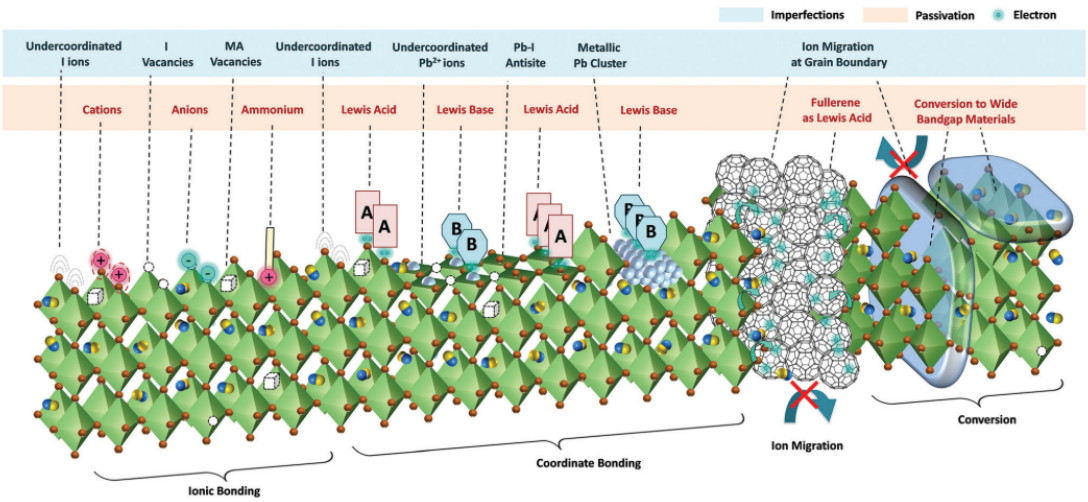

Figure 1.11 – Various defect types and methods for their passivation in perovskite materials. Perovskite surfaces can experience numerous types of defective states, many of which are detrimental to performance. Some are inevitable undercoordinated ions at lattice terminations, while others are due to vacancies or interstatials. In any case, the defect chemistry can be matched to a passivation mechanism, which are similarly numerous. Figure from [105], used with permission from the Royal Society of Chemistry.

base strategies got down to 0.37 V at best [106]. So, these methods already are bringing W_{OC} values of PSC down to the range of champion III-V and c-Si cells. Though all of the best values cited here came from perovskites with $E_g \leq 1.60$ eV, below the 1.65 - 1.70 eV range which is ideal for perovskite/c-Si tandems [47]. Finally, other unique methods that do not fit into any of these categories were also successful. These include simple I/Br/Cl tuning (W_{OC} = 0.44 V, [55]), using a self-assembled monolayer (SAM) contact material for an ideal bottom interface (W_{OC} = 0.44 V, [56]), and depositing an inert polymer above and below the perovskite (W_{OC} = 0.40 V, [117]). The comparison of these methods versus others is illustrated in figure 1.12. Multiple strategies produce W_{OC} below 0.40 V, but no one strategy dominates. In practice W_{OC} increases with E_g, meaning tandem-relevant materials are currently lower performing. Overall, chemical passivation of perovskites is an extremely diverse field, with multiple valid strategies, materials, and methods. There is no collective agreement on what the best strategy is, work continues on multiple paths. Still, this method was effective for our research, of which the results are discussed in section 2.4.

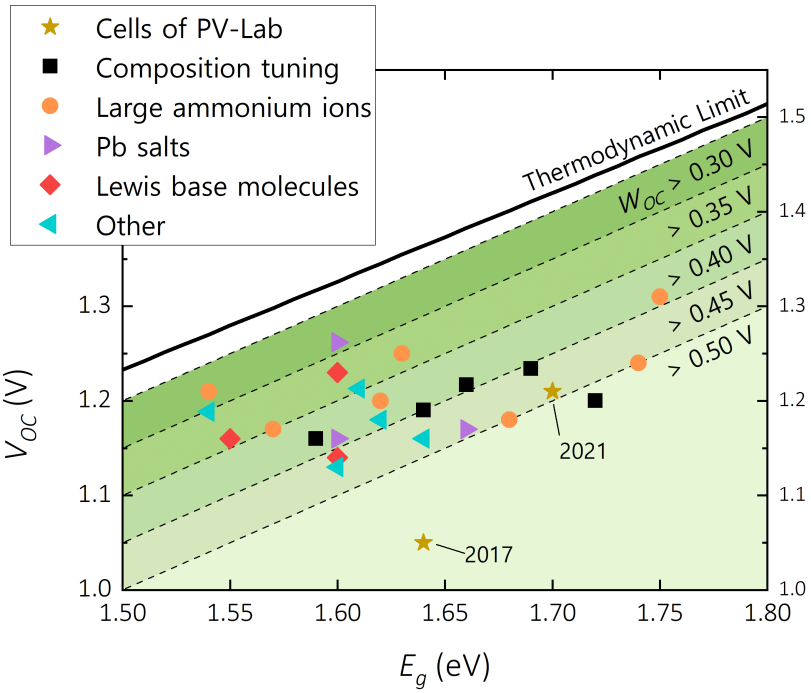

Figure 1.12 – V_{OC} values versus E_g for perovskite cells from literature. Multiple passivation strategies attain $W_{OC} \leq 0.40$ V, but not in the 1.65 - 1.7 eV E_g range that is relevant for perovskite/c-Si top-cells. V_{OC} values are the highest reported in each case, and E_g values are extracted from each publication individually. We used the point of maximum inflection in the reported EQE curve, according to the recommendation of [53]. The PV-Lab cells represent the champion PSC at the start and end of this thesis work. The "composition tuning" data comes from: [55]–[57], [81], [111]. The "large ammonium ions" data comes from: [94], [96]–[98], [100], [101]. The "Pb salts" data comes from: [112]–[114]. The "Lewis base molecules" data comes from: [106], [115], [116]. The "other" data contains multiple methods with only a single demonstration, and comes from: [99], [117]–[120].

Textured Absorbers

The material development and passivation efforts discussed so far succeeded in creating high-quality and well-passivated perovskite crystals, but this alone is not enough to make the highest-possible efficiency devices. The device stack as a whole must be designed with the goal of transferring the maximum amount of light into the perovskite layer. A cell's extracted current (J) depends on the material quality of the perovskite and the adjacent charge transport layers (CTLs), but is limited overall to the total photogenerated current (J_{ph}) of the cell. From the total AM1.5G spectrum that is incident on a given solar cell, some of it is reflected off the front surface, some is parasitically absorbed by the layers in front of the main absorber (perovskite in our case), and the remaining light which arrives at the absorber layer is then either absorbed (J_{ph}), reflected, or transmitted. Maximizing the J_{ph} therefore depends on the full device, and is not just about making a better perovskite.

As with any thin film based technology, the optics of a PSC is typically reduced to a 1-D problem consisting of parallel layers with varied thickness and refractive indices. Optimizing this for maximal absorption in a PSC is tricky however. For starters, the materials and layer thicknesses of the perovskite and CTLs are generally fixed to be what is optimal for charge transport and extraction. CTLs that are too thick will be resistive and too thin will risk pinholes. The perovskite should always be thicker for better absorption, but thicknesses greater than the average charge diffusion length will cause not all carriers to be collected. For example, the optical properties of perovskites can give absorption coefficients in the range of $10^4 - 10^5$ cm^{-1} [48], corresponding to needing roughly 1 - 3 µm layer thickness to achieve 95% absorption. Perovskite diffusion lengths have been measured in the range of 0.5 - 1 µm using time-resolved photoluminescence [129] and steady-state photocarrier grating [130], but also values up to 12 µm using a unique back-contacted selective contacts method [131] and 19 µm using solution-grown single crystals of perovskite [132]. Despite these reports of diffusion lengths well above the threshold for complete absorption, nearly all record-setting PSC use layer thicknesses below 1 µm [57], [85], [98], [106], [111], [133]. This may be because realistic diffusion lengths are closer to the commonly measured values of 0.5 - 1 µm [129], [130], or because labs find that thinner layers are easier to manufacture at high quality.

Surface texturing appears as a fitting solution to increase absorption in thin layers. This would cause light to scatter within the absorber, reflect multiple times off the textured interface, increase optical path length in the absorbing layer, and increase J_{ph}. It is known that for the case of perovskites on c-Si (in tandem configuration), surface texturing reduces the front-side reflection losses by 90%, and overall increases the absorbed current density by 1.7 mA/cm^2 [134]. In both tandem and single junction PSC cases, textured designs improve the angular response of the cell, which reduces the need for mechanical tracking systems in PV installations [135]–[137]. Thus texturing can have many benefits for both single junction and tandem cells. Transitioning from flat to textured architectures has helped improve optical performance in technologies similar to PSC, such as thin film Si [138]–[140]. And beyond thin films, surface texturing is used to increase absorption and reduce material consumption [141]. Various

methods have already been used to introduce textured interfaces to single junction perovskite cells, with varied success [137], [142]–[146]. These methods relied on etching of the glass substrate [137], an underlying textured polymer layer [142], [143], imparting texture on charge transport layers [144], [145], or an FTO substrate with intrinsic roughness [146]. All of these methods have their advantages, but they also have their flaws. We worked towards developing a better solution, which is the subject of chapter 3.

1.2.3 Tandem Research

Alongside single-junction development of PSC, much effort has been put towards realizing their potential as top-cells in tandem configurations. The basis of multijunction PV was discussed in the section 1.1.2, but perovskite/c-Si tandems are of particular interest, and make up a significant portion of this thesis work. Perovskites, as discussed above, are cheap, easily produced, and high-performing. On top of that, the range in which their E_g can be tuned overlaps entirely with the 1.6-1.8 eV range that is ideal for a top-cell on c-Si [47]. Thus, much research has been done towards adapting perovskite technology to work as top-cells.

The first major distinction to be made for perovskite/c-Si tandem designs is the cell architecture. Tandem cells can be made in four-terminal (4T) or two-terminal (2T, or monolithic) configurations (figure 1.13). 4T implies that the two sub-cells are each independently connected to a load resistance, and are electrically independent from eachother. 2T implies that the subcells are deposited directly onto one another (monolithic), and are electrically connected in series. The consequences of each design make them better suited to different situations, but both have similarly high efficiency potentials [47], [147]. Directly compared, the advantages of 4T structures are related to simplicity. Each sub-cell can be independently manufactured and later combined, releasing each cell from the manufacturing constraints of the other. They do not need to be electrically or optically matched to eachother. They can operate independently and one is not affected by the performance of the other. The advantages of 2T structures are related to feasibility. Monolithic integration reduces the cost and optical losses of the tandem stack relative to 4T, due to the removal of the top-cell rear and bottom-cell front electric contacts (figure 1.13). These contacts, which are generally a full-area transparent conductive oxide (TCO) with Ag fingers and busbars for current collection, cause optical losses due to parasitic absorption and shadowing, along with the added cost of low-abundance elements (such as In in the TCO [148]). Separate from the cell design, the additional processing steps of adding perovskite top-cell production onto an active c-Si line relative to building a novel perovskite top-cell line along with a separate line for sub-cell unification makes the 2T structure more economically appealing [22]. Finally, 2T architectures can allow the top-cell to benefit optically from the surface texturing of the c-Si [134], [149]. This is contingent on the perovskite being conformally coated on the c-Si surface, which is a development already realized in our lab [62]. Overall, the similar potential performance of 2T versus 4T and the economic advantage of 2T, makes 2T architectures the more realistic option for eventual industrial production, and a focus of recent literature.

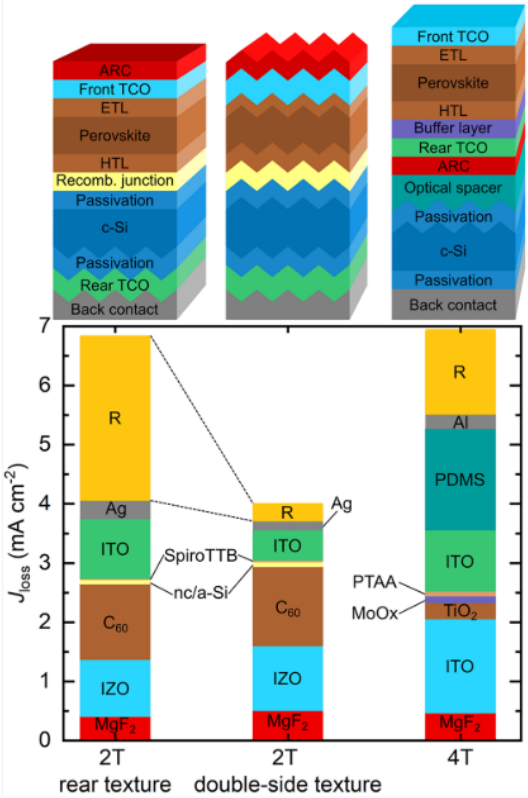

Figure 1.13 – Different perovskite/c-Si tandem architectures and their optical losses. Perovskite/c-Si tandem cells can be made in monolithic 2T or stacked 4T configurations. In the 2T configuration, the front surface of the c-Si bottom-cell can either be textured or not, giving significantly different front reflective losses. The 4T case loses optically due to the additional TCO layers and likely shadowing losses from metal fingers used to collect current between the sub-cells. Reprinted with permission from [134]. Copyright 2019 American Chemical Society.

There are disadvantages of the 2T structure, however. These come from the consequences of monolithic fabrication and serial electrical connection. For the fabrication, the perovskite deposition is constrained to the processing limitations of the bottom-cell. Early 2T perovskite/c-Si tandem reports used bottom-cells based on a diffused Al back surface field (Al-BSF) [150]. These were compatible with the high-temperature PSC processing (sintering of TiO_2 electron transport layer (ETL) at 500°C), but did not perform as well as other c-Si technologies. Specifically, bottom-cell performance was improved when the top-cell processing was modified to use lower temperatures and silicon heterojunction cells (SHJ) could be used instead [151]. This gain is shown between the first two cases in figure 1.16. SHJ are likely the ideal c-Si cell technology for tandem applications [152], and nearly all recent publications have used SHJ as bottom-cells[6] [111], [127], [149], [154]–[156]. For SHJ, the whole top-cell production must remain under 220°C[7], and either accommodate the c-Si texture [127], [149], [155], [159] or mechanically polish the front texture [111], [154], [160].

The production constraints of SHJ have been met in various ways. For our lab, the previous two theses [62], [63] developed of low-temperature CTLs, a hybrid deposition system for the perovskite layer, and vapor-phase deposition of all other layers; together enabling full

[6] Although we acknowledge that high-efficiency results have also been achieved with other bottom-cell technologies [153].

[7] Above 220°C, hydrogen and dopants from the passivation and extraction layers can diffuse into the bulk, degrading the quality of both [157], [158].

compatibility with SHJ. The details of the hybrid perovskite deposition method and why it is compatible with SHJ bottom-cells are given in the following chapter (section 2.2). Outside of our lab, other methods have been used to join PSC with SHJ effectively. One group succeeded in evaporating the full perovskite layer [159]. Some use SHJ with sufficiently small pyramids on the front, so that standard solution-processing techniques can be used for perovskite deposition [127], [155], [156], [161]. Larger and more optically effective front-surface textures on the bottom-cell do not generally allow for solution-processing techniques [149]. Others use SHJ with a polished front side, so that the same perovskite deposition parameters can be used in the tandems as is optimized on single junction PSC [111], [154], [160]. But regardless of the perovskite quality on these surfaces, the fully textured design is optically superior due to the near 10-fold reduction in front reflection losses (figure 1.13, and [134]). Each of these cases is optically compared in figure 1.13, and the improvement in demonstrated monolithic tandem EQE can be seen between the final two cases in figure 1.16.

The second challenge of 2T construction is that of the series electrical connection. This requires development of a recombination junction between the sub-cells for the electrons of one sub-cell to recombine with the holes of the other, and imparts the constraint of current-matching. For the recombination junction, we can again thank the work done by previous students of our lab, who demonstrated an efficient and optically-ideal nanocrystalline-silicon bilayer [62], [162]. The current-matching requirement comes from the fact that for two sub-cells in series, the total stack can only pass as much current as the least-productive sub-cell. This puts fixtures on the top-cell design, as the perovskite bandgap and thickness must absorb and transmit equal amounts. The optimal solution for this changes depending on the optics of the bottom-cell, recombination junction, and front TCO, as well as the overall performance of the individual sub-cells [152]. Thus the tuning and optimization of this condition is a problem to be solved experimentally, and will be discussed in section 4.2. As a final note, the current-matching condition complicates the simulated energy yield due to daily spectral shifts. 4T tandems do not suffer from these shifts, but the simulated loss due to current-matching is only 1.7% relative performance ratio or 0.5% absolute efficiency [147].

Once the perovskite is deposited directly on the c-Si bottom-cell, certain aspects of the top-cell design become more significant. Notably, the polarity of the tandem matters for cell optics. In the early days of perovskite research, all cells were fabricated in the n-i-p configuration (shown in figure 1.14). Due to the history of n-i-p devices in early PSC, development on p-i-n PSC typically refers to them as "inverted" (though modern PSC are flexible [163]). The n-i-p structure was used in early demonstrations of 4T tandems [150], [164], but this did not translate well to 2T designs (first two cases in figure 1.16). The issue was that single junction n-i-p PSC were illuminated in substrate (through the glass), but then would need to be illuminated in superstrate for monolithic tandems. This meant the light would have to pass through the p-type hole transporting layer (HTL). At the time this was typically a doped Spiro-OMeTAD layer, which imparted significant parasitic absorption in the blue and UV parts of the spectrum. For 4T tandems, the top-cell can simply be mechanically flipped, but for 2T tandems the top-cell polarity would need to be flipped. This was achieved via developments to CTL materials and

deposition methods [160], [163], [165], and the resulting improvement to the tandem optics is shown in figure 1.16 between the two middle cases. The optical improvement passed more light to the top-cell, and has remained this way in nearly all monolithic tandem publications since the start of this thesis.

These advancements to cell design and manufacturing capability, together with the perovskite material improvements discussed in the previous section, have enabled monolithic perovskite/c-Si tandems to climb in efficiency over the years. The progress of the overall field is shown in figure 1.15. As the field advances, more attention is applied to upscaling and novel deposition methods. These are necessary steps for transferring the technology to industry, but naturally lag behind the lab-scale champion devices. Still, the best tandems are > 10% absolute below their theoretical maximum [15]. So what still needs to happen to take perovskite/c-Si tandem efficiencies to their realistic limits? c-Si cells benefit from decades of research. There is still room to grow, but less so than for top-cells. On the perovskite side, advancement of record perovskite single junction efficiencies in the last few years has mostly come from fill-factor (FF) and V_{OC} improvement, along with smaller improvements to short-circuit current (J_{SC}) (detailed in [166]). This is a similar situation for tandem top-cells, where composition engineering, chemical passivation, and improved charge selective layer interfaces has led to V_{OC} values over 1.9 V in tandems on SHJ, but still with tandem FF below 80% [111]. There is some room for improvement to V_{OC} [104], but less so than for FF. Optical improvements and conformal coating of perovskite top-cells on c-Si pyramids have allowed for near-optimal J_{SC} values as well [149], [160], [167]. Thus, FF improvement remains the main route to higher tandem efficiencies. This is a complex problem, given that the FF depends on a multitude of factors. From the literature, the recommended paths are optimizing charge selective transport out of the perovskite layer [168] and reduction of current lost to recombination [166].

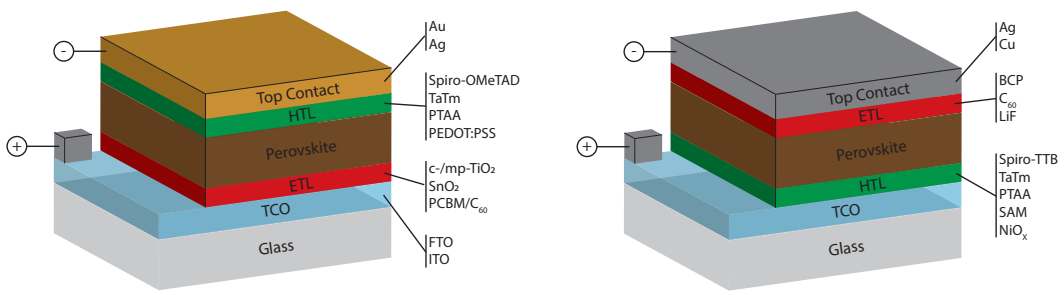

Figure 1.14 – Cell architectures with opposite polarities for PSC. PSC can be fabricated in either orientation, and with light incoming from either side. FTO stands for fluorinated tin oxide, ITO for indium tin oxide, Spiro-OMeTAD is 2,2',7,7'-tetrakis-9,9'-spirobifluorene, TaTm is N4,N4,N4",N4"-tetra([1,1'-biphenyl]-4-yl)-[1,1':4',1"-terphenyl]-4,4"-diamine, PTAA is poly[bis(4-phenyl)(2,4,6-trimethylphenyl)amine], PEDOT:PSS is poly(3,4-ethylenedioxythiophene) polystyrene sulfonate, c- and mp-TiO_2 stand for compact and mesoporous titanium dioxide, PCBM is [6,6]-phenyl-C_{61}-butyric acid methyl ester, C_{60} is fullerene "Buckyballs", BCP is bathocuproin, Spiro-TTB is 2,2',7,7'-tetra(N,N-di-p-tolyl)amino-9,9-spirobifluorene, and SAM can be 2PACz, MeO-2PACZ, or Me-4PACz.

For the first goal, it is proposed to either use highly doped materials for extreme charge mobility values, or extremely thin molecular monolayers with high selectivity. In both cases, the interface should be lossless. Such thin monolayer materials already exist for the HTL (self-assembled monolayers, or SAM, [56]), but have not yet been demonstrated for the ETL. For the option of highly doped CTL layers with high mobility, industrial compatibility is unlikely due to the high cost of the materials. Despite successful demonstrations of such layers [163], [168], [169], these required layer thicknesses of tens of nanometers. Accurate cost calculations are imprecise due to not knowing the density of the evaporated layers, but estimates based on the lattice spacing are possible. For C_{60} (a common ETL) with a lattice of 14.15 Å [170] and price of 500 CHF/g, each m^2 of deposition would be 0.403 CHF/nm; and for TaTm (a common HTL) with a lattice of 15.22 Å [171] and price of 750 CHF/g, each m^2 of deposition would be 1.686 CHF/nm. 50 nm of both would then contribute just over 100 CHF/m^2 in production costs. Given the additional cost justifiable by the efficiency gains of perovskite/c-Si tandems over single junction c-Si (roughly 75 \$/m^2, section 1.1.2), this is not feasible. This is compared to realistic current production costs of thin film solar which is in the range of 40 - 50 \$/m^2 [14].

For the second goal; the non-radiative recombination rates in the perovskite, on its surfaces, and at its interfaces should be reduced to near zero. This way all charges will be able to be extracted before recombining, even in the near flat-band conditions of the operating voltage. In practical terms, the realistic limit for PSC can be taken from the example of III-V solar cells. Like perovskites, III-V materials such as GaAs have a direct E_g transition and therefore experience similar radiative loss processes. The best GaAs cell has a W_{OC} of 0.31 V [13]. Perovskite cells have gotten below 0.4 V of W_{OC} [98], [106], [114], [116], but these were not for materials with tandem-ideal E_g values. This is illustrated in figure 1.12, where perovskites in the 1.65 - 1.70 eV range lag behind in demonstrated W_{OC}. These two goals, when realized, will enable high performance perovskite single junction and top-cells in tandems, with potentially over 21.0 mA/cm^2 of J_{SC}, 2.0 V of V_{OC}, 80% FF, and a total efficiency over 33%.

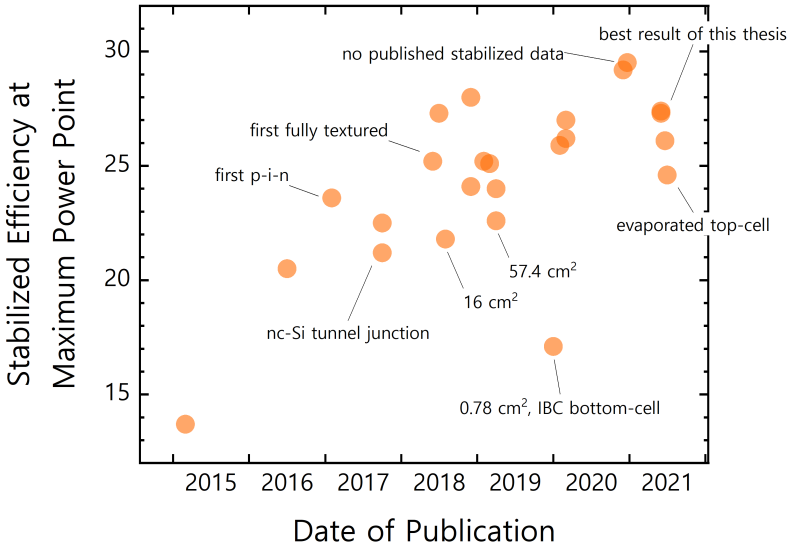

Figure 1.15 – Reported stabilized efficiency values for monolithic perovskite/c-Si tandems in literature. Except for the single noted case, all values come from stabilized maximum power point tracking. Other than the noted cases, all cells have an area of 1 - 1.5 cm^2. IBC stands for interdigitated back contact, and this cell was measured in 3T configuration. The data was obtained from: [12], [111], [127], [133], [149]–[151], [153], [154], [156], [160], [162], [172]–[181].

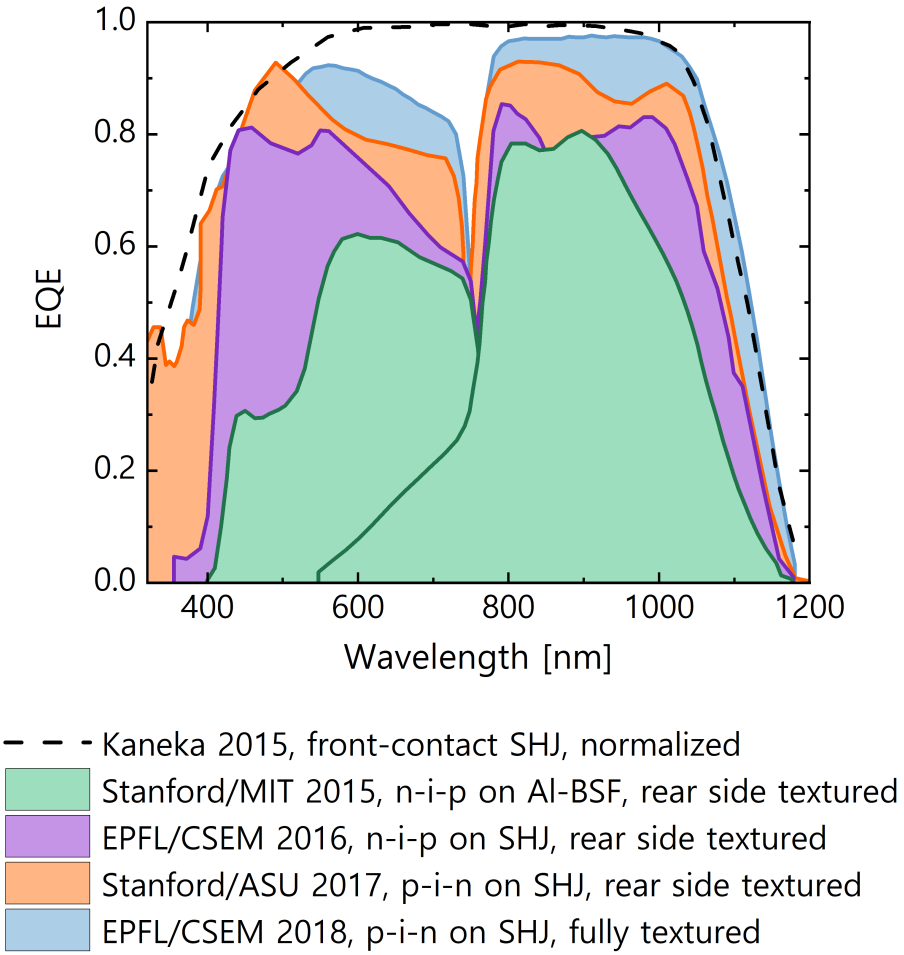

Figure 1.16 – EQE curves from major developments in monolithic perovskite/c-Si tandem history. Over time, advancements in manufacturing capability and perovskite material understanding enabled increasingly efficient use of the solar spectrum. The main milestones are shown here. In order, the summed current density (in mA/cm^2) of each result is: 26.2 [150], 34.3 [151], 37.4 [160], and 40.4 [149].

2 Material and Interface Development in Single Junction PSC

Abstract

In order to fabricate perovskite top-cells on the micron-scale pyramids of modern c-Si solar cells, certain fabrication restrictions must be adopted. These restrictions are met here by using a hybrid physical vapor deposition / solution process (PVD/SP) method. This process relies on two separate deposition processes, which creates a large experimental space. In this chapter, we unpack these variables and discuss how they affect the end device performance. This discussion is broken up into three parts, focusing each in turn on i) the isolated perovskite layer, the balance of constituent materials, and the reduction of bulk disorder; ii) the surfaces of the perovskite, and how they interact with adjacent layers to form interfaces of differing quality; and iii) the morphology of the perovskite, and the effect this has on the performance of full PSC. Overall, the hybrid PVD/SP method proves to be indeed complex, but understandable and predictable through effective characterization. The results shown in this section served as the foundation for the rest of the thesis work, for which the same PVD/SP method was used throughout.

2.1 Introduction and Motivations

The main motivation behind our choices of which methods and materials to use comes from the long-term goal of compatibility with industrial scale monolithic tandem cells. This is not to say that we are fully in line with industry and ready to transition at any moment. Rather that all of our methods are either already proven as scalable or are reasonably swapped out for a scalable process. The result of this is that we sometimes reject methods that are ubiquitous among record-breaking perovskite cells, such as the widely successful anti-solvent dripping method [182].

The main restriction applied in our lab is that of using a "hybrid" evaporation (physical vapor deposition, PVD) / solution-process (SP) method for our perovskite fabrication (figure 2.1). This consists of first evaporating a "template" layer consisting of the perovskite's inorganic components, then spin-coating a solution of the perovskite's organic components, and finally annealing the bi-layer to interdiffuse the materials and crystallize the perovskite. For the template, lead iodide and cesium bromide are co-evaporated at fixed rates in a vacuum. This process is easily scalable, and PVD processes are already present in industry [183]. For the spin-coating process, formamidinium salts with iodide or bromide (FAI or FABr) are dissolved in ethanol, and dynamically dropped onto a spinning substrate. This is not scalable, but can in theory be replaced 1:1 with a vapor transport deposition process (which is already in development [184]) or slot-die coating (already industrially scaled). Finally, the substrates are annealed to both interdiffuse the two layers and cause them to crystallize into the final perovskite film. The disadvantage of this method is the complexity, with three separate steps to form a single layer. The variables involved include the thickness, constituent ratio, and morphology of the PVD template; the solution concentration, solvent, solute, and spin speed of the SP layer; and the length, temperature, and environment of the anneal. These are many and interdependent variables, but all are controllable, and the work in this chapter aims to find the ideal balance.

The advantages of the PVD/SP method come from its compatibility with the ideal tandem process. As discussed in section 1.2.3, certain conventions of single junction PSC had to be adapted for compatibility with two-terminal tandems, such as the polarity, and removing the high-temperature mesoporous TiO_2 ETL. But one of the main challenges was to deposit the perovskite thin film (typically 0.5-1 µm) uniformly on the large (typically 2-10 µm) front-surface pyramids of SHJ. This surface texture is optically beneficial for the c-Si and would be as well for a top-cell that follows the same surface profile. But standard SP perovskite recipes both fail to cover the peaks of c-Si pyramids (of typical size) and fail to maintain the same morphology on their top surface as is present in the c-Si below [149]. This is all aside from the issue of common perovskite SP recipes using harsh solvents that can damage underlying layers [57] or are toxic [185]. Perovskites have nonetheless been used successfully on top of c-Si bottom-cells by engineering smaller pyramids (> 1 µm) [127], [155], [156], [161], or polishing the pyramids off entirely [111], [154], [160]. But these strategies incur optical losses, and even the cells that retain some of the c-Si texture have optically-poor flat front interfaces.

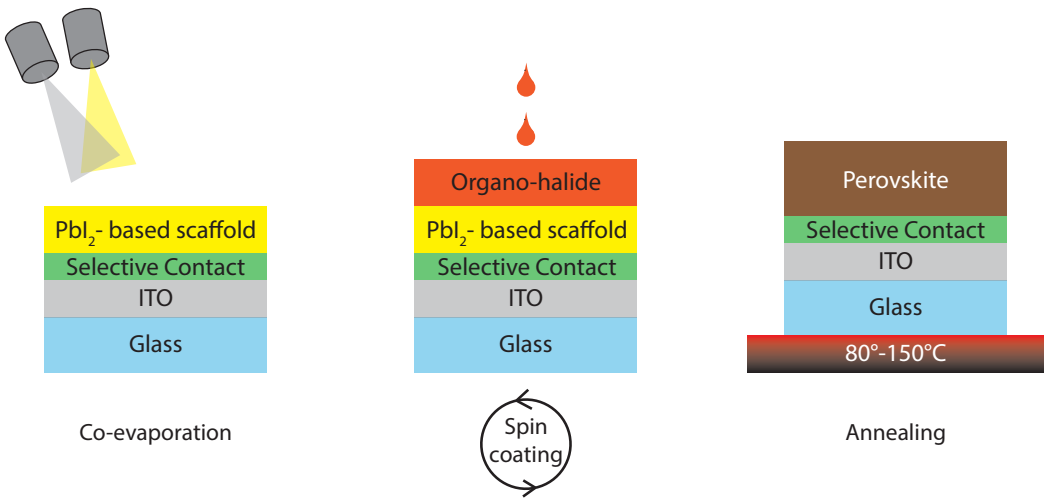

Figure 2.1 – Hybrid PVD/SP method for perovskite fabrication. Perovskite is formed in three distinct steps. First a PbI_2 based template is evaporated onto the substrate. This can include a co-evaporation of CsI, CsBr, $PbBr_2$, etc. at a fixed rate. Then a solution of organo-halide salts is spin-coated onto the template. This can include FA, MA, or other organics, ionized with I^-, Br^-, or Cl^-. Finally, the bilayer is annealed to interdiffuse the layers and crystallize the components into a perovskite.

PVD processes offer a solution, in that evaporated layers easily form uniform coatings over rough surfaces. PVD methods have been realized for perovskite materials in flat single junction PSC [163], [186] and even monolithic tandems on textured c-Si [159]. Although, this comes with significant reported challenges. Organo-halide salts are known to deposit over the entire chamber, even out of the line of sight of the evaporator [187]. This consumes excess material and causes contamination of other sources and unreliable thickness measurements as compared to directional PVD processes. The depositions are difficult to control due to organo-halides not sticking to the traditional quartz crystal balances used to measure evaporated thickness [188], and the adsorption of organo-halides to surfaces being highly dependent on the precursor purity [189]. Looking to our expected perovskite which is based on FA cations, FA is already known to degrade into non-viable compounds when heated to the vapor phase [62], [190]. So, despite the proof-of-concept demonstrations, full vapor-phase perovskite remains challenging. It is not considered in this thesis work, but is an active area of research in past and future theses.

By comparison, the hybrid PVD/SP deposition route solves many of these problems together, and allows complete compatibility with SHJ and other bottom-cell technologies [153]. No layers are deposited above 200°C, it is compatible with either polarity, and the only solvent used is the relatively weak ethanol. The PVD step ensures a uniform and conformal coating of the perovskite layer, and the porosity of the template acts as a sponge to capture the liquid-phase components without letting them simply pool in the valleys [149]. The SP step uses a weak solvent which doesn't dissolve the template, and allows for the facile testing of different halide

mixtures and passivating additives. It is restricted to lab-scale devices due to the uniformity limitations of spin-coating (around 100 mm limit); but once material development moves past the need for regular variation of the solution composition, the SP step could reasonably be replaced with a non-PVD method for large-area organo-halide deposition [184]. Overall, the hybrid PVD/SP method demonstrates likely compatibility with the expected tandem cells of the future, while retaining the capability of rapid experimentation. It is a tool that facilitates research towards bringing high-efficiency perovskite/c-Si tandems to the PV market, and was chosen as the experimental basis of this thesis work.

2.1.1 The Standard Cell Architecture and Perovskite Composition

Throughout this thesis, single junction perovskite solar cells will be presented, and referred to as PSC for brevity. In all cases, unless stated otherwise, this will mean PSC of a single standardized architecture, displayed in figure 2.2. This is a p-i-n stack with opaque rear contact, and illuminated through the glass substrate. Fabrication of these devices took place as follows. First, ITO-glass substrates (indium-tin-oxide, purchased from Kintec) are washed with a commercial detergent and further cleaned with one minute of 250 W O_2 plasma. Optionally, 15 minutes of UV-O_3 irradiation could be used (system from UVOCS Inc). Upon these, a HTL is deposited. This can be sputtered NiO_X (20 nm, followed with a 15 minute anneal at 200-300°C), evaporated Spiro-TTB (15 nm, 2,2',7,7'-tetra(N,N-di-p-tolyl)amino-9,9-spirobifluorene, from Lumtec), evaporated TaTm (15 nm, N4,N4,N4",N4" -tetra([1,1'-biphenyl]-4-yl) -[1,1':4',1"-terphenyl] -4,4"-diamine, from Lumtec), or a self-assembled monolayer (2PACz or MeO-2PACz from TCI, or Me-4PACz from Sikémia). SAMs are not evaporated, but deposited by spin-coating according to the method in [56]. Which material is used is significant, and the differences will be discussed in section 2.3.1. Generally, it is observed that PSC with NiO_X as HTL are lower in efficiency but very reliable, with near 100% yield and good sample-to-sample uniformity. Because of this, NiO_X was used heavily at the beginning of the thesis work. Next, the perovskite is deposited according to the hybrid PVD/SP method detailed above. Although the details of this method are adapted throughout the following section. The ETL is then deposited onto the perovskite layer by evaporation. This is always based on C_{60} fullerenes (optimally 20 nm, from Nano-C). The slowest evaporation rate is ideal for achieving high-quality layers. Typically C_{60} was evaporated at 70 - 80 W and 0.2 Å/s for low-purity material and 50 - 60 W and 0.1 Å/s for high-purity sublimated material (rated 99.90%, Nano-C). The C_{60} is occasionally preceded with a 1 nm evaporation of LiF. This has been shown to have good passivation abilities [110], but also cause problems to stability [191]. So, it was not always used, but it is noted in the text on the occasions where it is present. Finally, the cells are finished with 120 nm of evaporated Ag as the rear electrode. The Ag evaporation is done through a shadow mask to create three separate areas of about 0.5 cm^2 per substrate. For measurement, the cells area is masked to 0.25 cm^2, unless otherwise stated.

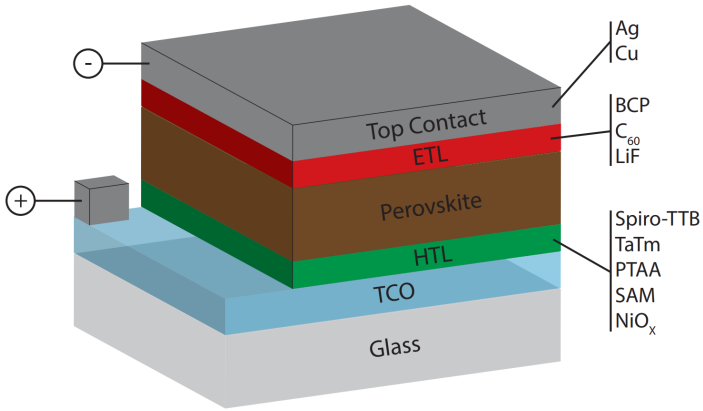

Figure 2.2 – Diagram of the typical single junction PSC cell stack. The orientation with p-selective contact on the illumination side makes this a p-i-n structure. For HTL, Spiro-TTB, TaTm, or NiO_X could be used. The ETL always included C_{60}, but could optionally include LiF as well. The top contact was either Ag deposited on the C_{60}, or Cu with a BCP interlayer.

For the hybrid perovskite deposition, some variables were held constant for the entirety of the thesis work, some for the majority, and some were adapted continuously. When referring to "baseline" material, this implies a standard template layer of 180 nm PbI_2 with 10% volume ratio of CsBr[1]; controlled by evaporation rate of 1.0 Å/s or 0.1 Å/s measured by quartz crystal monitors (for PbI_2 and CsBr, from Alfa Aesar, TCI, or Abcr); the use of ethanol as solvent for the SP step; a dynamic instead of static solution deposition[2]; spinning in a purged N_2 environment, 4000 rpm spin speed for 30 seconds; and the 1:2 ratio of FAI:FABr in the solution (generally 0.45 - 0.50 M). In any case where these values are not used, it is noted in the text. The more commonly changed variables are the annealing time and temperature, the annealing environment, and the SP concentration. Typically the annealing was 20 minutes at 150°C, but this was often varied and is stated in such cases. The estimated stoichiometry of this layer is $Cs_{0.19}FA_{0.81}PbI_{2.27}Br_{0.73}$ based on the above input parameters. The effects of variables such as the evaporation rate, CsBr ratio, and substrate-area uniformity are discussed in section B.6

2.1.2 Fabrication and Characterization Tools

For perovskite deposition, we used various commercial and homemade tools. ITO/glass substrates were purchased form Kintec, and rated at 15 $\Omega/\square$. A homemade deposition chamber was used to evaporate CTLs, evaporate metals and sputter InZnO. PbI_2 template layers were evaporated from a Lesker Mini Spectros system. Occasionally metals or MgF_2 were evaporated in a Leybold-Heraeus L560 system. Processing took place inside Jacomex glovebox systems, with O_2 and H_2O levels controlled below 1 ppm. The spin-coating unit was from Laurell, model WS-650Hz-8NPPB. Annealing took place outside, in a controlled humidity box (W-Tech, model GB250-A1) and on a hotplate from Präzitherm. Atomic Layer Deposition (ALD) took place in a Picosun R200-Std machine. TCO layers were deposited by sputtering in a MRC-II

[1] From energy-dispersive X-ray analysis of our films, we find that the 10:1 volume ratio of PbI_2:CsBr in fact gives a 1:0.19 molar ratio.

[2] Referring to the solution being dropped onto an already spinning substrate, instead of being deposited on the substrate prior to rotation. This was observed to give better sample-to-sample variation. Static methods were observed to introduce a significant dependence on the time between the solution deposition and the start of spinning, which is difficult to reliably control.

unit. ZnO layers were deposited using a homemade system. O_2 and Ar etching took place in a Oxford Instruments Plasmalab 80plus system, at 250 W and 100 W respectively. Silicon layers were made with a plasma-enhanced chemical vapor deposition (PE-CVD) reactor system, consisting of a PlasmaBox (Oerlikon Solar) chamber within a homemade vacuum system, and typically called a KAI reactor.

Many measurement and characterization systems were homemade, such as those for measuring external quantum efficiency, photothermal deflection spectroscopy, and photoluminescence quantum yield. For external quantum efficiency, the sample was illuminated by a halogen lamp split by a diffraction grating. The illumination was chopped and the current measure matched at 232 Hz. For photothermal deflection spectroscopy, the sample was again irradiated with a diffraction-split halogen lamp. The irradiated and transmitted intensities were directly measured. The sample was placed in a quartz cuvette with fresh FC-72 Fluorinert (from 3M). The deflection was measured by a 633 nm laser which was aligned to pass just in front of the sample and fall on a spatial intensity sensor approximately 400 mm away. For photoluminescence quantum yield, the samples were irradiated with a 532 nm laser which was attenuated to 0.05 - 1 sun intensity. All light was collected in a homemade integration sphere, and transfered to the measurement by fiber optic cable. The illumination spectrum was measured by an Ocean Insight Maya 2000 Pro spectrometer, and the luminescence spectrum by an Ocean Optics USB2000 spectrometer.

Current-voltage properties were measured with Kiethley models 2000, 2700, and 2601A. Solar AM1.5G radiation was simulated with a clas AAA WACOM Super Solar Simulator that combines Xe arc and halogen filament lamps. Measurements were typically taken at 0.1 - 1.0 V/s. Point measurements of photoluminescence were carried out with a 514 nm laser as part of a MonoVista CRS+ system, with capture times from 100-500 ms. A 10x objective lens was used to capture an area of the sample which is large relative to potential grain-to-grain inhomogeneity of perovskites, approximately a 80 µm diameter spot-size. The intensity was scaled with neutral density filters to always approximate 1-sun, which was measured as 5.0 µW total power for the 10x objective. Four-point probe measurements were done with Kiethley models 2700 and 2601A. Profilometry measurements for layer thickness were done on a Ambios XP-2 system. Transmission and reflection spectra were measured on a PerkinElmer Lambda 950 spectrometer, using a 150 mm InGaAs integration sphere, also from PerkinElmer. Atomic force microscopy was performed on a Bruker Dimension Edge system, using TESPA-V2 tips from Bruker. Scanning electron microscopy was preformed either with a JEOL JSM-7500TFE or Zeiss Gemini SEM 450, typically with 5 keV accelerating voltage. c-Si lifetimes were measured on a Sinton WCT-120 instrument. X-ray diffraction measurements were primarily carried out by Dr. Florent Sahli on a PANalytical Empyrean system, but also occasionally on a PANalytical X'PertPRO system. Both used Cu K α radiation of 1.54 Å. X-ray photoelectron spectroscopy was carried out externally by Dr. Mounir Mensi, using a AES: Kratos Axis Supra system. Grazing-incidence wide-angle X-ray scattering measurements were carried out externally by Dr. Julian A Steele on the NCD-SWEET beamline of the ALBA Synchrotron Light Source in Cerdanyola del Vallès, Spain. The source was 0.957 64 Å X-rays incident at 1° from parallel.

2.2 Bulk Material Quality of Perovskites from the Hybrid Method

Previous doctoral students and post-doctoral researchers started the development of the hybrid PVD/SP method [62], [63]. They determined what layer thicknesses, spin-coating methods, and halide ratios to use in order to fully convert the template into a perovskite with an applicable E_g for tandems (roughly 1.69 eV) [192]. They settled on optima that were not changed for the duration of this thesis, including the methods and variables listed in the previous section. This was a strong foundation on which my work was to build. The initial goal for this thesis work was to go beyond PSC efficiency as the main metric for material quality and expand to more detailed characterization, then to use this knowledge to build an understanding of what limits material performance, and finally to apply that understanding towards making higher-performance perovskite materials and perovskite/c-Si tandems. Thus, the first step was to dig deeper into the perovskite material formation. This includes the balancing of the PVD and SP steps, the annealing/interdiffusion of the layers together, and the crystallization into a high-quality semiconductor film.

2.2.1 Bilayer Interdiffusion

The hybrid PVD/SP method is most notable for separating the perovskite precursors into two different layers. As expected, this implies that the two steps be balanced relative to eachother. Achieving this balance depends on matching the deposition parameters of each layer, but also "mixing" them correctly. The quantity of template is defined by the measured thickness of PbI_2 during the evaporation. This is used to define the end layer thickness, as the other steps are tailored to fit with this. The quantity of organo-halide is determined by the spin-coating parameters. Increasing the solution concentration will increase the quantity deposited, and increasing the spin speed will reduce the layer thickness and increase uniformity. The iodide to bromide ratio is also relevant, but not used as a variable because of its connection to the perovskite's E_g, which is fixed for compatibility with c-Si as bottom-cell [47].

To illustrate the importance of a balanced layer, baseline single junction PSC were fabricated with either a strong excess or deficiency of organohalide, and the same template recipe. Current-Voltage (JV) and external quantum efficiency (EQE, a measure of electrons out per incident photons) measurements for these layers are shown in figure 2.3. In the JV plot, the unbalanced samples have worse performance and strong hysteresis between the forward and reverse-direction scans. The hysteresis can be attributed to mobile ion species in the layer; unincorporated ions left by the component in excess [74], [75]. For the EQE, both unbalanced samples have lower conversion over the spectrum. This could be due to current lost to recombination, screening of the electric field by mobile ions, or reduced absorption due to less perovskite material. Notably, the FAX deficient sample displays a characteristic loss in the low-wavelength regime that is due to the parasitic absorption of residual PbI_2 (below 500 nm). We note that it is commonplace to include a 5 - 10%mol excess of PbI_2 in perovskite

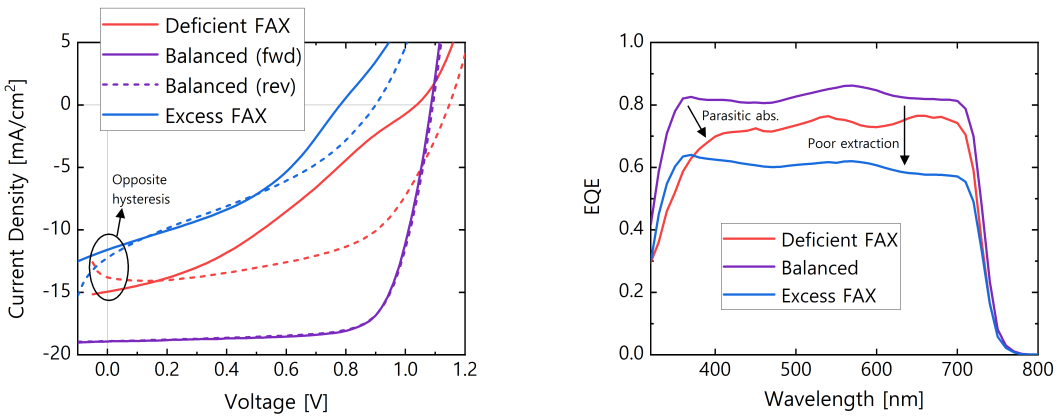

(a) **(b)**

Figure 2.3 – Performance of PSC made with unbalanced hybrid PVD/SP method. (a) JV and (b) EQE of cells were made with normal template and annealing, and with either excess or deficient concentration of the organo-halide (denoted FAX) solution. The hysteresis present in the JV curves is caused by mobile ions that stabilize at a rate slower than the scan speed (generally 0.1 - 0.5 V/s). Because of this, scans taken in both the forward and reverse directions are displayed.

films [64], [65], [182]. This imparts a gain in performance, but at the cost of lower long-term stability [66], [67]. Based on the examples in literature, we aim for a film with no or minimal excess PbI_2.

Achieving the ideal balance in the final perovskite depends on having the correct contributions from both PVD and SP steps, but also on correctly mixing them. We refer to this process as "interdiffusion", and treat it as separate from the crystallization of the mixed components into a perovskite ABX_3 phase. For our method, the interdiffusion primarily takes place during the annealing step. The quality of the interdiffusion can be observed in X-ray diffraction (XRD) diffractograms, which detects the crystal phases of perovskite and the component materials. Figure 2.4 shows such measurements, performed on layers from the same PVD/SP deposition which were then annealed at different temperatures in the same environment. After annealing at low temperatures, the bilayer is not fully mixed, and there is a peak at 10.1° which comes from crystalline FA-halide salts. As the temperature increases, this peak disappears and the film appears "fully converted" because only the perovskite diffraction remains. That is, until 165°C where a peak appears at 12.6°, from diffraction off the PbI_2 crystal lattice. The presence of crystalline PbI_2 indicates a deficiency of FA, which is likely due to FA evaporation above 150°C [107]. Despite equal starting conditions, either component can be found in excess depending on the heat applied, or neither.

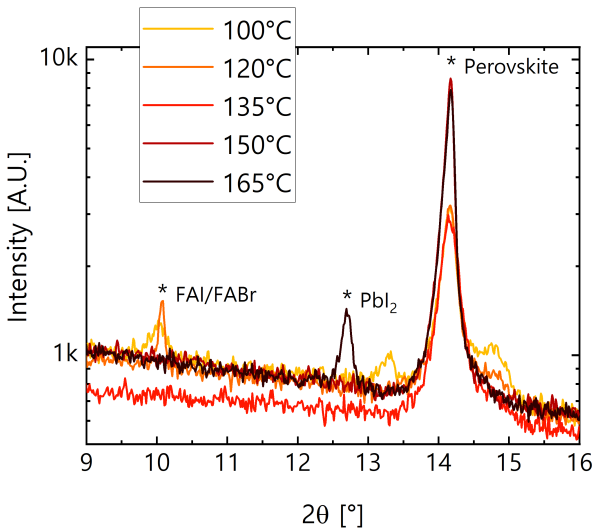

Figure 2.4 – XRD patterns for perovskite films annealed at different temperatures. The peak at 14.2° is representative of the perovskite material, while the peaks at 10.1° and 12.7° are representative of FAI and PbI_2 crystalline phases, respectively. Films were fabricated on glass/ITO/NiO substrates in order to mimic material formation in real PSC, the template used 12%vol CsBr, and annealing took place in air held at 35% RH.

2.2.2 Humidity and Solvent Effects

Besides the chemical ingredients intentionally deposited in the process, the water in the air and the residual solvent left over from the SP step both play a role in film performance. It is known that H_2O is relevant to perovskites in many ways [193]–[195], but specifically to our method, we observe that it aids in the interdiffusion. PVD/SP bilayers left in ambient air will interdiffuse and crystallize on their own, but much faster in more humid environments ([193], and observed in-house). This could aid interdiffusion and component balance, but with the caveat that H_2O degrades the end perovskite [195]. So to control the H_2O exposure of our perovskite, we carry out all steps except annealing in inert N_2 or vacuum, and control the the relative humidity (RH) in the air during this step (although it was later shown that the dew point is in fact the determining variable [196], it is linearly dependent on RH in our temperature range). Figure 2.5 shows the effect of RH variation on PSC JV performance. Comparing 15% to 35%, the average PSC efficiency by 3.4% absolute, negatively affecting all metrics (J_{SC}, FF, V_{OC}). Lower RH values were tested but not in parallel to these cells; for results at 0% RH, see section 2.3.2.

Aside from water, residual solvents (ethanol) from the SP step have an effect. We see this by incorporating a "pre-anneal" step, which applies low heat to the samples while still in N_2. Normally, the residual ethanol will evaporate over time (vapor pressure of 5.95 kPa, boiling point of 78°C), but this may give differences between the first and last sample processed (15 - 30 minute difference). But with a pre-anneal, this can be uniformly expelled to reduce sample to sample variation. Besides this effect, a pre-anneal may also induce a bottom-up crystallization path to prevent a top-down crystallization caused by H_2O in the air (in the time between removal from the glovebox and placement on the annealing hotplate). We first tested a wide range of pre-anneal times and temperatures, to try and capture the effects of

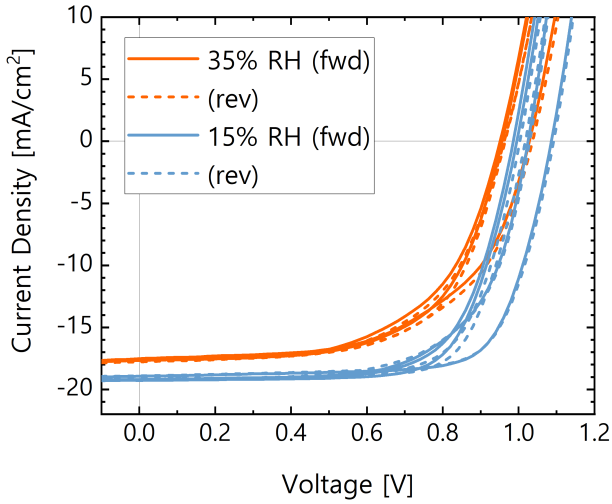

Figure 2.5 – *JV* curves of PSC with perovskite layer annealed in different humidity level environments. These PSC were produced in the same batch and only differ in their annealing environment. Data and discussion for 0% RH annealing can be found in section 2.3.2. The cell stack was glass/ITO/NiO_X/Pk/LiF/C_{60}/Ag, and used 12%vol CsBr in the template.

low temperatures (expected to expel ethanol without crystallizing) and high temperatures (expected to expel solvents, begin bilayer interdiffusion, and induce crystallization). The results of the initial test are presented in figure 2.6.

The main result from this wide sweep is that the best efficiency groupings came from opposite conditions, namely the shortest/coolest and longest/hottest pre-anneals. To further distinguish the effects of these two distinct temperatures, we performed XRD on the same samples (figure 2.7). The notable observation is the uniform presence of a crystalline PbI_2 phase in all of the 150°C pre-anneal samples, and none for the 70°C or 100°C conditions. This recalls the results of the previous section (particularly figure 2.4), where a PbI_2 peak in XRD was attributed to deficient FA due to evaporation [107]. For the pre-anneal experiment, we avoided this effect by using a main anneal of only 120°C. Thus, the only time that the cell stack experienced temperatures sufficient to cause the observed PbI_2 excess was during this 150°C pre-anneal step. As stated above, we want to avoid having excess PbI_2 in our films due to the negative long-term effects [66], [67]. If we eliminate the 150°C case due to PbI_2, the shortest 70°C pre-anneal remains as the best case in figure 2.6. It is worth noting that the 70°C pre-anneal samples had a uniformly lower perovskite (100) diffraction peak than the other conditions, despite having the same main anneal.

We followed this up with a finer tuning of lower temperature pre-anneals for shorter time (figure 2.8). The reference cells were intentionally spin-coated last out of all the samples, with the intention of maximizing the effect of residual ethanol. This manifests as the references being overwhelmingly shunted (figure 2.8a). Shunting of PSC can arise for many reasons. But in this case, the link to pre-annealing is clear, which we interpret as evidence that the expulsion of residual solvents is critical to the correct formation of the layer. We expect the crystallization taking place at 60 - 80°C to be minimal (shown below), and thus the main difference between here is the presence or absence of residual solvents. We theorize a mechanism in which

residual solvents escaping from the layer during the main anneal create voids between grains where the solvent is escaping (knowing that gas discharge can affect perovskite mechanically [59]). This mechanical disturbance then allows for physical contact between the top and bottom electrodes and the creation of shunt paths. In 2.8b, only the non-shunted cells are shown. Mostly, the efficiencies of the different pre-anneal conditions overlap. From this we conclude that the low-temperature pre-anneal is beneficial due to the removal of residual solvents, but that the duration of the pre-anneal is not very significant.

This still leaves undefined the role of crystallization during the pre-anneal, which we answer with in-situ grazing-incidence wide-angle X-ray scattering (GIWAXS) measurements. This method allows us to track the presence and orientation of different crystalline phases of perovskite and PbI_2, as the PVD/SP bilayers are heated from room-temperature to 150 or 70°C.

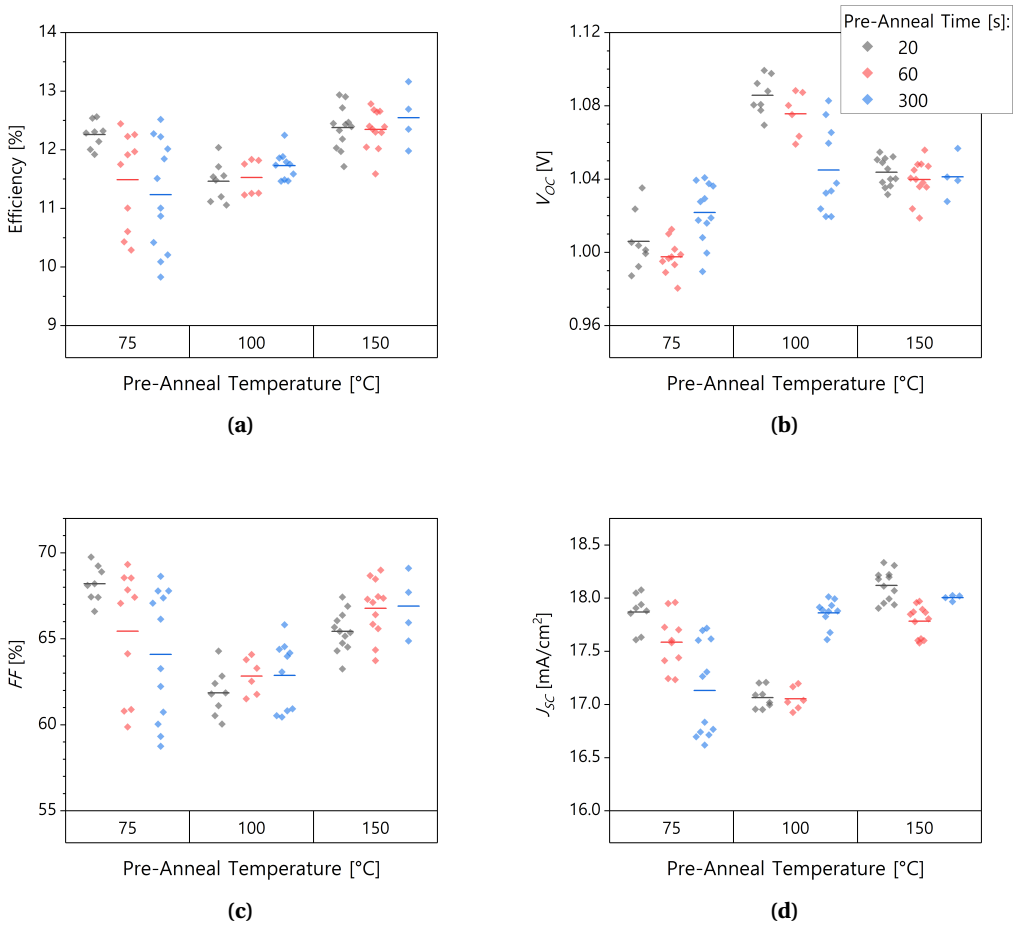

Figure 2.6 – *JV* performance for PSC made with pre-anneal steps of varied time and temperature. All cells were transferred to a hotplate immediately after the end of the spin-coating procedure. Once all cells had received their spin and pre-anneal, they were together removed from the N_2 environment to air for the main anneal. The main anneal was 30 minutes at 120°C in 35%RH air. The cell stack was glass/ITO/NiO_X/Pk/C_{60}/Ag.

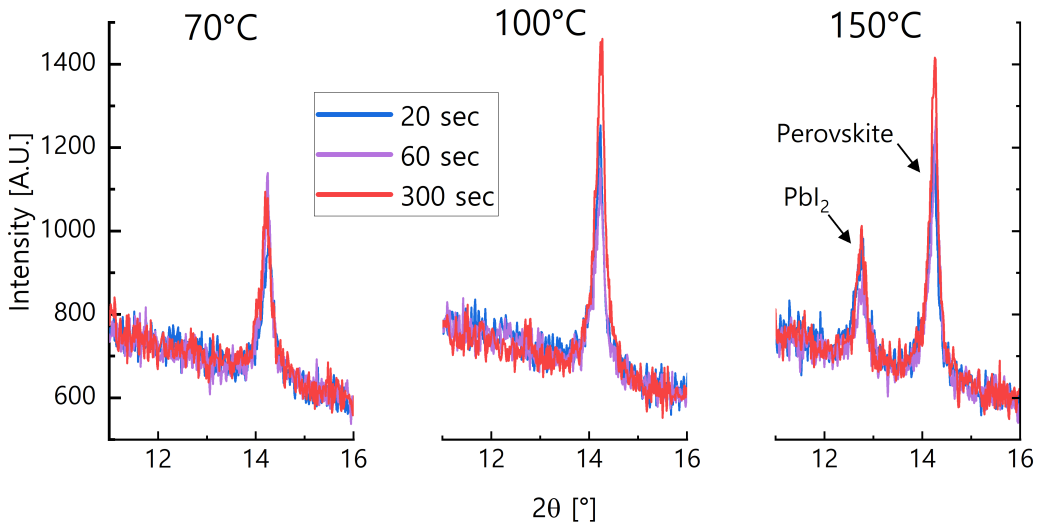

Figure 2.7 – XRD diffractograms for PSC made with pre-anneal steps of varied time and temperature. XRD measurements for the same PSC as were shown in figure 2.6. Only a subset of the scan range is shown, to highlight the peak at 14.2° from the perovskite (100) plane and the peak at 12.7° from crystalline PbI_2. This peak is only detected above noise in the 150°C samples. In general, these measurements have a poor signal-to-noise ratio, due to measuring on full PSC with absorptive layers (Ag, C_{60}) between the perovskite layer and the source/detector.

Figure 2.9 shows the results[3]. These data show that there is some slow crystallization at 70°C, but that the main crystallization process which takes place above 100°C is completely avoided by the pre-anneal.

As the samples are measured during heating from room temperature, we can compare how the samples behaved in different temperature ranges. Both samples follow the same trend in approaching 70°C. But from the 150°C sample, we see that the full crystallization takes place over three phases, of which the 70°C sample only experiences the first. These are: 1) a small dip and raise in the perovskite peak with slow decline of PbI_2, which takes place up to 100°C, 2) the rapid rise of the perovskite peak and drop in the PbI_2 peak, which we take to be template consumption and perovskite formation, from 100°C to 150°C, and 3) the plateau of the perovskite peak and simultaneous reverse of the PbI_2 peak, which rises over time. The peak positions also shift slightly in the same three regions. Most of the peak position shift comes simultaneous to the peak height change of period 2, with continued slower shifting over period 3. Changes in perovskite peak position during crystallization can be attributed to the

[3]These data were obtained by Dr. Julian A. Steele of KU Leuven. He carried out the SP deposition on site, and thus there may be variation between his results and the films we obtain in-house. We therefore do not draw conclusions from the relative intensity of scans, or the perovskite:PbI_2 ratio of individual samples. Secondly, we expect that the initial bilayer structure to somewhat shield the signal from the buried PbI_2 layer. The incidence angle of 1° should allow for penetration of the full layer, but does not guarantee that the signal strength will be constant throughout the layer depth. Thus, it is not considered that there is more PbI_2 present in the film at the end of the anneal versus the start, but simply that more signal is captured.

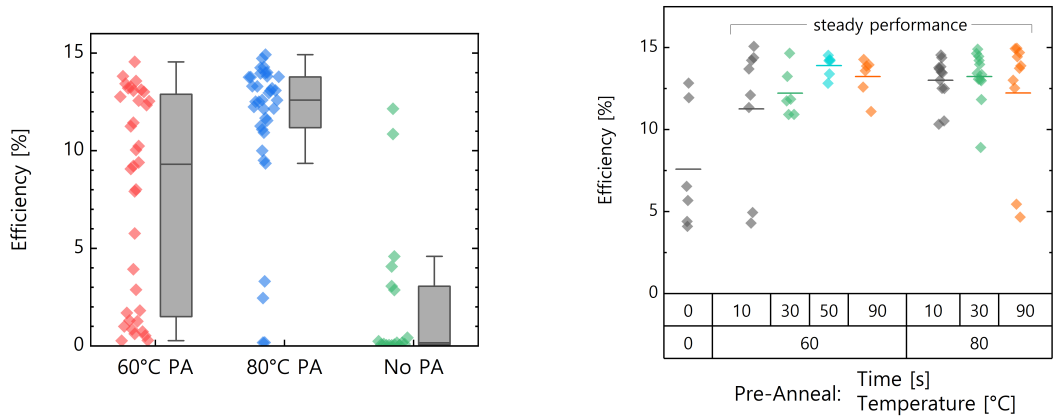

Figure 2.8 – *JV* efficiency of PSC made with finely tuned pre-anneal conditions. Cells were made with low-temperature pre-anneal steps and finer spacing of time conditions. (a) shows the measurements of all cells fabricated in the batch, regardless of shunts. The references were processed as to highlight the effect of the pre-anneal, and are far more shunted than what is usual. (b) shows the efficiencies of only the non-shunted cells, for the sake of clarity. The threshold for declaring a cell shunted was a FF value under 30%. The slight improvement in cell efficiency in (b) relative to (a) is due to all the measurements in (b) coming after a short MPP tracking measurement. This was not performed on all cells, so only pre-MPP measurements are shown in (a). The cell stack was glass/ITO/Spiro-TTB/Pk/LiF/C_{60}/Ag, used 12%vol CsBr in the template, and the main anneal was 60 minutes at 120°Cin 35%RH air.

mixing and uniformization of different perovskite phases during crystallization (observed and discussed in figure 2.10a), and the slow change of period 3 is more likely due to thermal effects on lattice spacing [197]. For the PbI_2 peak position shift, this may be due to different atomic organization in the evaporated PbI_2 template and the excess PbI_2 outputted by the perovskite. But overall, we conclude from the GIWAXS data that crystallization and material modification during the 70°C pre-anneal is negligible, and thus the main effect in cells is caused by removal of the residual solvent. There was some shift in peak height and position, but this took place over a ten minute timescale, and is irrelevant to the 15 - 60 second pre-anneal step. All of the crystal changes that did occur at 70°C were mimicked in the early seconds of the 150°C anneal anyway.

2.2.3 Bulk Disorder

Even for a chemically balanced perovskite with a pre-anneal and the correct RH during annealing, the resulting PSC can still behave poorly due to high crystallographic disorder. This can come in the form of ionic vacancies, interstitials, and substitutions; poor homogeneity of component ions or perovskite phases; a high density of grain boundaries; or uneven mechanical stresses on the lattice. Due to the difficulty in detecting and distinguishing

individual defect types, the likely simultaneous presence of multiple defect types, and the overlap of their effects on material performance, the term "bulk quality" will be used to refer to the collection.

This is not to say that all of these phenomena are correlated and vary linearly with eachother, rather the opposite is observed. This is illustrated in figure 2.10. While the XRD peak of the perovskite gets taller and narrower with annealing temperature, the V_{OC} drops. At lower temperatures, the XRD peak reduces, spreads out (indicating strain on the lattice [197]), and develops a secondary peak at 14.8° beside the main peak at 14.2°. Due to different compositions and the ionic radii of the species involved, organic-lead-halide perovskites

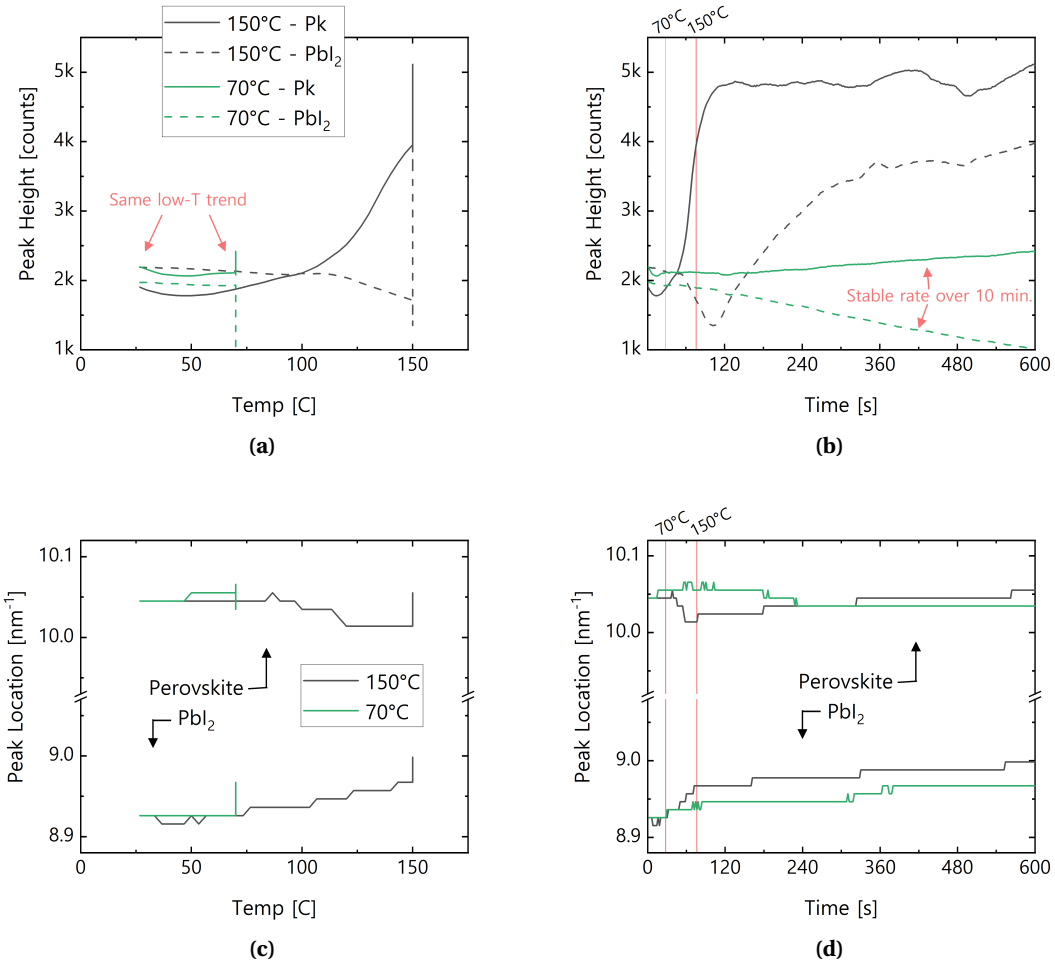

Figure 2.9 – Perovskite and PbI_2 diffraction peak heights and positions during heating to different temperatures. PVD/SP bilayers on flat c-Si were measured in-situ while heating from 25°C to 150°C or 70°C. All heating took place at the maximum rate of 100°C/minute. During this time, GIWAXS patterns were collected every 2 seconds. From this data, the (100) peak of the perovskite at 10.05/nm and the PbI_2 peak at 8.95/nm are radially integrated. Here we plot the height (a-b) and position (c-d) of the two peaks, as a function of both time and temperature.

display peaks throughout this range[4]; for example $FAPbI_3$ at 13.81°, $MAPbI_3$ at 14.07°, $CsPbI_2Br$ at 14.46°, and $CsPbI_3$ at 15.08°. Thus we would expect the high-temperature perovskite to have higher phase purity, lower disorder, and better performance. PSC were produced with 135, 150, and 165°C main anneal steps, and the results disagree with this expectation. The J_{SC} increased with annealing temperature, indicating better interdiffusion and conversion into perovskite. But the V_{OC} only decreases, and by over 10% relative. This shows that XRD peak height/width is not a complete quantification of perovskite bulk quality, and another method must be used.

[4]Values are obtained from simulations made with JEMS software [198].

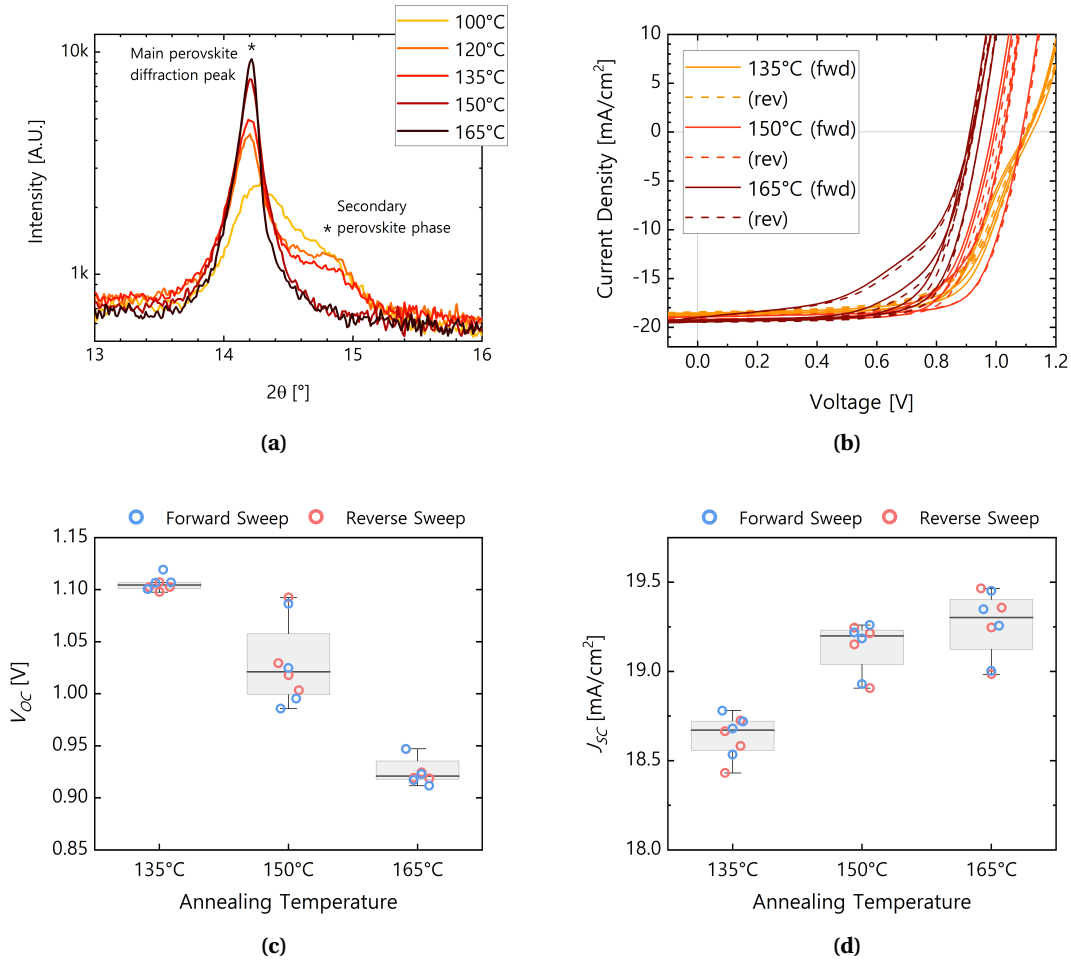

Figure 2.10 – XRD and *JV* data for perovskites annealed at different temperatures. (a) shows a zoomed-in view of the perovskite diffraction peak at 14.2°. Films were fabricated on glass/ITO/NiO substrates in order to mimic material formation in real PSC, and annealing took place in a N_2 environment. (b) shows the *JV* curves for cells produced at temperatures selected from (a), and (c-d) show the distribution of V_{OC} and J_{SC} parameters extracted from the curves in (b). The opposite trends lead to an efficiency maximum for the 150°C annealed cells. The cell stack was glass/ITO/NiO_X/Pk/LiF/C_{60}/Ag, and 12%vol CsBr was used in the template.

A known method in the literature for quantifying bulk disorder is that of measuring the sharpness of the absorption edge at open-circuit (often called the Urbach Energy) [48], [199]–[201]. This is quantified by taking the linear fit of the absorptance as plotted on a semi-log plot with photon energy (eV) on the x-axis. The inverse of this slope is defined as the Urbach Energy. This quantity corresponds to the "Urbach Tails" which are low-population allowed states of the conduction and valence bands which extend into the band-gap. The presence of these tails is associated with bulk disorder, which would bend and stretch the lattice and blur the band edges. Minimal energy states near the band edges would give a steep absorption onset and therefore a smaller value is indicative of a more ordered crystal. The absolute value of the Urbach Energy is important too. If the Urbach Tail is wider than the thermal energy at operating temperature (25.7 meV at 300 K), then the voltage of the cell will suffer [201].

We are able to measure absorptance over three orders of magnitude using photothermal deflection spectroscopy (PDS) [48]. However, in order to replicate the growth conditions of PVD/SP perovskite layers as used in full cells, we performed the measurements on the relevant substrates. The effect of the substrate is illustrated in figure 2.11a. As more layers, particularly metal oxides, accumulate below the perovskite, more absorption is measured below the perovskite E_g. The consequence of this is that less and less of the perovskite absorption onset can be resolved. In the literature, it has been shown that measurements of Urbach Energy are artificially inflated when measuring "higher" up on the slope (specifically, above 10^{-3} [200]). They note that the same trends between samples exist at either point on the slope, but the absolute value is important too (the limit of the thermal energy, 25.7 meV at 300 K). For the case of our PDS absorptance measurements, we are unable to resolve the slope much below 10^{-1} in the realistic case of growing the perovskite on top of metal oxides.

In the same publication that identified the problem of measuring "too high" on the slope [200], they investigate the cause of this and propose solutions. The main issue is that certain methods (such as PDS) probe band-to-band absorption as well as direct band-gap absorption, which causes signal below the E_g and reduces resolution. They identify alternative methods for obtaining the absorption spectrum without this effect, such as calculating from photoluminescence (PL) data. This is based on the reciprocity relation $PL(E) \propto Abs(E)E^2 exp(-\frac{E}{k_B T})$ where E is the photon energy, k_B is the Boltzmann constan, and T is the absolute temperature. This allows resolution of the slope below 10^{-3}, below which they consider the Urbach Energy accurately measured. However we do note the demonstrated failure of assumptions for the reciprocity relation in perovskites above E_g = 1.65 eV [76], due to phase segregation and charge funneling. Regardless, this measurement and calculation was performed for a perovskite within the full PSC stack, and compared to the same PDS measurements as discussed above, in figure 2.11b. From this comparison, we see that the spectral shape is not maintained, but the E_g and general scale of the values are. Some caveats of the PL measure are that it uses absorptance, not absorption coefficient as the PDS data does. Also, PL data is reliant on local excitation which causes non-uniform stresses in the perovskite [202], [203]. To compare this method to PDS, a fit was performed on three parts of the spectrum, intending to match with where the glass/ITO/NiO_X/perovskite sample was measured, where the glass/perovskite sam-

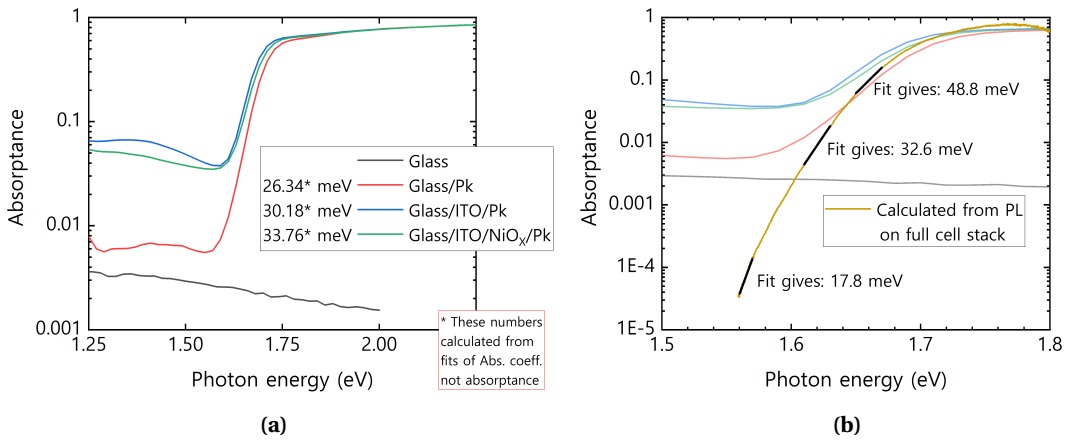

(a) **(b)**

Figure 2.11 – Absorptance measurements from PDS and PL for perovskite layers on different substrates. (a) For the same perovskite layer grown on glass, glass/ITO, and glass/ITO/NiO$_X$, different absorptance measurements are obtained. The Urbach Energy for each, as calculated from the absorption coefficient (not absorptance), is given in the legend. Measuring the slope of the red curve in the same range as the blue/green curves gives a value of 37.4 meV. (b) The absorptance as calculated from PL data is added. PL was measured for a full PSC on glass/ITO/NiO$_X$/Pk/LiF/C$_{60}$/Ag, and the Urbach Energy is calculated at three different points on the curve.

ple was measured, and as low as possible. This gives three different values, ranging from the "accurate" value taken low on the slope of 17.8 meV, to more than double that when measured near 10^{-1}. For reference, the PL method was regularly used on perovskites in all cell stacks, and reliably gives values in the range of 12 - 16 meV for all material stacks. This shows us that our perovskite has an Urbach Energy below that of the thermal energy at 300K (25.7 meV), above which the Urbach Tails would negatively affect device performance.

The measurement ranges available to us with these methods, combined with the difference in Urbach Energy values for the same perovskite on different substrates (figure 2.11a), tells us three things. First, PDS does not give a true quantification of the Urbach Tails, and should not be reported as such. We can still use the same measurement and calculation, as it provides a means to compare the bulk quality of different perovskite layers. But for the remaining analysis we will instead use the term "absorptance slope width" to call the resulting metric. Second, the values calculated from PDS are artificially inflated. This is the case between the Urbach Energy as accurately obtained from PL and the value from PDS on glass, and between the value measured on glass and that on metal oxides. From this, we expect to calculate values far above the true value of our material. Third, our material's Urbach Tails are likely under the meaningful limit of 25.7 meV. The PL measure passes this threshold already, and the PDS values for the absorptance slope width of perovskite on glass approach this limit, despite overestimation. Overall, we can move forward with either method as a means of quantifying and comparing bulk disorder.

Finally, we decided to use this PDS method to quantify relative bulk disorder in perovskite films made with different annealing conditions. The goal of this analysis was to explain the anti-correlation between the XRD and V_{OC} measurements of figure 2.10. Samples were made with different temperature and environment for the main annealing/interdiffusion step, their absorptance measured by PDS, and the absorptance slope width quantified (figure 2.12a). The extracted values indeed lined up with the JV performance (figure 2.10c), with the lowest values coming between 135°C and 150°C for all annealing environments. In all cases the value increased at 165°C, aligning with the drop in V_{OC}. We attribute this to the loss of FA^+ or I^- due to evaporation at high temperatures [59], [107]. This would leave behind vacancies in the crystal structure and increase structural disorder.

To rationalize higher bulk disorder with a taller and narrower XRD peak, we must distinguish what affects both of these measurements. XRD measures crystal planes. Stress within the crystal from disorder will cause strain, which in turn can stretch, compress, or bend the lattice planes, spreading out the diffraction peak. The heat of annealing can relax this strain, via providing the thermal energy for the disordered atoms to reorganize in ways that minimize stress and thereby sharpen the diffraction peak. Urbach Energy (and our approximation of it) measures disorder in a general sense. The missing ions lost to evaporation at high temperatures cause vacancies and undercoordinated ions in the lattice. These localized defects have modified electronic energy levels which can then contribute to the Urbach Tails. As long as these defects are sufficiently localized and not clustered, they can exist within the crystal without excessively straining the lattice, and thus the XRD peak will not be blurred. We

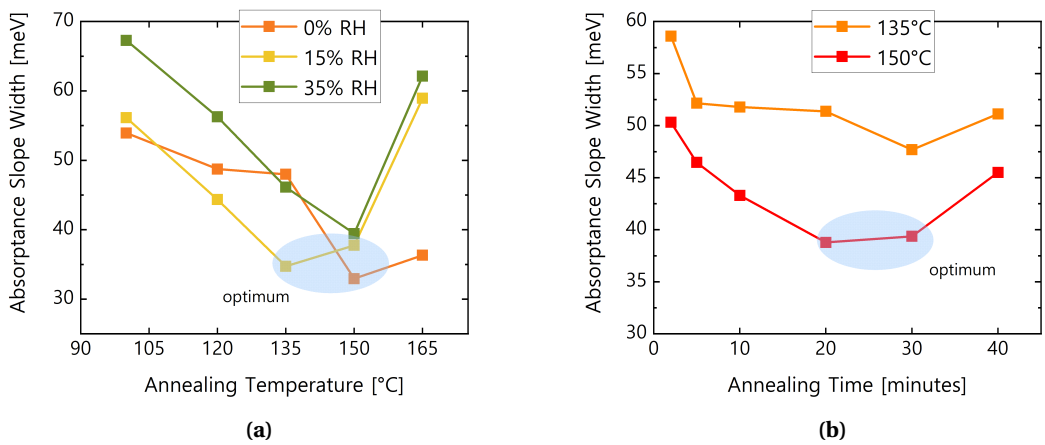

Figure 2.12 – Absorptance slope width measured for perovskite layers with various annealing conditions. (a) shows perovskite layers annealed at different temperatures and in different environments. For the sake of ensuring truly 0% water in the air, the 0% samples were annealed in a controlled N_2 environment. Samples were deposited on glass/ITO/NiO_X. (b) shows perovskite layers annealed at two fixed temperatures, in the same 15% RH environment, for different time durations. These samples were prepared on glass/ITO/Spiro-TTB substrates, to include the effects of potential changes in the underlying layers. All samples used a template with 12%vol CsBr.

therefore propose that the 165°C samples do have more uniform and ordered lattice planes as evidenced by XRD, but that there are sufficient point defects within those crystal planes to cause the high absorption slope width measurements, and the low V_{OC} of the full cells. For reference, the relevant segment of the XRD pattern for each condition is shown in figure 2.13.

Following this link between perovskite characterization and PSC performance, the bulk quality optimization method was extended to other production variables. This was an improvement over cell production, as it took less time than full PSC fabrication, and invited in fewer confounding variables (such as CTL transport properties). Figure 2.12b shows absorptance slope width measurements for perovskites annealed at different time intervals and two temperatures. This showed the progression of bulk quality during the annealing process, and the fact that eventually the annealing can make the perovskite worse. Likely this is due to the negative effects of component evaporation already being present at all temperatures, but progressing slowly enough that they do not cause meaningful damage until after a certain amount of time. This in turn implies that higher annealing temperatures could be used, just with shorter times. But the timing would have to be precise, and the trade-off between interdiffusion, crystallization, and component evaporation would have to be precisely tuned.

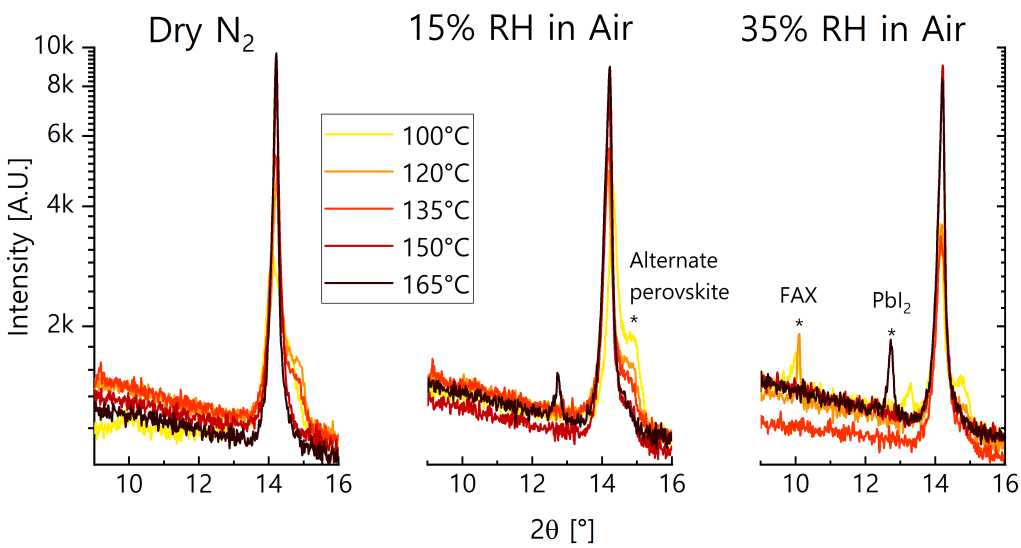

Figure 2.13 – Segments of XRD diffractograms for different annealing temperatures and environments. XRD measurements were performed on all of the samples from figure 2.12a. The plots are cropped to show the relevant peaks. The main perovskite (100) peak is at 14.2°, an alternate perovskite shows up at 14.8°, PbI_2 at 12.7°, and FA-halides at 10.1°.

2.2.4 Conclusion

In our lab we choose to use a hybrid PVD/SP method for our perovskite fabrication due to its compatibility with optically ideal textured c-Si bottom cells and its flexibility to include various organic precursors. However this is a complex deposition process, combining multiple steps and many variables. In order to advance this method to produce the highest-quality materials, we sought to first understand it deeply. We therefore varied different production parameters, and were able to identify which variables affect the end product in specific ways.

The observed effects were grouped in three categories. The first was the balance of constituent ions contributed by the PVD and SP steps. We showed the effect of imbalanced components in cells to be significant. XRD measurements revealed that the annealing, in addition to the PVD and SP steps, can push the balance in either direction. The second grouping was the effects of external chemical species. H_2O exposure from humidity in the air affected cell performance, and is linked to both the bilayer interdiffusion and the perovskite crystallization. A pre-anneal immediately after the SP step was shown to benefit batch yield, due to expulsion of residual solvents. The third grouping was the parameters that affected the bulk quality of the perovskite. This was mainly related to the annealing step, which can be varied in time, temperature, and environment. Studying the perovskite layer outside of full cells enabled faster optimization via measurements of relative bulk disorder. This showed that perovskites from the hybrid method can be limited by bulk quality, particularly at high and low annealing temperatures, but the ideal recipe was below the limit of bulk disorder affecting performance. The results were supported on the cell level, with lower bulk quality giving worse performance. Overall the final recipe was: 180 nm PbI_2 template with 18 nm CsBr, spin-coating 100 µL of 0.45 M solution of 1:2 FAI:FABr dynamically at 4000 rpm, annealing for 15 seconds at 80°C in N_2, and finally annealing for 20 minutes at 150°C in 15% RH air.

These results gave us better understanding of the hybrid PVD/SP method, and how its variables affect material quality. This led to better cell performance, but is ultimately limited by the contributing methods which only measured the perovskite layer, and particularly its bulk disorder. Having a good bulk is important to making good PSC, but not the whole picture. At this point the PSC shown are still far short of the potential V_{OC} and FF for a material of their E_g (W_{OC} = 0.6 V and FF < 75% at 1.70 eV). Thus, we conclude that bulk optimization is near complete, and should yield the stage to research on reducing losses from surface recombination, interface recombination, and charge transport.

2.3 Interface Passivation in Hybrid-Method PSC

After optimizing the bulk material, the next facet of the perovskite to understand and improve is the surfaces of the material and the interfaces that are formed with the adjacent materials. Surfaces are by definition a crystallographic defect. Whatever ionic layer terminates a grain, those ions will be undercoordinated, with dangling bonds covering the surface. These unsatisfied electronic states can exist on their own, or they can interact with those of the adjacent material layer to form new unique states. Depending on the materials used, these states can manifest as mid-E_g traps leading to limiting Shockley-Read-Hall (SRH) recombination, as shallow band-edge states that trap charges and create a band-bending effect, as states outside of the band-gap that are neutral, or any number of unique configurations [36]. Defects formed at perovskite surfaces and interfaces are already known to be a primary limitation to modern PSC efficiencies [102], [103], [109]. We therefore set this as the next goal; to characterize, better understand, and ultimately improve our perovskite's surfaces and interfaces.

2.3.1 Passivation via Material Selection

One strategy common in the literature is that of targeting treatments to the expected defect types [105], [106], and selection of CTLs that naturally form low-defect interfaces with perovskite [110]. We therefore applied this strategy, searching for treatments and CTL materials that would give our PSC low-loss surfaces and interfaces.

Photoluminescence Characterization Method

We chose to use PL measurements of the perovskite absorber to quantify the recombination losses. While PL does not directly probe the interfaces or recombination mechanisms, it does give relative information about the overall recombination rates of different material stacks. PL is produced by radiative recombination, which is one option for what can happen to excited charges, along with non-radiative recombination and extraction as useful current. If no current is being passed through the perovskite, then the PL signal is a measure of how much recombination is radiative or non-radiative. Thus, a good perovskite layer with minimal recombination losses will also have a high steady-state PL intensity at open-circuit. The work in chapter 2.2 probed the bulk directly, and found an optimum. From this, along with the known harmlessness of many bulk defect states in perovskites [204], we infer that our perovskite's recombination rate is not bulk limited. Therefore, we link the PL intensity to the surface and interfacial recombination rates.

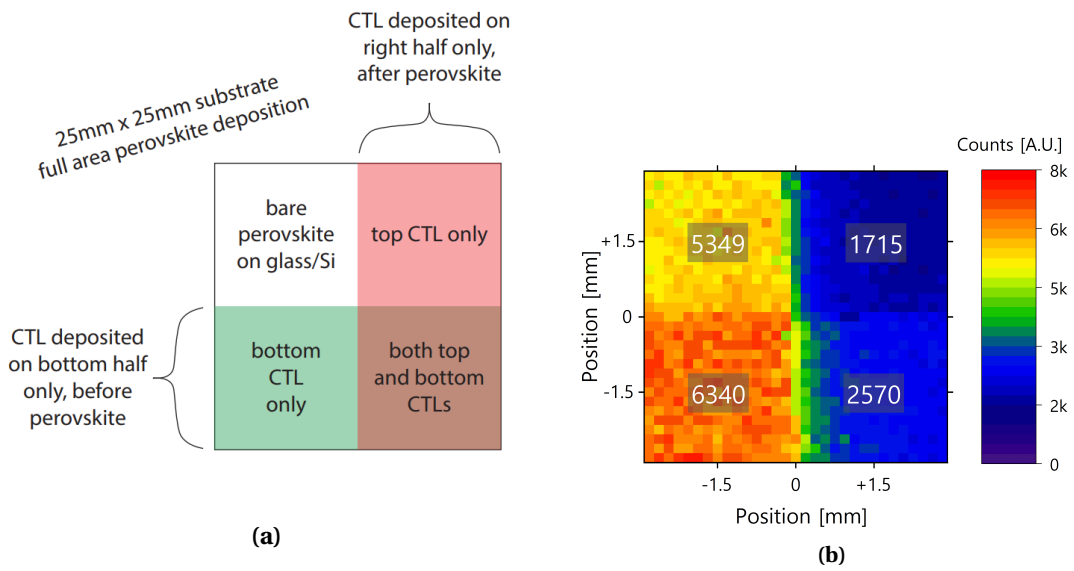

Figure 2.14 – Diagram and example PL measurement on a spatially varied CTL stack. (a) Generalized diagram of how CTLs were spatially deposited. Evaporations were done through a shadow mask to achieve spatial variation with a clean step. (b) PL intensity map for a sample deposited according to (a). TaTm was deposited on the lower half before the perovskite, and C_{60} was deposited on the right half after the perovskite formation. The substrate was a textured c-Si wafer. PL measurement was carried out with a 514 nm laser, focused to an 80 µm diameter spot size, and attenuated to 1-sun intensity. Pixels are spaced at 200 µm. The color refers to the maximum intensity of that pixel, and the average intensity of each quadrant is overlain.

In order to test various conditions against eachother without variation between samples, we developed the method shown in figure 2.14a. This involved depositing the perovskite as normally on the standard 25 mm by 25 mm substrate, but with each CTL spatially restricted[5] to one half of the substrate. For consistency, we generally kept the HTL on the bottom half of the sample and the ETL on the right half. The top left quadrant was left without CTLs on an inert substrate (glass or c-Si), for comparison of the interfaces to the neat perovskite surface. This gave us four distinct quadrants with different layer stacks, and therefore different interfaces with the same perovskite. Then, we spatially measure the PL using a microscope objective (80 µm diameter spot size). This allowed us to observe each stack and attribute variations in PL intensity to the different interfaces present. An example measurement is shown in figure 2.14b. Here we see that the bare perovskite PL is slightly enhanced when coupled with the HTL TaTm[6], while strongly suppressed underneath the C_{60}. Samples on glass were measured from both sides to confirm that the absorption of the C_{60} was a negligible factor towards the observed intensity loss. Examples of this measurement are shown in section B.4.

[5] In the case of thin films of organics, this is achieved via evaporation through a shadow mask. In the case of SAM, a thin ITO is sputtered on half the substrate via a shadow mask. Then the SAM is deposited as normally, and only adheres to the ITO.

[6] Chemical name: N4,N4,N4",N4"-tetra([1,1'-biphenyl]-4-yl)-[1,1':4',1"-terphenyl]-4,4"-diamine

Selection of Passivating Agents

For selecting optimal CTLs, we can filter out options in the literature by considering only those compatible with our mandate of all materials and processes being adaptable to perovskite on textured c-Si tandems. For example, we manufacture in the p-i-n configuration, and therefore the successful SnO_2 ETLs deposited from aqueous solutions [205] are not an option. Likewise, all materials must be able to deposit on KOH-textured c-Si pyramids and remain there during annealing at 150°C; thus the spun polymer HTLs such as PTAA are not an option either[7] [206]. From these restrictions, we selectively chose and tested bulk organic molecules Spiro-TTB and TaTm, and various self-assembled monolayer (SAM) HTLs against eachother. Both Spiro-TTB and TaTm can be thermally evaporated uniformly onto textured surfaces [22], [149], [163], while SAM molecules can be deposited from solvents and form conformal molecular monolayers on metal-oxide surfaces [56].

Spiro-TTB was the baseline used in the lab since prior to the start of this thesis work, before TaTm or SAM had been reported or became available [56], [163]. NiO_X was also used often in the beginning of this thesis, but it was not considered similarly. This is due to low performance and issues related to long-term degradation [207], despite reliable and repeatable performance which made it useful for experimentation. C_{60} remained as the ETL due to good selectivity and conductivity, and compatibility with textured surfaces. However, it causes strong interfacial recombination (figure 2.15, and in literature, [99], [104], [110], [208]) and is expensive (roughly 0.40 CHF/nm/m^2, see section 4.3), and therefore should be a target for replacement in future research.

For general surface passivation without considering interfaces, we again selected from the abundant proposals found in perovskite literature. This specific topic was the research focus of Dr. Xin-Yu Chin, who chose to test the molecule FBPA[8] [128]. Specifically, 5 mM are included in the SP solution. This molecule has a phosphonic acid group that acts as a Lewis base. This type of molecule has been widely used in the literature for chemical passivation of metal-terminated perovskite surfaces [108], [126], [209]. Further, its large fluorinated benzene ring was expected to keep it on the surface of grains where it was intended to act. This is especially important for our hybrid method, where larger organic ions were observed to cause problems with crystallization which reduced cell efficiency (see section B.2). We will discuss here only the passivation effect of FBPA, and its further effects on our perovskite will be discussed in the following section (2.4).

In order to compare these new materials and methods, we performed measurements as outlined in figure 2.14. To quantify the performance of the four quadrants, we calculated the relative quasi Fermi-level splitting (QFLS) for each. Since these PL measurements are not absolute (not all emitted light is captured), we cannot calculate the true QFLS of any case. By instead taking each quadrant's intensity relative to a reference, we can drop the unknown terms

[7] Though we acknowledge the success of blade-coating PTAA on c-Si pyramids [155]. This was published in the last year of the thesis work and could not be incorporated.

[8] Chemical name: 2,3,4,5,6-Pentafluorobenzylphosphonic acid

and find an accurate relative value: $QFLS = k_B T ln(\frac{J_{Gen.}}{J_0}) = k_B T ln(PLQY \frac{J_{Gen.}}{J_{0,rad.}})$, $\Delta QFLS = QFLS_1 - QFLS_2 = k_B T ln(\frac{PLQY_1}{PLQY_2}) = k_B T ln(\frac{PL_1}{PL_2})$, where $J_{Gen.}$ is the total generated current density, $J_{0,rad.}$ is the radiative thermal equilibrium recombination current density in the dark, k_B is the Boltzmann constant, T is the absolute temperature, and PLQY is the photoluminescence quantum yield (absolute PL), according to the method in [104]. We thus used this method to compare many conditions, and a selection of the results is shown in figure 2.15. This shows two comparisons, that between films with and without FBPA as surface passivation, and between the three HTLs discussed above (Spiro-TTB, TaTm, and SAMs).

First, the addition of FBPA imparts a gain in all quadrants. The bare perovskite improves by 22 meV, but also in the interfaces with the CTLs. The Spiro-TTB/perovskite stack goes from -46 meV to +13 meV, and the perovskite/C_{60} stack goes from -86 to -14 meV. The neat perovskite improves, but the perovskite/CTL interfaces gain nearly 3x more relative QFLS, and both bottom/top interfaces are improved similarly. From this, we interpret that FBPA is acting to passivate defects at the surface and further protect against the formation of interfacial states with both CTLs. Second, figure 2.15 compares three HTL options. Changing from the old standard of Spiro-TTB to TaTm causes a small increase for the HTL/perovsktie quadrant, and the full TaTm/perovskite/C_{60} stack gives higher QFLS than the untreated bare perovskite. Thus we interpreted TaTm to have a more favorable interface with our perovskite than Spiro-TTB.

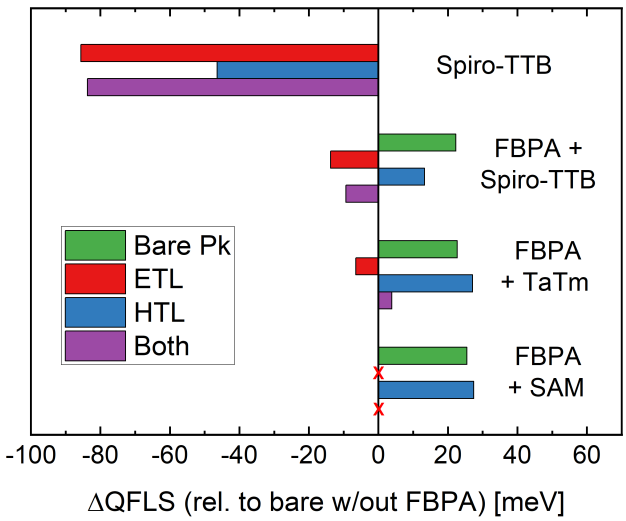

Figure 2.15 – Relative QFLS for different perovskite compositions and layer stacks. Non-absolute PL measurements were taken through a microscope objective on samples deposited and measured as in figure 2.14. Then the average intensity of each quadrant was used to calculate the relative QFLS, using the neat perovskite without FBPA as the reference case. In all samples, the ETL is C_{60}. The SAM material used was Me-4PACz. In the case of FBPA + SAM, no ETL was included, idicated by a red X. The substrate was c-Si, except in the case of SAM, where glass was used to ensure no SAM adhesion in the "bare perovskite" region.

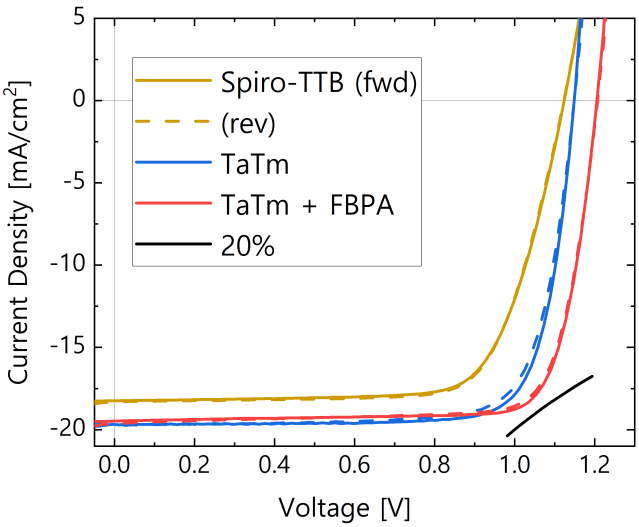

Figure 2.16 – *JV* curves for PSC with varied HTL and passivation. Spiro-TTB and TaTm were used in cells without FBPA, and both TaTm and FBPA were used together to form the three conditions shown here. A curve is shown in the bottom right to indicate the values that would give 20%. Cell production and measurement courtesy of Dr. Xin-Yu Chin.

Finally, we also tested SAMs below the perovskite (without C_{60}). We show the case of Me-4PACz in figure 2.15, and it behaves similarly to TaTm. More measurements using different SAM molecules can be found in section B.8.

To further compare these cases and confirm the improvement seen in PL, we fabricated full PSC. We compared Spiro-TTB and TaTm without FBPA, and again TaTm but with FBPA. We did not yet include SAM at the time of these tests, as these became available after work had progressed to full tandem cells. The comparison of SAM and TaTm is shown in section 4.3. Champion cells of each case are shown in figure 2.16. As expected, each improves upon the previous in succession. TaTm shows a slight voltage gain over Spiro-TTB, but mostly gains in FF and J_{SC}, due to different band alignment and transport properties of the two molecules. Adding in FBPA gave the jump in V_{OC} as predicted by the PL results, along with little change to FF or J_{SC}.

2.3.2 Passivation via Processing Conditions

Beyond the active passivation of defects through chemical treatments and CTL selection, surface and interface recombination is affected by background processing parameters. This can refer to the fabrication environment, solvents present, and ambient gasses during fabrication [118], [121], [123], [210]. These variables are therefore different for each lab and their individual methods and equipment. For the case of our perovskite, we find a powerful influence of oxygen exposure.

Annealing Environment and Cell Performance

The main effect of O_2 was discovered by testing the humidity in the air. To obtain 0% humidity, the annealing was done in a pure N_2 environment. The resulting JV curves are shown in figure 2.17a. The J_{SC} drops to under 1 mA/cm^2, along with drops in V_{OC} and FF. There was no visible difference to the films to suggest non-conversion of the bilayer, and the change was not in line with the trend expected for RH variations. So, the we hypothesized O_2 to be the relevant parameter. We then controlled the O_2 exposure to be before, during, or after the anneal, which showed that the J_{SC} loss occurred whenever the heat and air exposure were separated (figure

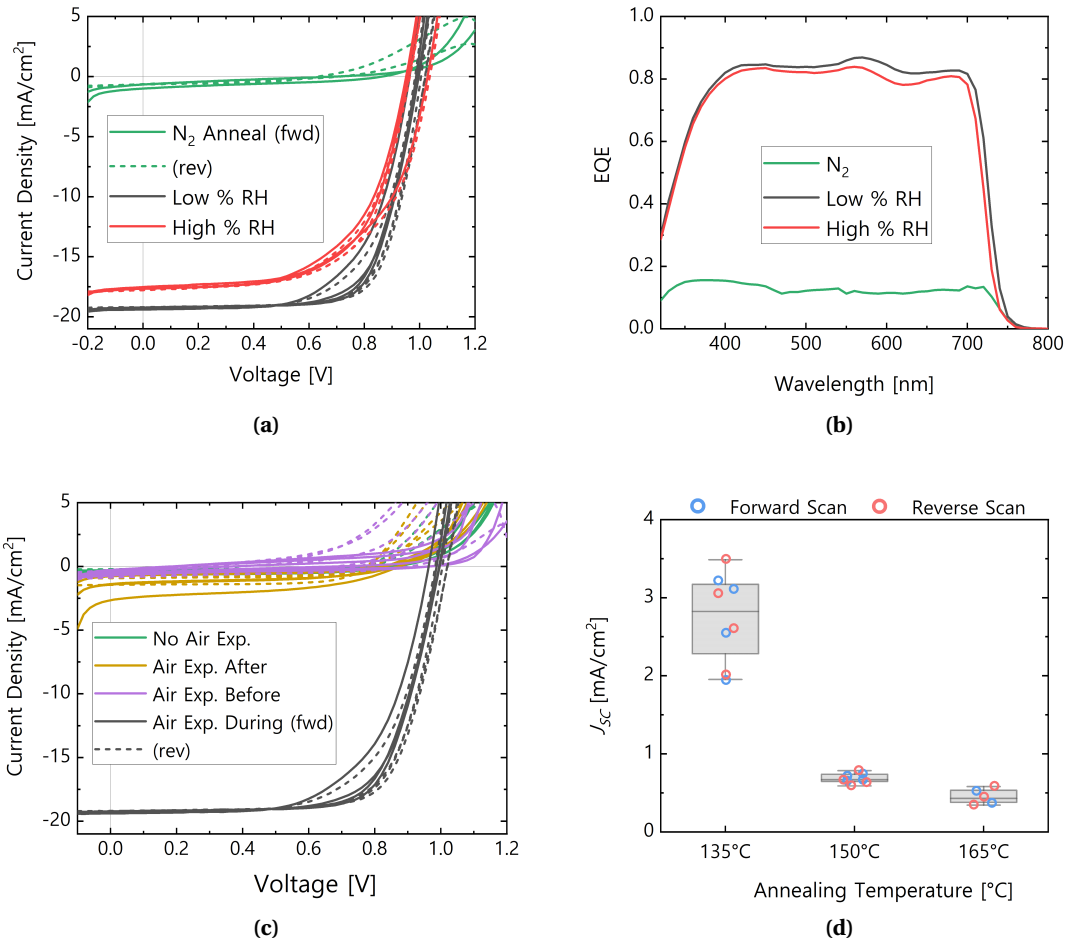

Figure 2.17 – Original measurements for air and nitrogen annealed PSC. (a) JV curves for a batch of identically produced PSC, only differing in their annealing environment. Low and high % RH refers to 15% and 35%. (b) EQE measurements for the same cells. (c) JV curves for cells made with air or N_2 annealing. Certain N_2 annealed samples were exposed to the same humid air as the reference cells were annealed in, either before or after their own annealing. (d) J_{SC} statistics for PSC annealed in N_2 at different temperatures. All cells used the same stack: glass/ITO/NiO_X/perovskite/LiF/C_{60}/Ag, and used a template with 12%vol CsBr.

2.17c). This was in line with literature results that claimed oxygen gas molecules require sufficient heat to break into individual atoms and diffuse into the bulk [121]. What did affect the J_{SC} loss was the anneal temperature in N_2 (figure 2.17d). As the temperature went up, the loss increased. This gives a clue to what is causing the issue, potentially linking it to ion loss via evaporation at elevated temperatures, discussed in section 2.2.1.

To distinguish the effects of the bilayer interdiffusion from that of O_2 + heat, we combined a normal 150°C anneal in air with a 60 minute anneal at 120°C in an N_2 environment. The results in figure 2.18. The second annealing would assure that the interdiffusion and crystallization is complete, while the first would assure air exposure. We found that despite the uniform anneal in N_2, PSC performance was entirely linked to how much time they spent at 150°C in air. The V_{OC} was rather constant, while the FF and J_{SC} dropped in line with the first anneal length. This tells us that it is not an effect of incomplete conversion, but a process linked to simultaneous heat and O_2 exposure.

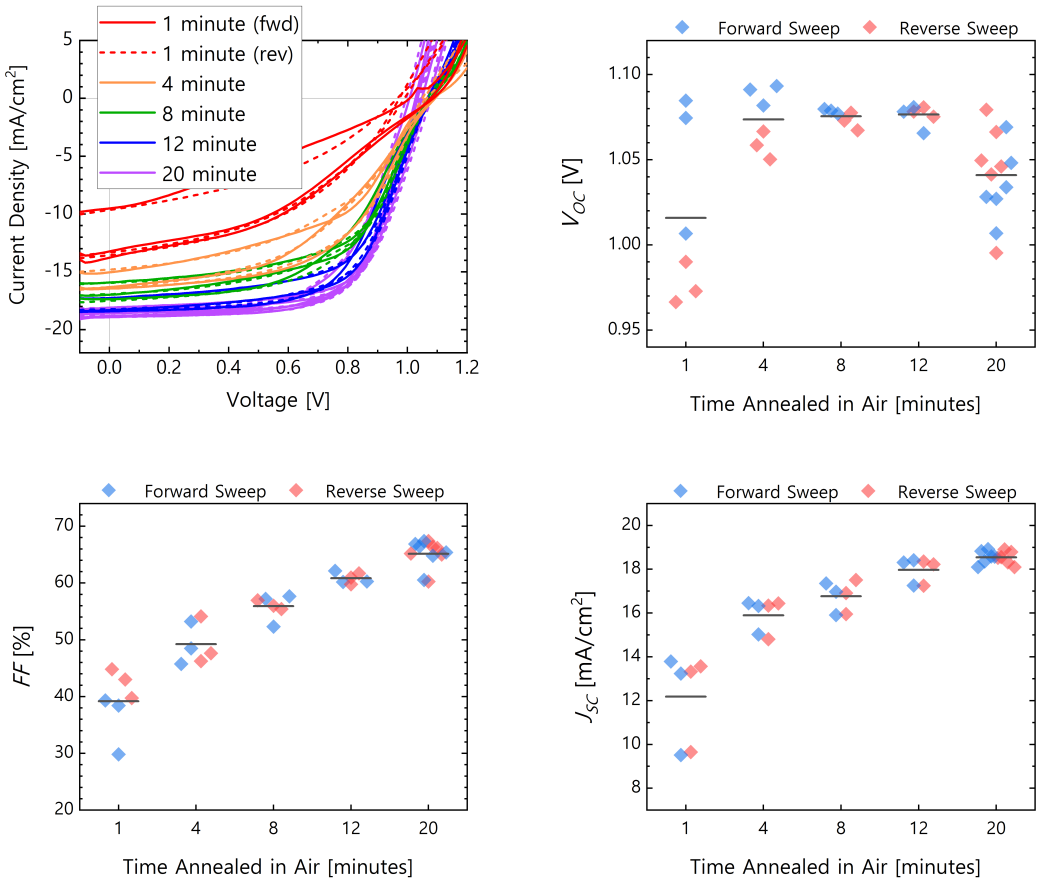

Figure 2.18 – Cell performance for perovskites with different annealing lengths in air. Cells were annealed in air for the indicated time, at 150°C. Then all were returned to the N_2 environment for an additional 60 minutes of annealing at 120°C, to control that the interdiffusion is complete in all cases. The cell stack was glass/ITO/NiO_X/perovskite/LiF/C_{60}/Ag.

Characterization of Nitrogen-Annealed Perovskites

The N_2 and air annealed perovskites were subjected to various characterization methods to help understand what was causing the JV losses. Initial measurements on the material structure are shown in figure 2.19. Further characterization methods are shown in section B.5. The XRD does not show peaks at 10.1° or 12.7° (representative of FAI and PbI_2 crystalline phases), which is a lack of evidence for incomplete conversion. The PDS curves show a slight improvement for N_2 annealed perovskite rather than any loss. Likewise the absorptance as measured by 1-T-R spectroscopy showed just under 1% absolute change in the 400-700 nm range. Atomic force microscopy (AFM, figure 2.19d-f) and scanning electron microscopy (SEM, figure 2.19g-i) were performed as well. There is a visible difference in the AFM height maps of the low and high-% RH films, but little change when going from low % RH to N_2. A film made of an abundance of small grains could explain low performance, but this reasoning is disputed in the literature [211]. The SEM images are of cleaved cross-sections of the same cells from figure 2.17a-b. The perovskite domains are predominantly vertical, with some horizontal boundaries in all films. Overall, the initial characterization methods used to probe bulk material quality did not detect changes that could explain the difference in performance.

Still, these measurements do allow us to disprove certain possible causes of the J_{SC} loss. First, there cannot be a charge-blocking PbI_2 layer below the perovskite. If so, we would detect it in XRD (none detected, figure 2.19a), and from literature we know the effect of having such a residual layer would drop the FF and V_{OC} more than the J_{SC} [212]. This possibility is further disproved by the hour-long annealed perovskites of figure 2.18, which assured full conversion but still suffered the same losses. Second, the J_{SC} is not lost to severe bulk recombination which reduces the charge transport length so much to only allow extraction from a fraction of the perovskite thickness. If so, the PDS measurements (figure 2.19b) would show a difference in bulk disorder.

It remains possible that undercoordinated Pb^{2+} defects at grain surfaces are the main source of losses. This type of defect has already been linked to O_2 passivation [118], [121]. The temperature dependence of the J_{SC} loss (figure 2.17d) further implicates Pb ions, as they would preferentially terminate the grain surfaces in the case of FA^+ or I^- evaporation which happens at similar temperatures [59], [107]. Given that exposing the top surface to air did not alleviate the problem (figure 2.17c), we theorized that the O_2 needed either break up into oxygen ions or diffuse through the layer via a heat-activated process as in [121]. Thus the bottom surface of the perovskite was expected to hold the primary Pb^{2+} defect concentration.

Looking past bulk metrics, we investigated the relative recombination losses via PL measurements. This revealed the significant role of the bottom interface, and the data are shown in figure 2.20. To test the surfaces, we compared perovskites with or without FBPA as surface passivation (established in section 2.3.1); and to test the interfaces we measured perovskite as deposited on different substrates. For the isolated perovskite without any passivation, the removal of oxygen reduced the PL dramatically (140x, figure 2.20a). This implicates the sur-

faces, as no other semiconductor materials are present to form an interface. This is supported by the near total recovery of PL losses upon the addition of surface-passivating FBPA, for the case on bare glass (figure 2.20b). So we can infer that our perovskite naturally has severe surface recombination which is normally passivated by oxygen. But this is not the whole story. Regardless of FBPA surface passivation, the PL again drops for N_2 annealed perovskites upon the inclusion of a TaTm/ITO interface. This uncovers a distinction between surface and interfacial recombination, and the similar but unequal roles of oxygen and FBPA in passivating

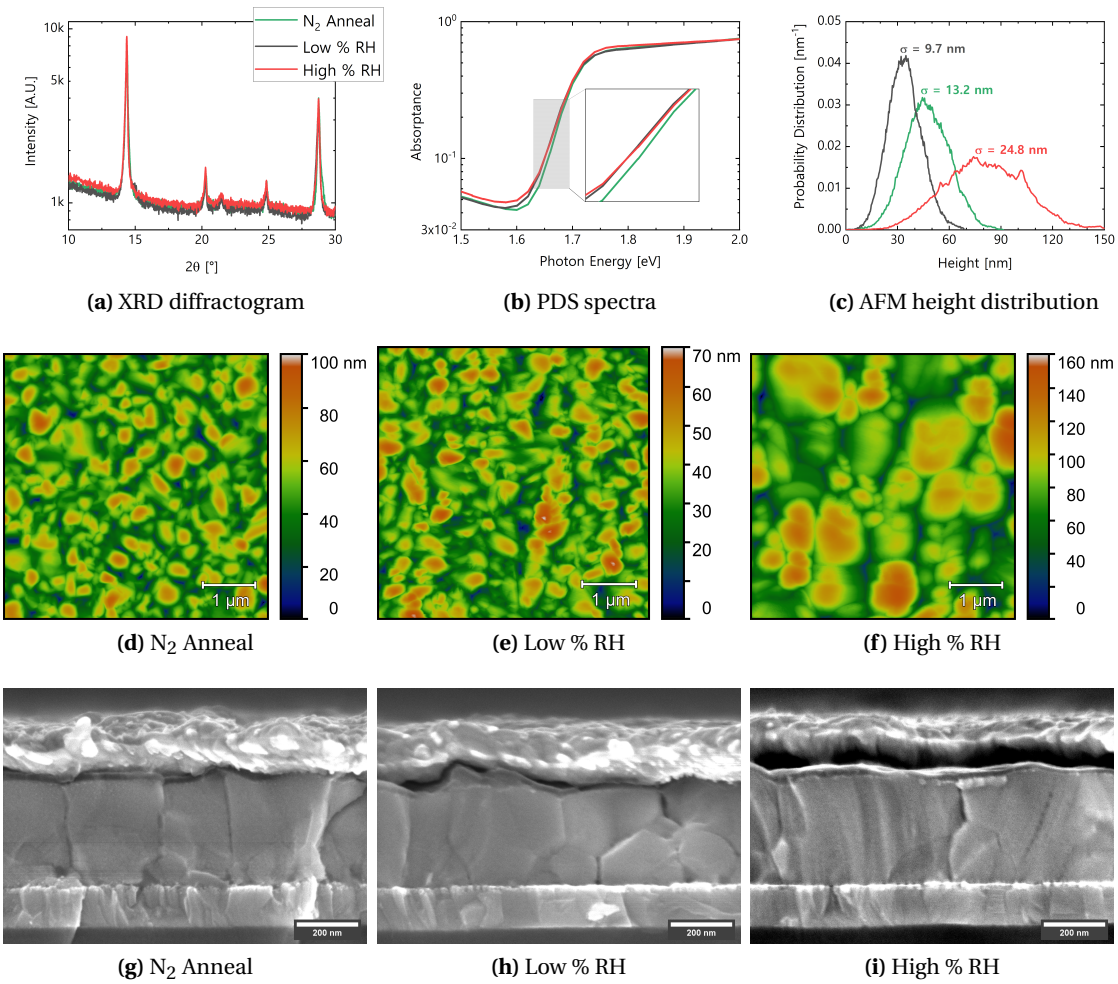

(a) XRD diffractogram **(b)** PDS spectra **(c)** AFM height distribution

(d) N_2 Anneal **(e)** Low % RH **(f)** High % RH

(g) N_2 Anneal **(h)** Low % RH **(i)** High % RH

Figure 2.19 – Further characterization of air and nitrogen annealed perovskite layers. (a) XRD patterns of cells annealed in three environments, all at 150°C. Low % RH was 15% and High % RH was 35%. (b) PDS measurements of the absorptance, for the same films. (c) Height distributions for the same films, as measured by AFM. The significance of these data is not the position of the distribution but the width. The zero-height point, and therefore the peak position, is fixed only by the probed depth of holes between grains, which depends on measurement parameters. (d-f) AFM height maps for the same films. The scanned area has 5 µm side length. The height scale in each image is different, to make that image readable. (g-i) SEM cross section scans of full PSC made with different annealing. Scale bar for SEM images is 200 nm. All samples used a template with 12%vol CsBr.

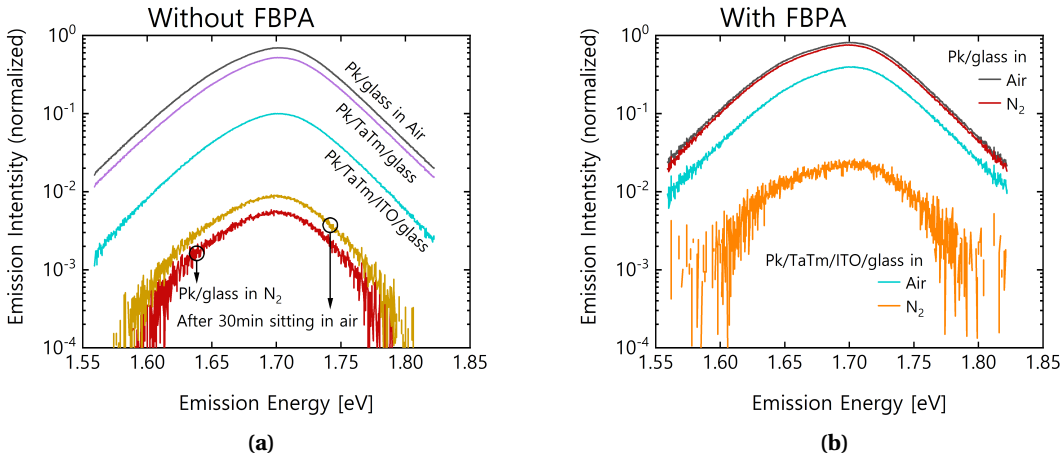

Figure 2.20 – Average PL peak for varied perovskite films and layer stacks, in different environments. Samples were made with or without 5 mM FBPA in the SP solution. PL measurements were taken according to the method in figure 2.14, across the whole substrate with 1 mm spacing between points. All the measurements were averaged together to create the spectra shown here. (a) shows perovskite PL for layers without FBPA, and (b) shows layers with FBPA. In (a), the perovskite/glass sample which was annealed in N_2 was then left in air at room temperature for 30 minutes before re-measuring. Each graph was normalized separately, in order to show the changes caused by annealing and layer stack, without being convoluted by the effects of FBPA on PL emission.

these defects. Perovskite/glass experiences predominantly surface recombination, and FBPA is enough to repair the PL losses of N_2 annealing. But enter another semiconductor material and the electronic states that form at the interface between them, and only oxygen is able to passivate enough to give PL close to the interface-free case.

These experiments bring us to an understanding of what types of defects are present in our solar cells, and how different passivation mechanisms affect them. These ideas are illustrated for clarity in figure 2.21. These show red dots as trap/defect sites and passivating agents that "cover" them. The severity of losses from trap states depends on their position within the E_g and the rate of capturing either an electron or a hole (proportional to capture cross sections and speed of transfer). Traps near the band edge are considered less severe, and traps near mid-gap are considered "recombination centers". There does not exist a characterization method that would allow us to determine defect nature, speed, and energy level at interfaces buried within the cell stack. So we are left to theorize what is happening in our PSC based on the PL measurements. Figure 2.21 first shows an unpassivated example (annealed in N_2, top right), with or without an HTL present. Based on the low PL of unpassivated N_2-perovskite on glass, we infer that there are natural damaging surface states in this case. These are illustrated as mid-gap defects. When the HTL is added, interfacial states are created and band bending occurs. The new states would increase recombination, in line with the slight PL loss on TaTm relative to glass for the air-annealed perovskite in figure 2.20a. The further loss with ITO below the TaTm is likely due to the conductive material aiding the collection of charges at active

defect sites. Finally, charge transfer and accumulation at the HTL interface will induce band bending [74]. For defect states near the Valence band, this brings them closer to the band edge, neutering their affect, while states near the conduction band will be pushed closer to mid-gap.

We now take this example as the base case, and theorize the passivation effects of oxygen and FBPA separately (bottom left and right). Oxygen exposure alone is enough to give working cells, and these samples also gave the highest PL in all cases. This is illustrated as oxygen covering the main defect states in the bare perovskite and the new states in the HTL/perovskite

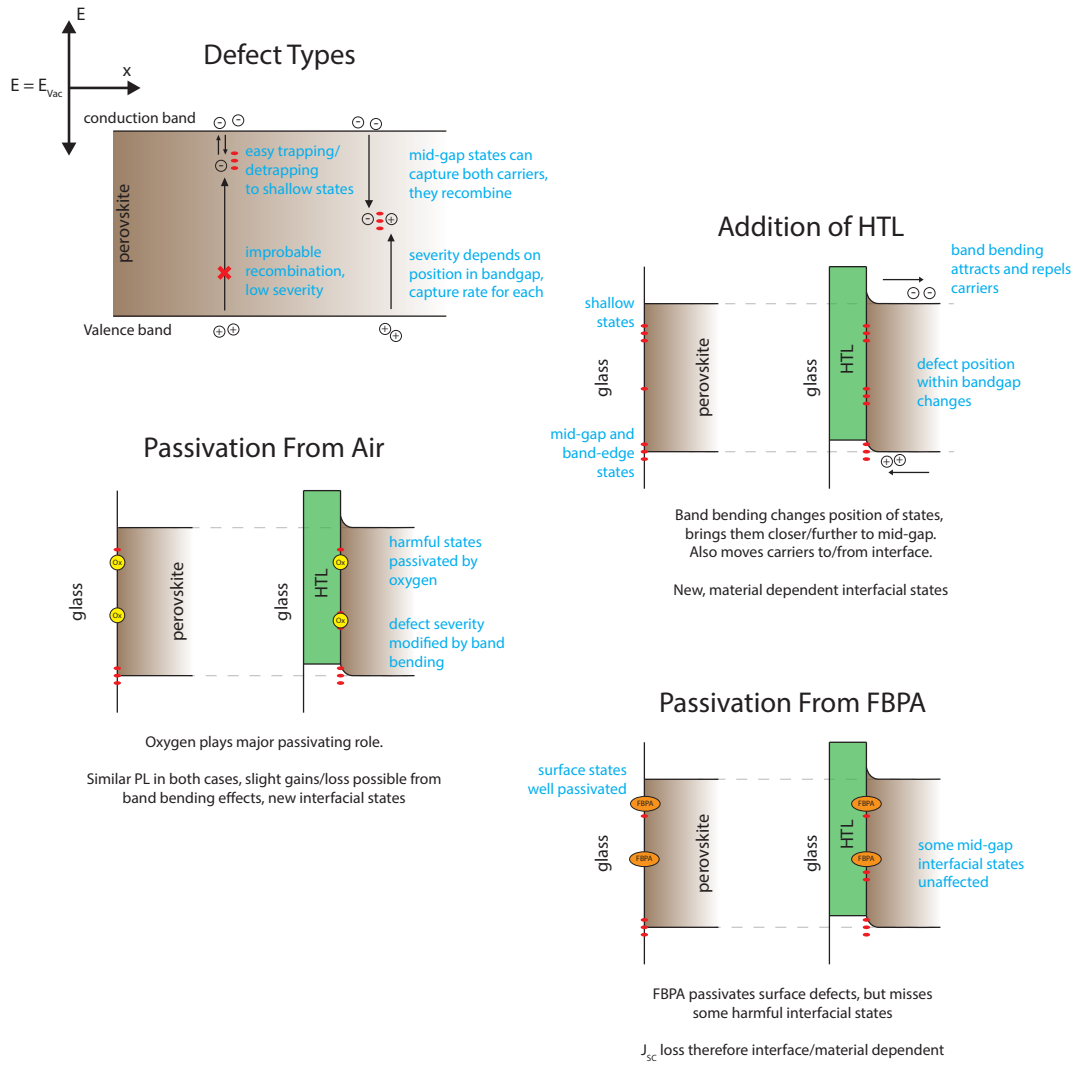

Figure 2.21 – Band diagrams of perovskite interfaces with qualitative defect and passivation schematics. Defect states with energy levels that fall within the bandgap can be detrimental in different ways. This illustration shows qualitatively how these states react to band bending and passivation mechanisms, as we understand from experiments. These do not represent measured values of defect count, energy level, or passivation effects.

case. FBPA-perovskite on glass gives good PL even in N_2, so we illustrate FBPA to cover the native surface states in the bare perovskite as well. But enter the HTL interface, and the PL drops significantly for all conditions without oxygen (figure 2.20b). Thus we believe that some of the new electronic states created at the TaTm perovskite interface are not passivated by FBPA, as illustrated by the FBPA covering different defects than the oxygen. The idea that these passivation mechanisms do not fully overlap is further supported by the fact that air-annealed samples improve their PL intensity upon FBPA addition (figure 2.15).

The effectiveness of oxygen as a passivant is supported by the diverse roles described for oxygen in the literature, such as binding to Pb and I defects in the bulk or at surfaces [118], [121]–[124]. But it also begs the question of if other HTL materials induce the same interfacial states with the perovskite, how harmful those states are, and if anything besides oxygen can be used to passivate them. As a quick cross check, since the original JV results took place on NiO_X and the PL measurements on TaTm, we checked the opposite cases as well. JV results on TaTm are shown later in figure 2.28, but fully agree with the PL results here. PL intensity on NiO_X likewise agreed with the JV results, dropping 460x in N_2 relative to air.

We next move to the work done towards identifying the electronic states that participate in this recombination. To this end, we sent samples to be measured by X-ray Photoelectron Spectroscopy[9] (XPS). Since this is a surface measurement that probes up to 10 nm into the sample, we prepared samples in air and N_2 in special ways so as to access the "buried" bottom interface of the perovskite. Two separate attempts were made towards realizing this measurement, first by using thin electron-transparent substrates and second by lifting up the perovskite to reveal the bottom surface. We thank Dr. Mounir Mensi, who performed all of the XPS measurements shown here, and for generously giving his time and expertise towards the analysis of results.

The first attempt was to deposit the perovskite on "TEM grids" (typically used for Transmission Electron Microscopy, TEM). These are small copper grids with 100 µm holes and a thin (8 nm) carbon film lain over the grid (from Plano). We made air and N_2 annealed perovskites on these grids, and measured XPS on the bottom surface. SEM measurements were used to confirm the correct deposition of the perovskite on the TEM grids, and these results are shown in section B.5.1. The comparison of the bottom and top surface measurements are shown in figure 2.22, along with measurements of the isolated TEM grids which were annealed in parallel. We note here that a uniform shift in the XPS x-values (binding energy of the measured electrons) can be caused by the sample charge. In the case of our measurement, the top-surface measurement was grounded, and the bottom-surface measurement was charge compensated with an electron beam to try and align the measures. This is imperfect however, and the data are later aligned to the iodine 3d peak.

[9] This method irradiates the samples with photons from the extreme UV to soft X-ray ranges (1-1000 eV) which then liberate electrons out of their orbitals near surface of the material, up to 10 nm deep. The electrons are collected and their energy is measured, which distinguishes both the element and orbital that the electron came from. This allows the identification of chemical states and bonds at the surface.

The first thing to notice about these measurements is that all of the samples showed similar quantities of oxygen. Despite being fully prepared in an N_2 environment, all samples were briefly exposed to air while being loaded into the measurement chamber. Though, since no heat was applied to the N_2 annealed samples while they were in air, it should avoid replicating the chemical effects of annealing in air. The oxygen signal on the bottom surface is different between the air and N_2 samples, but these signals overlap with that contributed from the TEM grid alone (seen in the graph below). Thus, there is no possibility of comparing the samples based on the oxygen peak. For the nitrogen signal, the top-surface peaks are again similar, and the difference in the bottom-surface peaks is most likely attributable to the TEM grid. Nitrogen is present in the perovskite in the organic FA cation, to which we attribute the top-side peak at 401.1 eV. The bottom-side peaks are shifted to lower energy and the air annealed perovskite has a secondary peak, but references from an XPS peak database [213] do not show any overlap with nitrogen-oxygen species (nitrite (-NO_2) has a peak at 403.9 ± 0.7 eV, and nitrate (-NO_3) has a peak at 407.2 ± 0.6 eV). There are multiple nitrogen-carbon species with peaks in this area (amide, nitrile, xyanide, imine) which may be produced in our samples due to the TEM grid or by a significant portion of the FA degrading. Though, we consider such FA degradation to be unlikely given the functionality of air annealed perovskites.

The carbon, bromide, iodide, and lead signals see no significant difference on either side. The bottom-side carbon signal is overpowered by the signal from the TEM grid, and the signals from the heavy elements are too similar to differentiate in any case. All conditions show a small shoulder of Pb_0 or metallic lead. This is a defect type commonly associated with oxygen passivation [118], [121], but for us is visible with or without air exposure. We also note the bromide and iodide signals measured on the TEM grids annealed in N_2. This indicates that the N_2 environment in which annealing took place was contaminated with these elements, if not others. The hotplate used for this experiment is in the same glovebox system that houses all spin-coating processes. Overall, across all the elements there is little to no discernible difference between the surface chemical states of air and N_2 annealed samples. Though, there was evidence of oxygen contamination and significant overlap between the signal contributed from the samples and substrates.

The second method used to measure XPS on the bottom interface was to perform a "lift-off" of the perovskite, where an adhesive tape was applied and removed, taking the perovskite with it to expose the bottom surface. This method had the benefit of directly exposing the bottom interface without the interference of a substrate, but also required briefly exposing both top and bottom interfaces to air in during the loading into the measurement chamber. Additionally, in order for the lift-off method to work, the perovskite was deposited on a glass/ITO/MeO-2PACz[10] substrate. Both this and the organic glue used in the tape may have left a reside on the bottom surface. The measured carbon signal on the bottom surface and significantly lower

[10] A SAM molecule for hole transport, [2-(3,6-Dimethoxy-9H-carbazol-9-yl)ethyl]phosphonic Acid.

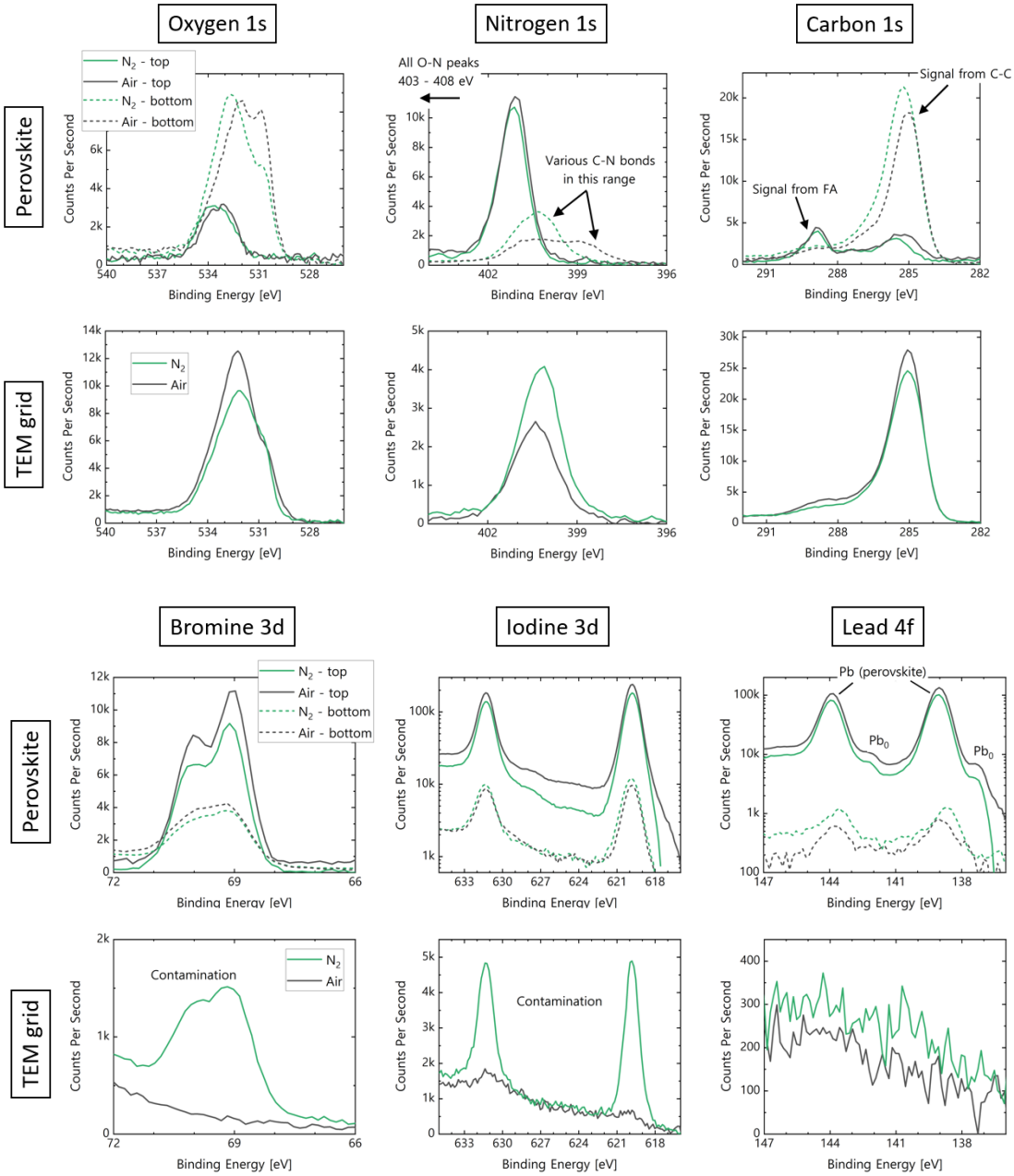

Figure 2.22 – XPS spectra for perovskites deposited on TEM grids, and of the grids. Standard hybrid PVD/SP perovskite was deposited on TEM grids attached to glass substrates, with annealing in either air or N_2. Multiple grids were prepared per condition, and half were left as-deposited, while half were flipped upside-down. Then XPS measurements were taken on both the top of the perovskite and of the bottom through the grid. Likewise, plain TEM grids without perovskites were treated to the same annealing and measurement, to identify what signal comes from the grids and how much contamination is present from the processing environment. Samples were sealed in vials in an N_2 environment before being sent for measurement. For the N_2 annealed samples, their only exposure to air was the transition of the measurement stage from N_2 glovebox to the measurement chamber (less than 1 minute). All curves aligned according to the iodide 3d low-energy peak. All samples used a template with 12%vol CsBr.

counts for all species on the bottom suggest that some amount of organics are present. For the nitrogen, oxygen, and carbon measurements, the bottom-side signal is multiplied by 10 for the sake of readability on the same graph. The results are shown in figure 2.23.

We again start by addressing the fact that the same oxygen signal is measured for both conditions. This likely comes from the brief air exposure during sample loading, and compromises the validity of the measurement. Though since no heat was applied while they were in air, it should avoid replicating the chemical effect of annealing in air. Regardless, there is no meaningful difference in the oxygen, nitrogen, or carbon XPS signals between the air and N_2 annealed perovskites[11]. We do observe a difference between the top and bottom surface signals for carbon. While the top-side measurement shows two nearly equal peaks, the bottom side is dominated by the lower energy peak. From expected peak locations of certain bonds (database at [213]), we attribute the higher energy peak to the carbon signal from the FA molecule and the lower energy peak to C-C single bonds. These bonds are present in the

[11] We note here that this measurement on Cu tape did not mimic the lower-energy nitrogen peaks of the TEM grid bottom-surface measurement. This further supports that the observed difference in nitrogen signal between air/N_2 was caused by the TEM grid.

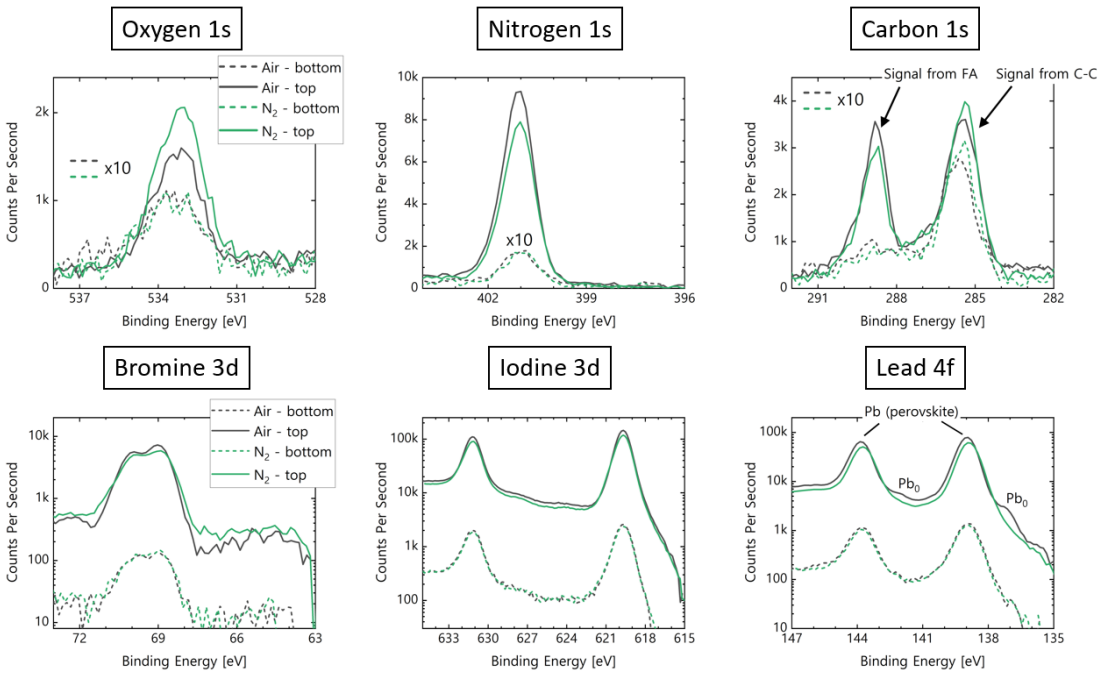

Figure 2.23 – XPS spectra for perovskite top and bottom surfaces, as revealed by a "lift-off" procedure. Perovskite was deposited as normally on glassITO/MeO-2PACz substrates, and annealed in either air or N_2. Then a piece of Cu tape was pressed into the perovskite and lifted off to reveal the perovskite bottom surface. The XPS measurement was then performed on both surfaces. Other than the air annealing, samples were fabricated, sealed in vials, and prepared on the measurement stage all within an N_2 environment. For the N_2 annealed samples, their only exposure to air was the transition of the measurement stage from N_2 glovebox to the measurement chamber (less than 1 minute). All curves aligned according to the iodide 3d low-energy peak. All samples used a template with 12%vol CsBr.

SAM molecule [56] and the organic glue used in the tape, indicating signal from species other than the perovskite. As for the top surface, there should only be FA (no C-C bonds). Possible explanations are that the samples are contaminated or that the FA has decomposed into different species. It is known that FA can decompose at temperatures already below 150°C [62], [190], but this only results in compounds with C-N and C-H bonds as measured by nuclear magnetic resonance [62] and mass spectroscopy [190]. Additionally, these compounds do not allow the formation of a perovskite [62]. So, we are left to conclude that the top surface has been contaminated by a foreign species during preparation or measurement. This could have come during the annealing step, which is done in the same glovebox as used for the spin-coating step, and is home to many different organic compounds in powder form. But otherwise, the nitrogen, oxygen, and carbon signals from XPS do not show any difference in the chemical surface states of air and N_2 annealed perovskites.

Looking at the bromide, iodide, and lead peaks, we again do not see extreme differences between the samples. There is a slight broadening of the top-side bromide peak in N_2, but this is likely because of sample charging. The iodide peaks are identical across conditions. The lead peaks show one small but potentially important difference, in that there is a small Pb_0 shoulder on the low-energy tail of the main peaks. This is a defect type commonly associated with oxygen passivation [118], [121], but for us is only visible in samples with air exposure. This disagrees with the results on TEM grids. In both cases, the top-side measurements were taken off of the TEM grid or Cu tape, and thus are identical in preparation.

Overall, the XPS data do not reveal a clear culprit for the recombination losses of N_2 annealed perovskite. All of the samples were contaminated with oxygen during the sample loading, which is unavoidable. The only sample that was fully protected from oxygen was the bottom surface as measured through a TEM grid, which was then obfuscated by the signal from the TEM grid itself. Otherwise, nearly every measurement was identical between top/bottom and air/N_2 annealing. This shows the level of sensitivity of perovskites to defects and surface chemistry, in that undetectable populations can cause enough recombination to reduce device current near zero.

Replicating Oxygen's Effect

One goal of this research was to replace the effect of oxygen with a more controllable method. To this end, we chose to use ethanethiol (ET). This molecule consists of two carbon groups and a thiol group (CH_3CH_2SH). The sulfur moiety makes it a Lewis base, meaning that it readily donates a pair of non-binding electrons (same as FBPA). This was expected to passivate under-coordinated Pb^{2+} defects in the same way as oxygen [118], [121], and modify the crystallization kinetics as observed for other Lewis bases [210]. Beyond its chemical nature, ET is of a similar size to FA (NH_2CHNH_2). We expect this to allow ET to diffuse through the template in the same way that FA does during the interdiffusion and reach the bottom interface where the recombination appears to be most active.

ET was included directly in the spin-coating solution of the hybrid PVD/SP method, and made into cells. The results of this first test are shown in figures 2.24 and 2.25. First, a sweep was done of ET molar percentage relative to FA, for PSC annealed in air. The optimum concentration improved J_{SC} and FF over the reference, shown in figure 2.24a, although with a loss to V_{OC}. It was observed that ET inclusion generally increased the J_{SC}, until losses from parasitic PbI_2 absorption reduced the gains (figures 2.24c, 2.25). FF similarly improved for all samples, while V_{OC} dropped quickly and plateaued. In the same batch of cells, the N_2 annealing experiment was repeated with and without ET. The JV results are shown in figure 2.24b. While the baseline behaves as normally, the N_2 annealed PSC with ET doping regain almost all of their J_{SC} loss. This confirms that the chemical role of oxygen can be at least partially replicated with ET, a Lewis base.

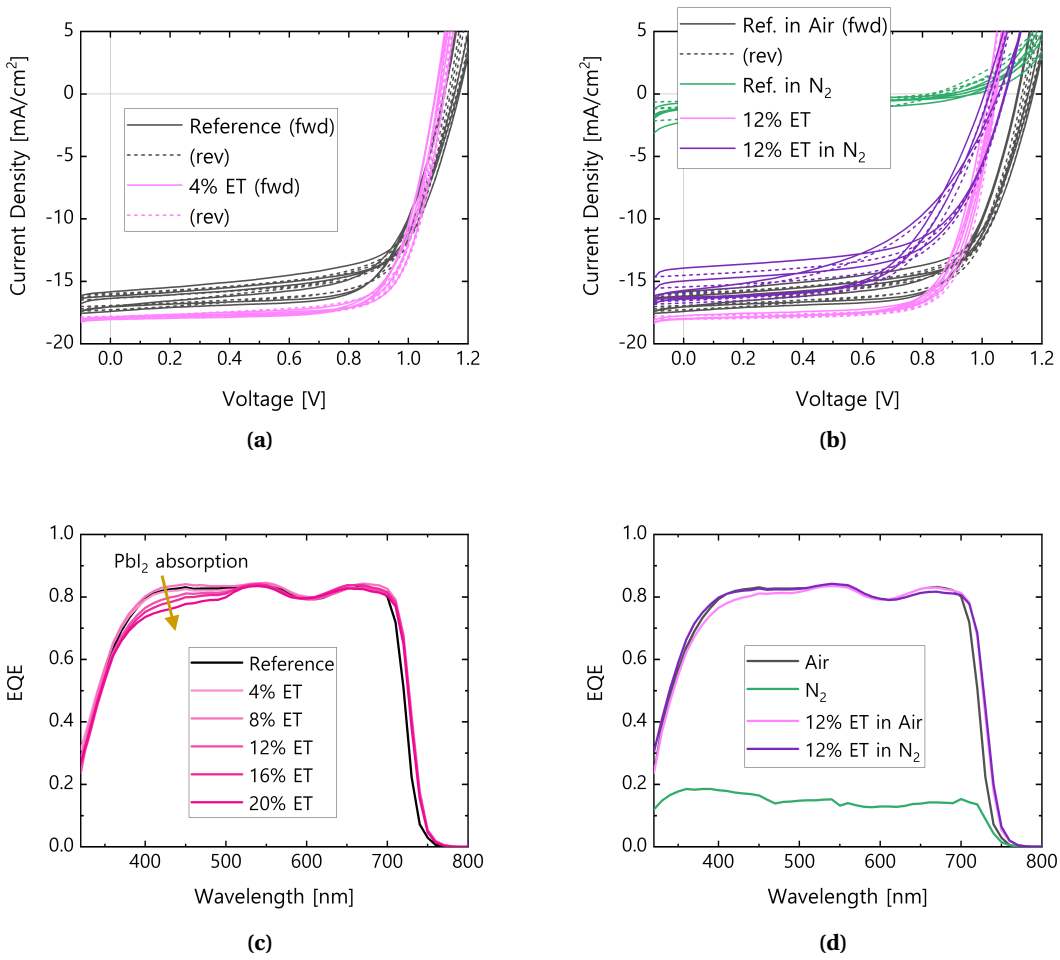

Figure 2.24 – *JV* and EQE measurements for PSC fabricated with ET. (a) JV curves for a batch of PSC with either 0% or 4%mol ET relative to FA. (b) JV curves for a batch of PSC annealed in air or N_2 and either no ET or 12%mol ET relative to FA. (c) EQE curves for increasing ET percentages. Note the uniform shift in E_g for the ET-doped PSC, about 10 meV. (d) EQE curves for the champion cells of each condition in (a). The cell stack was glass/ITO/NiO_X/perovskite/LiF/C_{60}/Ag.

To discern the role of ET in the perovskite, we did PL measurements. The first of these is shown in figure 2.26. Here, the PL is imaged for air annealed samples with different amounts of ET. Two effects are visible, in that the PL gets brighter and more uniform. Since these samples are annealed in air, the brightening tells us that ET has some passivation ability in addition to that of oxygen. The uniformization of the PL supports the idea of ET slowing crystallization due to formation of an adduct with PbI_2, as has been observed for Lewis bases [210]. A better converted bilayer also agrees with the improvement to J_{SC} observed in cells (figure 2.25). The best PL intensity at 4%mol and uniformity at 12%mol tells us that the mechanisms giving better uniformity and brighter PL are not the same. PL data also allows for calculation of the Urbach Energy, via the method of figure 2.11b. This was done with point PL spectra taken from across the substrate area, and used to calculate values of 12.91±0.35 meV for the reference perovskite, and 12.76±0.18 meV for perovskite with 6%mol ET. Thus, with ET there is negligible change to bulk quality, slower crystallization makes the perovskite more homogeneous, and a passivation effect separate to that of oxygen increases the PL output. For PL of ET in N_2 annealed perovskite and comparison to the passivation role of oxygen, see section B.5.

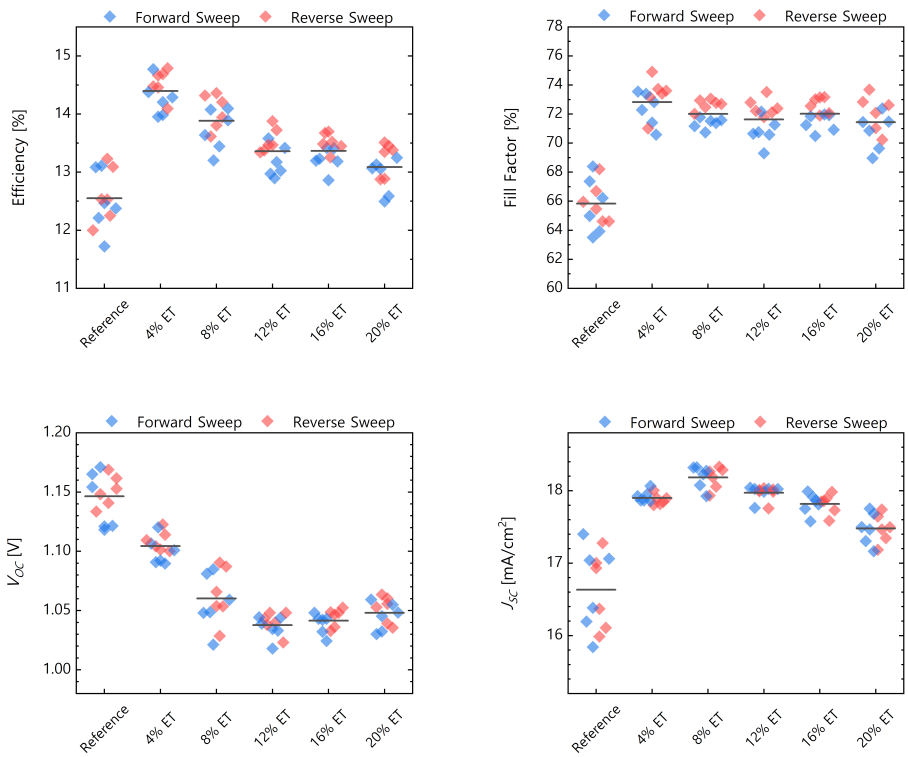

Figure 2.25 – *JV* statistics for a sweep of ET doping rates. The percentage refers to the molar ratio with respect to FA, measured in the spin-coating solution. To encourage ET adoption within the crystal, the FA concentration was reduced in parallel with the ET increasing. The cell stack was glass/ITO/NiO_X/perovskite/LiF/C_{60}/Ag.

Alongside characterization efforts, we continued to fabricate PSC with and without ET, optimizing production parameters and seeking to improve on the efficiencies obtained in figure 2.24a. Cells with NiO_X as HTL were reliable, but rarely exceeded 13% efficiency (compared to 16% upper limit for Spiro-TTB). Higher performing materials were tested, but the cells reliably failed. An example is shown in figure 2.27. On NiO_X, the cell with ET gives higher efficiency (despite still low V_{OC}), while on Spiro-TTB the cell gets worse with ET (at this point in time, TaTm and SAM materials were either not optimized in our lab or not yet discovered). This s-shape is characteristic of poor charge transport, which we attributed to ET damaging the organic HTL material. ET was thus considered incompatible with organic HTLs and was restricted to the lower performance of NiO_X.

Uniting the different themes of this section, we tried different HTL materials for N_2 annealed perovskites (figure 2.28). The motivation of this was the PL analysis and theorized recombination mechanisms described in figures 2.20 and 2.21. From these, interfacial states with the HTL appeared responsible for the recombination and J_{SC} losses, and that therefore some material may exist which does not form any damaging electronic states when interfaced with the perovskite surface. Thus, we returned to the N_2 annealing question over the years when new HTL materials were demonstrated. This led to the discovery that MeO-2PACz (a SAM molecule) does not experience the same J_{SC} loss upon annealing in N_2. It still does not fully recover the lost J_{SC}, but this is likely due to the absence of H_2O which otherwise helps

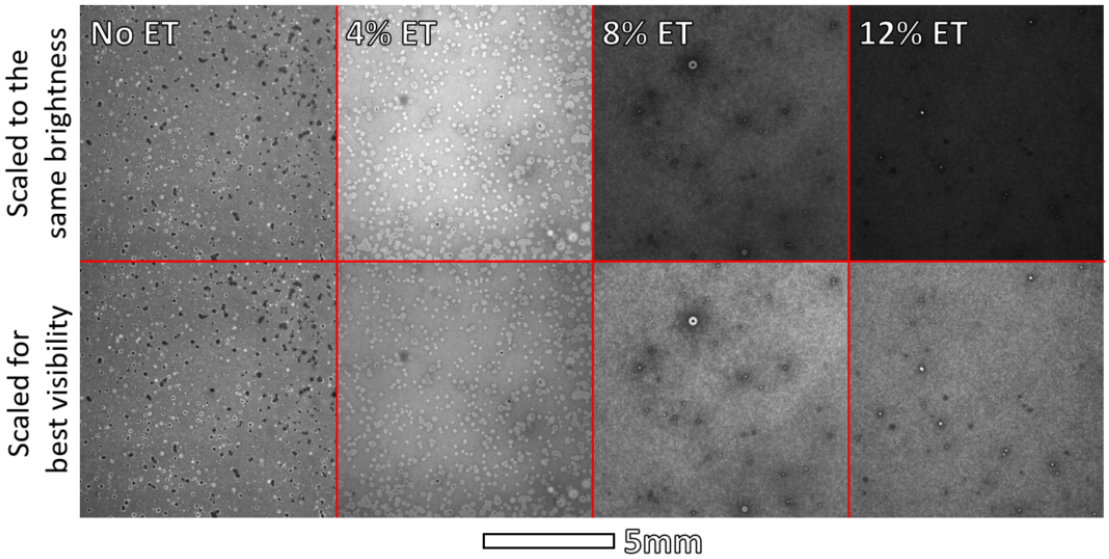

Figure 2.26 – PL images for PSC based on perovskite films with varied ET doping rates. PSC were exited with a red LED that was filtered to pass only below 670 nm. Their PL was imaged with a Nikon camera through a 670-715 nm bandpass filter to only take the high-energy emission tail ($E_g \approx 740nm$). The images were taken through the glass of the PSC and within the cell area. The percentage refers to the molar ratio with respect to FA, measured in the spin-coating solution. The top line of images have their brightness scaled to the same level relative to eachother, and the bottom line of images are the same but with brightness scaled for visibility.

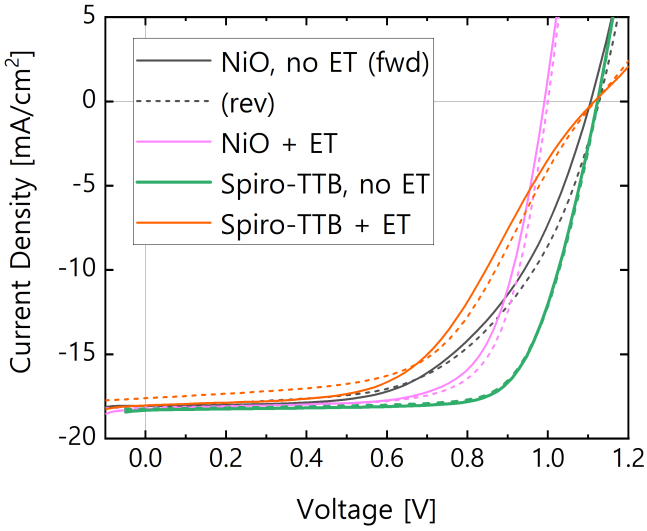

Figure 2.27 – *JV* curves for PSC on different HTLs, with or without ET doping. ET was included at 10%mol relative to FA. All samples were annealed in air, and the only thing changed about the cells was the HTL. The cell stack was glass/ ITO/ HTL/ perovskite/ LiF/ C_{60}/ Ag.

aid the bilayer conversion [193]–[195], as complete conversion has been linked to better J_{SC} previously (figures 2.5, 2.10d, and 2.25). But regardless, it does not experience close to the same losses as NiO_X or TaTm. We then conclude that this material does not form the same type of damaging interfacial states that require oxygen to passivate.

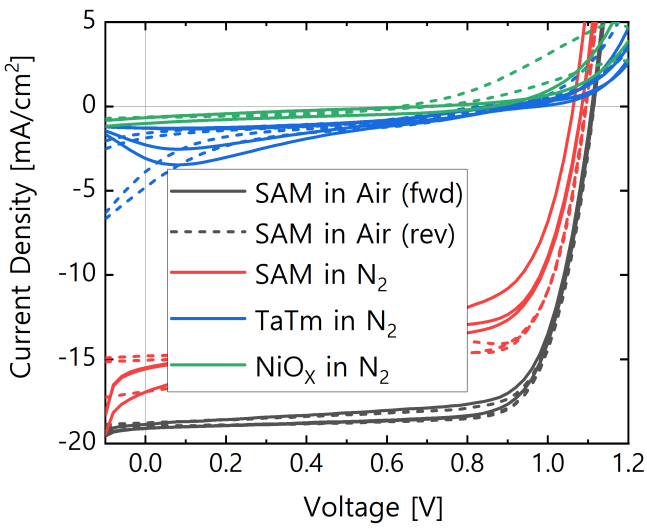

Figure 2.28 – *JV* curves for PSC on different HTLs, annealed in air or N_2. Due to the different availability of materials over time, these cells were not produced in parallel. Thus the template and spin coating may vary slightly, but the same recipe was used for all cases. FBPA was only used in the TaTm cells, and not in any other case. The SAM used was MeO-2PACz. The cell stack was glass/ ITO/ HTL/ perovskite/ C_{60}/ Ag.

2.3.3 Conclusion

This section looked at the various effects of surface and interfacial recombination in single junction PSC formed with hybrid PVD/SP perovskite. We first addressed the CTLs, and devised a method for direct comparison of different interfaces within the same sample. This showed that fluorinated benzene phosphonic acid (FBPA) can passivate surfaces, and that TaTm and SAM are better interface materials than Spiro-TTB. This was further verified in cells, which improved in V_{OC} and efficiency.

We also examined the role of processing conditions in material passivation, most notably the exposure to O_2 during the annealing. This was crucial to cell performance, giving a significant J_{SC} loss when annealing in N_2. We attributed this to oxygen passivating both surface and interfacial defects. FBPA was able to mimic this passivation, but only in the absence of material-dependent interfaces. We partially rectified the losses from annealing in N_2 by adding a Lewis base molecule (ET) with a size intended to allow it to diffuse to the bottom surface. Further characterization revealed that ET was passivating, but not by the same mechanism as O_2, while also modifying the crystallization to produce a more homogeneous material. This additive interacted poorly with organic HTL materials, and thus was both not viable in the highest efficiency cell designs. Finally, we discovered that a certain HTL material, the SAM MeO-2PACz, did not form the same damaging interfacial states as other HTLs. This succeed in making working cells without O_2 exposure.

2.4 Perovskite Morphology and Charge Transport

A high-performing perovskite material must not only have correct constituent ratios and low bulk disorder, but also transfer charges efficiently. This behavior is linked to material quality, and thus is governed by many of the same processing parameters as were optimized in the previous sections. Annealing temperature in particular affects the morphology and chemical makeup of the perovskite, and these in turn govern the material's ability to transport excited charges. This section discusses the trade-off between these properties and how the optimal point is affected by the surface-binding FBPA molecule. We find that modification of the perovskite surface can skew the balance and allow for a higher temperature limit before the onset of limiting degradation, which benefits the material's ability to transport charges and achieve high FF.

2.4.1 Modifying Perovskite Crystallization

At the beginning of this chapter, we described the effects of annealing temperature on the crystal uniformity, order, and chemical balance of hybrid PVD/SP perovskites (section 2.2). As the temperature increased, the perovskite diffraction peak became taller and narrower; the bulk disorder reduced; and the residual precursors dropped out of detection. These benefits continued up until the annealing passed 150°C, where the perovskite started to have excess PbI_2 and increased bulk disorder. Thus, the trade-off point between the benefits and detriments of annealing temperature was established at 150°C, which aligned with the best PSC efficiency. But the annealing temperature is important beyond just the crystalline quality, affecting also the morphology of the layer. As the annealing temperature is increased, the features of the perovskite layer grow larger and more uniform. Figure 2.29 shows this with top-down SEM images of perovskite layers formed over a range of temperatures, with and without the FBPA additive. The same trend is observed in both cases, with minimal changes when including the surface-passivating FBPA.

It is worth noting before the discussion that the features seen on the surface of these films are not strictly uniform crystallites, and may contain internal discontinuities [214]. Nevertheless, increasing the temperature of film formation reduces the density of boundaries between the visible perovskite domains, which are certainly also lattice terminations regardless of if other internal boundaries exist. This is beneficial to the perovskite quality, and is in line with the results of section 2.2.1. But again, the previous results showed an unavoidable trade-off, and cells produced above 150°C performed worse in V_{OC} and FF. We linked this trend to perovskite quality improving with annealing temperature, only to be limited by the evaporation of organic FA from the layer above roughly 150°C and subsequent excess of the inorganic components.

The SEM images of figure 2.29 do not distinguish between films with or without FBPA. But differences do appear when looking at the crystallographic compositionin XRD. The same samples were measured, and a subset of the diffraction pattern cropped to the perovskite and PbI_2 peaks is shown in figure 2.30. While the perovskite peak (at 14.2°) does not change

drastically with annealing temperature, the PbI_2 peak (at 12.7°) increases from non-detection to being nearly the same intensity as the perovskite. Importantly, the samples with FBPA show a lower ratio of the PbI_2 to perovskite peak intensity, and a higher temperature of onset for the PbI_2 peak. Figure 2.30c illustrates this by taking the ratio of the two peaks, for each temperature and with/out FBPA. In both cases, the peak ratios follow an exponential trend over the anneal temperature, but the layers with FBPA in them achieve the same proportion of PbI_2 relative to perovskite at roughly 20°C higher annealing temperature. We attribute

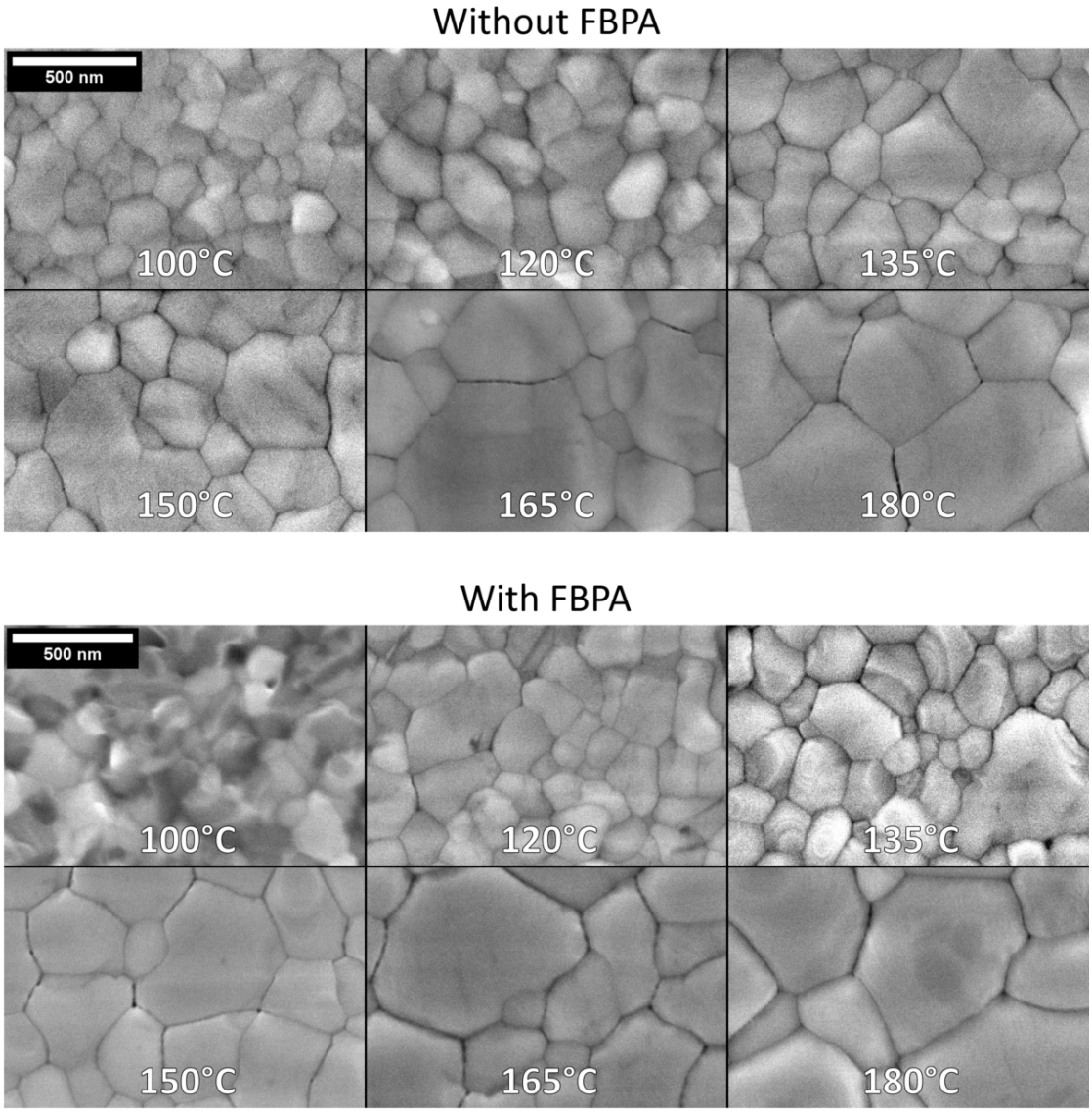

Figure 2.29 – SEM images of perovskite films annealed at different temperatures. Annealing took place in air, with a controlled dew point between 10 and 15 °C. All layers were made from the same PVD template and SP recipes, with or without 5 mM FBPA in the spin solution. The dark hazy mass in the 100°C film with FBPA is likely residual bilayer components which were not well mixed due to low annealing temperature.

this difference to the FBPA acting as a sealant of the perovskite surfaces. Organics with a phosphonic acid group have been observed in the literature to bind to metallic surface states [108], [126], [128], [209], which could provide a barrier at the perovskite surface which prevents the loss of ions such as FA^+ and I^- to evaporation [59], [107]. Achieving the right quantity of PbI_2 in the perovskite is important to achieve the highest efficiencies [64], [65], but too much excess PbI_2 is detrimental [59], [66], [67]. The limit of keeping PbI_2 at a tolerable level is what

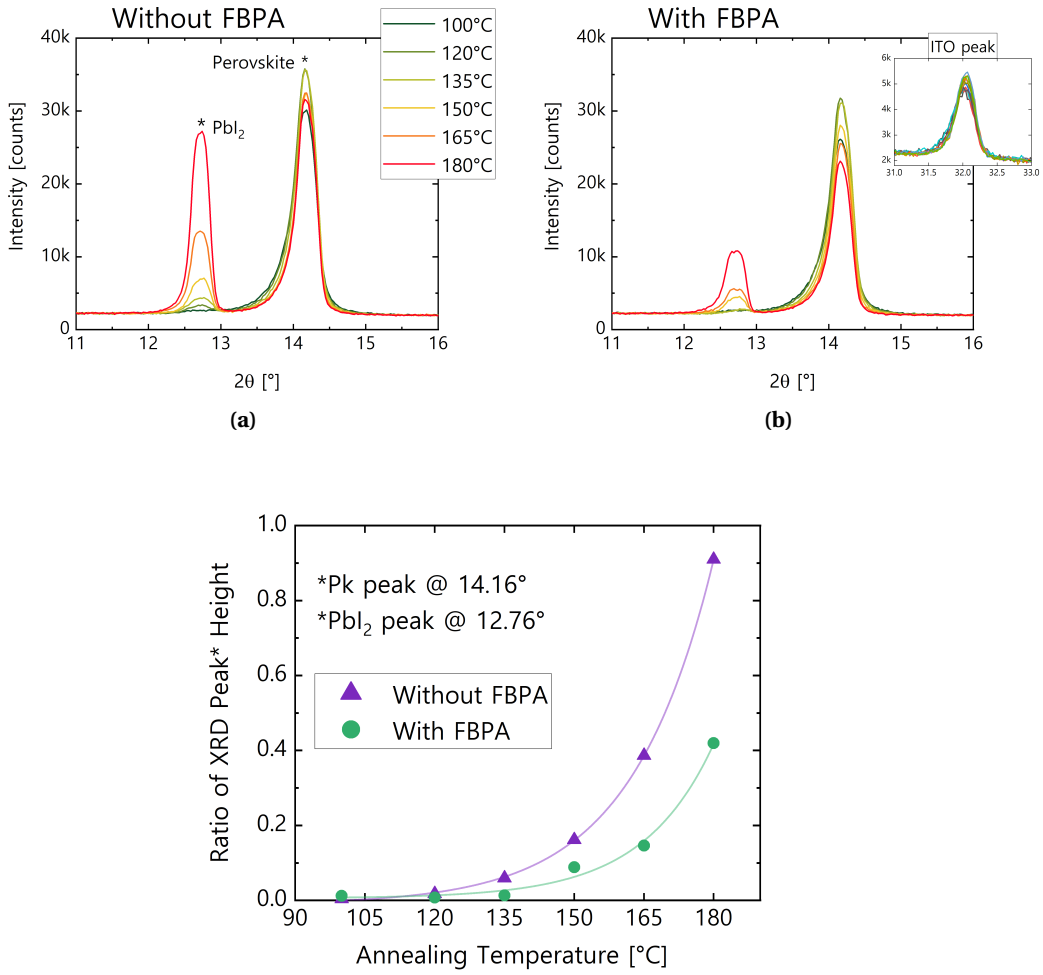

Figure 2.30 – XRD patterns for perovskite layers annealed at different temperatures, with and without FBPA. (a-b) show the XRD intensity patterns for the perovskite layers without (a) and with (b) 5 mM FBPA included in the spin-coating solution. (b) also includes an inset with the ITO diffraction peak from each of the 12 measures, to demonstrate the peak asymmetry which uniformly affected this measurement. (c) shows the ratio of the PbI_2 to perovskite peak heights for each measurement in (a-b). The lines are fitted $y = a * e^{bx} + c$ curves. The samples measured here are the same as the samples shown in figure 2.29. They were produced on glass/ITO, with the same PVD and SP steps, and annealed in air at 10-15°C DP. We note that these measurements were taken on a different measurement system (PANalytical Xpert Pro MPD) than the XRD patterns shown in section 2.2.

prevents us from otherwise using higher temperature annealing (a brief analysis of excess PbI_2 and material degradation is included in section B.9). However with FBPA included, the same relative fraction can be achieved with a higher annealing temperature, unlocking the benefits of the better morphology at these temperatures.

Looking to understand the role of FBPA in our films, we carried out in-situ GIWAXS measurements during heating to 150°C. The main plots are shown in figure 2.31. These are the same type of measurement as used to uncover the role of pre-annealing in section 2.2.2. Once again, we analyze these data by radially integrating the diffraction patterns to obtain a plot similar to the XRD measurements previously shown. This gives us a peak for perovskite (100) and PbI_2 over time, and from this extract information about the crystal growth[12]. The two main distinctions between the with/out FBPA cases are the growth rate and the PbI_2 level. The PbI_2 peak heights at the end of annealing align with the 150°C samples from our in-house XRD measurements (figure 2.30), but what the in-situ GIWAXS reveals is that the PbI_2 follows a non-linear path from start to finish. In all observed cases, the PbI_2 starts out with a slight decreasing trend, then at some point accelerates downward, before reaching a low-point and rising for the rest of the measurement time. The better consumption of PbI_2 and slower rise of the perovskite peak with FBPA included (a Lewis base) aligns with the slowed crystallization from adduct formation between Lewis base molecules and PbI_2 shown in literature [210] and previously attributed to ET (figure 2.26).

Next we focus on the different perovskite peak growth rate between the samples. The same pattern of growth and difference with/out FBPA is observed along multiple crystalline axes, showing that no particular growth axis is favored (figure 2.31b). Thus we performed our analysis on the brightest (100) diffraction peak. Using this data, we applied the Avrami method [215] to obtain information on the growth kinetics. This method allows for the computation of the dimensionality of grain growth, assuming random points of nucleation and a crystalline phase that expands outward from these points in 1 - 3 dimensions. The computation is based of the volume fraction of the crystallized phase, defined as Y, and the time (t) spent at a constant heating rate. These values are linked by the equation $Y = 1 - exp(-Kt^n)$ where K is a value encompassing growth parameters of the material and n is the dimensionality of the growth plus one ($n = Dim + 1$) [215]. Y(t) and t are known from the GIWAXS data, and the equation can be modified to $ln(-ln(1-Y)) = ln(K) + n * ln(t)$, enabling the determination of n from a linear fit of $ln(-ln(1-Y))$ versus $ln(t)$. This in turn gives the dimensionality of growth, from $n = Dim + 1$.

We applied this analysis to the data shown in figure 2.31a. Although, the peak evolution happened on different time scales for the films with/out FBPA, and thus the fittings were done over different ranges. These ranges are shown in figures 2.31c-d. Two regions were fit for each case, corresponding to different behavior of the peaks. Period 1 was selected for the portion

[12] It is important to note here that the spin-coating took place in air, in a different facility than our own, and by an external scientist (Julian Steele, from the Centre for Surface Chemistry and Catalysis, KU Leuven, Belgium). Thus, the absolute values of the perovskite and PbI_2 peaks might be affected, but comparisons between measurements are still valid.

of the conversion where the perovskite peak increased slowly and the PbI_2 peak decreased slowly. Period 2 was selected for the portions where both trends accelerate, up to the point where the perovskite peak growth slows and the PbI_2 peak trend reverses. Treating the data as described above and performing a fit for n over the time periods shown gives different values for the dimensionality of growth. For the baseline perovskite without FBPA, period 1 gave $n = 4.01 \pm 0.27$ and period 2 $n = 4.24 \pm 0.20$. For the perovskite with FBPA, period 1 gave

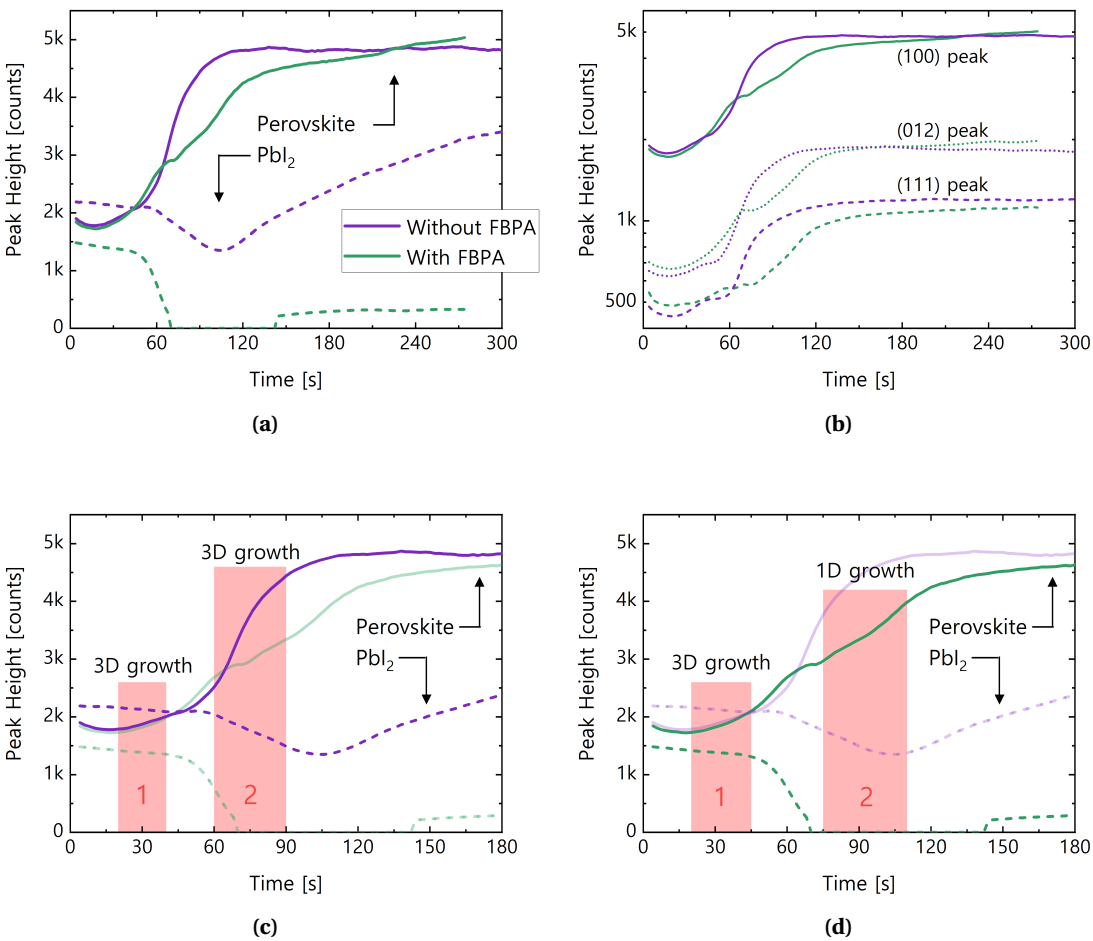

Figure 2.31 – GIWAXS peak heights over time for perovskites with or without FBPA. Samples were spin-coated in air with/out 5 mM FBPA, placed on the measurement stage (also in air), and heated from room temperature to 150°C at 100°C/minute. Measurement of diffraction patterns started simultaneous to the start of heating, and completed every 2 seconds. (a) shows the main perovskite and PbI_2 peak heights over time, for films with and without FBPA. For the PbI_2 peak with FBPA included, the peak intensity briefly dropped below the noise limit for clearly discerning the peak, and thus was asigned a value of 0 until it became resolvable again. (b) shows the perovskite peak heights for different diffraction planes, taken from the same measurements. (c-d) show the temporal regions used for Avrami method fitting, along with the dimensionality of growth extracted from this analysis.

$n = 3.98 \pm 0.17$ and period 2 $n = 2.27 \pm 0.08$. Thus, the film without FBPA grew consistently in three dimensions, while the film with FBPA started with three-dimensional growth, but then continued with mostly one-dimensional growth.

All together, it is unclear what amount of material improvement comes from the Lewis base chemical passivation of surface defects (section 2.3.1) and what amount comes from the different crystallization kinetics resulting in a better material. We can quantify the overall improvement using photoluminescence quantum yield (PLQY) measurements. The PLQY of the films from figure 2.29 and 2.30 was measured, and are shown in figure 2.32. First, the

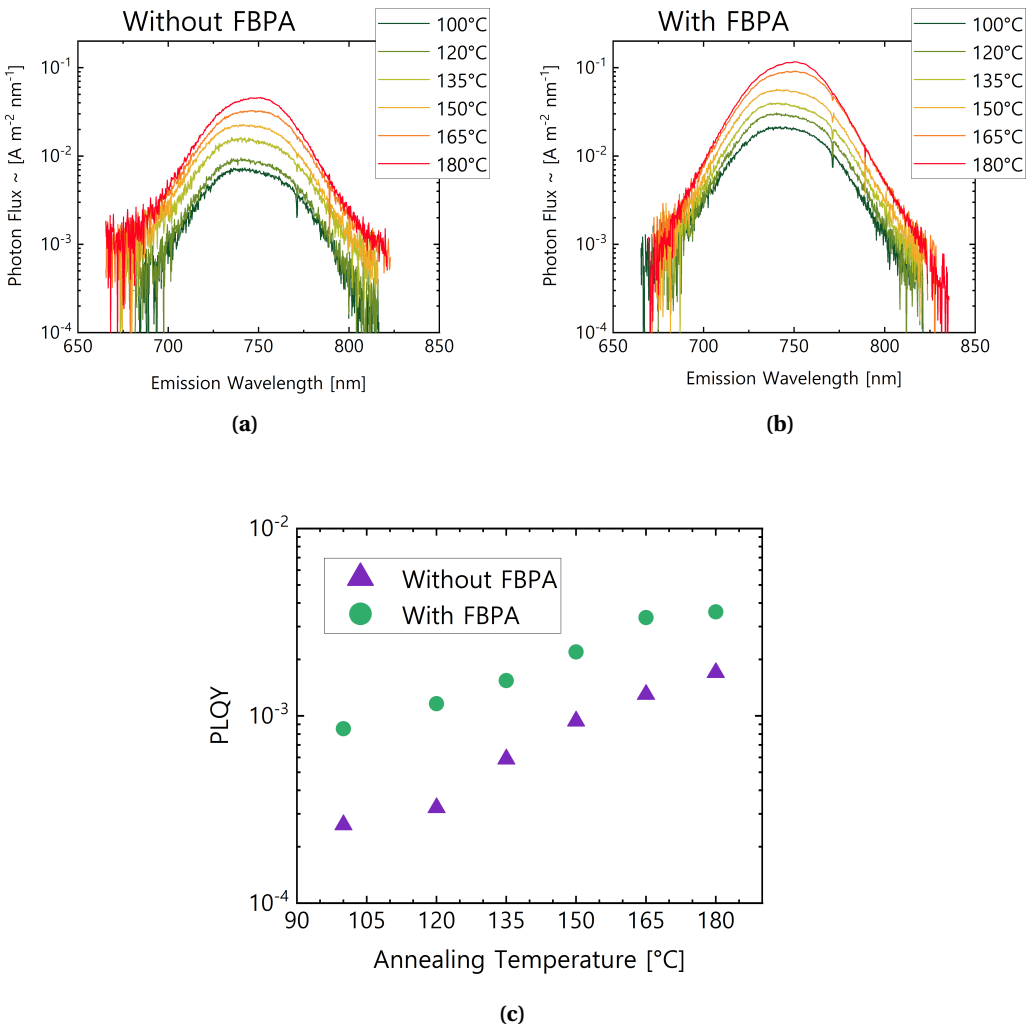

Figure 2.32 – PLQY measurements for perovskite films annealed at different temperatures, with and without FBPA. (a-b) show the photon flux spectra for the perovskite layers without (a) and with (b) 5mM FBPA included in the spin-coating solution. (c) shows the quantum yield of the curves in (a-b) relative to the absorbed photon flux (irradiated by laser at 1-sun intensity, 532 nm). Samples were deposited on glass and annealed in air. Samples of the same temperature were annealed together, to control for RH variations.

spectra in 2.32a-b show that in both cases the emission intensity goes up steadily with anneal temperature. These curves are quantified in figure 2.32c, which shows the calculated PLQY, which aligns with the improved morphology shown in figure 2.29. Following the trend in this graph, and including a 20°C increase in the annealing temperature (as established from the trend in figure 2.30c), the PLQY could conceivably be increased by 3.75x, which corresponds to 34 meV increase in QFLS.

2.4.2 Effect on Charge Transport

The higher temperature annealing enabled by FBPA affects more than just the QFLS of the perovskite. We find that the charge transport within the cell is also affected, specifically improving FF by 8.5% absolute. Figure 2.33a shows PSC made with a series of annealing temperatures, with an optimum at 170°C in line with the 20°C prediction of the previous section. The improvement in FF can be attributed to the R_{OC}, which reduced by 2.1 Ωcm^2 between the best cell at 150°C and 170°C. The V_{OC} behaves the same as in the previous temperature sweep (negative trend, figure 2.10c) while the voltage at the maximum power point (V_{MPP}) remains constant (figure 2.33e). Therefore the increase in efficiency follows only the increase in J_{SC} due to better conversion of the PVD/SP bilayer into perovskite (in agreement with the previous results of figure 2.10d). We also note here, that the cells without FBPA follow the same trend, albeit with slightly lower overall performance (due to lower V_{OC} without FBPA). The efficiency and FF are shown in figure 2.34. This stability is observed and discussed briefly in figure B.33.

An important distinction should be made between the results presented here and the annealing temperature sweep presented in the previous section, specifically figures 2.4 and 2.10. Previous attempts at the same experiment shown here in figure 2.34 were made with either NiO_X or Spiro-TTB as HTL. NiO_X cells were consistently limited to lower performance than organic HTLs, and Spiro-TTB has a glass transition temperature at 146°C [216] (observed to dewet from rough ITO surfaces at 150°C: figure 4.13, and in literature [62], [149]). Thus previous attempts were likely affected by these materials, and thus consistently gave an optimal annealing temperature of 150°C.

We next attempted to identify the source of this improved R_{OC} and FF. Simple checks were made to verify that the ITO and SAM were not responsible for the improved transport. The details and results of these tests are discussed in section B.8. Briefly, the ITO does not contribute meaningful improvement to the R_{OC}. The SAM contributes some improvement, but not enough to fully account for the FF gain in PSC. We therefore turned to the perovskite layer to find the source of these gains. We compared the measured FF values against pseudo-FF values obtained from reconstructed JV curves. The pseudo-JV curves were in turn created from Suns-V_{OC} and Suns-PL measurements [217]. The idea of each of these is to quantify the potential cell voltage at a given illumination level. From that, the cell current can be implied from the illumination, paired with the estimated voltage, and evaluated as JV data. This

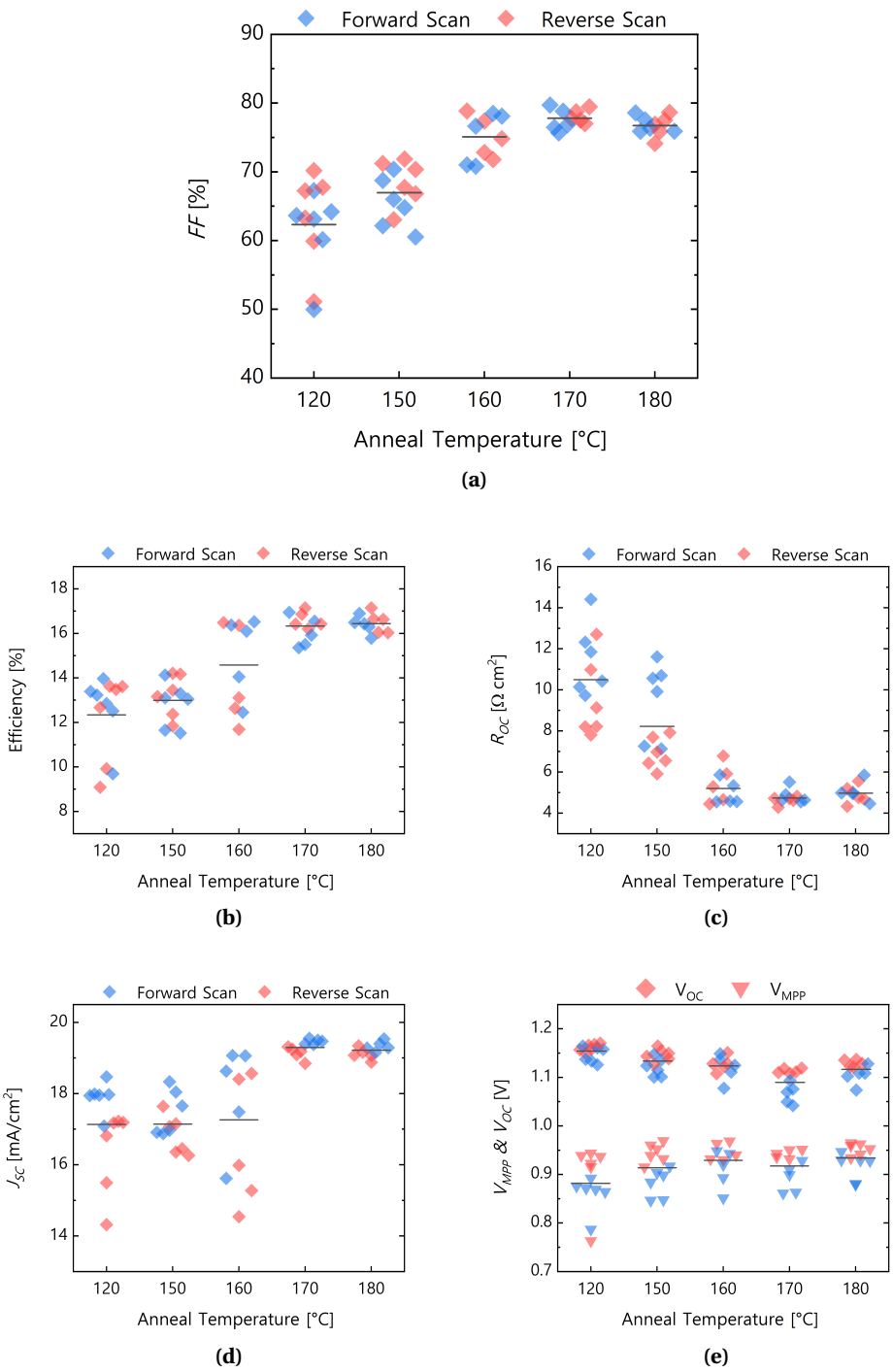

Figure 2.33 – *JV* statistics for PSC annealed at different temperatures, with FBPA. Cell efficiency improved with temperature and peaked at 170°C, mostly driven by gains in FF and J_{SC}. The FF gain was in turn reliant on changes to R_{OC}. The V_{OC} dropped with annealing temperature, but the operating voltage remained constant due to the improved R_{OC} and FF. The cell stack was glass/ITO/MeO-2PACz/Perovskite/LiF/C_{60}/BCP/Cu.

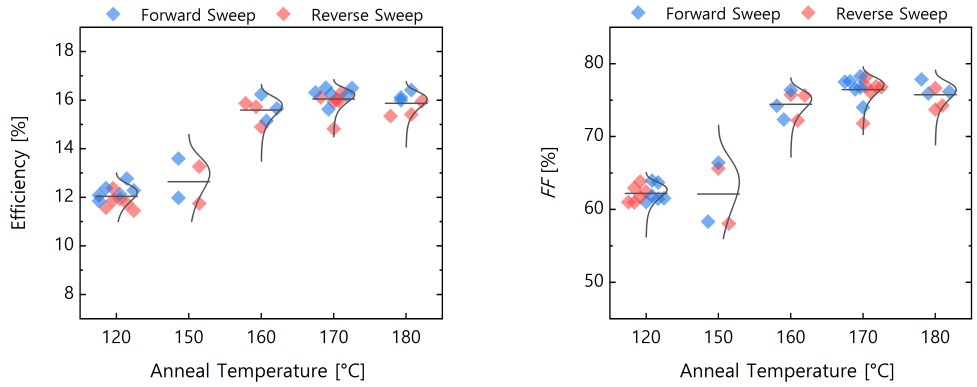

Figure 2.34 – *JV* statistics for PSC annealed at different temperatures, with no FBPA. The same general trend was observed for PSC both with and without FBPA. The cell stack was glass/ITO/MeO-2PACz/Perovskite/LiF/C_{60}/BCP/Cu.

results in pseudo-JV curves, without certain sources of loss. The first, Suns-V_{OC}, uses the V_{OC} and J_{SC} values obtained from JV measurements at different illumination levels. Because the series resistance of the cell is irrelevant (and dropped from the 2-diode model equation) when no current is passed, the JV reconstruction from Suns-V_{OC} gives the JV curve of a cell without any resistance losses from the circuit. Second, the Suns-PL method uses the QFLS as extracted from PLQY measurements of bare perovskite ($QFLS = k_B T * ln(PLQY \frac{J_G}{J_{0,rad}})$)[13], and the illumination level of the PLQY measurement as the V and J pseudo-data. Since there is no cell measured, the J_{SC} value of a full PSC with the same annealing is used and scaled according to illumination. This approximation removes the losses due to interfacial recombination and series resistance, and therefore gives the JV values for the perovskite layer with only surface/bulk recombination and optical losses. The measurements can be done on a neat perovskite film on glass, or in our case we used glass/ITO/SAM substrates in order to guarantee the same material growth as in cells. A comparison of the real or reconstructed JV curves obtained from normal measurement, Suns-V_{OC}, and Suns-PL are shown for a single condition in figure 2.35, and for all conditions in figure 2.36.

The implied FF values were extracted from these curves and those of other cells annealed at 150°C and 170°C, and compared in figure 2.36. In contrast to the real FF which was different according to the annealing temperature, the implied FF values are similar for both conditions over both methods. From this data we conclude that it is indeed the charge transfer within the perovskite which causes the improvement in FF for cells annealed at higher temperature. This is reasoned from the similarity of implied FF values across both Suns-V_{OC} and Suns-PL methods, and across the two conditions. Had the same gap been seen between the 150°C and 170°C cases in either of these two measurement methods, then the cell-level performance gap

[13] k_B is Boltzmann's constant, T is the temperature, J_G is the total free charge generation current density (approximated by J_{SC}), and $J_{0,rad}$ is the radiative thermal equilibrium recombination current density in the dark. $J_{0,rad}$ is obtained by integrating the cell EQE against the blackbody radiation at 300 K.

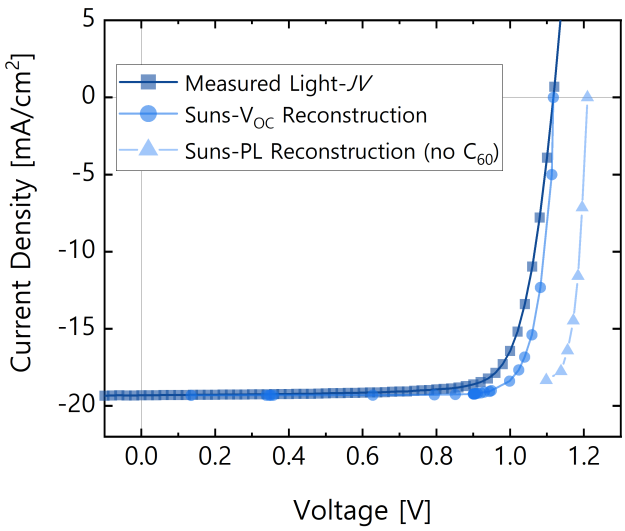

Figure 2.35 – *JV* data compared with reconstructed pseudo-*JV* data obtained form Suns-V_{OC} or Suns-PL measurements. The *JV* and Suns-V_{OC} data were obtained from the same *JV* measurement system, with metallic mesh filters used to reduce the illumination intensity. The Suns-PL reconstruction was formed from PLQY measurements of a perovskite layer on glass/ITO/MeO-2PACz, converted to QFLS and combined with implied current values defined by the cell J_{SC} multiplied by the PL illumination intensity. All measurements are for the standard perovskite composition, with FBPA, annealed at 170°C. The cell stack was glass/ITO/MeO-2PACz/Perovskite/LiF/C_{60}/BCP/Cu.

Figure 2.36 – Measured and implied *FF* values for perovskite cells and layers annealed at different temperatures. PSC and perovskite films were fabricated at 150°C and 170°C. The *FF* was extracted from the 1-sun *JV* curve, the Suns-V_{OC} reconstruction, and the Suns-PL reconstruction. For all curves, a fit was performed around the MPP to extrapolate the maximum *FF* from that data. The Shockley-Queisser theoretical limit for *FF* at this E_g is 90.92% (dotted line).

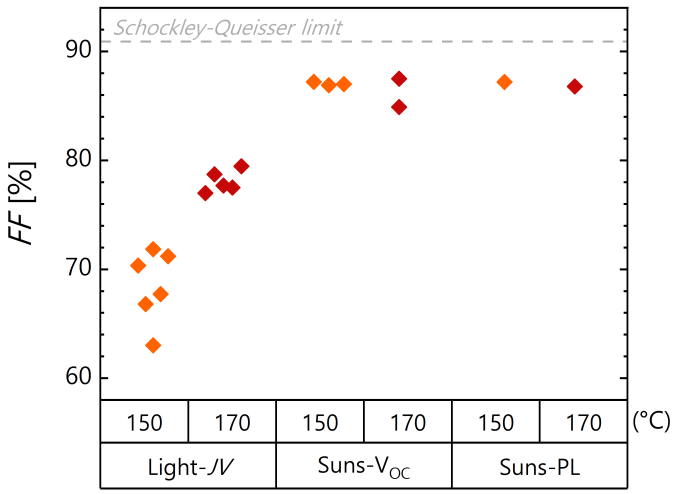

would be attributable to the effects probed by each of these methods. This is bulk, surface, and interfacial recombination in the case of Suns-V_{OC}; and bulk and surface recombination in the case of Suns-PL. But since neither of these show a meaningful difference, the cell-level gap must be caused by an effect outside of these lists, namely the resistance of the full circuit. Given that the layers outside the perovskite were identical, we attribute this fully to improved charge transport within the perovskite. This is notable in that it differentiates the improvement in FF from the improvement in PLQY. These are both enabled by a higher quality material, but the charge carrier transport and charge carrier population separation are separate. We link the transport gains to the change in morphology, which lowers the likelihood of excited charges encountering a boundary between the time of excitation and extraction.

2.5 Conclusion

This chapter focused on single junction PSC formed with the hybrid PVD/SP method. This method was chosen due to its compatibility with fully textured perovskite/c-Si tandems, which are a leading candidate for industrial-scale high efficiency PV with potentially low added cost. It is based on separately depositing the organic and inorganic components of the perovskite, then annealing them to crystallize the final perovskite material. We first looked at the chemical balance and bulk quality of the film, then examined the material surface and interfaces that it forms with other materials, and finally investigated the morphology of the film and its role in charge transport.

For the bulk and chemical balance, much depended on the input parameters and balancing the two steps against eachother. Including either constituent in excess led to poor performance of the final material, but also the annealing which mixes the layers could be tuned to give excess of either group. The annealing environment affected the perovskite formation, and thus was done in a controlled humidity box. A pre-anneal step was also added in order to remove the solvent from the layer before annealing, which led to a more robust process and more repeatable results. The effect of annealing temperature was further investigated based on its relationship to bulk crystalline disorder. It was found that the bulk disorder could be improved and an optimal recipe was established: 180 nm PbI_2 template with 18 nm CsBr, spin-coating 100 µL of 0.45 M solution of 1:2 FAI:FABr dynamically at 4000 rpm, annealing for 15 seconds at 80°C in N_2, and finally annealing for 20 minutes at 150°C in 15% RH air.

For the surfaces and interfaces, we showed that different HTL materials give different interface quality, and linked this to higher performance in cells. FBPA was used to passivate surfaces and increase cell voltage. We also uncovered the importance of oxygen passivation in our films, particularly to cell current. Parallel PL measurements attributed this to significant recombination losses for neat perovskite films annealed in N_2. These losses could be eliminated by passivating the neat perovskite surface with FBPA, but the losses returned when interfaced with most HTL materials. Via PL measurements and comparison with other passivation strategies, we proposed the most likely explanation to be Pb^{2+} defects on the bottom surface of the perovskite, which are normally passivated by oxygen through a heat-activated process. A Lewis base molecule (ET) was able to somewhat recover the losses, but was shown to do so without truly replicating the behavior of oxygen. Finally, SAM HTL was found which did not induce damaging interfacial states, and working cells were produced entirely in N_2.

The morphology of the layer was found to depend on the annealing temperature. This improved with higher temperatures, but the upper limit was set by component loss via evaporation. We showed that FBPA, in addition to its passivating role, reduces the onset of degradation products at high temperature and raises the viable processing window of our perovskite. This gave improved PL quantum yield in the bare layers, but the cell J_{SC} and FF were the main drivers of improved efficiency. Overall, the R_{OC} was reduced by 2.1 Ωcm^2 and the FF by 8.5% absolute. We extracted implied FF values from cells and plain perovskite layers, which showed

that the improved FF was caused by the series resistance of the full cell. Thus the gains were attributed to a better quality perovskite and layer morphology achieved with higher-temperature annealing.

All together, we have extensively examined the hybrid PVD/SP method as applied in single junction flat PSC. We have optimized the bulk, surfaces, interfaces, and morphology. The input parameters and processing steps have been thoroughly probed to find an ideal recipe, and the physical reasons behind these improvements have been theorized based on measurement results. Cell efficiencies were reliably above 16% for perovskite of 1.70 eV, with W_{OC} below 0.5 V. Overall, the perovskite formation of the PVD/SP method is well understood, and ready to be applied in more complicated and challenging situations, which is the subject of the following chapters.

3 ZnO Texture for Improved Optics in Single Junction PSC

Abstract

In this chapter we take a step away from perovskite/c-Si tandems to introduce the concept of textured absorbers for single junction PSC. Texturization of the absorber layer increases the optical efficiency of solar cells, and is a common solution in other PV technologies that has yet to become popular for perovskites. We therefore outline different methods available for texturization of PSC and choose ZnO thin films as the most promising candidate due to their versatility and past industrial success. First, we perform optical simulations to justify the approach. We then develop and tune a ZnO layer based on high scattering and low absorption. We move to PSC production, and adapt the hybrid PVD/SP method to give functioning layers on these substrates. Champion cell efficiencies reached 11%, but failed to demonstrate better absorption than the flat references. We discuss the challenges and limitations that caused this result. We link many of the setbacks to incompatibility between the PVD/SP method and ZnO substrates, and therefore switch to a one-step solution-processed perovskite deposition. This succeeds to form a quality perovskite material on the textured ZnO substrates. Cell efficiencies over 20% are achieved along with improved optics and 1.0 mA/cm^2 gain over flat cells. This validates ZnO as a method for improving PSC optically and gaining higher efficiency.

3.1 Introduction

In order for any type of solar cell to reach it's maximum realistic efficiency, all aspects of its performance must be optimized. Up to this point, the work presented has centered around the perovskite layer, its internal quality, surfaces, and the interfaces that it forms with the CTLs. This serves to increase the V_{OC} and FF, but the J_{SC} will remain limited by the optics of the cell, which encompasses the entire device architecture beyond the perovskite layer alone. Thus, it became a goal of my thesis to improve our PSC in this manner as well.

Increasing the extracted current depends on two things: generating excited charges through absorption of light, and extracting them from the absorber material. The first of these is referred to as the photogenerated current density (J_{ph}), which is defined by the total density of photons absorbed. Of this quantity, a certain amount is extracted as the short-circuit current density (J_{SC}). Absorption can be increased via larger layer thickness, but at a certain point the layer thickness will surpass the charge diffusion length [129], [130] and carriers will no longer be fully collected. In practice, perovskite layer thicknesses rarely exceed 1 µm (discussion of limits in section 1.2.2). Absorption coefficients[1] for perovskites are in the range of $10^4 - 10^5$ /cm across the absorbed spectrum [48]. These values require 1 - 3 µm thick layers to absorb 95% of light[2]. Thus, the layer thick enough for high J_{ph} would give poor extraction and low J_{SC}, and vice versa. Resolving this problem therefore requires new approaches outside of the perovskite layer.

Measured charge diffusion lengths in perovskites are usually in the range of 0.5 - 1 µm [129], [130], but have once been measured at 12 µm [131]. This result is discussed in the Literature Review (section 1.2.2), and is treated as an outlier that is not realistic for cell application.

Looking at PSC optics, J_{ph} depends on the absorption coefficient, optical path length, and light incoupling. The absorption coefficient is a fixed material property, and light incoupling depends on the substrate materials and thicknesses. These are pre-chosen for a good balance of electrical and optical properties, and again treated as a fixed quantity. The remaining controllable variable is the optical path length. This depends on the layer thickness and the direction of travel of light within the layer, meaning it can be increased via thicker perovskite or light scattering. As the layer thickness again has an upper limit, we turn to light scattering within a perovskite layer of fixed thickness as the most feasible option for increasing optical path length and J_{ph} of our cells. As long as we can incorporate light scattering in conjunction with the same perovskite as used previously, which achieved J_{SC} near its J_{ph} due to thick-

[1] Measured from PDS, using the same data as shown in section 2.2.3. We generally choose to display the PDS data as absorptance spectra, but this is not directly measured. Both absorptance and absorption coefficient are calculated from the raw deflection and transmission data, as a function of wavelength. The absorptance is used for easier comparison to other measurements such as EQE and T-R spectra.

[2] According to exponential decay of radiation in a medium: $I_t = I_0 e^{-\alpha t}$ where α is the absorption coefficient at the given wavelength, t is the thickness of the layer, and I_t and I_0 are the intensity at the point t and the initial intensity.

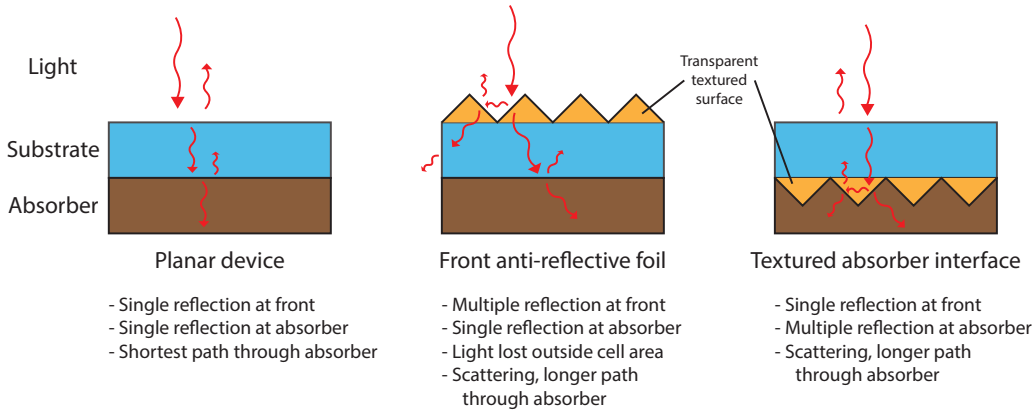

Figure 3.1 – Schematics of different texturing options for thin film PV. Optical enhancement over the planar case can be achieved via texturing at different interfaces. Texturing affects the reflection losses and the optical path length within the absorber, and how the texture is incorporated affects the scattering geometry.

ness below the charge diffusion length and the absence of resistive barriers within the cell (evidenced by absorptance, EQE, and JV measurements aligning), the improved J_{ph} from scattering should translate into improved J_{SC} in full cells.

Absorber interface texturing is a fitting solution for this role, sketched in figure 3.1. Adding a texture either at the front of the cell or at the absorber interface causes both scattering and multiple reflections (in addition to improving the angular response of the cell, which is a known advantage of textured designs [135]–[137]). Multiple reflections reduces the total front surface reflection, and scattering increases the optical path length within the absorber. However, scattering light before it passes through the substrate can lead to optical losses due to light being scattered out of the cell area. Thus, a textured absorber interface is the ideal case, assuming the same perovskite can be realized on that surface.

Transitioning from flat to textured architectures has helped improve optical performance in technologies similar to PSC, such as thin film Si [138]–[140]. Naturally, various methods have already been used to introduce textured interfaces to perovskites in both single junction and tandem designs, with varied success [127], [137], [142]–[146], [149], [155]. The details of these methods were discussed in section 1.2.2, but in summary, there is no reported method which combines large area scalable methods, efficient broadband scattering, and cheap materials. Lacking such an option, it became a goal of my thesis to develop a method with this potential.

3.2 Zinc Oxide as a Source of Texture

This chapter is based almost entirely on zinc oxide (ZnO) and our development of it as a source of surface texture for single junction PSC. Before outlining the research done on this material, we will briefly justify its role. This section outlines the historical context and optical simulations that together motivated our choice to work with ZnO as our source of texture.

3.2.1 History of Textured ZnO Use for Thin Film Photovoltaics

ZnO is a semiconductor material within the TCO class. It has an array of properties that make it attractive for the role of providing texture to PSC, and has already been proposed (but not demonstrated) for this role in the literature [218]. ZnO has a history in thin film solar such as CdTe [219] but also amorphous and multicrystalline Si [138]–[140]. It earned this role due to its naturally formed texture, the ease of depositing over large areas, high uniformity on these scales, and low material cost. These properties led it even to be brought to industrial scale production [220]. The simple fact that ZnO has already demonstrated this level of technological readiness makes it attractive for application in PSC, and preferable to technologies that require further development. Examples of a ZnO layer's micro-texture and optical scattering ability are shown in figure 3.2.

Other advantages of ZnO come from its versatility. For example, it has been used as an electrical contact at the same time as providing optical benefits [138]–[140]. Normally the role of electrical contact would be served by a "flat" TCO such as the common tin-doped indium oxide (ITO). But combining their roles into just the ZnO layer has the dual advantage of reducing the number of layers in the cell stack by one, and reducing or eliminating the usage of scarce indium [148]. Further, the ZnO texture can be controlled to scatter into the infrared

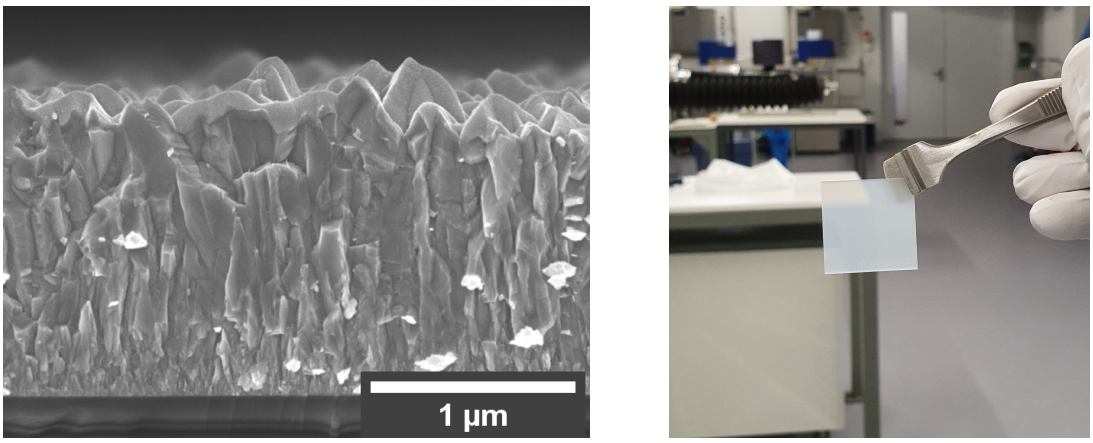

(a) (b)

Figure 3.2 – Examples of ZnO texture and light scattering. (a) Side-view SEM image of a typical textured ZnO film, deposited by LP-CVD. (b) A camera image of a textured ZnO film on glass.

or only the visible [221]. The randomness of ZnO texture ensures broadband scattering [222]. Its direct E_g at 3.18 eV filters out damaging UV light [221]. ZnO is compatible with flexible substrates, and is deposited below 200°C [223], [224]. All together, ZnO is more appealing due to its diverse benefits beyond optical scattering.

One of the keys to ZnO's usefulness is its deposition method. Tuning and optimization of ZnO deposition has been heavily researched in the past, which was an invaluable foundation for the work presented here [225], [226]. The deposition method of choice was low-pressure chemical vapor deposition (LP-CVD). This process is based on entering precursor gasses into a fixed-pressure chamber, where they react to form ZnO on the substrate. The details of this method are discussed in section 3.3.1. In brief, the gas phase deposition allows for large substrates to be used, and the controllable gas fluxes, chamber pressure, and reaction temperature allow for fine tuning of the end optical, electrical, and morphological parameters [224], [227].

3.2.2 Optical Simulations

We next sought to justify research into ZnO-textured PSC by performing optical simulations as to see what was realistic in terms of PSC improvement. In addition, simulations could be used for initial trouble-shooting without building full devices. In order to correctly simulate our devices, which combine 1-D thin film stacks and 3-D interfaces, we used a trial of Fluxim AG's Setfos package [228] was granted to the group. This package allows for combined wave and ray optical simulations, where wave optics are used for interfacial reflection and transmission, while ray optics are used to calculate scattering through rough interfaces. Additionally, this package allows for the import of surface profiles taken from AFM measurements. This enabled direct simulation of the layers we produce in-house. Two example results are shown in figure 3.3. A special thank you to Dr. Jérémie Werner for performing these simulations and sharing the results.

First, we used these simulations to validate the efficacy of ZnO texturing[3]. A step-by-step transfer from standard flat PSC to theoretical ideal architecture is shown in figure 3.3a. The starting point is a flat PSC on ITO with opaque Ag rear contact. The end point is textured ZnO with a transparent rear contact[4]. Between these two designs, we add flat ZnO as a layer, switch from an opaque to transparent rear-side contact, and from flat to textured absorber interface. The first step, going from gray to blue, shows the parasitic absorption caused by the ZnO E_g at 390 nm. This is not so serious, as the solar spectrum at earth's surface is relatively weak in this range (1.19 mA/cm^2 available from 320-400 nm, 5.40 mA/cm^2 from 520-600 nm). Still, just adding the ZnO layer loses 0.7 mA/cm^2 compared to without. The second step (green line)

[3]The n and k data used for these simulations, which determines their spectral transmission, is the same as that which was measured by Werner, Nogay, et al. in [192].

[4]Semi-transparent cells are not necessarily a design goal. They would be necessary for multi-junction solar or certain building-integrated designs. But in the scope of this work, they are used to illustrate the gains of texturing, as compared to back reflection from an Ag electrode.

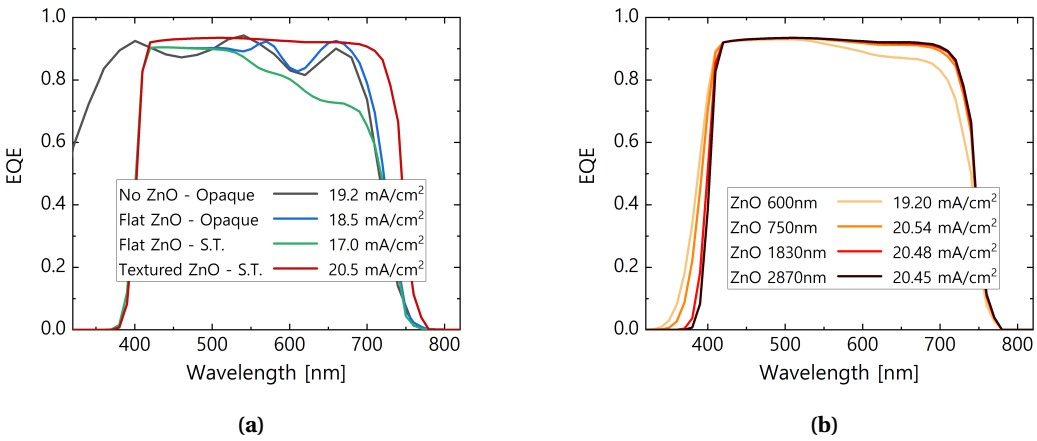

(a) **(b)**

Figure 3.3 – Simulated EQE curves for various flat and textured PSC architectures. (a) Simulations comparing opaque and semi-transparent device structures, with or without ZnO and rear reflective layers. (b) Simulated EQE curves for ZnO textured PSC, with the ZnO layer thickness varied. Surface morphology and scattering ability increase for thicker layers, but so do losses in the UV range. For all simulations, the main device stack was air/glass/ZnO/ITO/NiO_X/perovskite/C_{60}/top-contact. The top contact was either Ag for opaque devices, or SnO_2/IZO/air for semi-transparent. The perovskite thickness was 500 nm.

was to remove the opaque Ag rear contact and replace it with a TCO, referred to as a semi-transparent cell (ST). This loses 1.5 mA/cm^2 in the red part of the spectrum. Normally the Ag contact reflects un-absorbed light back into the perovskite, effectively doubling the optical path length. The removal of this layer both highlights the transmissivity of the perovskite at this thickness (500 nm), and the effect of doubling the perovskite layer thickness. The third and final step (red line) was to make the ZnO surface textured, and all interfaces above it be conformal to that texture. This immediately rectifies the red-spectrum losses of the ST design, flattens the interference pattern (due to non-parallel interfaces), and raises the EQE across the spectrum. Additionally, it pushes out the curve just above the perovskite E_g, due to the increased optical path length and the removal of an interference minimum. This gives a gain of 3.5 mA/cm^2 over the previous case, and 1.3 mA/cm^2 over the flat baseline.

There are multiple takeaways form these simulations. The first and most important, is that ZnO texturing is a worthwhile research effort. Increasing J_{ph} by 1.3 mA/cm^2 is a 6.7% increase, and corresponds to more than 1% absolute efficiency (for cells producing 1.1 V at open-circuit and 75% FF). Beyond that, texturing alone is more effective than an Ag back reflector. Having a back reflector doubles the optical path length. Texturing can only do this for light refracted 60° or more. This therefore implies that multiple reflections at the textured perovskite interface also play a role in our simulations, justifying a textured absorber design over a flat PSC with a front anti-reflection layer. To further differentiate these roles, simulations were done with and without texturing of the absorber interface. For the same ST cell stack as used previously, without ZnO, and using a 1000 nm perovskite; we simulated having no texture, texture at the

front of the glass (as an anti-reflection film used on a flat PSC), texture at the rear of the glass (making the absorber interface textured), and a fully-flat stack with rear Ag. The comparison shows us the difference between the three cases sketched in figure 3.1, and a standard Ag rear reflector. From the baseline of a flat ST PSC with 20.6 mA/cm^2, the front-side texturing with flat PSC gained the least, up to 21.3 mA/cm^2. The opaque rear Ag was next best with 21.6 mA/cm^2, and the fully-textured ST cell was best overall with 22.2 mA/cm^2. Thus, having a textured absorber interface is superior to a front anti-reflective foil, confirming our previous simulation.

Secondarily, we used the simulations to screen wide experimental spaces. An example of this is shown in figure 3.3b. ZnO has the property that the size of its surface features increases with increasing layer thickness (discussed in section 3.3.1). As the features get bigger, they become more efficient at scattering longer wavelengths, but also the UV absorption loss increases. To determine the trade-off between these to effects, we fabricated ZnO layers of different thicknesses and simulated them in full PSC. The four ZnO layers used in figure 3.3b had layer thicknesses of 600, 750, 1830, and 2870 nm, and root mean squared roughness (RMS) values of 12.4, 42.7, 96.4, and 134 nm. We observed the trade-off described above, in that the EQE above ZnO's E_g (395 nm) dropped off sharply when layer thickness passed 1 µm, but the thinnest layers did not fully exploit the red part of the spectrum. Thus, we concluded that a layer thickness around 750 nm was ideal. This gave us a target for designing the ZnO layer, discussed in the following section.

3.3 Zinc Oxide Layer Development

Before ZnO layers are ready to be applied in solar cells, the optical performance must first be optimized. ZnO has been heavily researched in the past [225], [226], but never for use with perovskite absorbers. The various deposition parameters during the ZnO LP-CVD process allow for wide control over the transparency, thickness, and surface morphology. In order to fine tune these aspects for PSC application, we must first be able to control them. Thus we ran initial tests of our deposition instrument to determine relationships between input parameters and layer output, and applied this knowledge to optimize a recipe for transparency and scattering.

3.3.1 Controlling ZnO Morphology and Optical Performance

Starting from the fundamentals of ZnO, previous research [229] establishes ZnO as a hexagonal crystal defined by an a-axis and a c-axis (figure 3.4). ZnO crystallites can grow along either of these axes according to the deposition parameters, and in turn this affects the end layer's morphological and optical properties[224], [227]. From this basis, we test the capabilities of our deposition system to identify the relationships which control the dominant axis of growth, and characterize these domains to understand what type of ZnO layer will be best for our PSC.

Initial System Testing and Characterization

Our first tests of the system were simple "from the book" recipes. These were not part of development towards use in PSC, but we show the results to introduce both the general characteristics of ZnO layers and the methods used to quantify film performance. We obtained recipes for flat and textured ZnO layers from literature [225], [226], and deposited on glass. We measured their optical and morphological properties, and the results are shown in figure 3.5. First, the total and diffuse transmission of the flat and textured ZnO recipes are compared to a stock ITO substrate (from Kintec) in 3.5a. The ZnO is transmissive on the same scale as the ITO

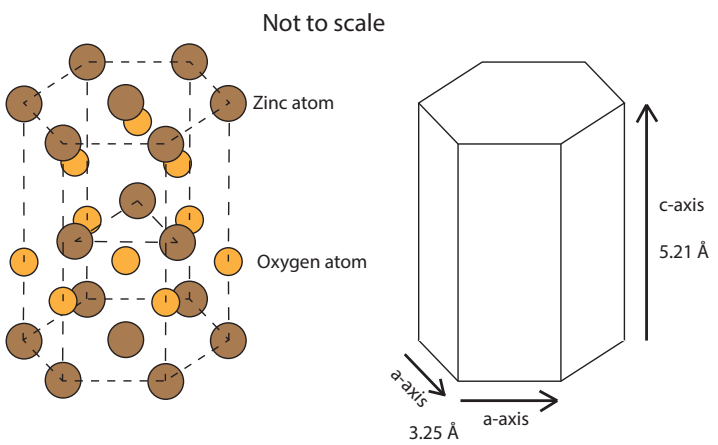

Figure 3.4 – Illustrations of the ZnO Wurtzite structure. ZnO follows a Wurtzite lattice defined by the a- and c- axes. The a-axis is radially symmetric, and the vertical c-axis is longer. The a-axis planes are of uniform atomic composition, and atoms are stacked along the c-axis.

(this plot does not account for reflection), and both flat and textured ZnO films transmit similar amounts to eachother. The diffuse transmission, however, is distinctly different for the textured ZnO. Both the stock ITO and the flat ZnO layer have near-zero diffuse transmission, while the textured ZnO rises to nearly 30%. The diffuse transmission measurement can therefore distinguish optical scattering, but also should not be mistaken for an absolute measurement of the total scattered light. This measurement depends largely on the setup geometry and the

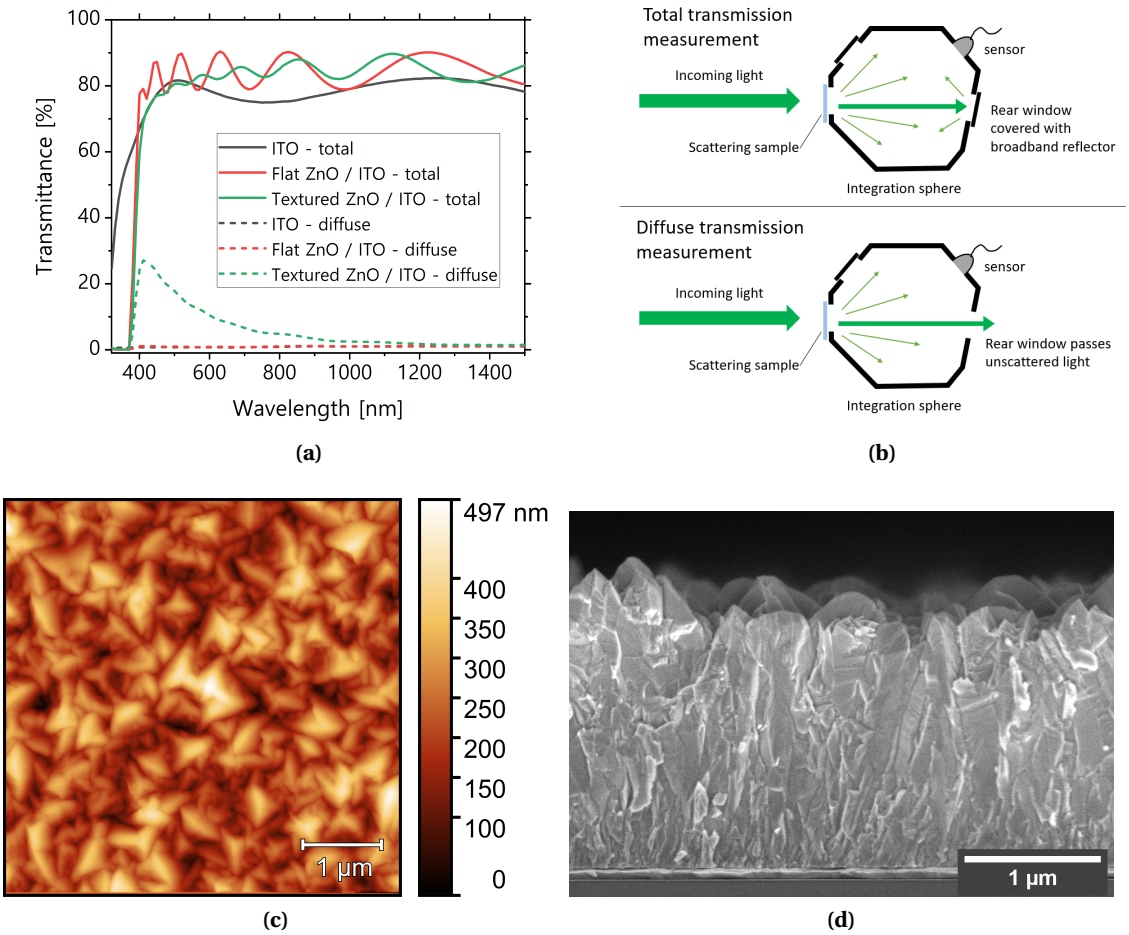

Figure 3.5 – General properties of ZnO observed from test depositions. ZnO layers were deposited according to recipes from the literature. The "flat" layer was measured at 5 µm thickness and 17.2 nm RMS, and the textured layer at 2 µm thickness and 69.5 nm RMS. A 100 nm ITO layer was deposited on the ZnO for the optical measurements. (a) Total and diffuse transmittance measurements for the two ZnO layers, compared to a stock ITO substrate (from Kintec). Measurements were taken from the glass side. (b) Description of the measurement setup which defines diffuse transmission. The light arriving at the sample is collimated, and unless scattered, will pass out of the chamber without being detected. When a broadband reflector is used to block the rear window, all transmitted light contributes to the measurement. (c) An AFM surface profile of the textured film measured in (a). (d) Cleaved side-view SEM image of a textured ZnO film on glass.

wavelength-dependent scattering angle, which is diagrammed in figure 3.5b. The spectral dependence is therefore not absolute, but the relative intensity of the curve between different samples is relevant.

The spectral variation of the diffuse transmission shows the film's ability to scatter short-wavelength light better than long-wavelength. This is expected, since the size of ZnO surface features is on the order of a few hundred nanometers (see figure 3.5c-d), and will thus become effectively flat as the light wavelength increases far past this length scale. Beyond the optical performance which distinguishes the two ZnO recipes, the morphological properties do so as well. Example AFM and SEM measurements are shown here for the textured ZnO case. The AFM surface profile shows a peak-to-valley distance of nearly 500 nm for the textured ZnO and an RMS value of 69.5 nm. The flat counterpart had only 123 nm peak-to-valley and 17.2 nm RMS. The side-view SEM likewise shows the 300 - 500 nm surface features of a typical textured ZnO film. Overall, these depositions and measurements confirmed the functionality of our tool, and the fact that we could distinguish the optical and morphological effects of these films with the measurement techniques available to us. We therefore moved on to more specific tuning of the layer based on the relationship between deposition parameters and layer growth modes, discussed below.

ZnO Growth Regimes and Their Morphologies

In the LP-CVD process, precursor gasses are introduced to a chamber at fixed flow rates. The chamber is held at a certain pressure, and the substrates in the chamber are held at a certain temperature. The gasses then react with eachother to form ZnO on the heated surface of the substrates. From previous research, we directly took the chamber pressure and relative flow rates of the precursor gasses, diethyl-zinc (DEZ) and H_2O, to be fixed at pre-determined optima (350 µbar and 1:1.3 DEZ:H_2O) [226]. These parameters affect the electrical properties and seed-layer grain orientation [224], [227], [229], [230], which are in turn important for layer properties, but were not varied within this work. Conversely, the deposition temperature and total flow rate would need to be optimized as they are the most relevant to the growth axis of the film [225].

A matrix of conditions was thus tested (with fixed chamber pressure, gas flux ratios, and deposition time), and the results can be seen in figures 3.6 and 3.7. The low-temperature side of the matrix is dominated by c-axis growth. This is characterized by small grains and low surface roughness, as well as thinner layers. As the temperature increases, the growth regime transitions through a mixed-phase range before arriving at the a-axis growth regime. a-axis films are characterized by larger grains and pyramidal surface features, and thicker layers. Whether a film was c-axis or a-axis could be discerned by eye, based on the haziness. This was shown for an a-axis film earlier in figure 3.2b, while c-axis films were clear like glass. Finally, at low flow rates and high temperatures, a third regime appears (top right in figure 3.6), defined

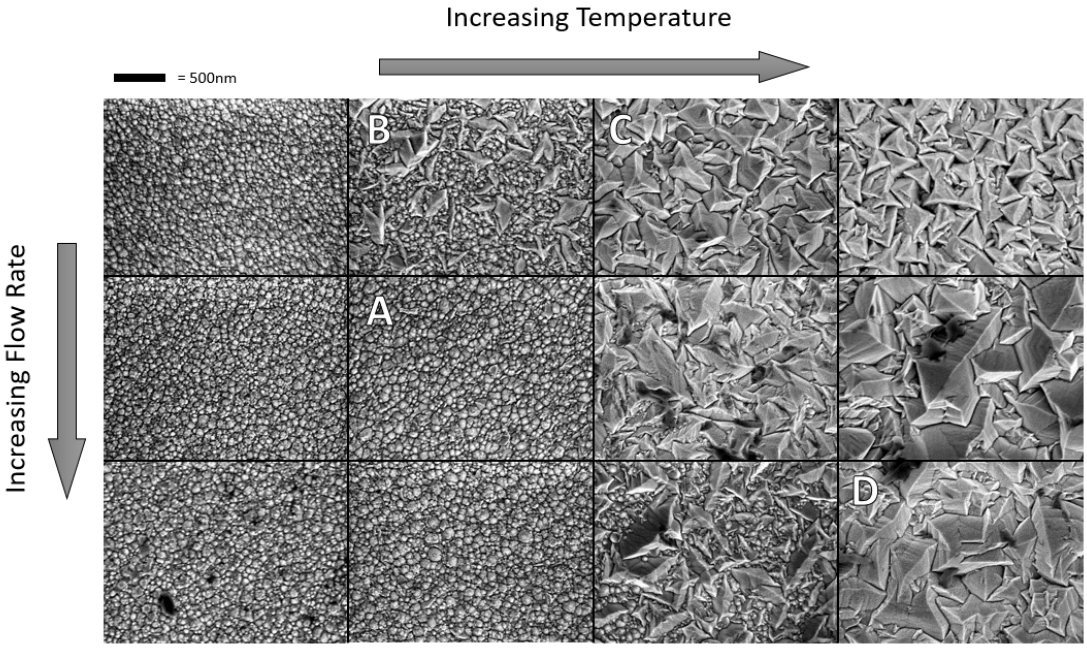

Figure 3.6 – SEM images of ZnO films grown under varied deposition parameters. The DEZ flow rates were 60, 120, and 180 sccm, and the temperatures were 150, 165, 180, and 195°C. The chamber pressure and relative DEZ:H_2O flow rates were fixed at 350 µbar and 1:1.3 DEZ:H_2O, and the deposition time was 8 minutes. Scale bar is 500 nm.

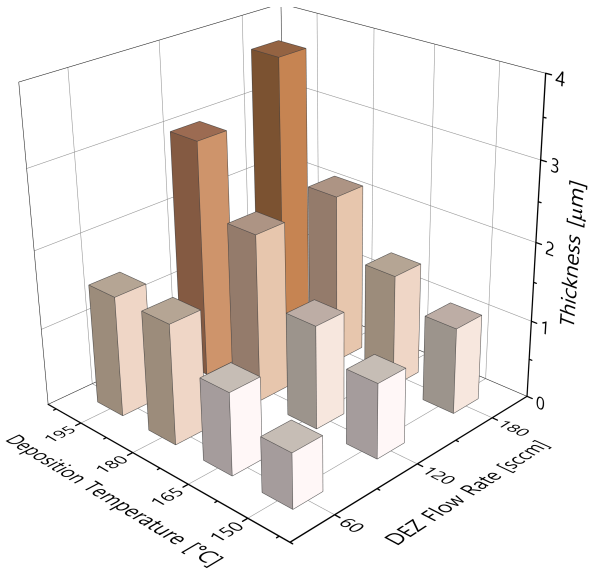

Figure 3.7 – Thickness measurements of ZnO films grown under varied deposition parameters. Thickness was measured by profilometer for all films in figure 3.6. All depositions were 8 minutes. Measurement was obtained from a chemical lift-off of ZnO, in which a felt-tip pen line is drawn on the substrate before deposition (visible in figure 3.9), and removed afterward with a few seconds soak in acetone. This leaves the ZnO around the line unchanged while removing all layers on top of the line.

by growth with no preferential direction. These layers is have steep cliffs and deep valleys between grains. This is not viable for thin film processing, and this deposition regime was not investigated further.

These surfaces and layer thicknesses are a consequence of the films' growth dynamics [229], [230]. Particular to a-axis growth, grains expand laterally as they grow vertically. This leads to a competitive growth mode, with fewer and larger grains surviving over time, and forming a V-shape when viewed from the side (see the TEM crystal orientation mapping and growth simulation results of [230]). This imparts the property that feature size scales with deposition time. This means one temperature and flow rate combination can be used, and just the reaction time varied in order to get different surface morphologies. For figures 3.6 and 3.7, the same deposition time was used for all.

The first characterization performed was AFM and SEM of the different growth regimes. These results are shown in figure 3.8. The SEM images are accompanied with the surface morphology metrics from AFM, in order to give scale to the top-down images. Not only do the pyramids grow laterally, but their vertical height grows substantially. The a-axis ZnO has much larger grains both laterally and vertically. For these specific samples, the c-axis film was 1.32 µm thick and the a-axis film 1.53 µm thick. For comparison, plain ITO substrates were measured with and RMS roughness of 3.5 nm, compared to 8.0 and 81.0 nm for the a-axis and c-axis ZnO. These differences in surface texture present themselves in the layers' optical properties as well, which we will now discuss.

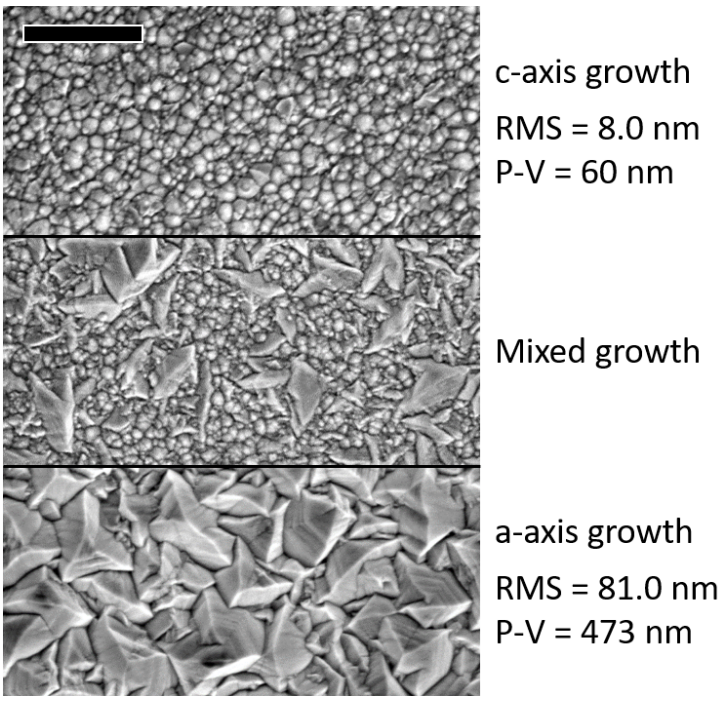

Figure 3.8 – Surface characterization of different growth regimes of ZnO. SEM images of c-axis, mixed, and a-axis LP-CVD ZnO films. RMS roughness and peak-to-valley distances are measured by AFM. The scale bar is 500 nm.

ZnO Growth Regimes and Their Optical Properties

The optics of all ZnO films in figure 3.6 were characterized in the same manner, and four illustrative cases were selected for the plots below. They are the films labled A-D in figure 3.6. From here forward, they are referred to as c-axis, mixed, a-axis, and "high temp/flow", respectively. The c-axis, mixed, and a-axis films are of the same recipes as figure 3.8, and illustrate the general behavior of films made in these growth regimes. The high temp/flow sample is included to show the variation within a-axis dominated films. Already this recipe showed a much faster deposition rate, evidenced by the thicker layer from the same deposition time (figure 3.7). But also these films were visibly different. For example, images of the four conditions from immediately after deposition are shown in figure 3.9. The coloration of the high temp/flow case is clearly visible in the picture. This coloration likely comes from faster and less ordered growth allowing more defects to enter the layer.

The non-yellow films appear similar in the images, but are different when observed with spectrographic measurements. Looking first at the absorption of the films (figure 3.10a), calculated from taking 1-reflectance-transmittance, the high temp/flow sample stands out distinctly as having significant low-wavelength absorption. This corresponds directly to the color in figure 3.9. The non-yellow films are distinct as well, which is highlighted in the zoomed view of the same data (figure 3.10b). From 500 nm to 1500 nm, the a-axis film averages 130% more absorptance relative to the c-axis film, and the mixed film is between these two. Next, figure 3.10c shows the transmittance of each film. What is notable in this plot is the presence or lack of interference fringes. These oscillations are produced by the interference of the waves reflecting off of the front and back of the ZnO layer, and can only be produced by parallel surfaces. This indicates that the c-axis and mixed films have a significant amount of flat area

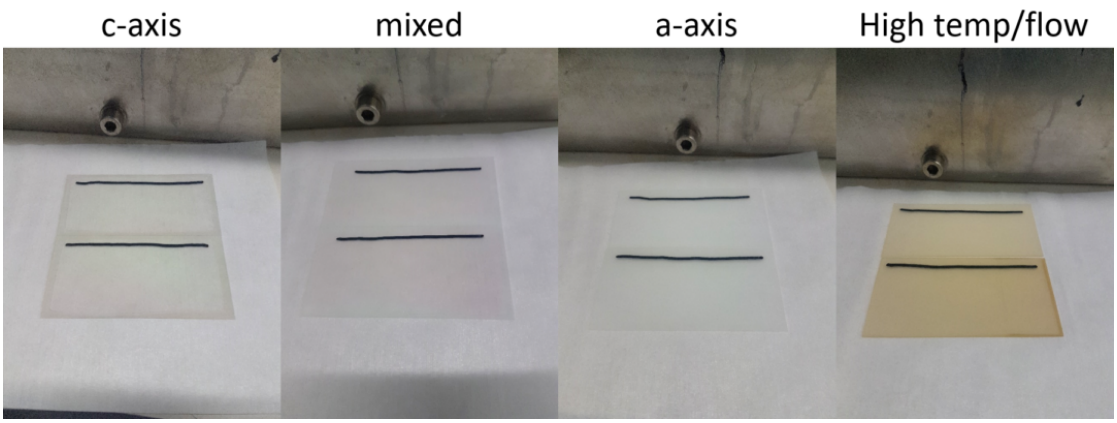

Figure 3.9 – Images of different growth domains of ZnO on glass, taken immediately after deposition. The films at high temperature and flow rate produce a strong yellow/brown color. This is easily identified and to be avoided due to parasitic absorption.

on their top surface relative to the a-axis and high temp/flow films. Though, the a-axis film does develop oscillations towards the longer wavelengths within the measured spectrum, indicating that the surface is "flat" relative to the length scales of these photons.

Next, figure 3.10d shows the diffuse transmittance, or scattering, of the films. This is defined by the system geometry, as described in figure 3.5b. It is not an absolute measurement, but the relative values of the four samples verify that the films with larger features scatter more light, and do so at longer wavelengths. The c-axis film has almost no scattering, and the mixed film has some scattering. Between the a-axis and the high temp/flow films, we find the limiting trade-off of ZnO optical scatterers. Clearly the high temp/flow film scatters more, even despite its higher absorption losses (recall that this is a transmission measurement), but those losses still prohibit its use in cells. The a-axis film is a good compromise, but the presence of the high temp/flow film shows that the a-axis is not as good of a scatterer as ZnO films can be.

This optical characterization matches well with the SEM and AFM measurements, in that the surface roughness scales with the scattering. But overall, this experiment established which deposition regimes are available to us, how we can control our deposition to c- or a-axis growth, and what optical performance each of these types of films will give. But the important question is how much scattering can be obtained with minimal absorption. To quantify this, we looked at the haze and average absorptance for all 12 samples from figure 3.6, which are shown in figure 3.10e-f. The c-axis films with low surface roughness showed low haze and low absorptance. As the deposition temperature rose and surface features began to appear, haze increased, but so did absorptance. High temperature and high flow rate layers had very high absorptance, which reduces the appeal of their high scattering. The highest temperature and lowest flow rate is an outlier in this graph, as it was in the SEM images, which was discussed briefly above. Overall, we decided that the best balance was the low flow rate sample deposited at 180°C. This was the same sample as was used for the a-axis data in (a-d) of the same figure. This sample gave both good scattering (relative to c-axis) and low absorptance (relative to high temp/flow), but still both are not the best. So, we progressed to doing a detailed optimization based off of this condition.

3.3.2 Fine Tuning the ZnO Recipe for Cell Application

Continuing from the widely spaced matrix of conditions in the previous section, we iterated off the best condition with smaller variations. As stated, the chamber pressure, constituent flow ratios, and deposition time were kept constant, and we only varied the deposition temperature and the overall constituent gas flow rate. The chosen conditions are shown in figure 3.11. The "reference" condition was repeated, along with four small perturbations in each direction. Additionally, one condition was performed to try and mimic the "high temp/flow" condition of the previous section, for the sake of comparison with a high-scattering ZnO film. This condition was slightly modified based on trends observed in previous research [225] to try and get a layer in the same deposition regime but with less severe coloring.

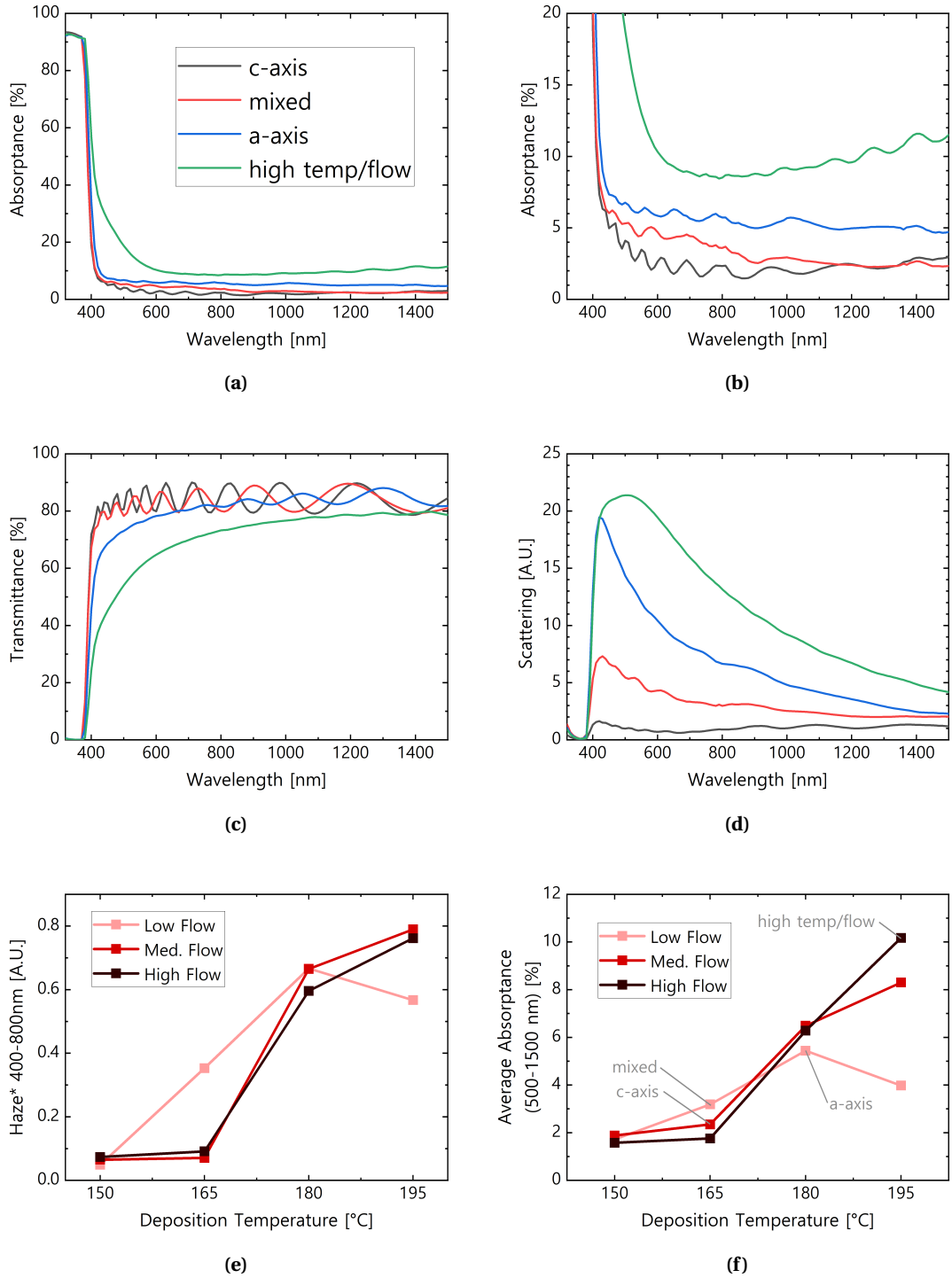

Figure 3.10 – Optical measurements of the main growth domains of LP-CVD ZnO films. The same measurements were performed for all of the samples in figure 3.6, of ZnO deposited on glass with the same deposition time. (a-d) show just the four illustrative cases. (a) and (b) are the absorptance, with different y-scales. (c) is the transmittance. (d) is the diffuse transmittance of each film, as measured with the setup detailed in figure 3.5b. (e) shows the ratio of (d) to (c), integrated from 400 nm to 800 nm. This is referred to as the film "haze", and is shown for all samples. (f) shows the average absorptance values for the same films, this time integrated from 500 nm to 1500 nm.

The pertinent optical spectra are shown in figure 3.12, with the letters corresponding to the conditions labeled in figure 3.11. As expected, the sample "X" has the higher low-wavelength absorptance characteristic of its deposition range. The rest of the spectra are rather similar in absorptance, with A and B being about the same as the reference, and C and D slightly lower. The scattering differentiates the films more. C and D, while less absorptive, were also less scattering than the reference. B was about the same, and A was significantly better. As expected, X scattered much more than the reference. Comparatively, sample A combined the low absorptance of the reference film with the high scattering of the X film, and thus was chosen as the optimal recipe to be used for the tests to follow. The details for this finalized recipe are: DEZ - 70 sccm, H_2O - 91 sccm, temperature - 175°C, time - 15 minutes.

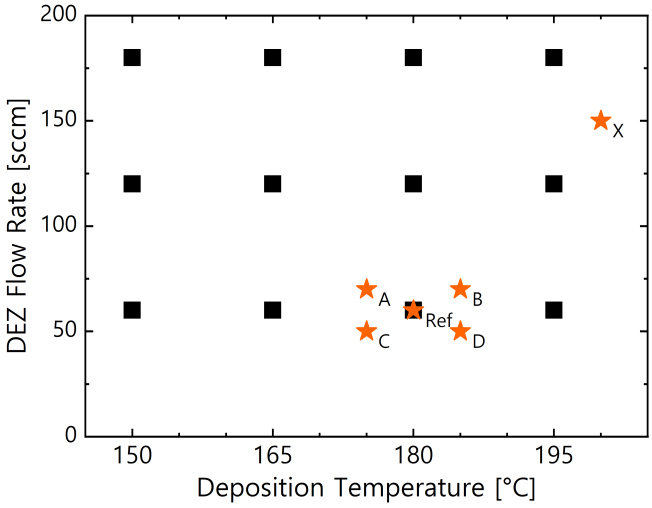

Figure 3.11 – Parameters selected for fine-tuning of ZnO optics. Black squares represent the parameters used in the initial experiment, shown in figure 3.6. Orange stars represent the new tests, with letters to indicate their spectra in figure 3.12. The chamber pressure and relative DEZ:H_2O flow rates were fixed at 350 µbar and 1:1.3 DEZ:H_2O, and the deposition time was 11 minutes (aiming for 2 µm).

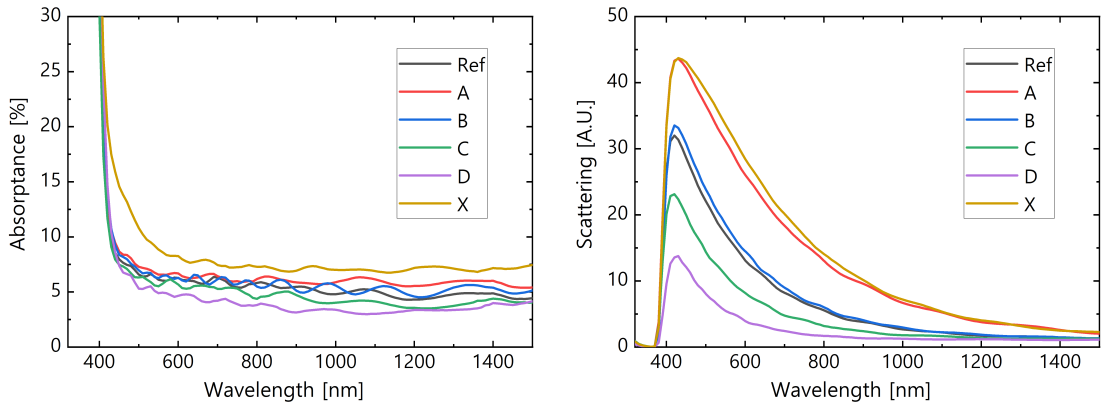

Figure 3.12 – Optical characterization for ZnO recipe fine tuning. Absorptance and scattering (diffuse transmittance) values for the films shown in figure 3.11 (with corresponding labels). The reference condition was re-deposited at the same time as all the films for this test. The samples average absorptance (integrated from 500 nm to 1500 nm) was: Ref-5.2, A-6.0, B-5.5, C-4.5, D-3.8, X-7.4 %.

An XRD diffractogram of this layer is shown in figure 3.13. This measurement detects diffraction off of both the a- and c- axes. This does not mean that the film is a mix of the two types, since all ZnO by definition contains both axes. Rather, the crystal grains within the layer are not uniformly oriented relative to the axis of diffraction (normal to the substrate). This is expected from the diverse orientations of crystallites that form the initial seeding layer [230]. The full layer thickness can also contain a mix of orientations, but the observed surface texture is evidence of a-axis growth being favored through much of the layer volume.

We must also briefly comment on the ZnO layer thickness. The layers presented here are all well in excess of the goal established from the optical simulations of the previous section, and particularly figure 3.3b. We initially attempted to find a texture recipe with a total thickness of less than 1 µm to minimize parasitic absorption losses. However, as we developed the ZnO layer we frequently made cells in parallel, to control that the optical effects were in line with expectations. In this process, we found that the simulations did not predict the correct trade-off point between reduced parasitic absorption and increased feature size. However, as these results came on full cells, they are presented and discussed in the appropriate section (3.4.1). For now, layers over 1 µm were the target of ZnO optimization efforts, despite the previous simulation results.

The final step of ZnO layer development for PSC use was testing the addition of an argon plasma etching step, simply called an Ar-Etch. This has been used in the past for modifying ZnO layers [221]. Ar-Etching (after the ZnO deposition and before the ITO) was found to be beneficial to the ZnO layer's absorptance, but detrimental to its scattering ability, shown in figure 3.14. Integrating the absorption of the un-etched and 15 minute etched samples against the AM1.5G spectrum showed that the etching reduced parasitic absorption by 0.9 mA/cm^2. However, the total scattering also drops by 25%. Optimization of this parameter was done via full PSC fabrication, due to its influence on perovskite layer formation. The results are

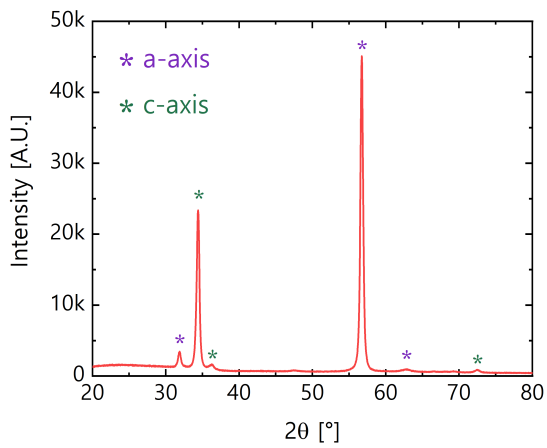

Figure 3.13 – XRD measurement of the final ZnO film used in cells. Diffraction is measured from both a- and c- axes. The sample was oriented horizontally and rotated during measurement, with 0° as parallel to the substrate. Peak identification from [224].

discussed along with other PSC on ZnO in section 3.4.1. AFM scans of the layers are also presented in figure 3.15. As expected, over time the etching reduces pyramid height and overall surface roughness.

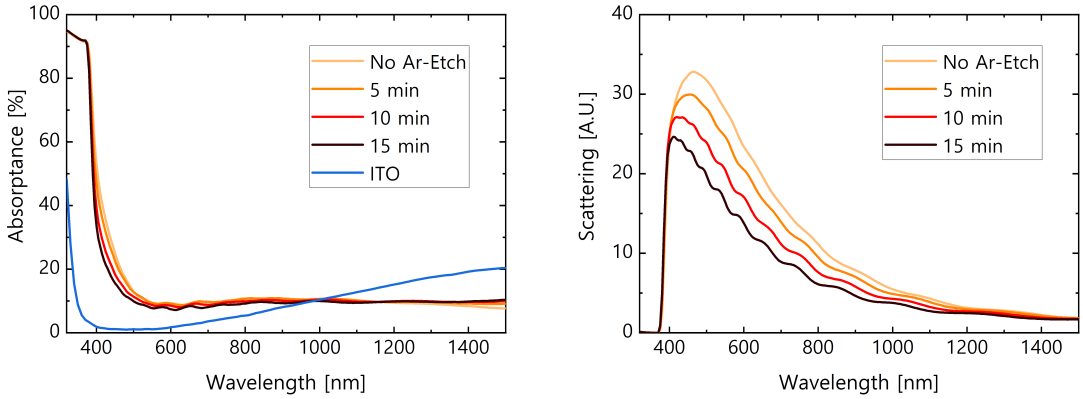

(a) (b)

Figure 3.14 – Optical characterization for ZnO with Ar-Etch. (a) absorptance and (b) scattering (diffuse transmittance) values for the same ZnO film on glass with varied Ar-Etch times. Scattering is measured according to the method in figure 3.5b. ITO/glass absorption is included for reference.

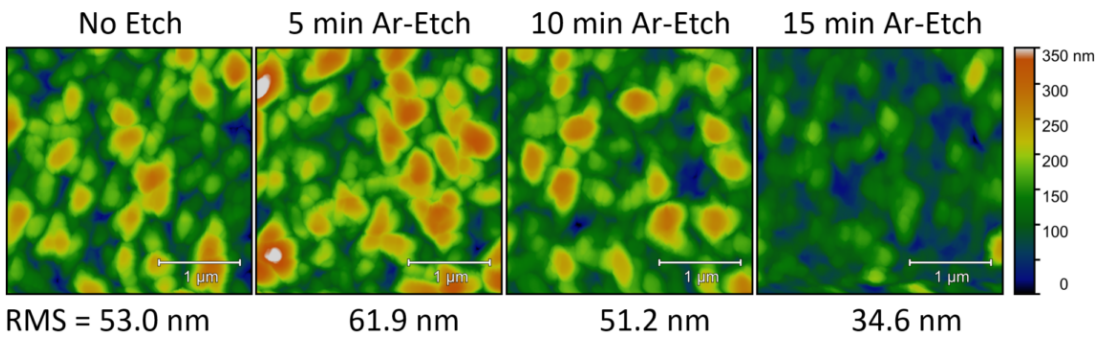

Figure 3.15 – AFM surface profiles of ZnO layers with Ar-Etch. All ZnO layers came from the same deposition, and were etched separately. RMS roughness values were calculated from these data and displayed below the corresponding map. The height scale for all is the same.

3.4 Perovskite Solar Cells with ZnO-Textured Active Layer

Finally, we directly applied the hybrid PVD/SP method as described in chapter 2. The recipe had to be modified to account for the different challenges of textured substrates, mainly with regard to the thickness of the perovskite and the probability of shunting. In parallel, we found the preparation of the ZnO layer to affect perovskite formation, which led to changes in the ZnO layer design. The resulting cells did not benefit enough from the optical enhancement to overcome the material quality losses associated with forming PVD/SP perovskite on an irregularly textured surface. The processing difficulties and material limitations of the PVD/SP method on ZnO are discussed. Finally, a pure SP perovskite deposition was used to avoid these challenges, which resulted in superior optical performance and efficiencies up to 20%.

3.4.1 Cells Made with the Hybrid PVD/SP Method

PSC were deposited on the ZnO substrates in the same layer stack as on flat substrates at the time: glass/ITO/NiO_X/perovskite/LiF/C_{60}/Ag, and shown in figure 3.16. The only difference with the ZnO cells was the insertion of the ZnO layer between the glass and ITO, and the change to a home-made ITO rather than the purchased substrates (the home-made ITO was sputtered in the MRC-II, 100 nm and roughly 80 $\Omega/\square$). The ZnO substrates were made from 4 x 8 cm^2 glasses which were first washed, then stored in N_2 until the ZnO deposition. Once the ZnO was deposited, the glasses were cut to 2.5 x 2.5 cm^2 squares. These were rinsed with IPA and blown dry to eliminate dust, before being masked and having ITO sputtered on as the front electrical contact. Masking of the ITO was important for avoiding direct parallel shunting between the front and rear electrodes when pins are used to electrically contact the opaque rear electrode. Then, a kapton-tape shadow mask was applied to block all subsequent layers from coating

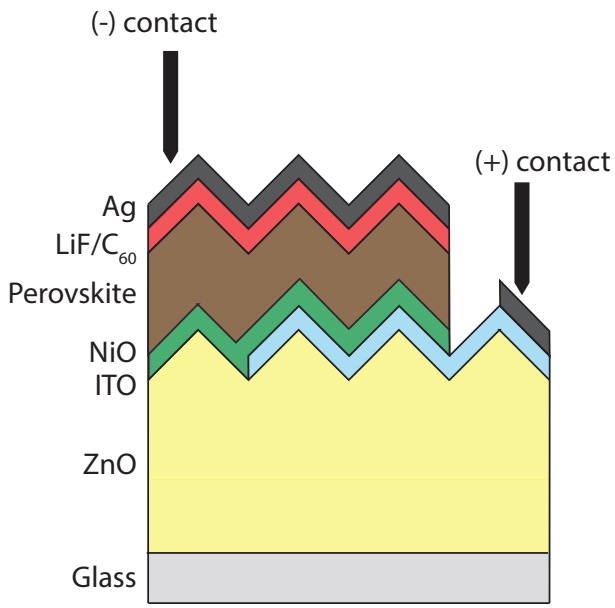

Figure 3.16 – Diagram of typical PSC on ZnO. Layer thickness not to scale. Layers that do not cover the full device area were masked with Kapton tape during their deposition, other than Ag which was evaporated through a shadow mask.

the area that would be used for contacting the front ITO (below the perovskite), and the PSC deposition preceded as normal. The HTL of NiO_X was sputtered in a custom chamber, and was 20 nm thick. The PbI_2 template was evaporated at 1.0 Å/s with a co-evaporation of CsBr at 0.12 Å/s. The spin coating was done at 4000 rpm, with 1:2 FAI:FABr dissolved in 100 µL of ethanol. The concentration was regularly changed, and therefore will be noted each time. The LiF/C_{60} ETL was 1/19 nm thick, and evaporated in a custom chamber at 0.2 Å/s. Before the Ag electrode evaporation, the kapton-tape mask was removed to expose the ITO. The silver was the evaporated in the same custom chamber, through a shadow mask, and was 120 nm thick. Cell area was 0.3 cm^2, and masked to 0.25 cm^2 for measurement.

Tuning of Perovskite Deposition Parameters

As stated, the first attempts at PSC fabrication on ZnO substrates involved the direct transposition of the same recipe for flat cells onto the ZnO substrates. The results of this first test was near complete shunting, shown in figure 3.17. Still, the cells were able to produce some voltage, which indicates that the overall layer structure still forms a diode. The lack of a difference between the three spin-coating concentrations indicates that a change in material quality is not the controlling variable. Past that, the likely explanation is mechanical shunts, which could form due to the ZnO layer piercing through the perovskite.

We checked how well the perovskite covered the ZnO texture by cleaving samples and viewing the cross-section in SEM. This is not a full-proof method, as we cannot examine the whole cell area, but it can give an indication of the severity of the problem. Some example SEM images are shown in figure 3.18. (a) and (b) show cells following the same recipe as those

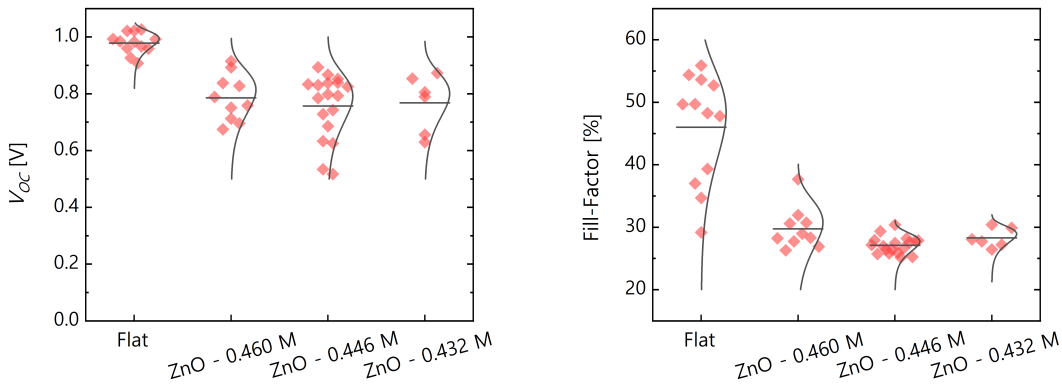

Figure 3.17 – Cell V_{OC} and FF from the first attempt at PSC on ZnO. This batch suffered from an error in the front ITO deposition, leading to a high series resistance and low FF. Regardless, the FF and V_{OC} of the cells on ZnO drop in ways that are not attributable to this. The group names refer to the concentration of the spin-coating solution, which should result in different perovskite material quality and performance. The flat cells used 0.446 M.

measured in the heavily shunted figure 3.17. Despite this, the perovskite appears to fully cover the ZnO surface. This was not always the case, as in 3.18c, where the perovskite is very thin or missing on the peak of a pyramid (indicated by red arrow). The variations in perovskite thickness over the ZnO peaks and valleys suggest that the PVD and SP steps do not deposit uniformly over the texture. Beyond layer thickness, this would give excessive or deficient FA:Pb ratios. Spatial variation of perovskite material quality could then lead to areas with poor diode behavior and facile shunting. In theory, both pinholes and thin points are addressed with a thicker perovskite. Figure 3.18d shows an example of this, where 250 nm PbI_2 is used in the template, and the perovskite appears to wrap uniformly around the peaks. As a reminder, the perovskite thickness is typically measured by the thickness of the PbI_2 measured during template evaporation (full details in section 2.1.1). In reality, the actual perovskite layer is roughly double this thickness.

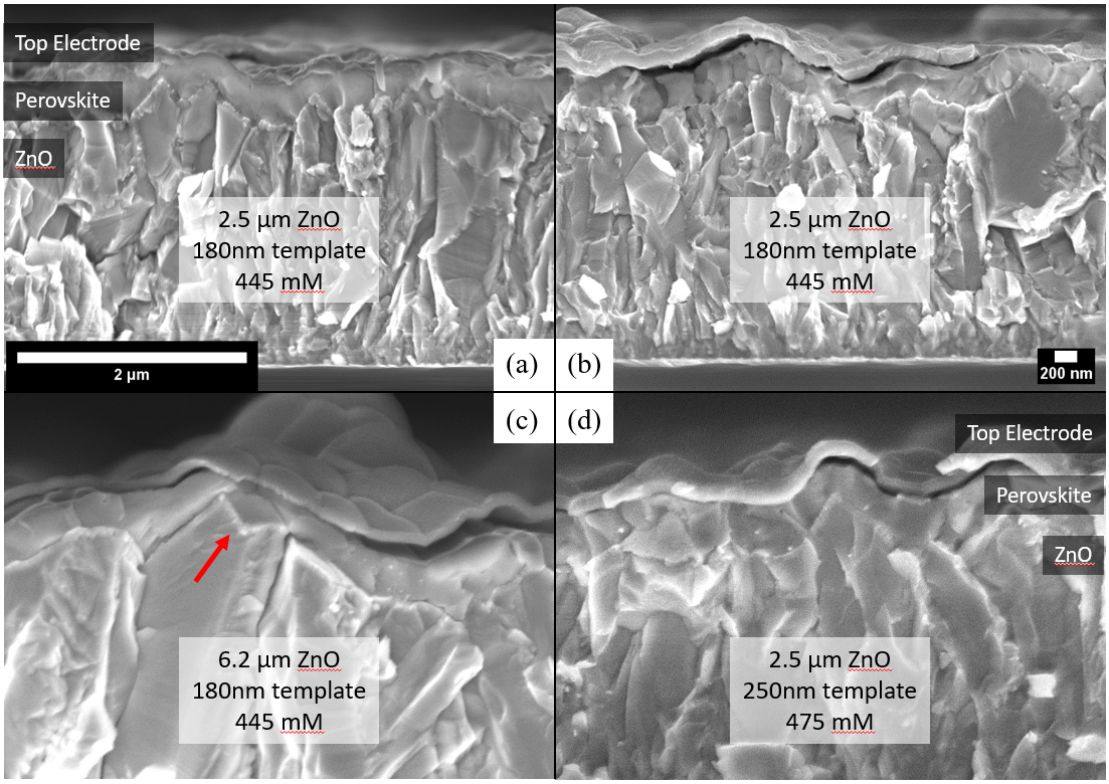

Figure 3.18 – SEM images of PSC on ZnO substrates. All images are at the same scale. ZnO thickness, template thickness, and spin-coating concentration are given in each image. (a) and (b) are from the same batch, to show general uniformity of the layer thickness across the textured surface and from sample to sample. (c) shows an uncovered portion of the ZnO substrate. While uncommon, regions with thin or no perovskite covering the ZnO peaks were occasionally found in SEM. Note that this sample uses the same perovskite recipe on a ZnO layer with larger layer thickness and surface features. (d) is from a later deposition, with 39% thicker perovskite.

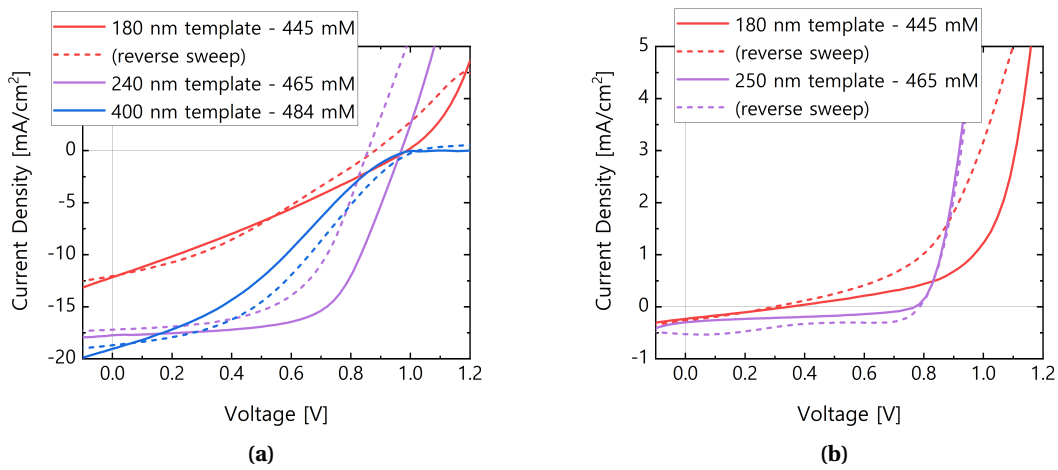

Figure 3.19 – *JV* curves from PSC on ZnO substrates with varied perovskite layer thickness. (a) Full-sun illumination JV curves of perovskites with three different template thicknesses. (b) JV curve taken at 1.6% solar illumination, for PSC with 180 nm and 250 nm template thickness. The spin-coating concentration is given for each case.

In cells, the thicker template layers required re-optimization of the SP concentration. This was done for templates of 240 nm[5] and 400 nm. Comparing these three layers, the cell results match that the thicker layer reduces shunting (figure 3.19). The 180 nm devices shunted as normal, but already at 240 nm the JV behavior was much improved. Looking at low-illumination JV curves for a cell with 250 nm template (figure 3.19b), they retain a V_{OC} of 786 mV, and the short-circuit resistance is as high as 936 Ωcm^2. Moving to thicker, however, introduced new problems. As is the case with the hybrid PVD/SP method used throughout this thesis, there is an upper limit to how thick of a layer can be produced. Eventually, it becomes impossible for the solution-processed organohalide layer to diffuse all of the way through the PbI_2 template. This manifests as unreacted PbI_2 remaining below the perovskite. PbI_2 is non-conductive, and a compact layer between the perovskite and HTL would manifest as an S-shape in the JV curve, as seen in figure 3.19a. Therefore we chose this medium thickness as the ideal recipe to move forward with, and continue to optimize the other aspects of the cell design.

ZnO Processing and its Effect in Cells

Using the same 240 nm template thickness as determined above, we tuned the thickness of the ZnO layer to observe the trade-off between UV transmission and long-wavelength scattering. As discussed in section 3.2.2, optical simulations showed that thicker ZnO layers would scatter light better and enhance long-wavelength absorption, and thinner ZnO layers would suffer

[5] Both 240 nm and 250 nm were used, due to a processing error with the evaporation tool used for the template. The mistake was realized in time to tune the SP step in response. But the 240 nm template cells of figure 3.19 are not the same as the 250 nm template cells of figure 3.18d.

less from parasitic absorption above the ZnO E_g. The simulations indicated that there was a trade-off point in the middle that could benefit from both, which we wanted to experimentally verify.

Textured ZnO layers were made with 0.45 µm and 1.9 µm thicknesses. Recall that scattering increases with surface feature size, which in turn depends on layer thickness (due to ZnO's competitive growth along the a-axis, section 3.3.1). Thus these layers were chosen based on being the thickest that still transmitted some UV light (thus rather thin), and a very thick layer with high scattering and no UV transmission. JV and EQE measurements for the champion cells of each condition are shown in figure 3.20. The thin ZnO PSC generated 0.22 mA/cm^2 above the ZnO E_g (integrated from 320-395 nm) while the thick ZnO PSC gained only 0.09 mA/cm^2. This increase is fully offset by the efficiency in the red part of the spectrum, enough to equalize the total current of both at 17.7 mA/cm^2. Thus, the thin ZnO does indeed reduce parasitic absorption, but the better scattering of thicker ZnO fully makes up for these losses.

With the two curves coming out to be equal in the end, we looked to the JV performance to further distinguish the cases (figure 3.20b). The FF is worse for the PSC on thin ZnO, indicating a substrate-dependent change in the perovskite material quality or external circuit. We observed the thin ZnO layer morphology under SEM, and attributed the FF change to both CTL and perovskite layer quality loss. This is caused by the many gaps between the surface features of the thin ZnO film (figure 3.21). These steep vertical valleys between pyramids prevent conformal coating of the subsequent ITO and NiO_X. Evaporated PbI_2 would fill the crevasses and trap itself from accessing the SP organo-halide layer, giving an unbalanced perovskite. In either case the FF would suffer. Looking at the JV curves, the R_{OC} values for

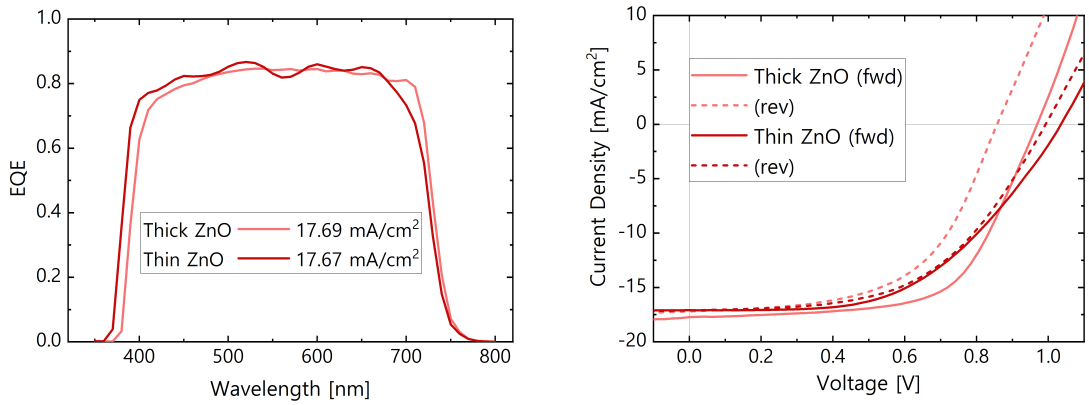

(a) **(b)**

Figure 3.20 – *JV* and EQE measurements of PSC on ZnO textures of different thicknesses. (a) EQE curves for the same PSC deposited on two different ZnO textures. The template was 240 nm thick and the spin-coating solution was 465 mM. (b) JV curves for the same cells. Average J_{SC} values for the thick and thin ZnO PSCs were 17.7 mA/cm^2 and 17.2 mA/cm^2, respectively.

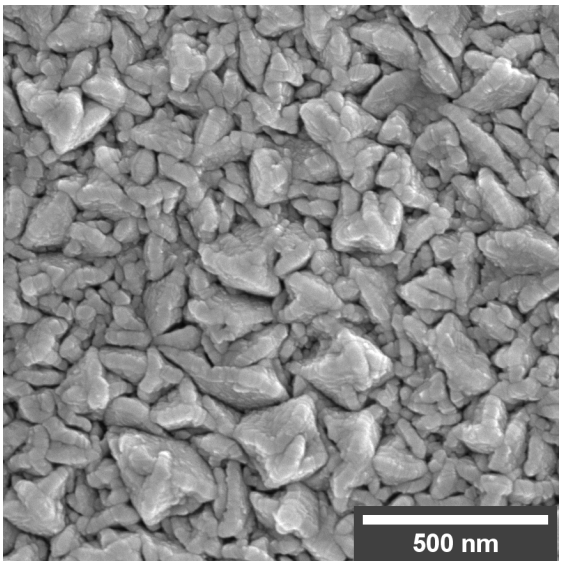

Figure 3.21 – Top-down SEM image of a thin ZnO/ITO substrate. This ZnO layer was produced with the same recipe as the "thin ZnO" in figure 3.20. It was coated with 50 nm ITO before taking this measurement.

the thin ZnO (18.3 Ωcm^2) are much higher than those foe the thick ZnO (12.7 Ωcm^2). Thus, despite the equal total current generation in the EQE curves, we can distinguish the thicker ZnO layers as being better suited for PSC based on the JV performance. Additionally, the thick ZnO produces a flat-topped EQE curve, absent of interference fringes seen with thin ZnO.

Next, we discuss the Ar-Etch step first introduced in section 3.3.2. As shown, this plasma etching step reduces both parasitic absorption and scattering efficiency. Full PSC were fabricated to find trade-off between these two effects, as optical measurements do not capture the perovskite material quality. The main gain from this step, however, turned out to be cell reliability. Figure 3.22 shows the V_{OC} measured for a batch of cells with three different etching times. The samples with only 3 minutes of etching were all fully shunted, samples with 5 minutes were mostly shunted but a few worked, and cells with 7 minutes mostly were not shunted.

To understand this trend, we looked at the effect of the Ar-Etch on the ZnO layer alone. In past research, argon plasma had been used to smoothen ZnO pyramids into large bowl-like structures which were better for infrared scattering [221]. This smoothing and reduction of features is in line with the optical and AFM measurements discussed in section 3.3.2. We confirmed this with top-down SEM, which showed the sharp pyramid edges and peaks becoming smooth and rounded after four minutes (figure 3.23). After a longer time, entire pyramids begin to disappear and much of the area in between the cells appears flat. This lines up with etched films shunting their cells less, which could be due to any of: sharp edges being difficult for perovskites to form on, shorter/rounder ZnO peaks that less likely to pierce through the perovskite thickness, or lower density of large features which reduces the probability of a single feature poking through to the opposite side. Regardless, the perovskite formed with less shunts on Ar-Etched layers.

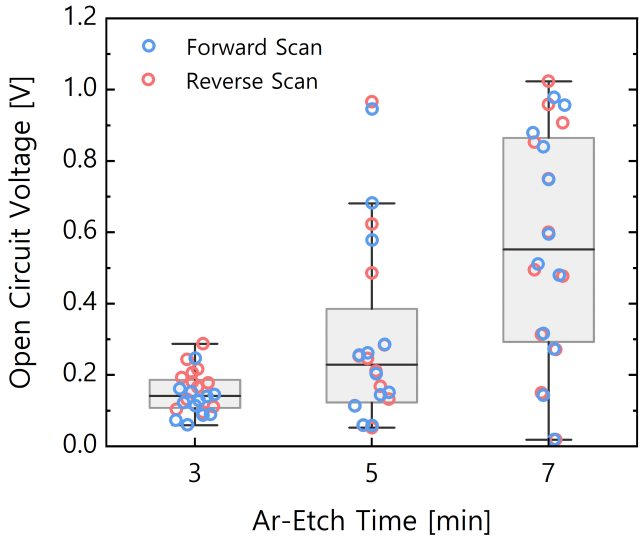

Figure 3.22 – V_{OC} measurements for PSC on ZnO layers with different Ar-Etch times. ZnO layers were deposited according to the "thick ZnO" recipe of figure 3.20 and Ar-Etched for 3, 5, or 7 minutes. They were deposited with the same perovskite, using a 250 nm template and 445 - 448 mM spin-coating solution (all conditions plotted together).

We further investigate how the perovskite quality is affected by the ZnO substrate by returning to the PDS "absorptance slope width" method previously used in section 2.2.3. This quantifies bulk disorder based on the absorption spectrum of a perovskite layer, and a lower number indicates less bulk disorder. Results are shown in figure 3.24. The data displays an opposite trend depending on if the ZnO received an Ar-Etch or not, confirming that the benefit of etching comes partially from substrate-dependent perovskite layer quality. For the sample with a 10 minute Ar-Etch, the perovskites progressively got better as they were annealed, which is well in line with films on flat substrates (figure 2.12b). The non-etched films however, quickly got worse as time went on. Since this metric only depends the absorbing layer, we can conclude that the perovskite formation is happening differently on these two different substrates, and that the recipe for an ideal perovskite material will be different for each case.

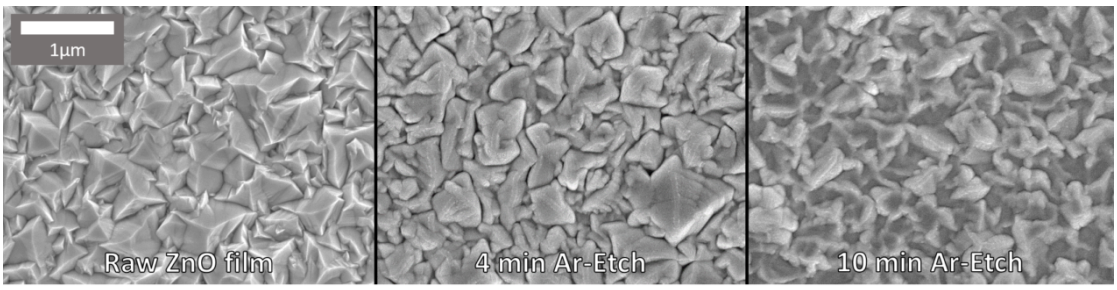

Figure 3.23 – SEM images of a ZnO layer with different Ar-Etch times. ZnO films were deposited according to the "thick ZnO" recipe of figure 3.20 and etched in an argon plasma for 0, 4, or 10 minutes. RMS roughness values for these three samples were in order: 92, 88, and 78 nm.

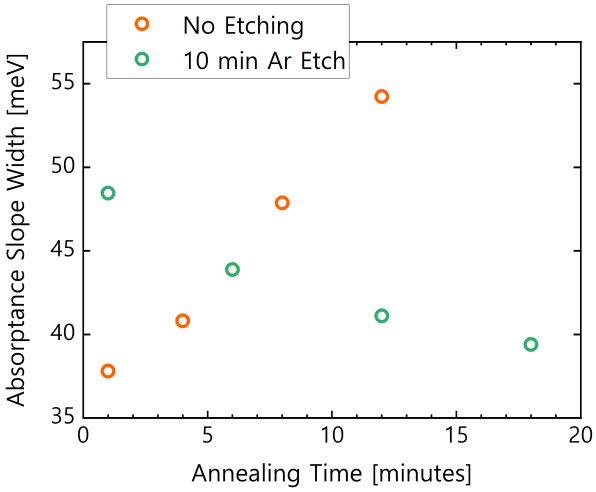

Figure 3.24 – Absorptance slope width measured for varied perovskite layers. The slope width was extracted from absorption coefficient plots, which are measured via PDS. Perovskite was deposited on glass/ZnO/ITO substrates. Samples used a 180 nm PbI_2 template with 10%vol CsBr and a 500 mM spin-coating solution.

With this lesson learned, we directly applied it in cells, in combination with the best ZnO recipe (the "thick ZnO" from figure 3.20). Cells were made in parallel on flat ITO and textured ZnO substrates, and the ZnO was either etched for 10 minutes or not at all. The etched samples were annealed for 18 minutes and the un-etched samples for 4 minutes, to match the optimal condition of figure 3.24. The full batch results are shown in figure 3.25. In line with previous results, the un-etched samples experienced significant shunting while the samples with a 10 minute Ar-Etch are not significantly affected. The average R_{SC} values for flat ITO, etched ZnO, and un-etched ZnO cells were: 1681, 1362, and 155 Ωcm^2. The EQE response of the etched samples shows slightly larger interference fringes and a worse response in the red (losing 0.44 mA/cm^2 total), which we attribute to the ZnO morphology being flattened and giving less scattering. Still, both types of ZnO-textured PSC gained EQE in the middle of the spectrum against the flat ITO. From 450 to 650 nm, the flat ITO, Ar-Etched ZnO, and un-etched ZnO samples averaged 83.9, 85.5, and 85.6 % EQE. The optical improvement in the middle of the spectrum was not enough to compensate for the parasitic absorption of the ZnO, and full-spectrum integrated EQE values dropped for all ZnO textured cells relative to the baseline flat PSC. We note that in eventual application, UV-blocking polymers are used as part of cell encapsulation in most c-Si modules, reducing the severity of parasitic absorption in the ZnO. Beyond J_{SC}, the FF of all textured cells dropped. This partially comes from the increased R_{OC} values (average values: 9.5, 15.5, and 67.9 Ωcm^2). All samples used the same ITO layer, but the effective thickness is less on the ZnO textured samples due to geometrical effects of a flat layer covering a textured surface. The rest of the FF loss likely comes from worse material quality of performing the PVD/SP method on a non-flat substrate, and the material quality loss on un-etched ZnO. We recall that the absorption slope width from PDS reached as low as 30 meV for perovskite on flat ITO, but is nearly 40 meV in the best case on ZnO.

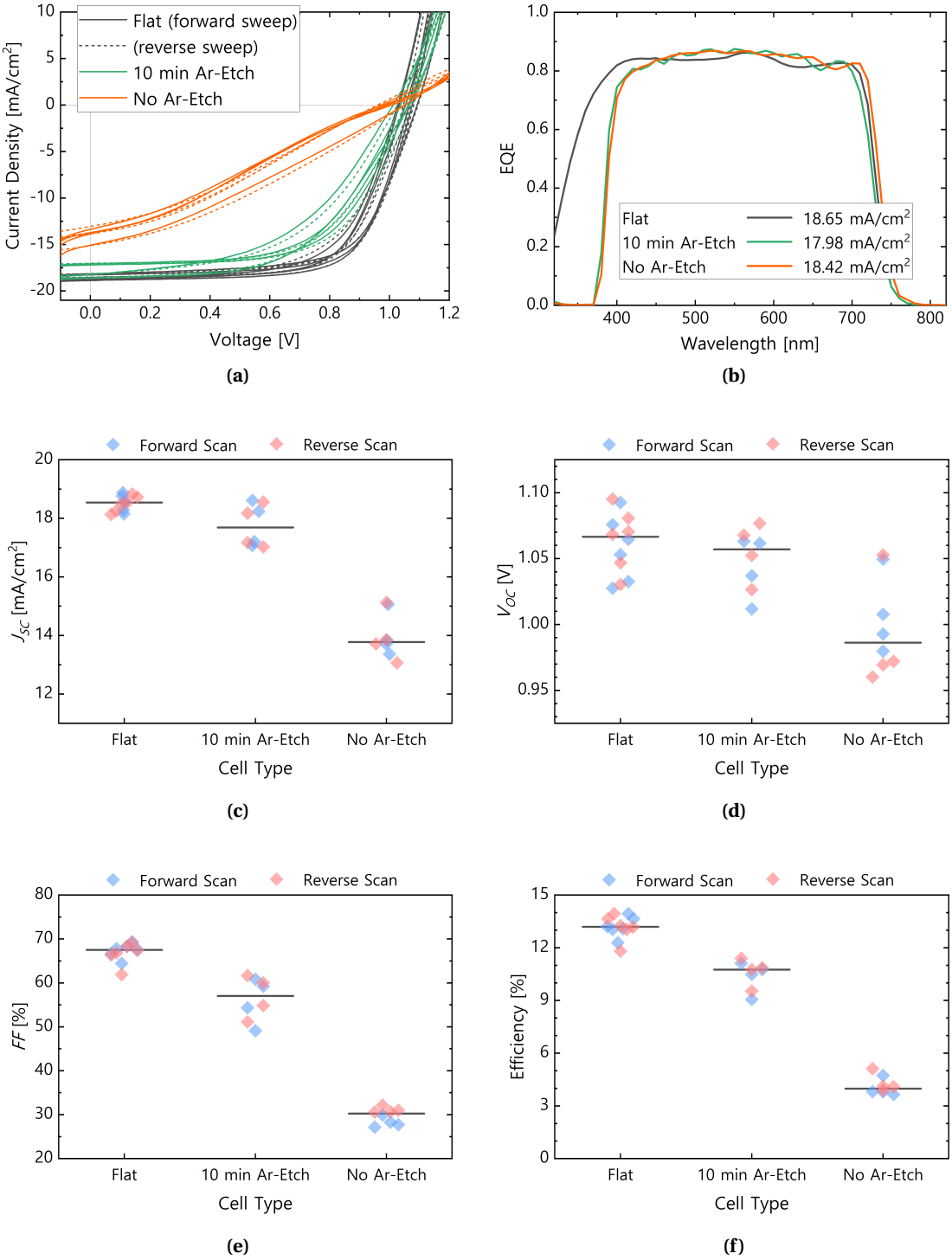

Figure 3.25 – *JV* and EQE measurements of optimized PSC on ZnO from the hybrid PVD/SP method. (a) *JV* curves for a full batch of cells produced on flat ITO, as-deposited ZnO with ITO, or Ar-etched ZnO with ITO. (b) EQE for champion cells of each condition. (c-f) *JV* statistics for the full batch. All conditions used the same 180 nm PbI_2 template with 10%vol CsBr and 500 mM spin-coating solution. Flat cells were annealed for 20 minutes, ZnO-textured cells without etching for 4 minutes, and ZnO-textured cells with Ar-Etch for 18 minutes. The cell stack was glass/ZnO/ITO/NiO_X/perovskite/LiF/C_{60}/Ag.

Limitations and Challenges

The PSC results of PVD/SP method perovskite on ZnO speak for themselves, but it is important for anyone looking to recreate or further develop these results to understand the limitations and challenges involved. Here we outline some of these challenges, and demonstrate solutions that were found. Full details and extended testing can be found in section B.7.1.

One of the main barriers to performance was the lower material quality of PVD/SP perovskites on ZnO textures relative to flat ITO substrates (from PDS in figure 3.24 and lower FF in figure 3.25e). We attribute this to the irregularity of the PVD and SP steps when deposited on non-flat substrates. ZnO textures are unlike flat surfaces, where the thickness of evaporated and spun films is essentially constant over the area of deposition; and unlike KOH-etched c-Si textures, which are regular, repetitive, and large enough that PVD films are essentially a uniform thickness at an angle (see figure B.1). We performed SEM cross-section measurements of PbI_2 templates on textured ZnO and flat c-Si, shown in figure 3.26. The template on c-Si is compact, and the top surface is parallel to the substrate. The template on ZnO is irregular, with gaps visible below and a top surface that somewhat planarizes the texture below. This means an inconsistent template thickness and perovskite with spatially inhomogeneous component

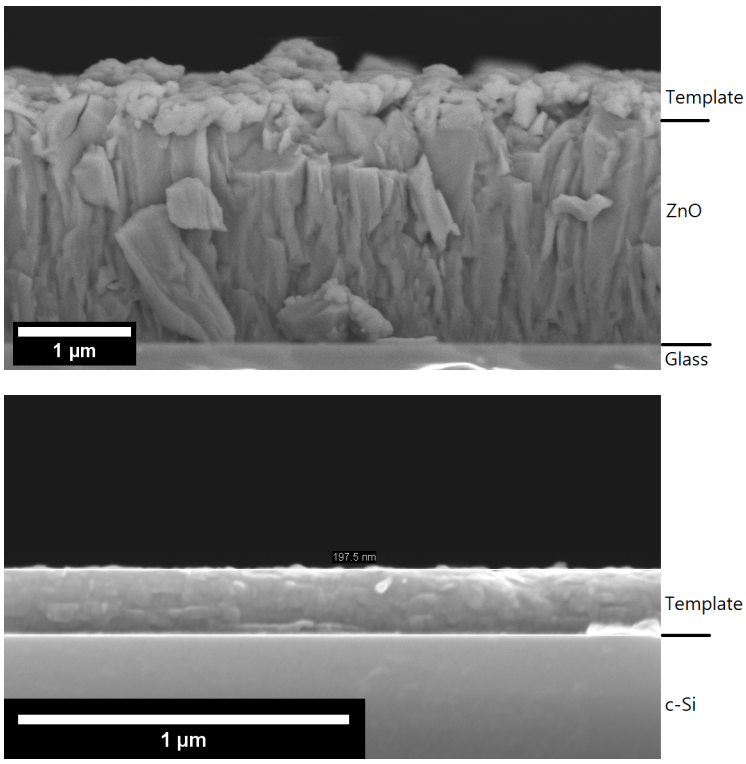

Figure 3.26 – SEM image of a PbI_2-CsBr template on ZnO and flat c-Si. This template was deposited by PVD following the baseline recipe. 180.0 nm was measured for the PbI_2 thickness and 18.0 nm for the CsBr thickness, via quartz crystal monitors during deposition. The top image is on a typical glass/ZnO/ITO substrate, and the bottom image is on a flat c-Si wafer. The horizontal lines in the bottom image are overlayed on the image for measuring vertical distance.

balance. As we know from PVD/SP layers on flat substrates, an imbalance in either direction can ruin cells (figure 2.3). This puts ZnO-textured PSC in the difficult position of at best having inconsistent perovskite quality, and at worst being forcibly over/under converted. In practice, it necessitated frequent sweeps of SP concentration, which occupied significant experimental space and slowed development.

Another consequence of the PVD/SP method on ZnO was substrate-dependent progression of the annealing (recall figure 3.24). As established in section 2.2.1 and figure 2.4, the annealing step can push the perovskite component balance between inorganic and organic components in either direction. An example of this effect in ZnO-textured PSC is shown in figure 3.27. Here, we tried to form PVD/SP perovskite on seven different texture recipes in order to compare their scattering ability. Each horizontal pair is one condition, and each shows different formation dynamics after just a few minutes of annealing. Some turn dark slowly, some not at all, some immediately and then degrade into yellow. This amount of variance required a re-optimization of the annealing time for each new batch of ZnO substrates, which occupied significant experimental space and slowed development.

The second major problem with this cell design is that ZnO is a conductor, and is deposited full area on the substrates. Thus, when physically contacting the top and bottom cell electrodes for measurement, accidental shunting could occur if the probes pierce through the cell stack and connect both terminals to the conductive ZnO (in the range of 60 S/m or 50 $\Omega/\square$). This would inevitably produce a shunted measurement, even if the cell area was fine. A solution was eventually found, which was to deposit an AlO_X layer directly on the ZnO (by ALD, 10 nm). This isolated the ZnO from the cell, eliminating the problem of contacting the ZnO with

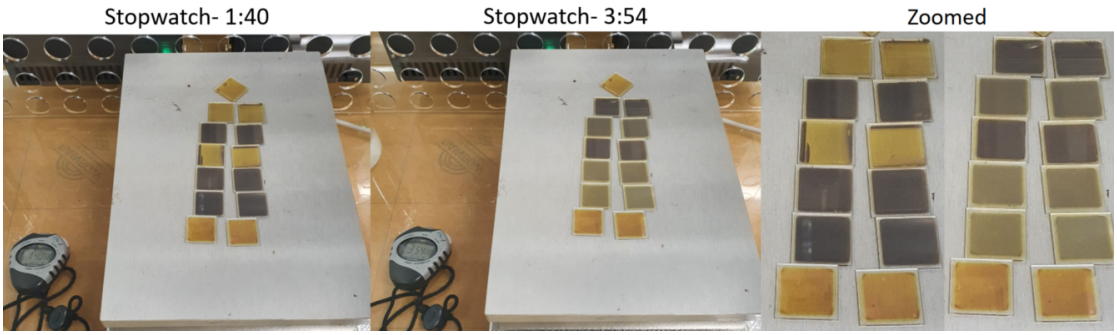

Figure 3.27 – Images of PSC on various ZnO textures during annealing. This experiment sought to compare different thicknesses of perovskite on various ZnO textures. The template used 100 nm PbI_2, and each set of two from the top down is: flat ITO, flat ZnO, "thin" textured ZnO, "thin" textured ZnO with 10 minute Ar-Etch, "thick" textured ZnO, "thick" textured ZnO with 10 minute Ar-Etch, and UV-cured polymer replicas of c-Si pyramids. It can be seen that after only a few minutes of annealing at 150°C, some perovskite films crystallize quickly then degrade over time, while others take minutes to crystallize but then are stable.

the measurement probes. It also meant the ITO layer had to be made more conductive and that the cells no longer had the possibility of eliminating indium use. But the reduction in shunting was preferable to these benefits, at least at the proof-of-concept level.

To observe shunting of ZnO textured PSC directly, we took lock-in thermographic images of cells under voltage bias. This test puts the perovskite under -1 V of stress, which promotes the formation of shunts paths in order to pass negative current [77], [78]. These electrical conduits then heat up due to their resistance, and we are able to image that heat via an infrared camera. The measurement is left to run until shunts form, at which point it evolves little more and the measurement is stopped. Shorter measurements therefore indicate shunt-prone films, and fewer/brighter hot-spots indicate more efficient current pathways. An initial infrared image is taken, then overlayed with the measured in-phase heating. This allows for spatial identification of shunts, along with analysis of shunt population and severity. An example is shown in figure 3.28, where the initial image, lock-in measurement, and overlay are shown together for a single cell. Overlay images for cells with and without ZnO texture, Ar-Etch, and AlO_X buffer layer are shown in figure 3.29.

From these measurements, we see that all the ZnO-textured PSC shunt roughly 20x faster than flat films, regardless of Ar-Etching. In a matter of 5 - 10 seconds, all the ZnO-textured PSC had formed 2 - 3 hot-spots, and these shunt paths passed all the induced current. In contrast, none of the shunt paths in the flat cells were conductive enough to pass all of the current, which caused more small shunt paths to form. The observation that shunts appeared in the cell area and not at the probe locations indicates that even without piercing through the layer with probes, ZnO cells shunt faster than flat cells. Next, the film without AlO_X heated uniformly all over the cell. We attribute this to a high density of small and quickly-formed shunting paths.

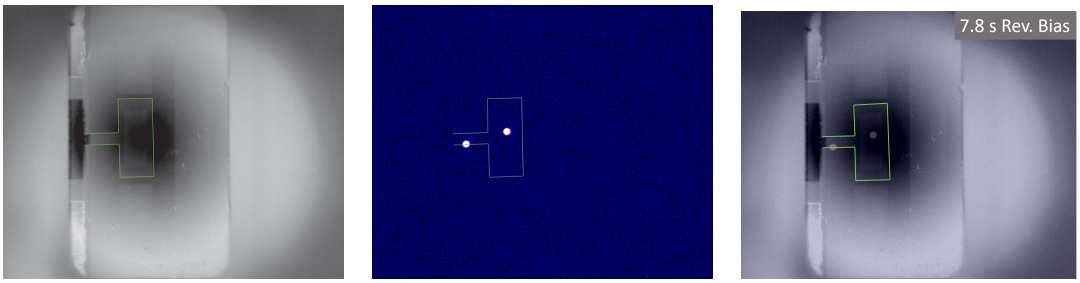

(a) Infrared image of a cell being measured

(b) Image of in-phase heating, showing two hot-spots

(c) Overlay of (a) and (b)

Figure 3.28 – Example components and overlay of a lock-in thermography measurement of PSC under reverse-bias stress. This test pulses a negative voltage (-1 V) on the cell at 25.0 Hz and takes thermal images at the same frequency. An initial image is taken before the bias is applied, and then the two images are overlayed to see where the hot-spots are located. In these images, the cell area is outlined in green for clarity. The cell is a ZnO-textured PSC with an AlO_X buffer layer and no Ar-Etch.

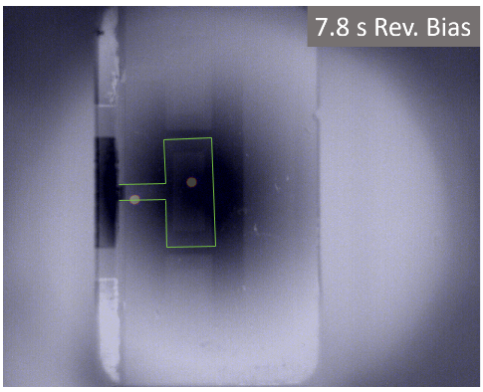

(a) ZnO PSC without Ar-Etch, with AlO_X buffer

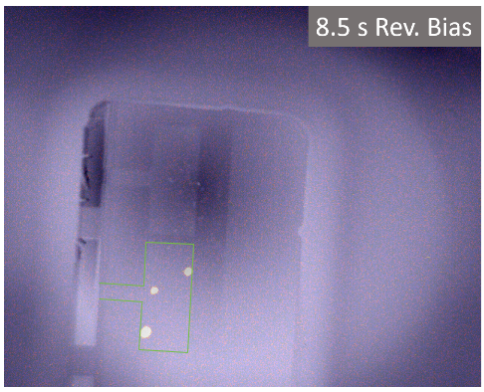

(b) ZnO PSC with 5 minute Ar-Etch, with AlO_X buffer

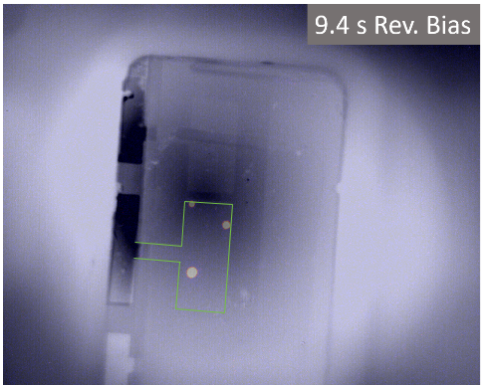

(c) ZnO PSC with 10 minute Ar-Etch, with AlO_X buffer

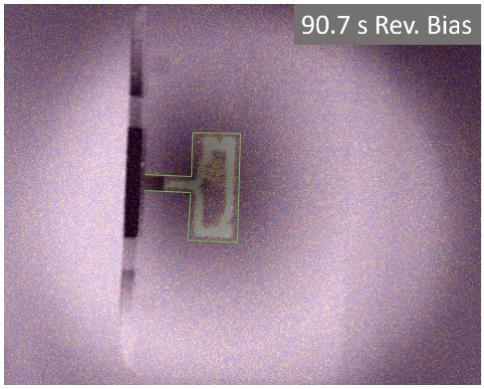

(d) ZnO PSC with 10 minute Ar-Etch and no AlO_X buffer

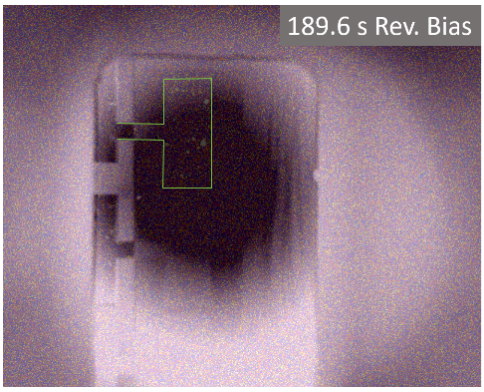

(e) Flat PSC

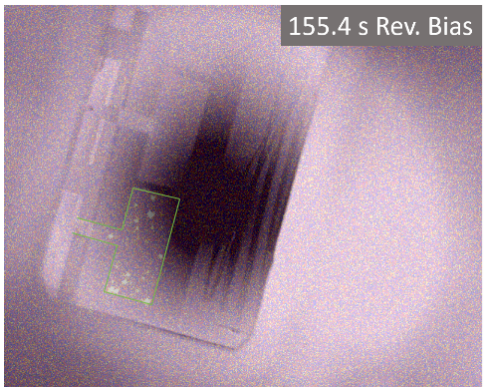

(f) Flat PSC

Figure 3.29 – Lock-in thermography images of varied flat and ZnO-textured PSC under reverse-bias stress. Each image (a-f) is an overlay of a normal image and the lock-in amplitude heating image. The cell area is outlined in green for clarity. Cells were stressed until hot-spots started to appear, then the measurement was stopped, and the duration is shown in the upper right corner. All of the cells here used the HCl method for removing the ZnO from the area of the top-contact.

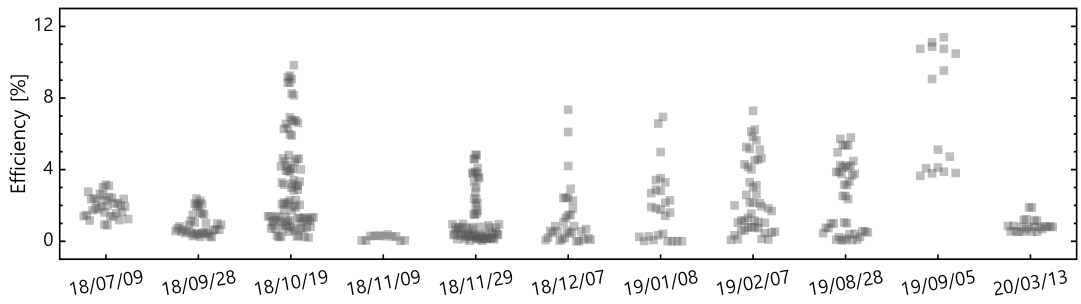

Figure 3.30 – Efficiency for each ZnO PSC in each batch over time. Most batches were dominated by shunting or low FF. Thus optimization was difficult and many experiments had to be repeated. Long breaks were taken to focus on other work, but we occasionally returned to try again.

The difference in shunting behavior between ZnO-textured cells with and without an AlO_X buffer is likely due to the chemical protection afforded by the AlO_X, without which Zn ions could enter the perovskite, lower material quality [231], and permit shunts in more locations.

Overall, there were many production problems that stood in the way of this cell design working well. Some were related to cell architecture and accidental shunting (full-area conductive ZnO, inability to disconnect the areas probed during JV measurement) and some were related to reduced material quality from PVD/SP perovskite (varied annealing times, inconsistent template/perovskite thickness, Zn contamination, residual PbI_2 in ZnO valleys). Combining these struggles, the cell results were low yield. Figure 3.30 shows the efficiencies of most ZnO-textured PSC batches over time. Not all are shown, as some had reasonable external factors for being poor quality. But for nearly every batch the median cell efficiency was below 3%. Furthermore, the champion cells in figure 3.25c were the only instance where a ZnO-textured PSC achieved a J_{SC} as high as that of flat cells. We attribute this to the various issues related to the PVD/SP process which were discussed above. However, with the development of the AlO_X buffer layer and new materials such as SAM, it was conceivable for these problems to be resolved, so long as the hybrid PVD/SP method could be replaced with a method which is more compatible with ZnO textured substrates.

3.4.2 Cells Made with Solution-Processed Perovskite

For comparison with the hybrid PVD/SP method, we fabricate ZnO textured PSC with a fully solution-processed perovskite deposition. The ZnO recipe was the same as was used in figure 3.25, and did not include and Ar-Etch. The feature size of this ZnO layer was on the order of 500 nm, similar to the perovskite layer. The relative scale can be seen in figure 3.31. Certain research groups have reported successful attempts to put solution-processed perovskite on various textured surfaces, so long as the surface morphology is sufficiently small [142], [149], [155]. Thus we applied the same recipe on flat and ZnO-textured substrates. For these tests, we used an updated cell stack, adding the AlO_X buffer layer, replacing the NiO_X HTL with

a SAM molecule (MeO-2PACz), and adding an SnO_2 layer between the C_{60} and the Ag. The solution-processed perovskite films had little issue covering the ZnO surface (figure 3.31). As the ZnO conductivity was removed by the AlO_X layer, the ITO layer was modified by reducing O_2 content and increasing the layer thickness (120 nm, 30 $\Omega/\square$). Thank you to Dr. Christian M. Wolff, who fabricated all the samples shown in this section.

This was successful, with cells reaching over 20% efficiency and showing significant optical improvement in the EQE measurement (figure 3.32). The average EQE in the 500 – 700 nm range increases from 90.9% to 95.9%. This translates to an average gain of 1 mA/cm^2 in the measured JV curves, and an efficiency boost of 1.1% on average compared to cells without ZnO texture. Compared to notable literature results, particularly the textured PSC of Tockhorn et al. [142] and a record reported PSC from Jeong et al. [232], our results show similar J_{SC} values relative to the Shockley-Queisser limit for that bandgap (compared in table 3.1). Notably, our cell reaches this J_{SC} value despite the ZnO parasitic absorption below 395 nm. This corresponds to roughly 0.5 mA/cm^2 of current lost, and 2.0% of the Shockley-Queisser limit. This current would likely be blocked for all cases in any realistic application, as most module encapsulants absorb UV light in order to protect the cells (such as ethylene-vinyl acetate [233]). For the sake of high-current device demonstration, the ZnO could be replaced with a highly transparent molded polymer. Though this would forgo the possibility to reduce or eliminate indium use.

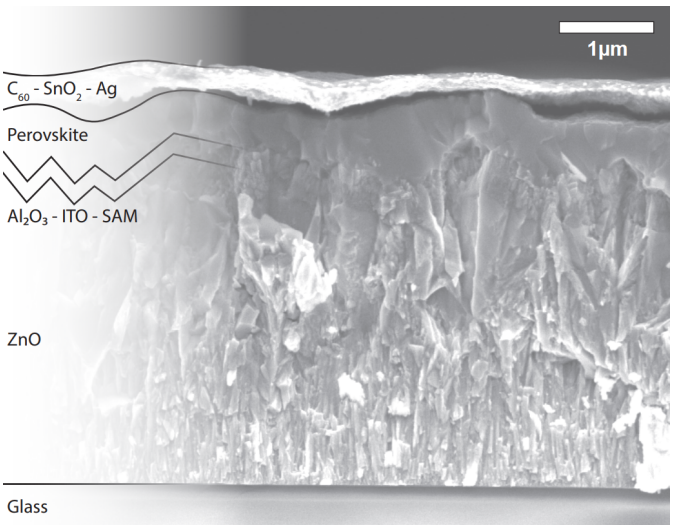

Figure 3.31 – SEM image of PSC based on solution-processed perovskite on ZnO textured substrate. SP perovskite layers were deposited on ZnO textures with the same recipe as on flat substrates. This was able to fully cover ZnO pyramids of a limited size, but which were still large enough for beneficial optical scattering. The cell stack was glass/ZnO/AlO_X/ITO/MeO-2PACz/perovskite/C_{60}/SnO_2/Ag

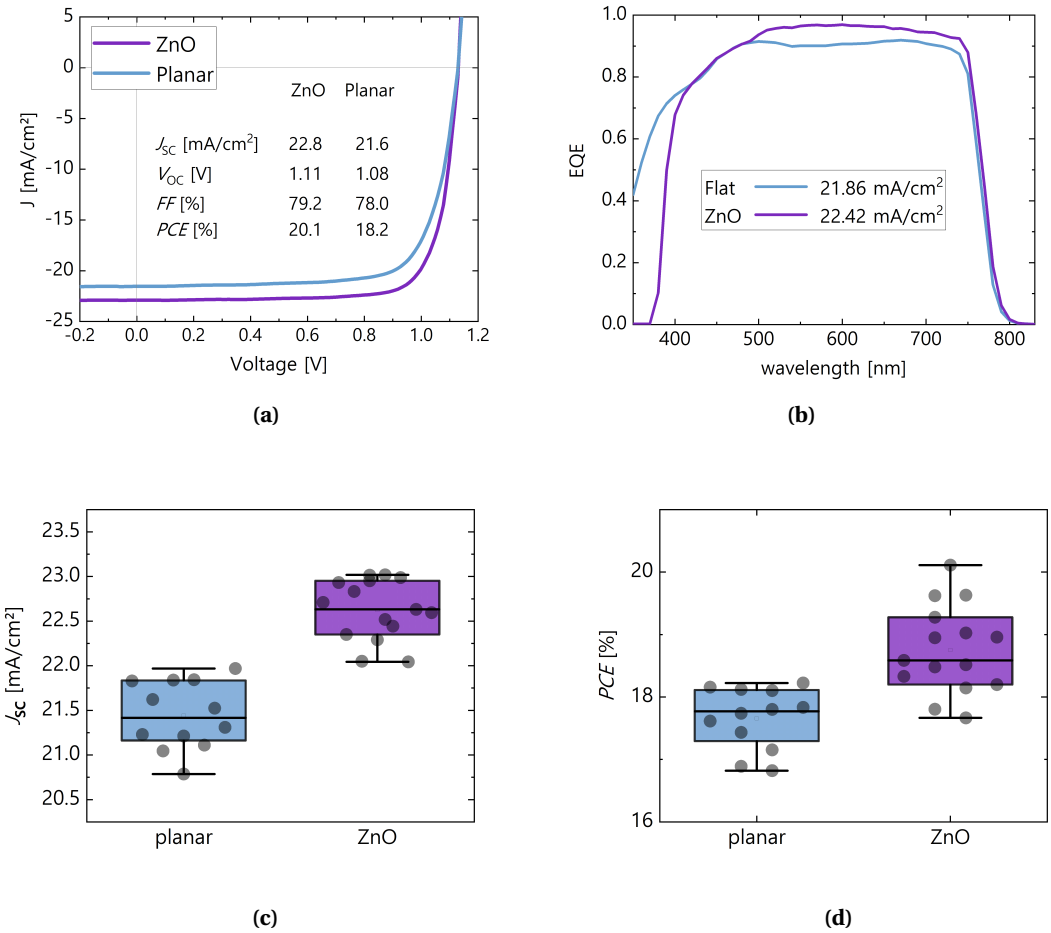

Figure 3.32 – *JV* and EQE measurements of solution-processed PSC on ZnO. (a) JV curves and metrics of champion cells on flat and ZnO-textured substrates. (b) EQE measurements for champion cells of each condition. (c) and (d) J_{SC} and efficiency statistics for the full batch. The cell area was 0.1 cm^2. Cells fabricated by Dr. Christian M. Wolff.

Group	Structure	Perovskite E_g [eV]	Reported J_{SC} [mA/cm^2]	% of S.-Q. Limit [%]
This work (flat)	p-i-n	1.61	21.6	85.98
This work (ZnO)	p-i-n	1.61	22.8	90.76
Tockhorn et al. [142]	p-i-n	1.62	23.1	93.07
Jeong et al. [232]	n-i-p	1.53	26.7	94.11

Table 3.1 – Performance of our champion J_{SC} and other notable literature results against the Schockley-Queisser Limit. J_{SC} and E_g values were extracted from published EQE data. The device structure is notable, as the n-i-p device benefits from the optical effects of a mesoporous TiO_2 layer which induces anti-reflection due to a gradient interface.

3.5 Conclusion

In this chapter, we sought to improve the optical performance of our PSC by incorporating a textured absorber interface. Specifically, we looked at ZnO as a source of texture. This material is transparent and forms nanometer to micrometer sized pyramids on its surface depending on how it is grown. It uses cheap and abundant materials, can be deposited over large area, and has already been applied on an industrial scale for thin film Si PV. Inserting this layer below the perovskite absorber could bring optical enhancement from scattering and multiple reflections, improve the angular dependent response of the cell, and potentially replace ITO to reduce the consumption of indium in PV. Thus, we considered it the most promising candidate for bringing optical scattering to PSC.

Growing ZnO via LP-CVD allowed control of the favored crystalline axis of growth, the c-axis or a-axis. c-axis ZnO films are relatively smooth (RMS = 8.0 nm for a film of 1.32 µm) and exhibit no optical scattering. a-axis ZnO films experience competitive growth, where the crystallites expand laterally while growing vertically, causing them to overtake eachother. This manifests as large pyramidal surface features (RMS = 81.0 nm for a film of 1.53 µm) and high optical scattering. Test depositions were characterized and their data used to carry out optical simulations. These simulations confirmed the potential J_{SC} benefits of a textured absorber interface and provided rough guidance to the design of the ZnO layers. We then tuned the deposition parameters of our LP-CVD instrument to identify the a- and c- axis deposition regimes. From these, a recipe that balanced high scattering and low parasitic absorption was chosen and transferred to use in PSC.

Parallel testing of PSC deposition on ZnO-textured substrates allowed for confirmation of designs, and uncovered effects of the substrate on perovskite film quality. Both the perovskite deposition and the ZnO layer had to be modified to best work together. The perovskite was made thicker, and the ZnO layer was etched with an argon plasma. The plasma etching step was particularly influential on the bulk quality of the perovskite, and drastically reduced the probability of shunting. This led to a better recipe and a "champion" batch of PSC, where the ZnO-textured cells showed optical improvement in the EQE spectrum. However, due to persistent losses in material quality and the parasitic absorption above the ZnO E_g, the overall cell FF and J_{SC} dropped compared to flat references.

We discuss reasons for the loss in material quality and general difficulty in producing this type of cell, and conclude that it is largely related to the hybrid PVD/SP method which has been used exclusively so far in this work. We thus compare to a full SP perovskite deposition, and find that this resolves the problems of material quality. Cells with over 20% efficiency are produced, with a 5% enhancement in the EQE (500 - 700 nm), on average 1 mA/cm^2 gain at short-circuit in JV measurement, and an overall efficiency boost of 1.1% relative to flat cells. This shows that using ZnO layers for creating textured absorber interfaces is a viable strategy for improving the optical performance of PSC, and maximizes efficiency in a way that cannot be achieved through improvements to perovskite material quality.

4 Development of Monolithic Perovskite/c-Si Tandem Solar Cells

Abstract

The culmination of this thesis work was to apply the understanding gained from research on single junction PSC to the practical case of monolithic perovskite/c-Si tandem solar cells. From the established basis of the 25.2% efficient cells produced by previous students, we looked at each aspect of the cells to find how they could be further improved. The first goal was to increase the thickness and E_g of the perovskite layer. Achieving this would allow for a more equal split of the solar spectrum and increased cell voltage from a higher top-cell E_g. This was realized via optimization of all of the processing parameters that were first studied in single junction PSC and detailed in section 2.2, and resulted in J_{SC} values over 20.0 mA/cm^2. The next goal was to increase the extracted voltage of the solar cells. This was done via direct application of the processes and layers described in section 2.3.1, and resulted in V_{OC} values over 1.9 V. Finally, the last aspect of the cell performance that was left to improve was the FF. For this we separated the two sub-cells, and improved them separately. The bottom-cell performance was improved with annealing and a mechanical protection layer. The top-cell FF was improved via the same method as detailed in section 2.4, using FBPA and higher-temperature annealing to give better morphology and charge transport. This overall resulted in a champion perovskite/c-Si tandem with 20.26 mA/cm^2 of J_{SC}, 1.81 V of V_{OC}, 75.7% FF, and stabilized efficiency of 27.3%.

4.1 Tandem Cell Architecture

Perovskite/c-Si tandem solar cells were deposited via the following process flow, forming the cell stack shown in figure 4.1. Production started with the bottom-cell, which was handled by the SHJ research group of PV-Lab. The baseline process is outlined in figure 4.2. First, a 100 mm diameter, 200 µm thick, 2 Ωcm n-type float-zone mono-crystalline wafer is used. Wafers are etched in an alkaline-based solution to achieve a double-side random pyramid texture. They are then cleaned in an HF solution for 1 minute before being loaded into a KAI-M plasma enhanced chemical vapor deposition (PE-CVD) system, from Oerlikon Solar. There, the deposition of passivating and selective layers takes place at 200°C. On the rear side, the passivating layer is intrinsic amorphous Si (a-Si:H(i)) and the charge-selective layer is boron-doped amorphous Si (a-Si:H(p)). On the front side, the passivating layer is the samea-Si:H(i) and the charge-selective layer is phosphorus-doped amorphous Si (a-Si:H(n)). Details on the contact layers can be found in: [234], [235]. These are followed immediately by an ultra-thin SiO_X layer via CO_2 treatment and hydrogenated n- and p-doped nanocrystalline Si layers (nc-Si:H(n) and nc-Si:H(p), also at 200°C) to obtain a tunnel junction stack as in: [162]. Following this, the cell rear contact of ITO/Ag is deposited by sputtering in an MRC chamber. This is done through a shadow mask to match the eventual metalization geometry of the front electrode. As the sample is still a 100 mm diameter wafer, it is laser scribed to define nine squares with 25 mm edges. This is done with a Trumpf TruMark 1000 system, which uses a pulsed 1064 nm laser. The wafer is cleaved along these lines, and the resulting samples are ready for top-cell deposition. All bottom cells were produced by Vincent Paratte and Deniz Türkay.

For the sake of top-cell development, we also occasionally used a test structure based on a nearly identical layer stack. In this case, we simply deposited the same a-Si:H(n) selective layer on the rear of the cell as we did on the front. This way, there was no junction in the silicon, and it did not function as a solar cell. Instead, it was simply a conductive substrate that mimicked perfectly the surface and morphology that we would otherwise have on a SHJ bottom-cell. This way, we could characterize the top cell individually, without confounding effects of varied bottom cell quality. This enabled accelerated development, and some of the top-cell optimization results which are presented below were performed on such a structure. In this case, it is denoted as using a "symmetric SHJ" bottom-cell.

We note here that in this chapter we will report thicknesses of the layers in the top-cell as they are measured along a line normal to the c-Si pyramid surface, rather than their equivalent thickness on a flat substrate. This imparts a factor of 1.7 due to the geometrical effects of depositing over a larger surface area. This difference is relevant for the perovskite deposition parameters, and the measurement orientation will be repeated regularly for clarity.

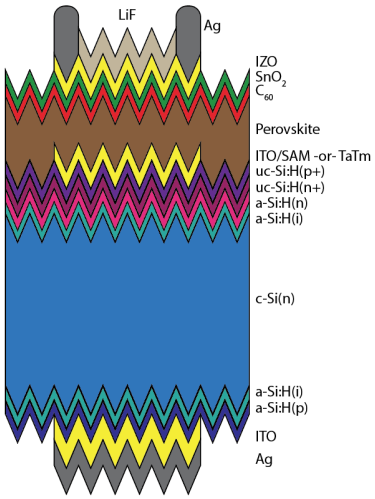

Figure 4.1 – Cell architecture for a typical perovskite/c-Si tandem. Layers are not to scale. Typical thicknesses are 100 nm for the rear ITO, 5 nm for the a-Si:H(i) layers, 20 nm for the a-Si:H selective contacts, 50 nm total for the nc-Si recombination junction, 7 nm for the ITO used to anchor the SAM, 700 nm for the perovskite, 5 nm for the C_{60}, 10 nm for the SnO_2, 80 nm for the IZO, 250 nm for the front Ag grid, and 55 nm for the LiF anti-reflective coating.

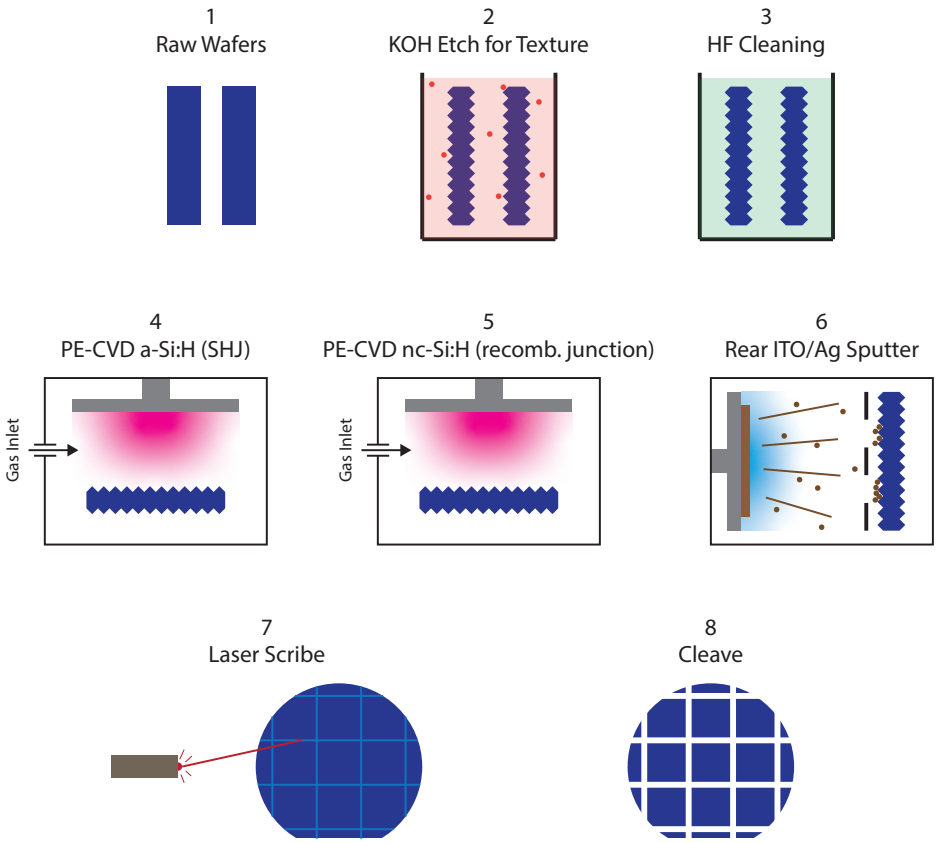

Figure 4.2 – Process flow for the production of SHJ for use as tandem bottom-cells. Wafers are etched and cleaned before they can be brought into the PE-CVD chamber. In the case of bottom-cells being used as single junctions, the front electrode is deposited after cleaving.

The top-cell process starts differently depending on if the top-cell will use a SAM or bulk polymer HTL. For SAM-based cells, a thin[1] ITO layer was sputtered on top of the nc-Si recombination junction, so that the SAM would have the correct surface to bind to. This surface was then modified via a 15 minute treatment of combined UV light and ozone gas (machine from UVOCS Inc.). From there, the samples were brought into a N_2 filled glovebox and the SAM (typically MeO-2PACz from TCI or Me-4PACz from Sikémia [111]) was spin-coated statically from a 2 mM solution in ethanol. The samples sat for 10 seconds with the solution, before accelerating 100 rpm/s to 3000 rpm. The samples are then annealed for 10 minutes at 100°C. For cells with a bulk polymer HTL (Spiro-TTB or TaTm, from Lumtec), usually 5 nm of the material was evaporated in a home-made evaporation system, at about 0.1 Å/s and below $1x10^{-5}$ mbar.

Next, we deposit the perovskite layer via the hybrid PVD/SP method. A step-by-step SEM view of the final top-cell perovskite deposition process can be found in section B.1. This starts in a thermal evaporator (Lesker Mini-Spectros), where the template layer of PbI_2 and CsBr are evaporated at a 10:1 volume ratio (measured as mass via quartz crystal microbalance), at rates of 1.0 and 0.1 Å/s. The template layer thickness is optimized in the following section, and thus not specified here. The samples are then dynamically spin-coated with a solution of FA-halide salts (GreatCell Solar, or Dyenamo) in ethanol. They are then removed from the N_2 environment and annealed in air with a fixed dew point, to control the water exposure of the perovskite.

Finally, the samples return to the home-made evaporation system for deposition of the C_{60} ETL (from Nano-C, again 5 nm at about 0.1 Å/s and below $1x10^{-5}$ mbar). Next the samples are transferred to an atomic layer deposition system (Picosun), which deposits 80-150 cycles of H_2O and tetrakis-dimethyl-amine tin pulses under vacuum (10 hPa). This serves as a buffer layer to protect the underlying layers from damage that might otherwise occur during the following step, which is deposition of the front TCO via sputtering. In our case, we use indium zinc oxide (IZO), which is deposited by radio frequency (RF) sputtering in a home-made system, and masked to the area of the front metalization. Again, the thickness of this layer is varied in the following section, and will be specified at this point. Finally, the front metal (Ag) is deposited by thermal evaporation through a shadow mask to form the busbars and fingers, typically 200 to 260 nm in thickness. Two cell designs are used, either 1.43 cm^2 or 1.02 cm^2, shown in figure 4.3. Both have similar series resistance, and which design was used is noted alongside any results. Optionally, an anti-reflective film of MgF_2 or LiF is deposited via evaporation as well, at 35 and 55 nm, respectfully. All thicknesses are measured normal to the c-Si pyramid face, and thus are 1.7x larger if measured on a flat surface.

[1] ITO thickness is defined by the speed of the sample plate as it passes in front of the sputtering target. Assuming linearity of sample speed, we can estimate the thickness based on measurements of thicker layers. This deposition used 300 cm/s sample speed, which implies a 12 nm ITO layer as measured on a flat surface. This corresponds to 7 nm on textured c-Si.

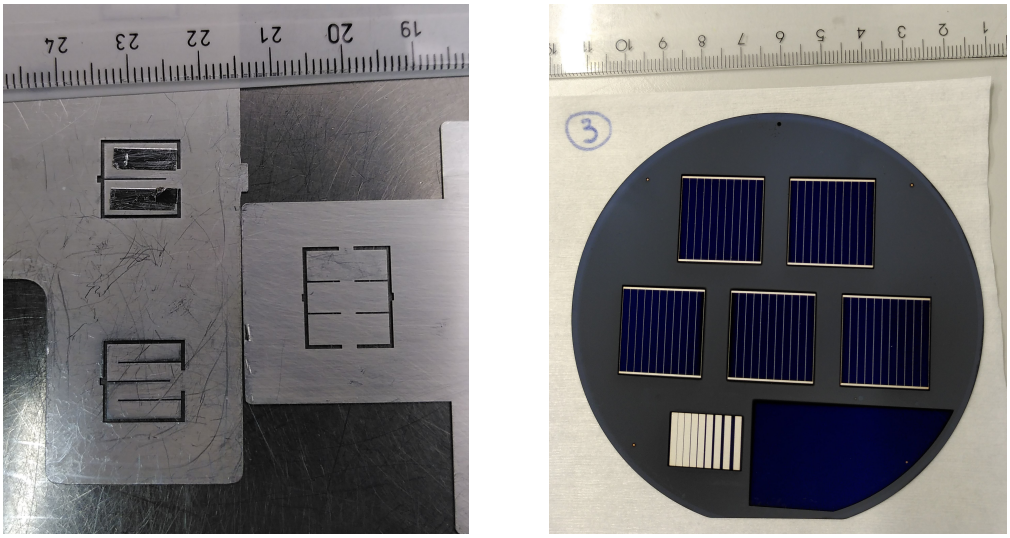

(a) Tandem cell designs

(b) SHJ cell design

Figure 4.3 – Cell designs used regularly for tandems and SHJ. (a) Two grid designs were used regularly for tandem cells. This image shows the shadow masks used for evaporation of the Ag fingers and busbars. The left design is a 1.02 cm^2 and the right design is 1.43 cm^2. For the smaller design, typically the two side fingers are masked, leaving one finger in the middle. Finger width (of the mask) is 200 µm and thickness is 0.3 µm. (b) Standard design for single junction SHJ cells. Five cells are made on each wafer, each 4.0 cm^2. Ten fingers cross the cell area, and are roughly 10 µm tall 40 µm wide. In both cases a ruler with centimeter markings is included at the top of the image. Images not to scale.

4.2 Increasing Tandem J_{SC} via Top-Cell Design

At the outset of this thesis work, one of the limitations of our perovskite/c-Si tandems was that of the generated photocurrent. We had achieved tandems with 19.7 mA/cm^2 of J_{SC} using a 450 nm / 1.64 eV perovskite layer, but this was more than a full mA/cm^2 short of the realistic potential for this type of solar cell, which we will establish here. As we are committed to developing monolithic tandems, we accept the constraint of current-matching between our sub-cells. Meeting this requirement depends primarily on the E_g and thickness of the perovskite. The c-Si bottom-cell can be assumed to absorb nearly all of the light transmitted by the perovskite, up to its absorption onset[2]. Besides the absorptive ability of the two active layers, current-matching is affected by losses that come from front reflection and parasitic absorption [134]. These losses are not equal across the solar spectrum, and thus they affect each sub-cell differently. Taken together, the optics of the full tandem stack is considered in figure 4.4.

This analysis estimates the maximum possible J_{ph} by calculating the spectral magnitude of each source of optical losses for a theoretical monolithic perovskite/c-Si tandem. In the idealized case, there is still some reflection off of the front and each of the layers in the front electrical contact will parasitically absorb some light. We start from the front reflective losses (measured on a real device), and calculate the minimum practical parasitic absorption loss of each layer (using data obtained on PV-Lighthouse [233]). We can approximate the ideal case by assuming the front reflection touches to 0 at its minimum, and using the minimum reasonable thicknesses of the front TCO (80 nm IZO, enough to give < 100 $\Omega/\square$), buffer layer (10 nm SnO_2), and selective contact (5 nm C_{60}). What remains after passing these losses is the light usable to the solar cell, equal to $J_{ph} = 42.36$ mA/cm^2. From this, we find that 1.714 eV is the ideal top-cell E_g, assuming each cell absorbs 100% of light on either side of that point. In practice, high-efficiency literature results on both flat and textured surfaces have used top-cell E_g values in the range of 1.65 - 1.68 eV [111], [127], [149], [155].

This use of lower-than-ideal E_g values is due to incomplete absorption and thus transmission of photons through the perovskite and into the c-Si, particularly in the 200 nm wavelength range above the perovskite's E_g. The consequence of this is that the bottom-cell receives more than half of the usable photons, the top-cell E_g has to be lowered to maintain current-matching, and the cell voltage drops in turn. The solution to this loss is therefore to increase absorption in the perovskite layer, enabling current-matching with a higher E_g top-cell. This is a limited solution however. We recall the calculations of section 1.2.2, in which realistic perovskite materials would require thicknesses (3 µm) greater than their average charge diffusion length (usually 0.5 - 1 µm, [129], [130]) in order to absorb 95% of light across their whole spectrum. Thus we should attempt to make thicker perovskite layers to increase absorption,

[2] The steepness and absorbed volume in the range of the absorption onset (1050 nm - 1180 nm) in turn depends on the thickness of the c-Si wafer, but in our case we restrict ourselves to using an industrially-realistic 200 µm wafer thickness. This is justified by the high material cost of purified c-Si relative to other materials in the cell, and the industrial trend of consistently reducing c-Si usage [6].

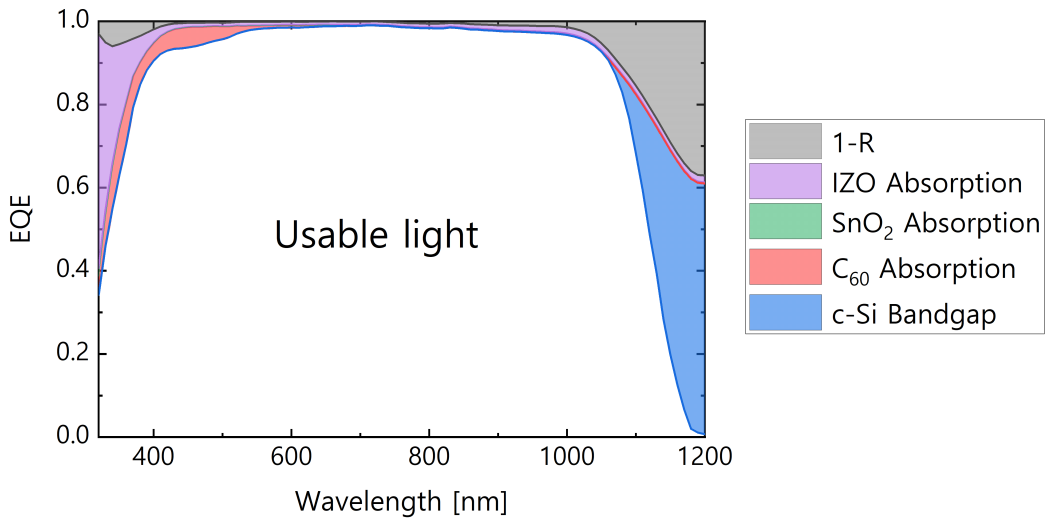

Figure 4.4 – Practical optical limitations for perovskite/c-Si tandems. 1-R is measured from a real cell with an anti-reflective coating, and shifted to give R = 0 at its peak, to capture the idealized case. IZO absorption is measured in-house from the same layer as used in cells. The SnO_2, C_{60}, and c-Si absorption is calculated from optical data available on PV-Lighthouse [233], and attributed to literature sources: [236], [237]. The thickness for SnO_2 was 10 nm and for C_{60} 5 nm. Since this did not account for the effects of texturing, the c-Si thickness was scaled to match typical EQE data, and is thus simulated as 5 mm.

but there is an upper limit set by the material properties. This limit further values the use of a textured absorber interface, which increases the optical path length within an absorber without thickening the layer [134]. Applied to our cells, the 19.5 mA/cm^2 J_{SC} result of the previous theses [62], [63] used a perovskite with 450 nm thickness normal to the c-Si pyramid face. So there is still room to improve before arriving to the limit set by charge diffusion.

Before discussing how we pursued this goal, it is necessary to discuss the current-matching condition and its effect on tandem performance. The relationship between sub-cell performance parameters and those of the full tandem are straight forward for voltage and current. The FF, however, is not so direct [152]. First, the electrons extracted at the top of the c-Si cell and the holes extracted at the bottom of the perovskite cell do not need to be conducted laterally into an external circuit. This removes the resistive losses to the FF associated with lateral transport of charges at the front of the c-Si and rear of the perovskite sub-cells. Secondly, and what is relevant to the present discussion, is that having a mismatch of current generation leads to whichever sub-cell produces less current (dubbed the "limiting cell") to be more influential in determining the overall tandem FF [152]. If one sub-cell has higher FF, then the overall tandem FF can be raised by making it the limiting sub-cell. This can improve the FF enough to offset the J_{SC} loss and give a higher efficiency [152]. In short, the sub-cell with higher isolated FF should be made slightly current-limiting. In practice, this mismatch can be experimentally realized from a matched baseline by slightly shifting the halide ratio

in the SP step, or by changing the thickness of the anti-reflective layer. Either option will shift how much current goes into each sub-cell, and thus the current-matching condition of individual tandems can be varied within the same batch. Thus, we primarily develop our recipe towards the goal of a current-matched tandem, knowing that we can convert to an ideal mis-match when so desired without re-optimizing the recipe. For now, we will focus on the development of perovskite layers increased thickness using the hybrid PVD/SP method, and general optimization of tandem optics to maximize total current.

4.2.1 Manufacturing Thicker Perovskite Layers

Achieving the goal of increasing the perovskite layer thickness required revisiting the PVD/SP parameters discussed in section 2.2. The parameter that defines layer thickness in this method is the thickness of PbI_2 measured in the evaporated template layer, and the E_g is controlled by the halide ratio in the spin-coating solution[3]. In the previously optimized tandem recipe, they used a template with 400 nm PbI_2 (measured flat on the quartz microbalance) and a spin solution with 3:1 iodide:bromide. This gave a 450 nm perovskite (measured normal to c-Si pyramids) with E_g of 1.64 eV, and incomplete absorption near the perovskite E_g (visible in figure 4.9b). In order to increase this absorption to 95%, we estimated to need about 50% thicker perovskite (which would in turn allow a E_g near 1.70 eV). This estimate was based on the exponential decay of radiation in a medium: $I_t = I_0 e^{-\alpha t}$ where α is the absorption coefficient at the given wavelength, t is the thickness of the layer, and I_t and I_0 are the intensity at the point t and the initial intensity. This would mean a 600 nm (measured flat) template layer, which we thus sought to experimentally realize.

We proceeded by evaporating a 600 nm (measured flat) template, and increased the SP solution concentration to try and convert it completely. Figure 4.5 shows the results of initial tuning. J_{SC} is used as a metric to determine how well converted the template is into perovskite, and FF to determine the material quality. Both are maximized at 0.7 M. Above and below the correct concentration, either excess template below the perovskite or excess organics above can reduce both of these values. Residual template can act as blocking layer to charge transfer, and excess organics can create an overpopulation of mobile ions which migrate and screen the electric field over the cell [75]. As for the optical performance, the EQE measured for these top-cells (figure 4.6) showed that in the ideally converted case, the long-wavelength absorption of the perovskite maintains a flat plateau from its usual peak at 560 nm up to the band edge. This confirmed that 600 nm is indeed a sufficient template thickness to fully split the spectrum and not transmit above-E_g photons to the bottom-cell.

Still, the best result displayed less J_{SC} and less FF than would be necessary for ideal top-cells, so we continued to tune other variables. We specifically adapted the spin speed, pre-anneal time, and dew point (DP) during the main annealing. This process was a direct optimization

[3]This is assuming a fixed template chemistry. But the ratio of PbI_2:CsBr in the template is well controlled by the PVD process with less than 1% noise in the evaporation rate.

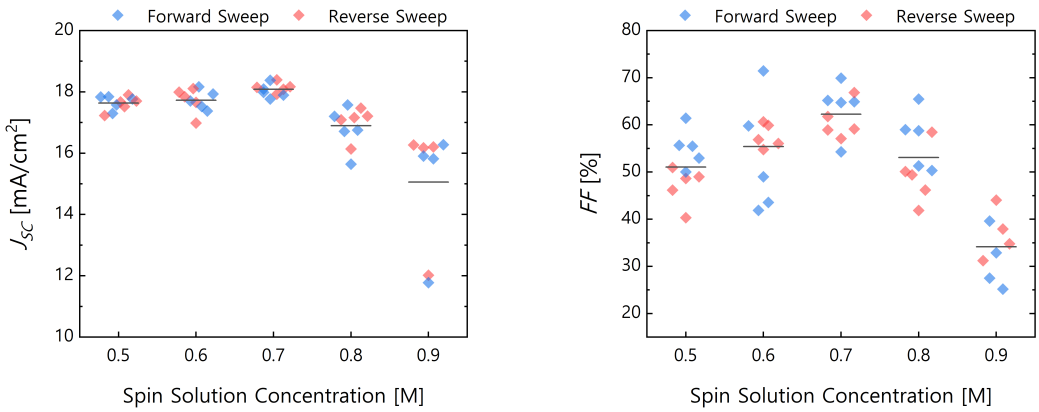

Figure 4.5 – Cell performance for perovskite on c-Si made with varied SP solution concentrations. Single junction PSC were fabricated on symmetric SHJ using the 1.43 cm^2 design, and no anti-reflective coating. The template thickness was 600 nm (measured flat) and the spin speed was 2000 rpm. Annealing took place in air at a fixed DP near 12°C. Cells and measurements courtesy of Dr. Xin-Yu Chin.

based on SEM cross-section images of the perovskite layer to evaluate if the template was fully consumed, and cell results of J_{SC} and FF. The experimental process and some results are shown in section B.10. This resulted in a final recipe for a 1.70 eV perovskite that absorbs fully above its E_g: 600 nm PbI_2 (measured flat) with 10%vol CsBr evaporated template, 0.72 M solution concentration, 2200 rpm spin speed, 90 second at 80°C pre-anneal in N_2, 20 minute at 150°C main anneal in air, and 11°C DP water content during annealing.

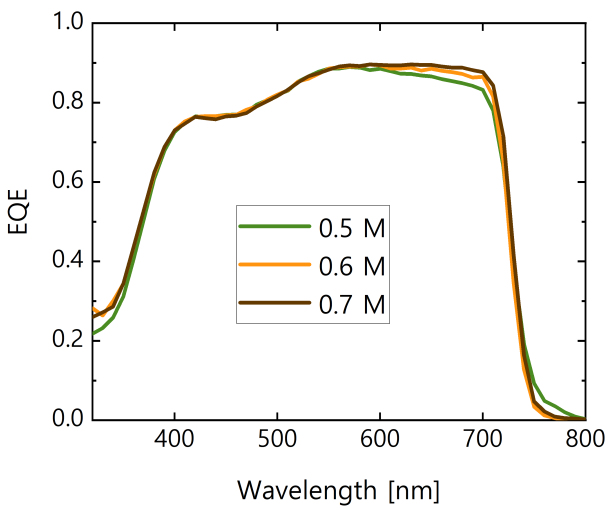

Figure 4.6 – EQE measurements for perovskite on c-Si made with varied SP solution concentrations. Cells were made on symmetric SHJ with the 1.43 cm^2 design, and no anti-reflective coating. The loss in the 400-550 nm range is attributed to C_{60} absorption, as these cells were made with a 20.4 nm layer. Cells and measurements courtesy of Dr. Xin-Yu Chin.

4.2.2 Tuning of the IZO Front Contact

Another aspect of the tandem fabrication that was developed during this thesis was the IZO front contact. This is most relevant to the J_{SC} of the cell, and therefore is included with the rest of the J_{SC} optimization discussion. This layer is deposited by radio-frequency (RF) sputtering in a gaseous environment (Ar and O_2). The thickness can be tuned by the deposition power and time, which in turn affects the absorption and sheet resistance. Additionally, the O_2 content of the gas mixture can be controlled, with more O_2 leading to more transparent and resistive layers. This material is attractive for tandems, as IZO can be made with excellent transparency in the infrared [167]. However, the previously optimized recipe was found to be non-ideal in terms of the balance between absorptive and resistive losses. We instead found that removing the O_2 entirely was preferable for a number of reasons.

The first change due to O_2 removal was the observed shift in the layer's absorptance (figure 4.7). The absorptance decreased in the 300-500 nm range, and increased in the 500-1200 nm range. This did not majorly change the total absorption, but it did shift the "usable light" spectrum (as defined in figure 4.4). With fewer photons available in the c-Si absorption range and more in the perovskite range, the top-cell receives more J_{ph} and can achieve current-matching with a still higher E_g, or promote bottom-limited conditions with the same E_g. Upon inserting both cases into the analysis presented in figure 4.4, the E_g which perfectly splits the spectrum increases by 10 meV in the case of IZO without O_2, relative to the "old" recipe (the figure shows the "optimized" recipe).

The second effect of O_2 removal was that the sheet resistance of the layer improves significantly (table 4.1). The trade-off between absorptive and resistive losses is complex, and depends on the front metal grid design, operating resistance, current-matching conditions, and the surface texture. Another doctoral student, Deniz Türkay, performed simulations of

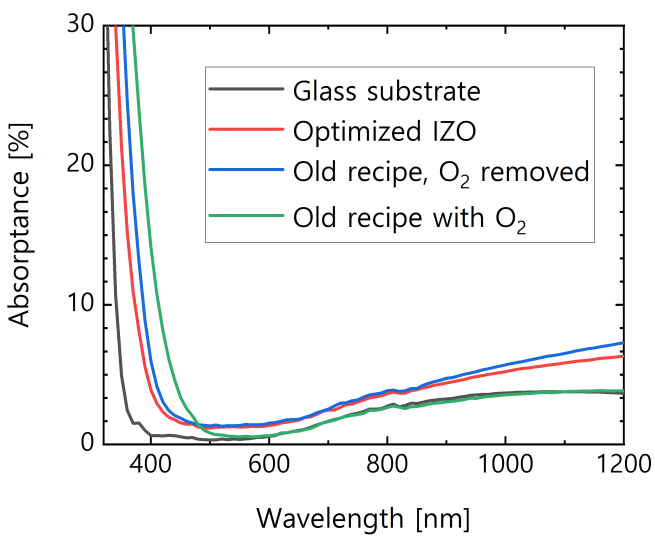

Figure 4.7 – Absorptance curves measured for varied IZO layers deposited on glass. The "old" recipe refers to that which was used in previous theses [62], [63]. The other recipes were based off of this, modified by changing the RF sputtering power and time, and the O_2 gas content. Absorptance data was obtained from measuring the transmitted and reflected intensity of IZO layers on glass, measured from the layer side.

IZO recipe	Abs. loss in perovskite range [mA/cm^2]	Abs. loss in c-Si range [mA/cm^2]	Total abs. loss [mA/cm^2]	Sheet resistance [$\Omega/\square$]
Old + O_2	0.56	0.00	0.56	345
Old - O_2	0.49	0.40	0.89	47
Optimized	0.35	0.31	0.66	67

Table 4.1 – Absorptive and resistive performance of different IZO layers. Absorption loss determined by integrating the curves shown in figure 4.7, minus the glass curve, against the AM1.5G spectrum, either from 320-760 nm (perovskite range) or from 760-1200 nm (c-Si range). Sheet resistance measured via four-point probe method.

the front IZO/Ag grid using the Griddler software from PV-Tech [238], which directed us to choosing low-absorption high-resistance layers and developing an optimum. Between the "Old recipe with O_2" and the same without O_2, the parasitic absorption increases by 60% while the sheet resistance decreases by 86%. Sheet resistance depends inversely on layer thickness ($R_{sheet} \propto \frac{1}{Thick.}$), while absorption follows thickness according to a negative exponent ($Abs. \propto e^{-\alpha * Thick.}$). Thus increasing the layer thickness of the old IZO layer with O_2 enough to match the sheet resistance without O_2 would also increase the absorption by nearly 500%, to the point that it is significantly more than the IZO layer without O_2. Thus, we chose to follow the path of low-absorption high-resistance layers, in agreement with the simulations. We further developed the IZO recipe based on sputtering power and time, all without O_2. This led to an optimized recipe (10 minutes at 70 W, 10 minutes at 50 W RF power, roughly 80 nm on texture) that was used in our tandems, and is described in figure 4.7 and table 4.1.

Results - Increasing Tandem J_{SC}

In this section we detailed the efforts made towards maximizing the J_{ph} of our tandem stack. This included increasing the perovskite thickness, increasing the E_g, and improving the front IZO layer. We were able to fabricate a 50% thicker perovskite layer through tuning of the various deposition parameters of the hybrid PVD/SP method, including template thickness, spin concentration, spin speed, a pre-anneal, and the annealing DP. The resulting perovskite layers are shown in figure 4.8. The old recipe gave a 450 nm perovskite (measured normal to the c-Si pyramid face) which was tuned to 1.64 eV to achieve current-matching, and the new recipe gives a 700 nm perovskite which is tuned to 1.70 eV to achieve current-matching. Outside of the perovskite, we removed O_2 gas from the IZO sputtering chamber and further tuned the deposition power and time to reduce this layer's parasitic absorption in the top-cell spectrum by 35%. Together these improvements increased the top-cell J_{ph} of our tandems, and enabled us to meet the current-matching requirement of monolithic tandem architectures with a higher E_g perovskite. The cell results of this optimization can be seen in figure 4.9a. The cell shown here had a J_{SC} of 20.0 mA/cm^2 and a V_{OC} of 1.83 V when measuring a full JV curve under 1-sun illumination. We compare this same result to the best tandem EQE obtained prior to this thesis work, which used the old perovskite recipe and un-optimized IZO, in figure

4.9b. The cell in question had a J_{SC} of 19.7 mA/cm^2 and a V_{OC} of 1.76 V when measured under the same conditions. Specifically, figure 4.9b shows how the absorption in the c-Si above the perovskite bandgap is reduced from the old to new recipes, and the corresponding E_g increase of the top-cell. From this baseline, we were then able to investigate and improve other aspects of the tandem cells, towards reaching higher efficiencies.

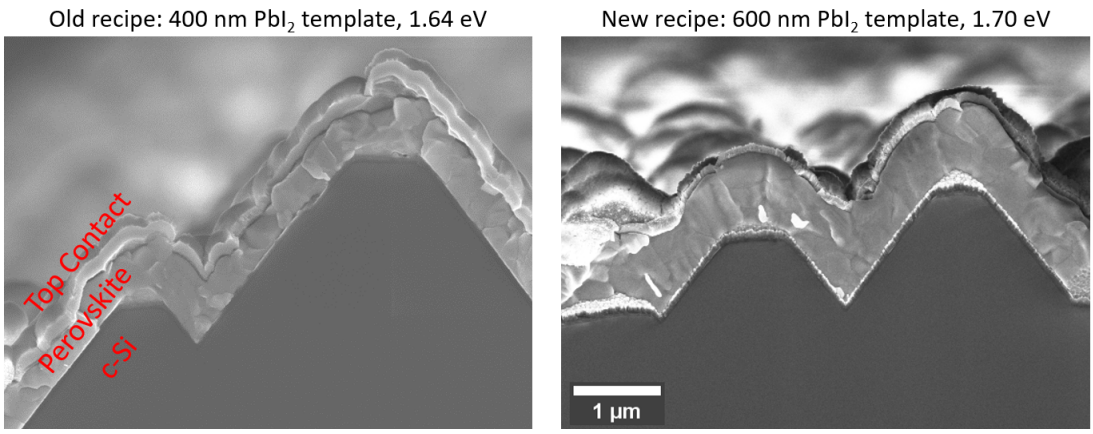

Figure 4.8 – SEM side-view images of perovskite top-cells made with the old and new recipes. The old recipe used a template with 400 nm PbI_2 (measured flat), a 513 mM solution of 1:3 FAI:FABr, and was spun at 3000 rpm. This gave a 450 nm perovskite layer with E_g = 1.64 eV. The new recipe used a template with 600 nm PbI_2 (measured flat), a 720 mM solution of 1:2 FAI:FABr, was spun at 2200 rpm, and had a 90 second pre-anneal at 80°C in N_2. This gave a 700 nm perovskite layer with E_g = 1.70 eV. In both cases, the template included 10%vol CsBr, the solvent was ethanol, and the main annealing was 20 minutes at 150°C in air. Images are to the same scale.

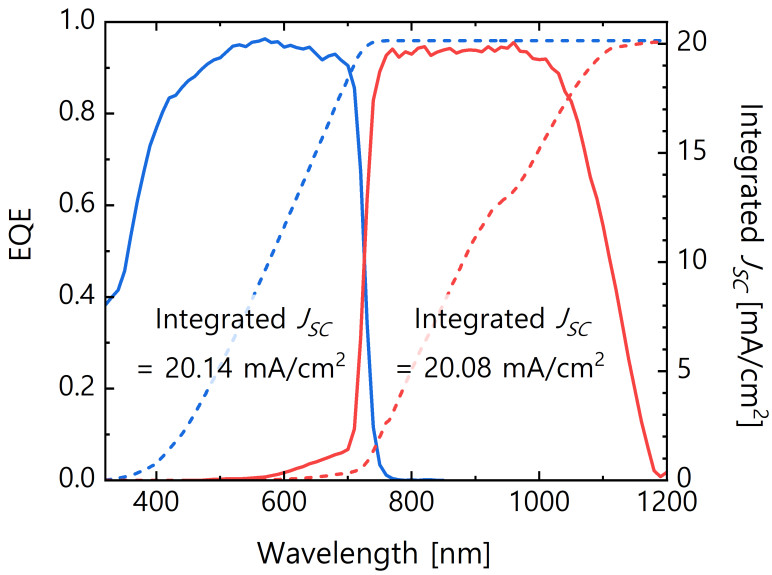

(a)

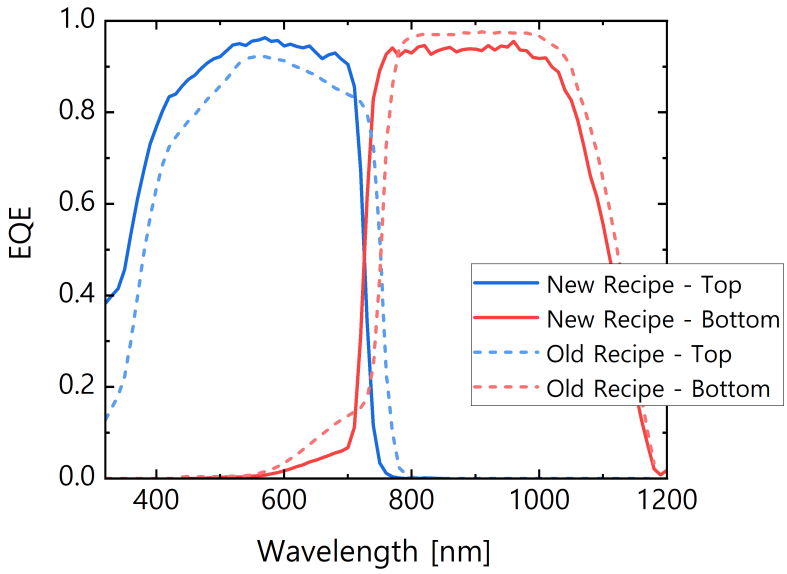

(b)

Figure 4.9 – EQE measurement for a perovskite/c-Si tandem with optimized high-E_g top-cell. (a) shows the highest EQE measured for an optimized tandem cell, along with their integrated J_{SC}. (b) shows the comparison of this EQE to that of a champion tandem cell from prior to this thesis work. The point where the two curves cross eachother was shifted 50 meV higher, while keeping the same current-matching condition. The loss in the "new recipe" bottom-cell comes from increased parasitic absorption in the IZO (table 4.1) and reduction of the c-Si wafer thickness from 240 µm to 180 µm.

4.3 Increasing Tandem V_{OC} via Interface Tuning

As discussed previously in section 2.3.1, the HTL used below the perovskite (in p-i-n polarity cells) can affect PSC performance, most notably the device voltage. In this section, we examine the same parameters and how they apply to tandem cell operation. We primarily worked with TaTm and SAMs, which are upgrades to Spiro-TTB in terms of performance. Recalling the PL results shown in figure 2.15, both TaTm and SAM (Me-4PACz for this particular measurement) improved the QFLS slightly over that of the bare perovskite. The difference between the samples was below the variance in the measurement, however. So determining which material was better for cells had to be performed as such, in cells. Further measurements of SAMs and a comparison of different SAM options are shown in section B.8. We found that the differences in performance were minimal, and thus will refer to them collectively as SAM, specifying where necessary. As SAM materials require an oxide layer to bind to [56], tandems with SAM require an extra deposition of a thin sputtered ITO layer on top of the nc-Si recombination junction (roughly 7 nm, as described in section 4.1), while the TaTm (5 nm) is thermally evaporated directly on the recombination junction. The resulting cell performance is shown in figure 4.10.

The results show that TaTm has a slight improvement in V_{OC} over SAM, with the difference in average values (37 mV) corresponding to a 0.47% absolute gain in efficiency. This is far more than the gain predicted from the previous PL measurements (2.4 meV, figure 2.15). We attribute this difference to the fact that the PL measurement used a microscope objective to focus the illumination and collect from a larger étendue. Light has a multitude of effects on perovskites, but the act of focusing 1-sun intensity on a small spot while the surrounding

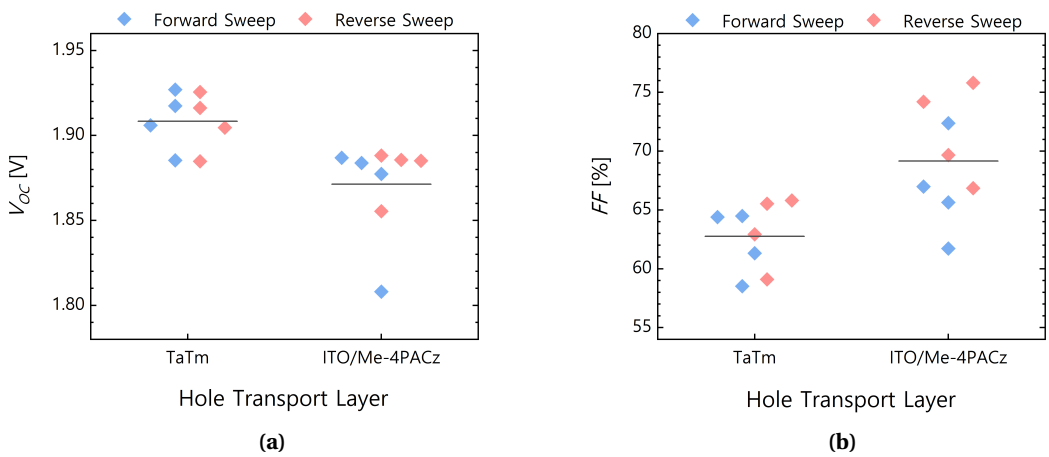

Figure 4.10 – Cell performance for perovskite/c-Si tandems made with bulk polymer or molecular monolayer HTLs. Samples were prepared in parallel with the same perovskite and bottom-cells from the same wafers. In either case, the noted HTL stack was deposited directly on the nc-Si recombination junction, and immediately followed by the PVD/SP perovskite process. The TaTm layer was 5 nm, the SAM used was Me-4PACz, and the 1.43 cm^2 front electrode design was used. Cells and measurements courtesy of Dr. Xin-Yu Chin.

perovskite is not illuminated is known to cause significant local modification to the perovskite [202], [203]. Ions diffuse away over micrometer scales, the material is put under non-uniform stress, and overall the perovskite in the illumination spot is not the same physical system as when it is uniformly illuminated [202], [203]. Thus, it is reasonable that the perovskite does not behave the same in the case of locally-illuminated PL measurement and the full-area illuminated PLQY and V_{OC} measurements. Inversely to the V_{OC}, the FF is higher in the cells with SAM, with the difference in average values (6.4%) corresponding to a 2.36% absolute gain in efficiency.

This change likely comes from the transport properties of TaTm versus SAM. Current state-of-the-art bulk polymer transport layers are known to be just on the edge of limiting cell efficiency due to low mobility [168], [169]. For example, PTAA[4] is commonly used in flat single junction PSC due to high performance. When deposited above 10 nm thickness, it sharply reduces cell FF unless alloyed with a p-type additive[5] [169]. Even at these thicknesses, fitting measured JV data to simulations estimates the best mobility values for the PTAA layer to be 10^2 lower than that of pure C_{60} (1.5×10^{-4} cm^2/(Vs) and 1.0×10^{-2} cm^2/(Vs)), and simulated FF dropped nearly 10% absolute when lowering another 10^1 [168]. Specifically to the TaTm that we used (claimed 4×10^{-3} cm^2/(Vs) from a supplier website, Dyenamo [239]), it has been shown to require alloying, which improved conductivity 30x and FF by nearly 20% absolute upon increasing p-type additive concentration from 3% weight to 11% weight (no 0% reference reported) [163]. This is compared to SAMs, which do not have reported mobility values, as the molecular monolayer is so thin that it does not truly "transport" the charges rather than selectively pass charges to the TCO [56]. Typical mobility values for ITO films are in the range of 30 - 50 cm^2/(Vs). Thus, we conclude that the difference in FF between tandems with TaTm and SAM comes from this difference in the two materials' relative abilities to conduct charges through the device. As evidence for this, the R_{OC} of the TaTm cells was 26.5 Ωcm^2 compared to 9.2 Ωcm^2 for the SAM cells[6].

We note here that we choose to minimize transport losses by using thin layers of TaTm rather than trying to alloy it. Alloying has been successful in the studies cited above [163], [168], [169], but in each case required layers with sufficient thickness as to correctly control the HTL:additive ratio (50 nm in the case of TaTm). A cost forecast for each of these layers was done in section 1.2.3, and determined that 50 nm layers would totally consume the cost increase justified by the higher efficiency of tandems. Thus we choose to continue with thin CTL layers and SAMs.

[4] Chemical name: poly[bis(4-phenyl)(2,4,6-trimethylphenyl)amine]

[5] The term alloying is used instead of doping, due to the quantity of new material being high enough that it is more a mix of two materials than an addition. Doping generally refers to quantities on the order of 10^{-3} molar concentration or less.

[6] This is unusually high, which we attribute to an un-optimized SnO_2 layer at the time of experiment. We discuss the R_{OC} of our cells in the following section (4.4)

Overall, we conclude that TaTm is slightly better than SAM for reducing interfacial recombination, but that ultimately SAM is better for cells due to better charge transport and the resulting higher FF. One of the primary distinctions between the two HTLs is the thickness of the layer. Thinner layers of TaTm would reduce their transport losses, but evaporated materials do not form a continuous layer when deposited below a certain thickness [240]. Before this, the surface coverage is less than 100% and the layer is shunted. Specifically to our machines and materials, many trials were run to determine the minimum necessary thickness of C_{60} in order to reduce its parasitic absorption. We found that J_{SC} does improve directly with C_{60} thickness reduction, but that V_{OC} drops as well when going below 5 nm. We attribute this to the C_{60} being shunted, and thus treat 5 nm as the processing limit for layer thickness (which becomes 8.5 nm when depositing on c-Si pyramids due to the 1.7 geometrical factor). This therefore disallows deposition of TaTm with thickness similar to molecular monolayers.

This limit still leaves another possibility. Having a < 5 nm TaTm layer on top of SAM would bypass the losses due to HTL shunting, since the gaps in the TaTm would only expose another HTL instead of the recombination junction. This way, the areas with TaTm can improve interface quality over SAM to raise the cell V_{OC}, while the thickness can remain low enough that its mobility is not a hindrance to FF. Thus we created cells with the structures shown in figure 4.11. These compared the previous conditions of SAM and 5 nm TaTm against a bilayer of SAM and 1 nm TaTm (thus 8.5 nm and 1.7 nm TaTm, measured flat). JV results are shown in figure 4.12. The main hypothesis of this experiment proved to be true, but not by a big

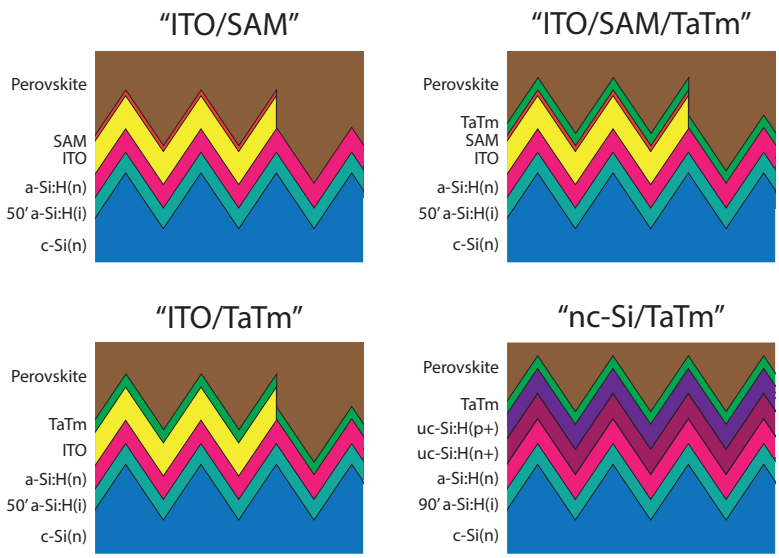

Figure 4.11 – Diagram of hybrid recombination junction / HTL stacks which were tested. The front contact of the bottom-cell used an a-Si:H(i) layer that was deposited for either 50 or 70 seconds. The thicker layer is used to protect the c-Si from damages from the nc-Si:H recombination junction deposition. The TaTm layer thickness was 5 nm measured normal to the c-Si pyramid face when deposited alone, and 1 nm for the SAM/TaTm bilayer.

enough margin to improve the overall efficiency. The plain SAM and TaTm cells preserved the V_{OC} - FF trend that was previously observed. When combined into a bilayer, there was much overlap between the SAM and SAM/TaTm conditions, but the average V_{OC} improved over SAM alone while the average FF dropped. We rationalize this as The TaTm reducing recombination losses relative to SAM at the perovskite/HTL interface, but also increasing transport losses (despite the minimal thickness). But overall, this produced three conditions with comparable efficiency spreads, and no solution to combine the best of both materials with regards to FF and V_{OC}.

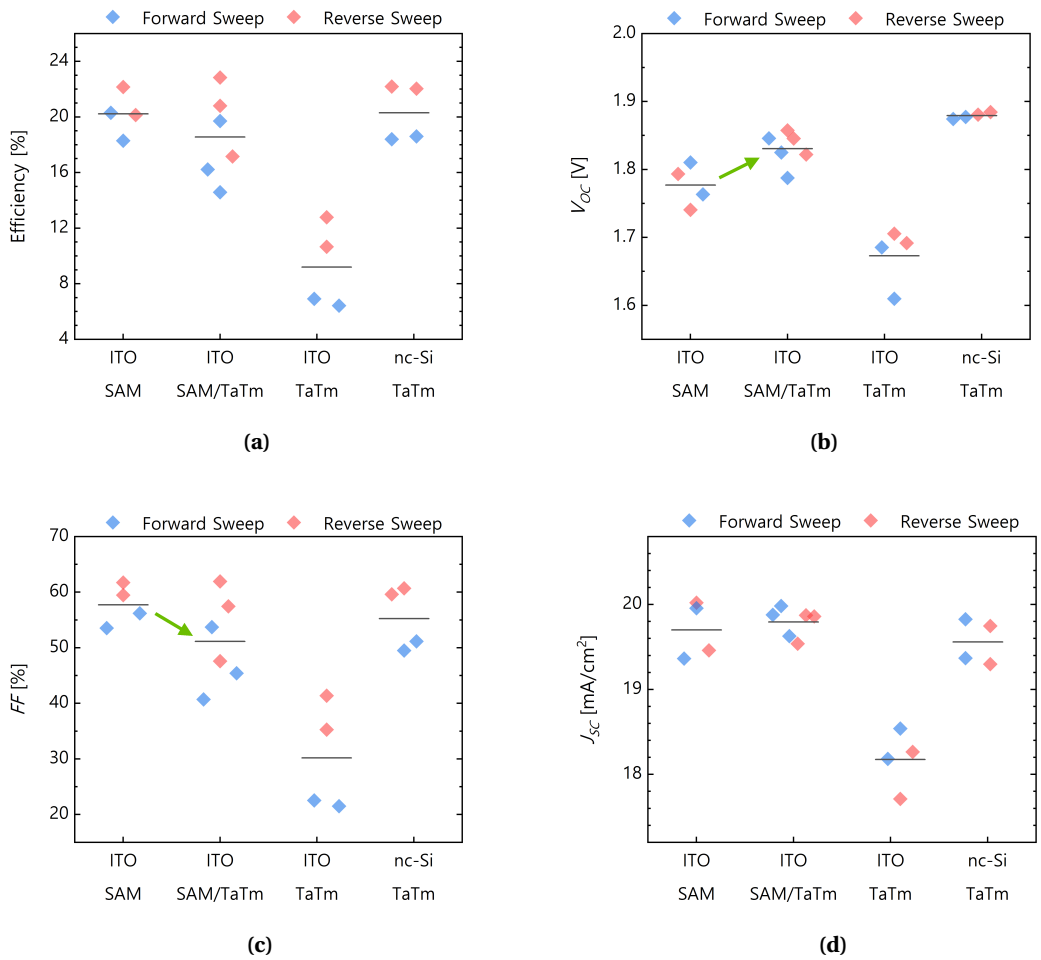

Figure 4.12 – Cell performance of perovskite/c-Si tandems prepared with varied HTL stacks. Bottom-cells were prepared with or without the nc-Si recombination junction. In the case without the junction, a thin ITO was deposited (7 nm). TaTm (5 nm) was evaporated onto some bottom-cells of both conditions, and MeO-2PACz was deposited on the remaining cells with ITO. Some of the SAM cells then received a TaTm evaporation (1 nm), before all cells were finished in parallel with the same perovskite and top contact stack. The 1.43 cm^2 front electrode design was used.

This left us with three seemingly equal options, depending on which JV parameter we wanted to maximize. Still, the two materials are different enough that their behavior is not identical when viewed from a wider perspective. In the previous experiment, we also included a sample of TaTm directly on the same ITO recombination junction as the SAM. It performed worse in every category, despite only including layers that were successful in the other conditions. In the end, the problem of the ITO/TaTm cells was not of recombination or transport, but rather of material compatibility. We know from experience that bulk HTL molecules (in this case Spiro-TTB [62], [149]) have glass transition temperatures around 150°C [216] and dewet from ITO surfaces to "melt" down the sides of c-Si pyramids, resulting in concentrations in the valleys and uncovered surfaces above. This problem was reduced by using a nc-Si recombination junction, which is less prone to dewetting with bulk polymer HTLs [62], [149].

To observe the dewetting directly, we do SEM on TaTm layers coated onto different surfaces, on c-Si pyramids. This was done for ITO and the nc-Si recombination junction, and the samples were either left as-deposited or annealed for the standard 20 minutes at 150°C (in N_2), then observed top-down in SEM. The resulting images are shown in figure 4.13. The dewetting on ITO is clearly observed in the exposed ITO (light areas) and "melted" TaTm in the valleys (dark areas). The effect is still present, albeit less severely, on the nc-Si layer. Thick dark areas fill all of the valleys, and the pyramid surfaces are not uniformly covered. Despite this effect,

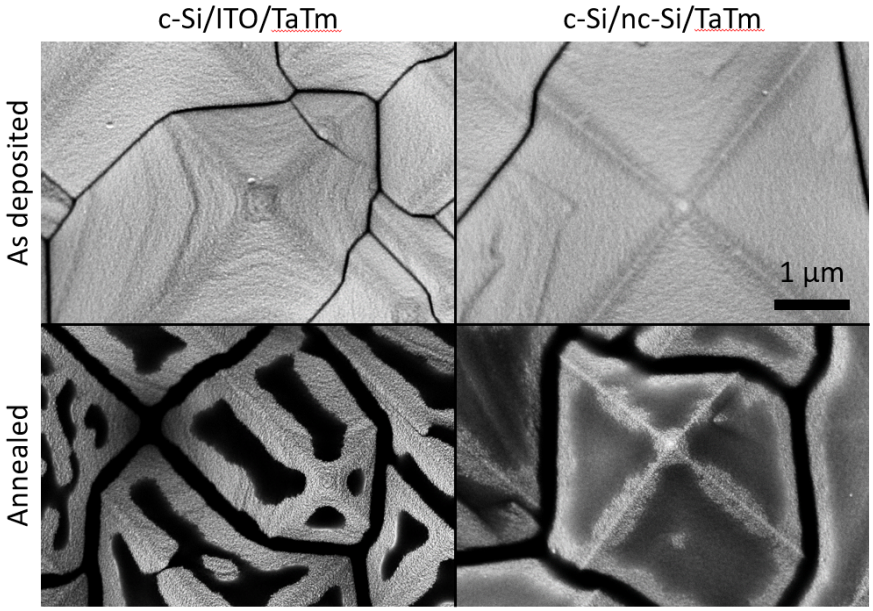

Figure 4.13 – TaTm temperature stability on c-Si pyramids as viewed in SEM. 12 nm of TaTm was evaporated onto textured c-Si substrates either with the nc-Si recombination junction or a standard ITO on the top surface. They were then annealed at 150°C in N_2 for 20 minutes. Top-down SEM was performed on annealed and un-annealed samples of each layer stack. The thick black lines in the valleys between pyramids is attributed to accumulation of the TaTm which dewetted from the pyramid faces. Samples courtesy of Dr. Xin-Yu Chin, measurements courtesy of Dr. Quentin Jeangros.

the nc-Si/TaTm tandems still perform as well as observed. But still, the incomplete surface coverage and non-uniform thickness of TaTm on nc-Si could add some explanation to the lower FF in such cells.

Results - Increasing Tandem V_{OC}

We have demonstrated multiple cell designs with similar efficiency, but different specific performance. Tandems made with ITO/SAM as HTL have better FF due to their charge mobility, relative to TaTm. But TaTm reliably gives higher V_{OC}, meaning that SAM materials do not form an ideal interface. The observed gains in FF with SAM translated to a larger efficiency gain than the V_{OC} gains of TaTm, but still less voltage than we knew possible from our perovskite. We thus tried to combine the two into a bilayer, expecting a sufficiently thin TaTm layer to provide an improved interface while still capitalizing on the complete surface coverage and efficient extraction of the SAM. This did improve the SAM cells' V_{OC}, but at the expense of FF, giving the same overall efficiency. Thus, there was no cell design that displayed the best V_{OC} and FF simultaneously, but still we succeeded to make cells with V_{OC} values above 1.9 V. The JV curve with the in-house record for highest voltage is shown in figure 4.14, along with another high-voltage cell that is less hysteric.

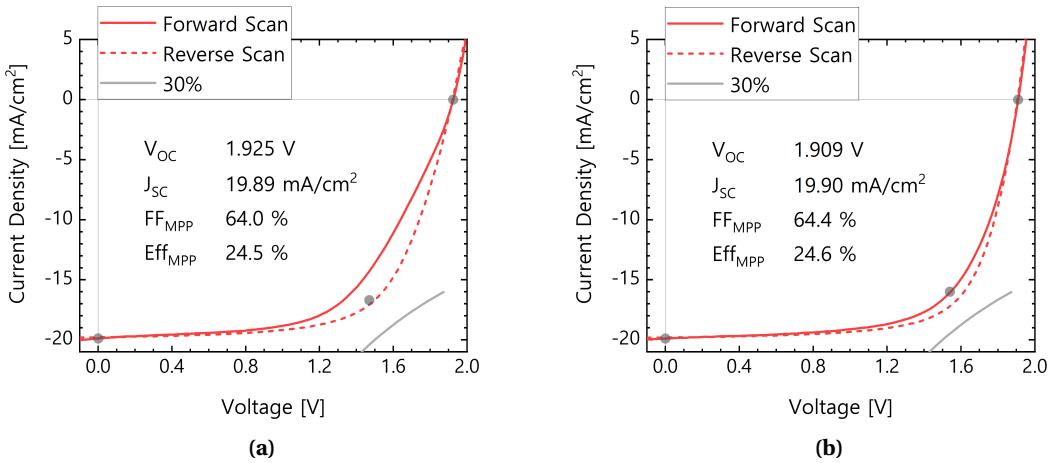

Figure 4.14 – *JV* curves for perovskite/c-Si tandem cells with high V_{OC}. (a) The cell with the best V_{OC} value obtained, but with significant hysteresis. (b) Another cell with high V_{OC} but less hysteresis. The cells were produced in parallel, with a nc-Si recombination junction, 5 nm of TaTm as HTL, the same perovskite, and the 1.43 cm^2 front electrode design. The measured V_{OC} and J_{SC} values are marked, along with the MPP obtained during tracking. The curve in the bottom right represents the threshold of operating points which would give >30% efficiency.

4.4 Improving Tandem Fill-Factors Through Sub-Cell Optimization

From the final results shown in the previous sections (figures 4.9 and 4.14), the J_{SC} and V_{OC} achievable in cells means that 30% cells would require a FF of only 78%. This has been demonstrated in single junction PVD/SP cells already (section 2.4.2), and of course in SHJ, so it should certainly be possible in tandems. We can even expect tandem FF values to be higher than those of the individual sub-cells due to the fact that the recombination junction releases the need for lateral current transport and the series resistance that comes with it. But still, the determining factors of tandem FF are numerous, and depend on multiple aspects of each sub-cell [152]. Thus the task of understanding the source of losses in our cells and addressing them can be complex.

The first step is to understand where the problem is coming from. As stated above, either sub-cell can cause reductions to the overall FF, but there are many relevant factors. Due to SHJ commonly achieving FF of 83 - 84% and thin/flat single junction perovskites only barely getting to 80%, we expect the better sub-cell in our tandems to be the bottom-cell. One way to probe the source of FF loss is to exploit the effect of sub-cell mismatch. If the operating current of the two cells is not equal, then the sub-cell which outputs more current over-saturates the recombination junction with its charge type, meaning the overall charge flow is set by how well the limiting sub-cell can extract. This effect can be exploited to determine the relative performance of the two sub-cells. In practice, we can induce such mismatch by shifting the amount of light entering each sub-cell. Then we observe the change in tandem FF with each in limiting condition to show the relative performance of the sub-cells.

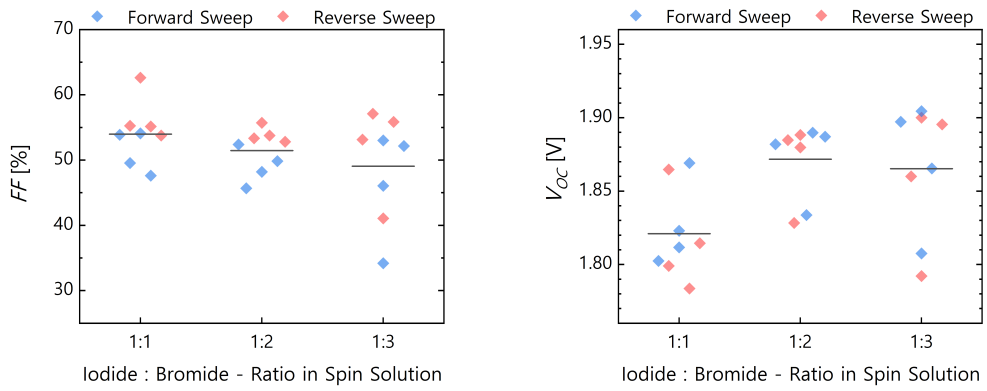

Figure 4.15 – Performance of perovskite/c-Si tandem cells with varied iodide:bromide ratios in the perovskite absorber. Cells were made on bottom cells from the same wafers, and all other details of fabrication were held constant. The bandgaps extracted from EQE were 1.68, 1.70, and 1.72 eV (in order of appearance in these graphs). The 1.43 cm^2 front electrode design was used. Cells and measurements by Dr. Xin-Yu Chin.

First, we varied the E_g of the perovskite by changing the halide ratio in the perovskite spin-coating solution. Increasing the perovskite E_g reduces J_{ph} and makes the top-cell limiting, and the inverse for lowering the E_g. The results are shown in figure 4.15. We have current matching with a 1:2 I:Br ratio (1.70 eV), as this was the case in the champion EQE of figure 4.9. Therefore, the 1:3 ratio (1.72 eV) makes the top-cell limiting and the 1:1 ratio (1.68 eV) gives the c-Si E_g larger influence. We see from the FF results in 4.15a that the FF changes negligibly in either case, other than one high outlier. Generally, there is so much overlap between the conditions that the changes in average value are not statistically significant. Thus neither sub-cell stands out as being significantly superior. We therefore move on to changing the illumination spectrum to favor either sub-cell in current-matched tandems, as this gives a larger possible range of induced mismatch. This method also avoids the potential confounding effects of using different halide ratios, which give different materials and thus may modify top-cell performance.

We varied the sub-cell current mismatch by switching to another illumination setup from the halogen/Xe double lamp setup used throughout this work, to a homemade system based on multiple smaller halogen lamps (providing infrared and long-wavelength visible) and many light emitting diodes (providing visible and ultraviolet). The spectral intensity was tuned based on the measured tandem EQE, which allowed us to determine how much current was being produced in each sub-cell according to the voltage sent to each illumination source. We then illuminated with a series of different spectra, each totaling the same 1-sun intensity, and measured a JV curve under each. The FF values extracted from the reverse sweeps are shown in figure 4.16. These data display a downward trend when shifting the current from the bottom-cell to the top-cell. This means the tandem had higher FF when the perovskite sub-cell was limiting, and lower FF when the c-Si cell was limiting. Thus in this case the top-cell was contributing more FF than the bottom-cell, and the overall tandem FF was limited by the c-Si performance.

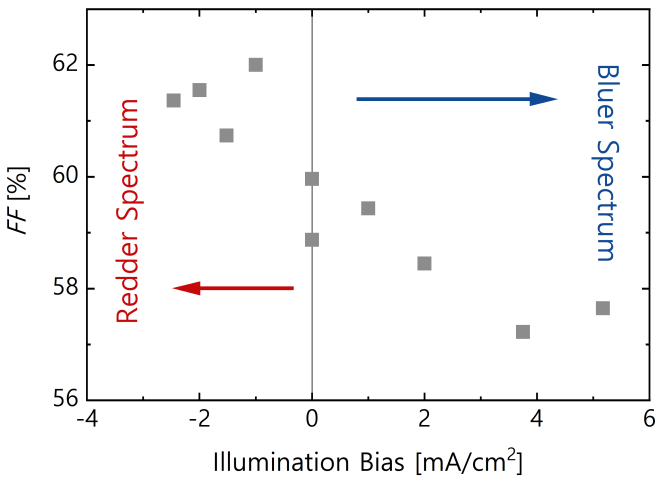

Figure 4.16 – *FF* measurements from a single tandem cell measured with spectral bias of current to one sub-cell or the other. Points show the FF extracted from the reverse-direction JV sweep. Measurements were made in sequence from red to blue with one balanced spectrum taken at the beginning and end. The tandem cell was measured to be in the current-matching condition from EQE, and the spectrum was shifted via a mix of halogen bulbs and LEDs. The 1.43 cm^2 front electrode design was used.

4.4.1 Eliminating Processing Damages in c-Si Bottom-Cells

Before discussing the scientific results obtained, we must address the progression and distribution of work towards this goal. This is the first period of the thesis with c-Si as the focus. A Ph.D. student (Deniz Türkay) was hired around this time with the specific goal of developing SHJ for use in tandems. Thus after about three months of my work, the responsibility of this project was passed to him. Being uniquely occupied with the task outlined here, Deniz performed many experiments and was successful in improving performance. The entirety of his work will not be shown here, but rather all of my work will be shown, and his further advancements will be summarized at the end.

The first check made in order to understand bottom-cell FF losses was to compare them to standard SHJ cells produced for single junction use. This is not a perfect comparison however, since the production of their cells and our bottom-cells differ in a few key ways which affect FF. For reference, the process flow for our bottom-cells is given in figure 4.2. Most notably, they do not cut their wafers, they use a different cell size, they use a different metallization geometry, and their front Ag fingers are screen printed. Images of the cell and metallization designs are shown in figure 4.3. Their different metallization design and screen printed Ag fingers (several µm thickness) are important for single junction SHJ, since they must extract twice the current at a quarter of the operating resistance, compared to tandems. The tandem front grid design uses thinner (0.3 - 0.4 µm, as measured on flat) evaporated Ag fingers which are spaced further apart. A side effect of this is that we artificially lower the FF of our bottom-cells when we

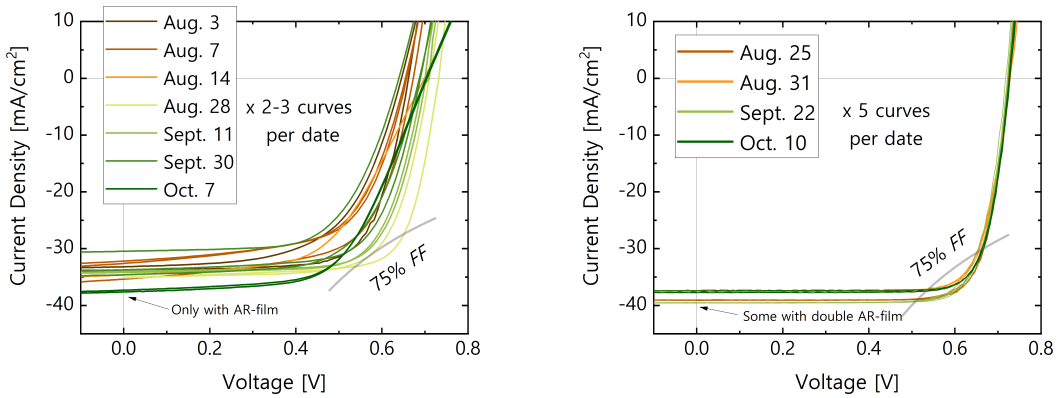

(a) Bottom-cells measured as single junctions

(b) Standard single junction SHJ

Figure 4.17 – Comparison of SHJ cells which were processed as bottom-cells and those completed without extra processing, over time. (a) JV of SHJ cells that were processed as if to use as bottom-cells in tandems. (b) JV of SHJ cells designed for single junction use. Each batch was processed separately, from the same stock of c-Si wafers. The bottom-cells used the 1.43 cm^2 cell design and were each on a unique 25 mm x 25 mm cleaved square. The SHJ were processed without a recombination junction, used a 4 cm^2 cell area, and were all five on the same unbroken wafer. The certain groups with notably higher J_{SC} are explained by the use of a single- or double-layer anti-reflective coating.

put the tandem front grid directly on the bottom cells to measure them as single junctions. Thus overall, the direct comparison of SHJ designed to be bottom-cells and SHJ designed to be single junctions is not 1:1. But still we can juxtapose the two cases and evaluate the differences with these effects in mind.

This was done for cells produced through the end of summer - early fall of 2020, and the results are shown in figure 4.17. The most pronounced difference between the two cases is the overall variance. In order to explain the variance, we will sort the sources of loss into two groups. First, there is the resistive losses due to the different front grids, and second there is the recombination losses due to material damage and edge effects. For the front grid effect, this includes the changed TCO, finger geometry, and finger thickness between the designs (figure 4.3). The collective effect of these elements can be summarized in the series resistance (or open-circuit resistance, R_{OC}). Series resistance affects the operational FF according to $FF_{real} = FF_0(1 - \frac{R_{OC}}{R_C})$, where R_C is the characteristic (operating) resistance and FF_0 is the "innate FF" before resistive losses. The R_{OC} measured from the single junction SHJ of figure 4.17b was in the range of 1 - 1.5 Ωcm^2, while the R_{OC} of the bottom-cells in figure 4.17a was typically 2 - 3 Ωcm^2. From this we can calculate that the standard SHJ lose 6 - 10% relative FF and the bottom-cells lose 12 - 18% relative[7], based on an operating resistance of 16 - 17 Ωm^2. This partially explains the lower FF values of the bottom-cells overall, but not the variance between samples nor the variance of V_{OC} and J_{SC} in figure 4.17a.

We therefore look to material damage and edge effects to try and explain the variance. Specifically we investigated the additional processing steps which the SHJ go through in preparation for use as bottom-cells (figure 4.2). These steps include the laser scribe and cleaving discussed above, but also the processing of samples with perovskite deposition equipment, samples sliding on the hotplate during annealing, and the additional manipulation during this processing. Any process in which the c-Si wafers are touched could be a source of mechanical damages to the c-Si. These damages could reduce material quality and increase recombination in the bottom-cell, potentially leading to lower and varied performance of cells as was observed relative to normal SHJ.

The first process step to be examined was the laser scribe and cleave (steps 7 - 8 in figure 4.2). Here, the round 100 mm wafer is laser-scribed with lines that enable facile cleaving by hand into 25mm x 25 mm squares. We theorized that the dopant type of the c-Si wafer would be relevant at this point, as it determines if the lasering is on the side of the cell with the p-n junction. Due to the dust created with the laser scribe, we always laser on the rear of the wafer to avoid dust particles causing shunting of the top-cell, and we always perform the scribing after the PE-CVD processing of the a-Si:H layers, due to the dust not being compatible with the cleanliness requirements of the PE-CVD machine. Thus, the lasering always happens on a complete SHJ, and always on the rear side. Further, this is always the p-doped contact

[7] This is a significant source of loss for bottom-cells when measured alone, but rather insignificant as a R_{OC} value for tandems. Tandems produce half the current at more than double the voltage, leading to operating resistances in the range of 75 - 80 Ω. Thus the same R_{OC} values in tandems would only produce 2.5 - 4% relative loss.

since the bottom-cell orientation is fixed to match that of the top-cell. Thus n-type wafers would have the main p-n junction at the rear of the cell where the lasering occurs, while p-type wafers would have their junction "protected" at the front.

We tested this by measuring the charge lifetime of a p-type and n-type wafer at each stage in the process. These data are shown in figure 4.18a. We see that indeed the n-type wafer (with junction at rear) is more damaged by the laser than the p-type. Upon cleaving, the lifetime of the nine small square pieces varied more for the n-type than p-type. Overall, the n-type wafer suffered more, indicating that the laser scribe does indeed damage the junction, but the higher initial lifetime of n-type wafers versus p-type meant that the final lifetime was higher for rear-junction bottom-cells regardless of greater laser damages. This lower lifetime is a consequence of the boron-oxygen defects that are endemic to p-type wafers due to their dopant [241], and is thus realistically unavoidable.

In order to examine the edge effects of the 25 mm x 25 mm cleaved wafers, we further processed the small squares of figure 4.18a into single junction cells with differently shaped active areas. The cell area was kept the same at 1.02 cm^2, but the dimensions were changed from a 1:1 square to a 3:1 rectangle. This tests if proximity to the wafer edge affects performance. The results of this test are shown in figure 4.18b, for both the p-type and n-type wafer pieces. The n-type wafers produce slightly higher *FF* in line with their higher lifetime, but overall both the active area dimensions and wafer doping type produce changes well within the spread observed in figure 4.17. Thus we concluded that proximity to the wafer edge was not the dominant loss mechanism.

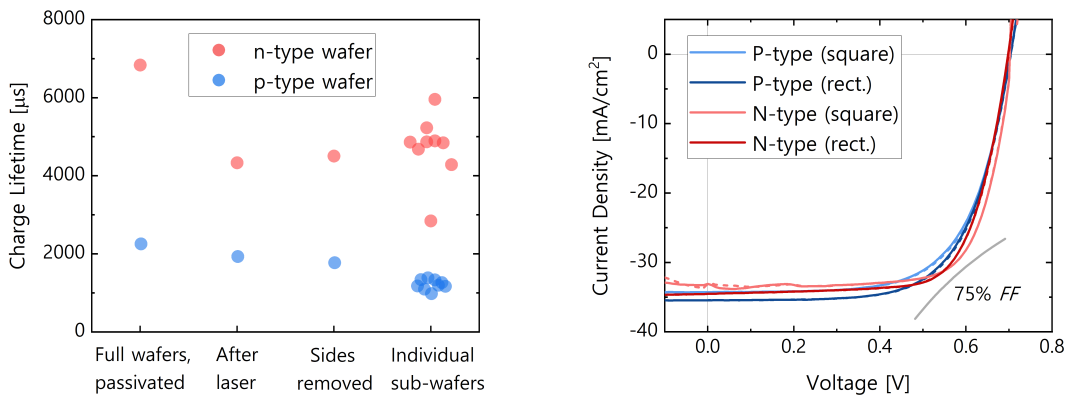

(a) **(b)**

Figure 4.18 – Lifetime measurements and *JV* curves for p- and n-type wafers processed as bottom-cells for tandems. Two wafers of opposite doping types were co-processed according to the recipe for tandems, and finished as bottom-cells without a perovskite. (a) shows the lifetime measurements of the wafers initially, after laser scribing, after cleaving the four edges, and of each resulting 25 mm x 25 mm sub-wafer. (b) shows the JV curves for p- and n- type cells processed with square (1:1) or rectangular (3:1) front electrode designs, with the same 1.02 cm^2 cell area.

To isolate the effect of the laser damage from other damages which confound cell data, we took PL intensity images of an n-type SHJ cell before and after the standard laser scribe. These results are shown in figure 4.19. Excitation was scaled to 7% of 1-sun intensity, to mimic the carrier concentration at MPP. The PL loss along the laser lines is clear, but upon relating the two images to find relative loss, we see that the damage does not extend far into the active area. For reference, outlines of the cell area defined by our two top-cell metallization designs (1.02 and 1.43 cm^2) are included as black squares in figure 4.19c. The PL loss in these areas is nearly zero, and only reaches close to 20% at the very edges of the larger cell design. Given that cell V_{OC} varies with the logarithm of PL intensity, this is a negligible loss. Thus, we conclude that the laser damage and edge effects are not significant sources of the overall FF losses observed.

This leaves general damage from sample manipulation as the suspect for causing the losses. We cannot change the fact that samples must be moved from one machine to the other for different depositions, but we can characterize the damages to identify the most significant sources. We again quantified the damage via charge lifetime measurement, and the data are shown in figure 4.20. Over the remaining top-cell process steps there is no clear dominant source of loss. The C_{60} step has slightly more than the others, but is less than half the overall loss. We do note that the SnO_2 and IZO/metal depositions both improve the lifetime. The SnO_2 deposition holds the samples at 100°C and the IZO/Ag PVD also heats the substrates, both of which could induce a mild annealing to repair some damages. Also the ALD SnO_2 can form on all surfaces within the chamber and potentially forms a passivating oxide on the damaged rear surface. But overall, there is not one clear source of damages, and in any case we cannot remove any of these steps.

Following these results on lasering and manipulation damages, we chose to instead focus on treating the damages afterward. Some attempts at this are demonstrated in figure 4.21. First, we did the laser and cleave on a bare wafer before adding the heterojunciton passivating contacts (moving the laser scribe in after step 3 as shown in figure 4.2). This required an additional HF washing step to clean off the dust produced by lasering, before putting the wafers in a clean environment for PE-CVD. This did not produce a significant difference in FF (figure 4.21a). We attribute this to the weak binding/passivating of hydrogen, the directionality of the PE-CVD proceess, and the increased manipulation of the small 25 mm x 25 mm squares relative to full wafers during PE-CVD. Next, we treated finished bottom-cells with both an annealing and an ALD AlO_X layer. The FF values after each step are shown in figure 4.21b. Annealing is known to help recover the plasma-induced damage to the c-Si/a-Si interface while also diffusing some hydrogen ions from the a-Si:H into the ITO [242]. With the correctly tuned temperature and time of annealing, this diffusion can improve carrier density and contact resistance without too much increase in free-carrier absorption [243]–[245]. The ALD AlO_X layer was similarly inspired by past literature results showing its ability to passivate c-Si surfaces [246]. In our own tests on normally-prepared bottom-cells, the annealing (20 minutes at 200°C) did help, but the ALD AlO_X layer did not (figure 4.21b). This could be because the

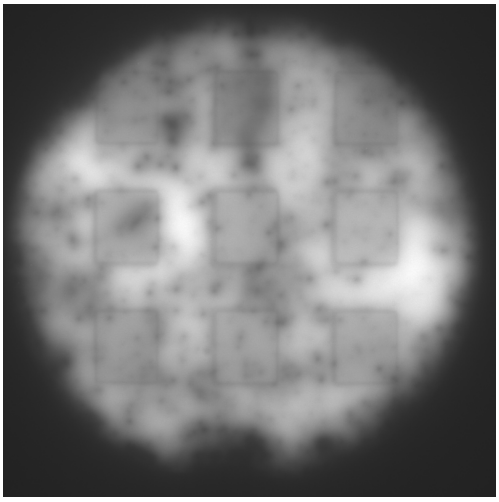

(a) Before Laser Scribe

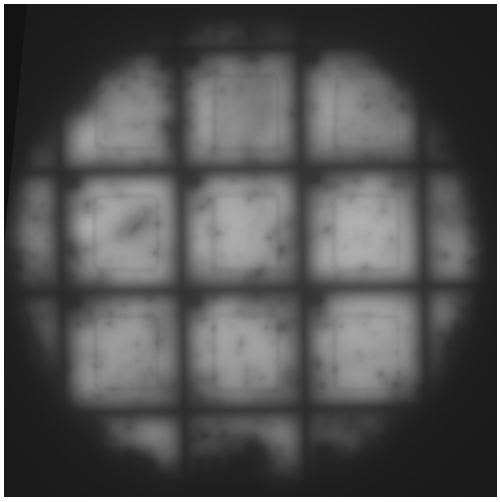

(b) After Laser Scribe

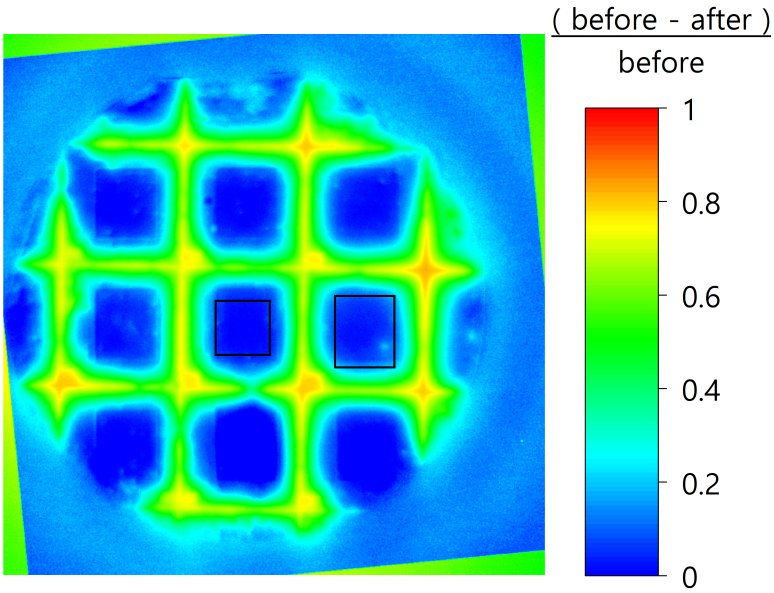

(c) Relative Loss

Figure 4.19 – PL images of c-Si wafer before and after laser scribe. (a-b) show the PL intensity for the same c-Si wafer, before and after laser scribing. Both images are scaled to the same brightness. The illumination intensity was 7% of 1-sun to approximate carrier concentrations at MPP. The rectangles visible in the image are from the rear ITO/Ag contact (1.43 cm^2 design), which alters PL emission due to modified surface recombination and optical reflection. It was included to clearly indicate the cell active area location. (c) shows the relative loss between the two images, which was obtained by subtracting the pixel values of "after" from "before" and dividing by "before". The 1.43 and 1.02 cm^2 cell design areas are shown by black rectangles in (c). Measurements by Dr. Gabriel Christmann.

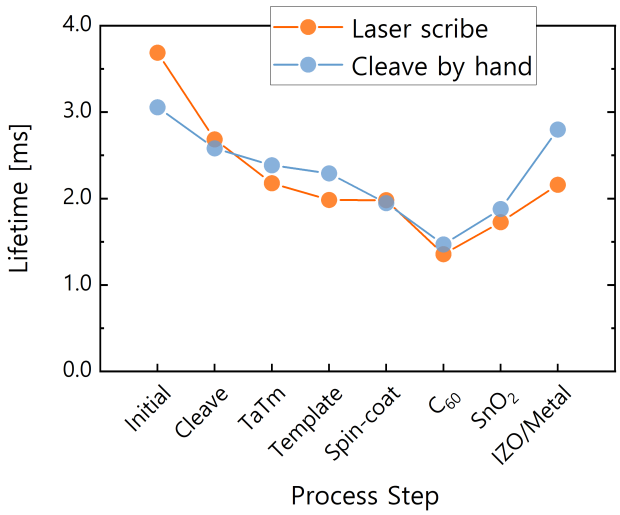

Figure 4.20 – Lifetime measurements taken for c-Si wafers as they are passed through each top-cell processing step. Starting from two 100 mm c-Si wafers, they were either cleaved by hand or with the aid of a laser scribe. Then they were carried along with a top-cell batch and remeasured after each step, to quantify manipulation damages. Measurements by Deniz Türkay.

AlO_X only treats defects on the exposed edges, while the annealing can treat damages closer to the active area and within the material. This would be in line with the previous understanding that the edges do not affect the cell area.

At this point in the progression of work on the bottom-cell, the Ph.D. student Deniz Türkay arrived and took over the project. He continued to develop the annealing step and further devised new methods for protecting and passivating our bottom-cells. Specifically, the an-

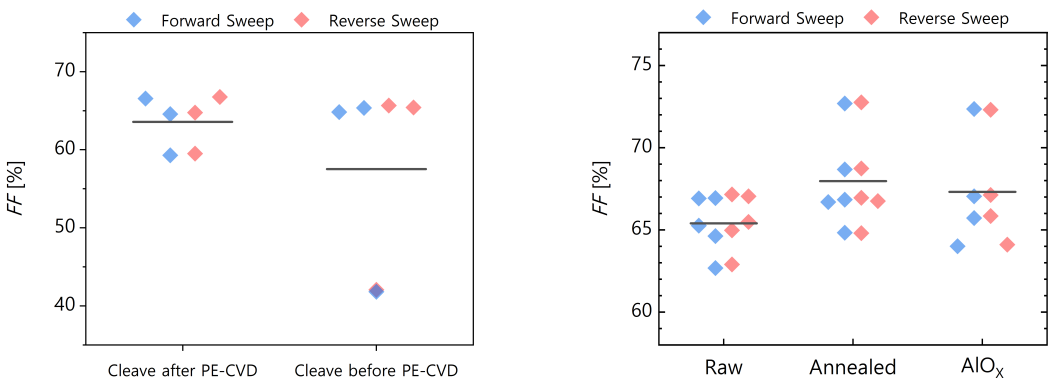

(a) **(b)**

Figure 4.21 – Effect on *FF* of various passivation treatments in single junction bottom-cells. SHJ were processed as if to use for bottom-cells in tandems, but rather finished with a front electrode and no top-cell. (a) shows the effect on FF of cleaving the wafer into sub-samples either before or after the PE-CVD deposited a-Si:H(i) passivation layers. (b) shows SHJ bottom-cells that were processed normally and measured, then treated with a 20 minute anneal at 200°Cand remeasured, then treated again with an ALD coating of AlO_X and measured a final time. All cells used the 1.43 cm^2 front electrode design.

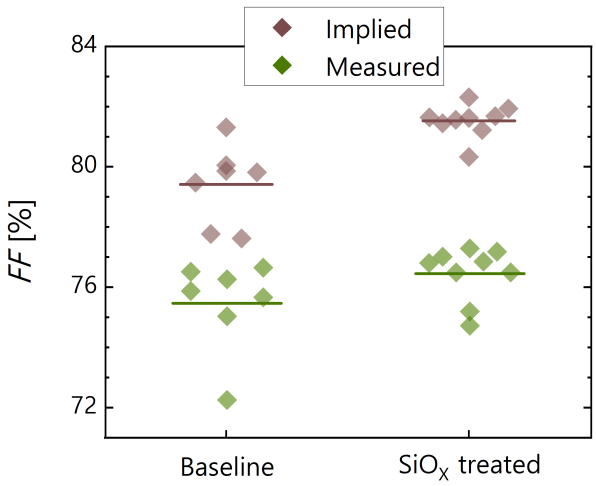

Figure 4.22 – Implied and measured *FF* values for bottom-cells with or without rear SiO_X passivation. Bottom-cells were produced as normal or with a 300 nm SiO_X layer deposited on the rear side. Their implied *FF* was measured in the active area via intensity-dependent PL, after the laser scribe. Then, the front contact (1.02 cm^2 design) was deposited and normal *JV* measurements taken. Cells, development, and measurements all by Deniz Türkay.

nealing step was optimized and the rear surface made more durable with a PE-CVD SiO_X layer. This served as a mechanical barrier to scratches and other processing damages normally incurred via manipulation. As evidence, he measured both the resulting *FF* of cells and the implied *FF* obtained from intensity dependent PL. These data are shown in figure 4.22. Both values improve upon the addition of the SiO_X, and the variance between samples reduces. This gave the best performance to date in bottom-cells alone. The final process we then arrived at was: texturing and cleaning of wafers, PE-CVD of passivating contacts, PE-CVD of the recombination junction, sputtering of the rear ITO/Ag electrode, PE-CVD of SiO_X rear protection, 210°C anneal for 20 minutes, laser scribe, and cleaving into sub-samples ready for top-cell deposition. This recipe was then used in tandems and the champion cell is shown in figure 4.23.

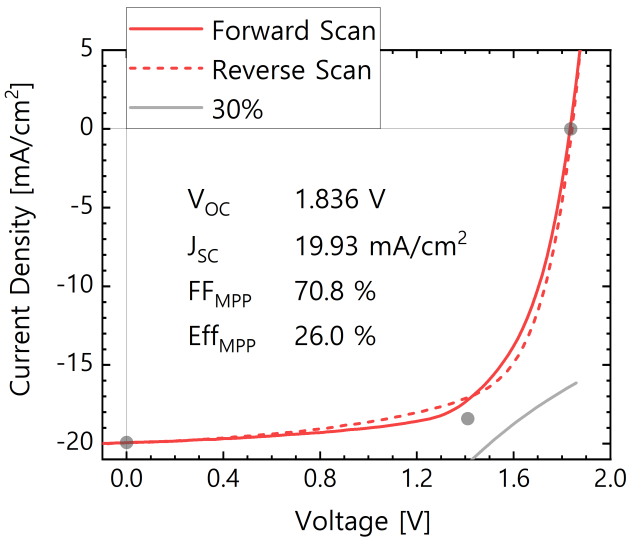

Figure 4.23 – *JV* curve of the best tandem cell produced on improved bottom-cells. This cell was produced according to the optimized top-cell recipe detailed in the previous sections, and with a bottom-cell passivated with a 210°C annealing and SiO_X rear protective layer. A reference bottom-cell from the same wafer was finished as a single junction, and had 651 mV V_{OC}. This cell used the 1.02 cm^2 front electrode design.

4.4.2 Applying Single Junction Improvements to Tandem Top-Cells

Finally, the last phase of this thesis work was to improve the perovskite top-cell FF to match the improvements of the bottom. We demonstrated FF around 80% in flat single junction cells in section 2.4, so we expected similar values to be possible in top-cell configuration. But still, our tandems were in the range of 70%, even with bottom-cells over 75%. In theory, two sub-cells at 75% each would give a tandem with nearly 80% FF [152], so our results implicate the top-cell severely.

To improve the top-cell FF, we first tested the most simple explanations. One of these was that of a band mis-alignment causing an extraction barrier. The difference between the front stack of perovskite/C_{60}/Ag in single junction and perovskite/C_{60}/SnO_2/IZO/Ag in tandems raised this possibility. If indeed there is an extraction barrier due to band alignment, it could be surpassed by heating the cell, so that thermal carriers could provide the energy needed to overcome the barrier. This was tested, and quickly ruled out as a problem in our cells. Figure 4.24 shows FF and V_{OC} measurements taken as a tandem cell was heated and cooled from room temperature (25°C) up to 65°C. The FF drops, rather than increases, and the V_{OC} falls by 10% as well. Not only does the heating not improve the FF, but it seems to damage the cell. The V_{OC} recovers immediately with cooling, but the FF remains low and even decreases more. The cell was left for 2 - 3 minutes at each temperature to stabilize before measuring, and the V_{OC} values during cooling justify that the cell had returned to the same external condition as experienced during heating. But the FF did not behave the same when put back to the same temperature during cooling, which gives evidence of degradation to the transport layers.

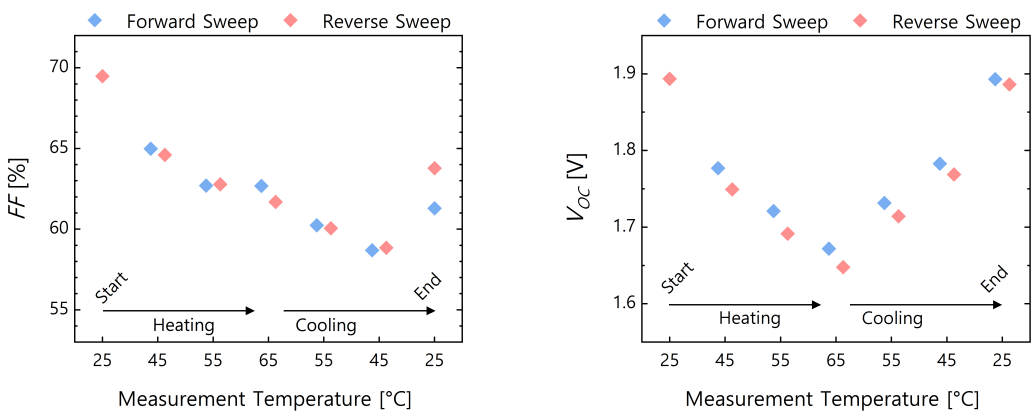

Figure 4.24 – FF and V_{OC} measurements for a single tandem cell, measured at different temperatures. The same cell was left on a temperature-controlled measurement chuck and heated from 25°C to 65°C. It was held 2 - 3 minutes at each temperature for measurement, and the same was repeated while descending back to 25°C. This cell used the 1.43 cm^2 front electrode design.

The second quick test was to evaluate the severity of shunting on our top-cell, which were found to be negligible (figure 4.25). Shunts in the perovskite stack will lead to FF losses in the top-cell, which then correspond to greater than 1:1 losses in the overall tandem FF [152]. To examine the effect of shunting in our top-cell specifically, we measure JV curves at reduced illumination, using the "symmetric SHJ" cell architecture described in section 4.1. This isolates the top-cell as a single junction while maintaining the same cell stack and fabrication as for tandem top-cells. The results confirm that shunting is not an issue, shown in figure 4.25. The effect of shunting is seen in the slope of the JV curve at short-circuit. Flat curves mean negligible shunting and any slope indicates low parallel resistance and reduces the operating current. This slope holds constant regardless of J_{ph}, and thus is more visible at low J_{ph}. From the flat curves at all illumination levels in figure 4.25, we conclude that there is negligible shunting in a typical top-cell stack.

From these results, we believe that the top-cell FF is not limited by an energetic barrier or shunts, and now look to the charge transport and recombination properties of the perovskite and CTLs. For the CTLs, we already know that we are near optimal transport with SAM and C_{60} [168]. As for the nc-Si, SnO_2, and IZO, we can conclude from the R_{OC} of bottom-cells which include the nc-Si junction and the R_{OC} of tandems in general that there is not a major problem of conductivity (although the R_{OC} of tandems is higher than ideal, which is discussed in section 4.6). These layers accounted for, the perovskite remains as the most likely cause of the FF losses.

To address the perovskite FF, we look to the results of section 2.4. Here, we included the additive FBPA in the perovskite, which both passivates the surfaces and increases the temperature stability of our material. This temperature stability enabled a higher annealing temperature and the better layer morphology, PLQY, charge transport, and FF which came with it (figures 2.29, 2.32, 2.36, and 2.33a). We thus applied the same 170°C annealing to tandem cells. First,

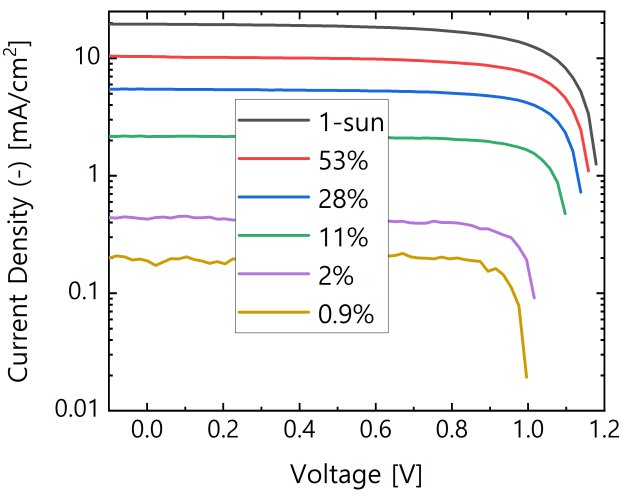

Figure 4.25 – Single junction perovskite top-cell on symmetric SHJ, measured at low illumination intensities. A perovskite top-cell was fabricated according to the established recipe, on a symmetric SHJ. Metal mesh filters were used to reduce the intensity of the light from a solar simulator, and JV curves were measured at each intensity. This data was used to calculate and ideality factor of 1.79 and an implied FF of 86.2%. For this graph, the sign of the current density measurement is flipped and plotted on a semi-log scale. This cell used the 1.02 cm^2 front electrode design.

we checked to see that the morphological improvements translated to the textured c-Si surface and thicker perovskite. SEM of perovskites with both 150°C and 170°C anneal steps are shown in figure 4.26. These perovskites were deposited on c-Si wafers with larger pyramids than typically used in bottom-cells, for the sake of visibly distinguishing pyramid facets, valleys, and peaks. In these images, the grain size as viewed from the top of the layer is larger for the 170°C annealed samples. Likewise, some horizontal features are visible in the cross-section of the 150°C samples, while the 170°C counterparts have predominantly vertical domain boundaries. This confirms that the same morphological benefits translate to tandem fabrication, but we must also verify the improvement to charge transport.

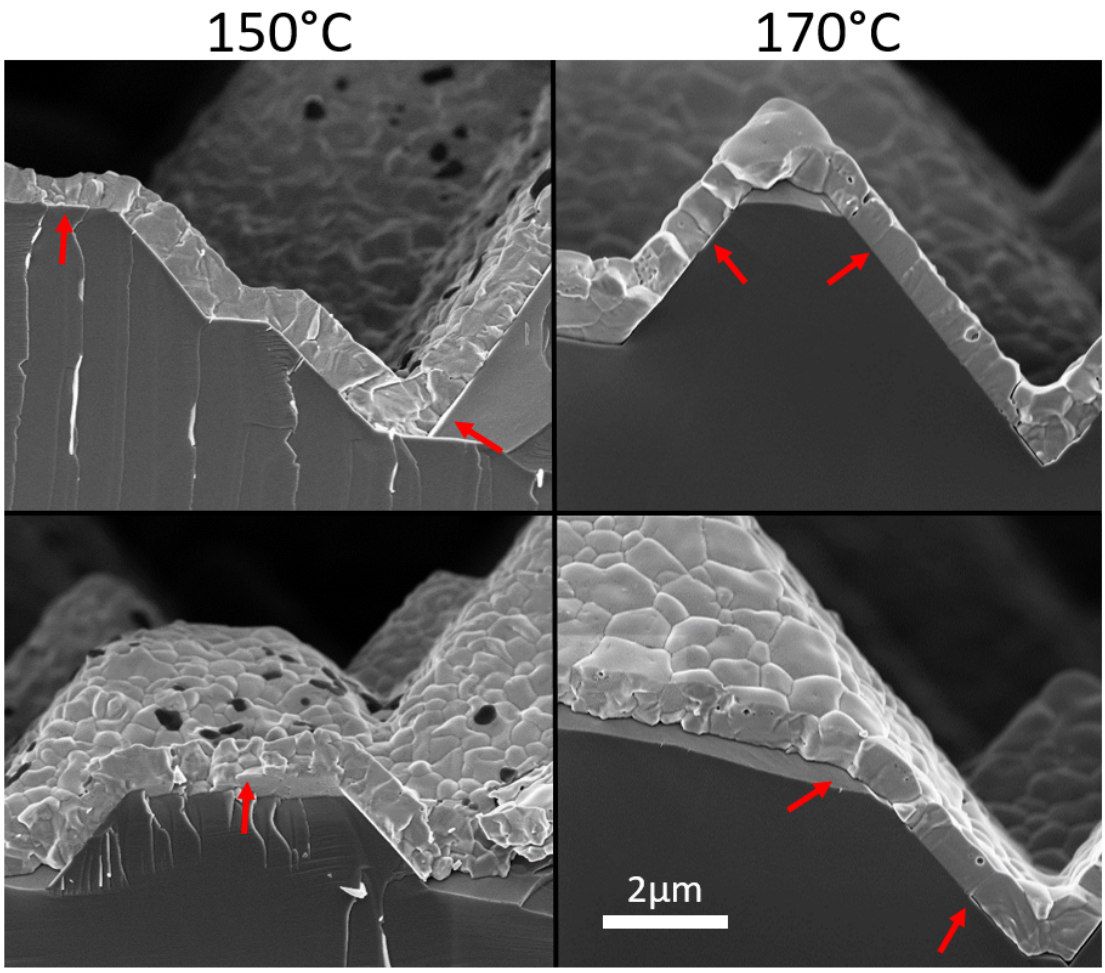

Figure 4.26 – SEM images of perovskite layers on textured c-Si, annealed at different temperatures. Perovskite layers were produced in parallel, with the same PVD/SP steps (600 nm PbI_2 with 10%vol. CsBr, 720 mM with 5 mM FBPA). The only difference was the temperature of the annealing step. These c-Si wafers have a larger pyramid size than what is used in bottom-cells. We chose this larger size to improve perovskite visibility. Residual FBPA is responsible for the black formations on top of the perovskite layer. All images are the same scale.

In single junction flat PSC, we confirmed the improved charge transport in 170°C annealed perovskites by comparing the measured JV curves against those reconstructed via Suns-V_{OC} and Suns-PL (figure 2.35). We cannot repeat this for tandem top-cells, as Suns-V_{OC} will probe the sample-to-sample variation in bottom-cell shunting and FF, and in Suns-PL the c-Si will absorb perovskite luminescence. In the place of these measures, we can perform voltage-dependent EQE to quantify relative bulk transport issues. This technique relies on spectral variations in average absorption depth in conjunction with the cell architecture. From the p-i-n cell design, electrons are collected at the top of the perovskite layer and holes at the bottom. Likewise, we know from the PDS measures of section 2.2.3 that the absorption coefficient of our perovskite varies across the absorbed spectrum. This means that the average blue photon will be absorbed closer to the top of the perovskite layer ($\alpha = 2x10^5$ at 450 nm, 50% absorbed after 35 nm) than the average red photon ($\alpha = 3x10^4$ at 700 nm, 50% absorbed at 231 nm). Combining these two, blue photons will create electron-hole pairs closer to the ETL while red photons will create electron-hole pairs closer to the HTL. Carriers generated closer to their respective CTL have a higher probability of being collected, and any bulk transport losses will mean less current is produced by carriers that have to travel across the layer thickness. Thus, we can observe losses due to charge transport by measuring the relative ability to extract current induced by blue or red light (after controlling for optical effects). In short, the measurement described here is a standard EQE spectra. However, to control for cell optics and enhance the spectral effect, we apply a voltage bias and compare to the zero-bias case. As the bias is increased, the cell approaches flat-band conditions and charge drift is reduced. This enhances transport losses to make them more easily detected. We then use the short-circuit measurement to account for the cell optics, and observe how the blue- and red-generated currents relatively respond to the increased extraction difficulty.

To verify this method, we used SCAPS simulations. SCAPS (Solar cell CAPacitance Simulator) is a one dimensional solar cell simulation program developed at the Department of Electronics and Information Systems of the University of Gent, Belgium [247]. Using this program we simulated a tandem top-cell as a single junction (parameters given in section B.11). We controlled the charge transport in the layer by specifying the electron and hole mobilities and the bulk defect density. Results of these simulations showed that indeed the EQE will tilt in one direction or the other depending on which carrier is more limiting (figure 4.27a). Next, we show in 4.27b how an initially flat EQE curve will lower and tilt to one side as bias is applied. We can then extract the average values in the red and blue regions and compare them, to quantify how much the curve is tilted. This was done for perovskites with different values for the bulk defect population. The red and blue average values are subtracted from eachother, so that a cell stronger in the red will give a positive value, which then becomes negative when the curve tilts past flat. This analysis is visualized in figure 4.27c. At 0 V bias, the EQEs start out slightly stronger in the red. As the bias is increased, all eventually tilt towards the blue, but the bias required for this inversion lowers as the bulk defect population is increased. This correlates with device FF as well, fully linking this analysis back to its original goal.

We performed this measurement for tandems manufactured with 150°C and 170°C annealing temperatures, and the results are shown in figure 4.28. We observed variations to the blue- and red-light induced current for both samples, in that the EQE tilted towards the blue with added bias. The direction of tilt means that electrons are the limiting carrier, as confirmed by the simulation in figure 4.27a. To quantify these results we plotted the average value of the EQE for both the 400 - 500 nm range and the 600 - 700 nm range (figure 4.28c). From these data, we can see that in both cases the red range starts with higher EQE, but that it dips below

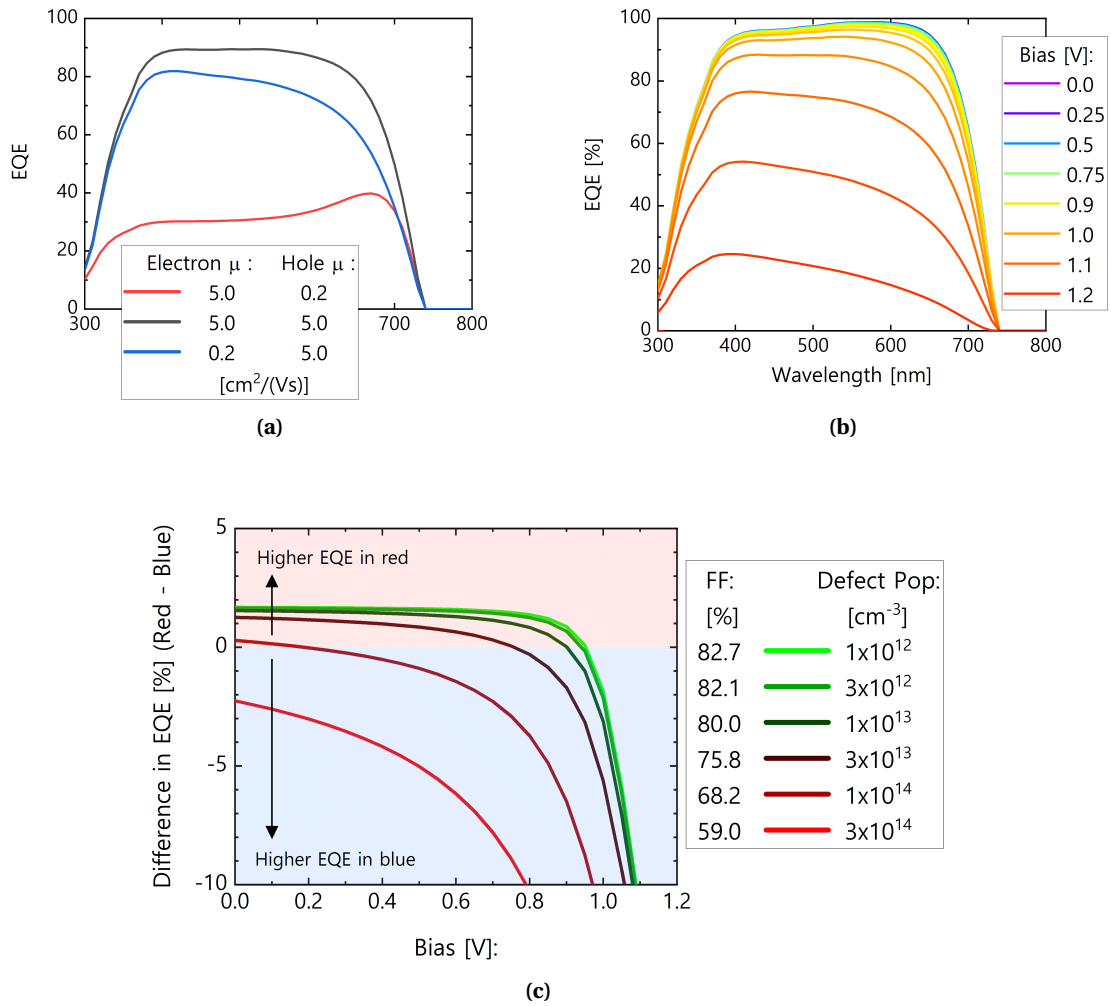

Figure 4.27 – SCAPS simulations of EQE under voltage bias. Simulations were designed to mimic perovskite top-cells. (a) EQE curves simulated at 0.9 V bias and $3x10^{13} cm^{-3}$ bulk defects, with varied mobility (μ) values for electrons and holes. All other simulations used 5.0 $cm^2/(Vs)$ for both carriers. (b) simulated EQE curves over a range of bias voltages, for a perovskite with $1x10^{13} cm^{-3}$ bulk defects. (c) the difference between EQE values in the red (600 - 650 nm) and blue (400 - 450 nm) over a sweep of bias voltages. The same simulation was carried out for different bulk defect populations. The legend shows the populations in cm^{-3} along with the FF value from a JV curve simulated for the same perovskite.

the blue range average value once 1.7 V of bias is reached. However, the 170°C tandem resists this switch for longer, remaining stronger in the red as high as 1.6 V. This gives the conclusions that in both cases there are bulk transport losses, but the 170°C perovskite is less vulnerable than the former baseline of 150°C.

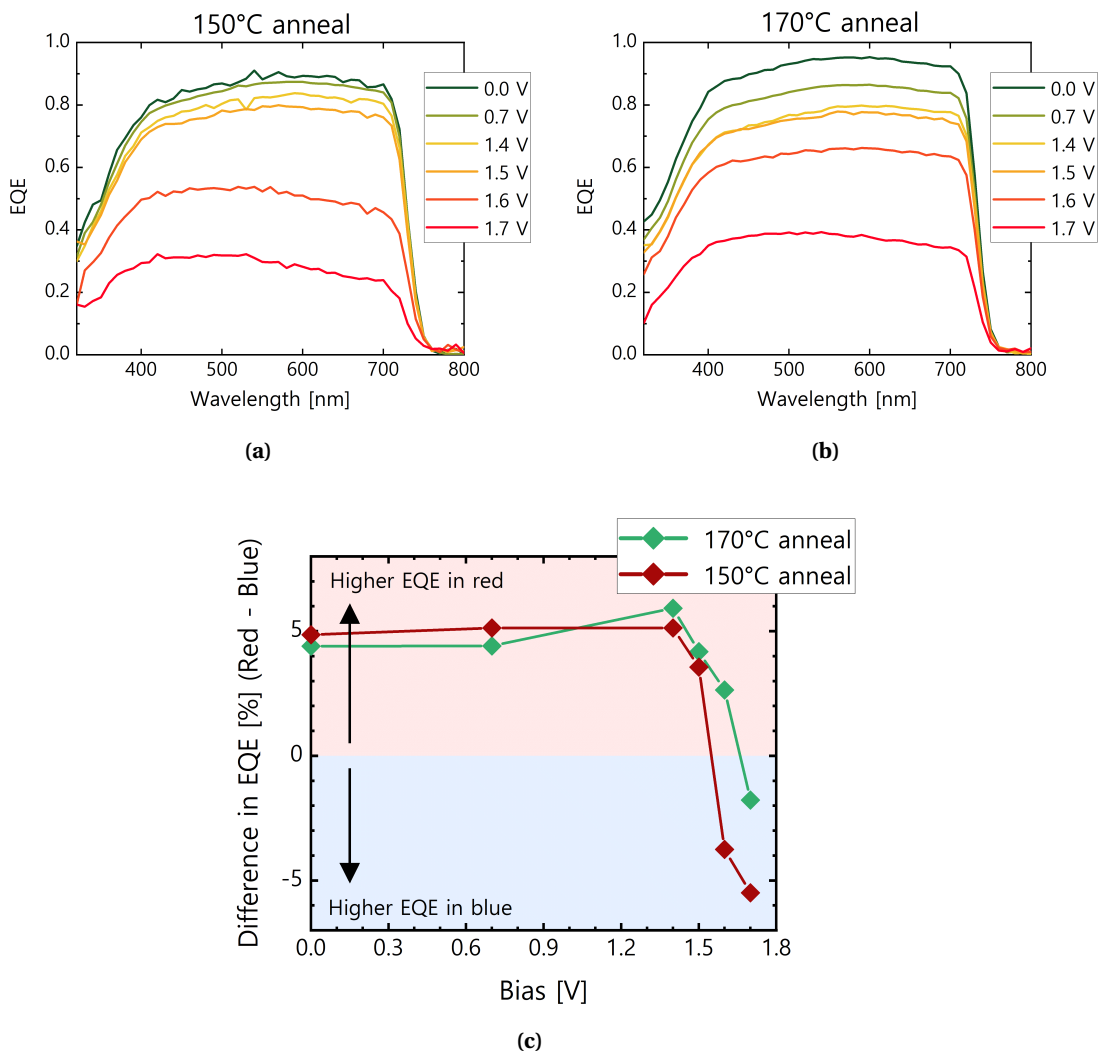

Figure 4.28 – Voltage-biased EQE measurements of tandem top-cells made with different perovskite annealing temperatures. (a) measurements for 150°C annealed perovskite, and (b) for 170°C annealed perovskite. Measurements are taken with a saturated bottom-cell, via a halogen lamp and 830 nm long-pass filter. The average value of the EQE is taken from 400-500 nm and 600-700 nm for each spectrum, the blue subtracted from the red, and the values plotted on (c). Due to the low light intensity of the measure, values are more susceptible to shunting, which is the likely cause for the rapid decline in EQE at moderate bias voltages.

So, with the confirmation that the morphology and bulk transport in top-cells are improved with higher-temperature annealing, we now show the full tandem-level results for verification of FF improvements (figure 4.29). For comparison, results of 170°C annealed tandems with TaTm as HTL are shown in section B.12. These fail due to the dewetting of TaTm above 150°C. SAM materials have no compliance issues at 170°C, and thus we produced tandems specifically with Me-4PACz. We see the same FF trend as with single junction PSC, which translates to a better efficiency. The champion cell[8] displayed a stabilized efficiency of 27.3% during five minutes of MPP tracking. We attribute these gains to the same mechanisms as discussed in sections 2.2.3 and 2.4, where a higher temperature anneal created a perovskite with lower material disorder, better morphology, and improved charge transport. The gain in FF can again be linked to improved charge transport via the voltage-dependent EQE measurements shown above. The champion cell had a forward sweep JV measurement with J_{SC} = 20.26 mA/cm^2, V_{OC} = 1.808 V, FF = 75.8%, and efficiency = 27.8%. The stabilized efficiency and FF obtained from MPP tracking were slightly lower than this; these data are written/plotted alongside the champion cell JV curves in figure 4.29.

[8]We note that an error in the measurement setup was discovered about five months after cell production. Stray light from the illumination was not fully accounted for, contributing 0.60 - 0.70 mA/cm^2 extra current. Thus the data here has been modified from its original values to reflect the expected true values.

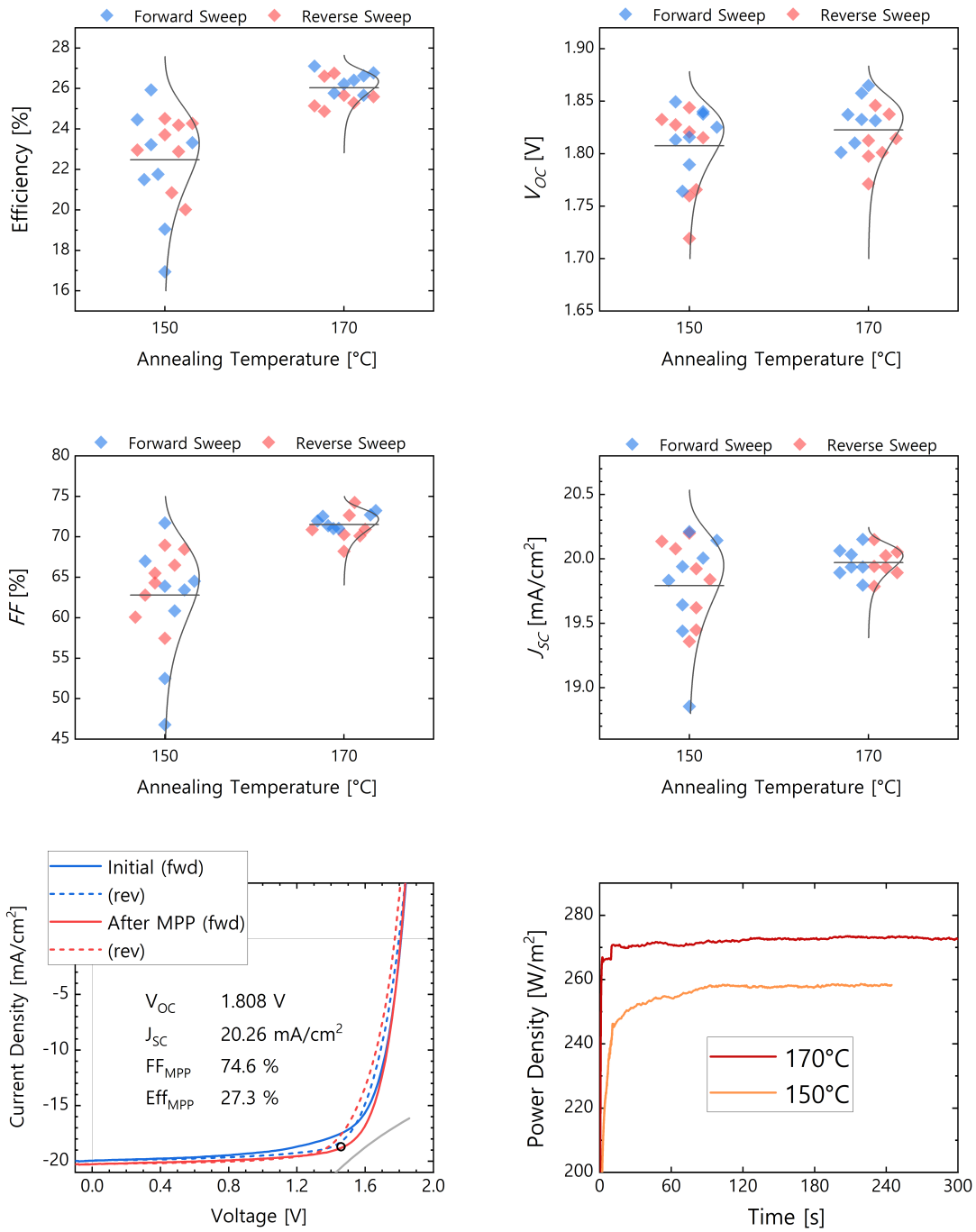

Figure 4.29 – *JV* performance statistics for the champion tandems made with different perovskite annealing temperatures. Eight tandems were made in each condition. *JV* curves are shown for the champion 170°C cell, before and after MPP tracking, along with the MPP attained after five minutes of tracking. The power output over time during MPP tracking is shown for the champion cell of each condition. All statistics are from *JV* measurements done before MPP tracking took place, as this was not performed on each cell. These cells used the 1.02 cm^2 front electrode design. The bottom-cells for this batch were measured at 650 - 670 mV V_{OC}.

4.5 Conclusion

This chapter amassed the developments of the previous chapters and applied the collective knowledge of this thesis work towards perovskite/c-Si tandem solar cells. First, we increased the perovskite layer thickness by 50%. This added J_{ph} in the top-cell, thereby enabling a 60 meV higher E_g perovskite to be used. This was realized by tuning the spin-coating concentration and speed, the pre-anneal, and main anneal dew point for the perovskite formation, which overall gave a perovskite with roughly 700 nm thickness as measured normal to the c-Si pyramid face (opposed to 450 nm previously). We further improved the cell J_{SC} by tuning the front IZO deposition parameters, and found a better balance of transmission and resistance. With this, we reliably achieved over 20.0 mA/cm^2 in our tandems, with a champion over 20.2 mA/cm^2. This represents 90.2% of the radiative limit for a top-cell of 1.70 eV E_g [10], and a significant improvement over the highest reported J_{SC} values for tandems with a polished front-surface (19.3 mA/cm^2, [111]) and partially textured front-surface (19.6 mA/cm^2, [156]).

Next we moved on to improving the V_{OC} of our cells. We applied the advancements from single junction PSC to tandems, such as surface passivation with FBPA and choice of HTL. We found that TaTm performed better in cells than SAM materials in terms of V_{OC}, but that the SAM cells always had higher FF due to superior charge mobility. Between these two effects, the efficiency gain on SAM was larger. We were able to improve the V_{OC} of SAM cells with a thin 1 nm layer of evaporated TaTm, but this simultaneously reduced the FF and gave the same end efficiency. TaTm likewise was observed to dewet from the c-Si pyramidal surface at 150°C, further jeopardizing its feasibility in cells. Still, perovskite/c-Si tandem cells were realized with over 1.9 V of V_{OC} using TaTm as HTL.

Finally, the last aspect of our cells to improve was the FF. We started this process by varying the current-matching condition in order to detect which sub-cell was limiting the overall tandem. This revealed that the c-Si bottom-cell was contributing less FF than the top-cell, and much less than would e expected for a SHJ. We compared the processing steps of tandem bottom-cells to those used for single junction SHJ, and found that mechanical damages to the c-Si were responsible for the lower performance. Particularly, the laser scribe step caused the largest drop in charge lifetime, but these losses were localized far enough from the cell area to cause meaningful loss to performance. Thus, we focused on reducing and repairing damages to the c-Si incurred from the extra manipulation inherent to top-cell processing. Thanks to the work of colleague Deniz Türkay, a SiO_X rear layer for passivation/protection and an annealing step for defect repair were developed, and bottom-cell FF surpassed 75%. For the top-cell, we applied the same advancement of FBPA and higher-temperature annealing to tandems as was previously successful in single junction PSC. This was incompatible with the bulk polymer HTL TaTm, but did work with SAM materials. This improved the morphology and bulk transport properties of our layer, and gave higher FF in tandems. Overall, this produced tandem cells with stabilized FF of 74.6% and efficiency of 27.3%.

4.6 Remaining Losses and Oulook

What improvements remain to build on these results and gain another 5%abs. of FF or 100 mV of V_{OC}? To investigate this, we return to the Suns-V_{OC} method of quantifying cell potential which was previously used in section 2.4.2, and tells us the implied FF that a cell would have without the effects of series resistance. Examples of the reconstructed JV are shown in figure 4.30. For the best tandems at both 150°C and 170°C, the implied FF was roughly 80% over multiple samples. Already this demonstrates two paths to tandem FF improvement.

First, these implied FF values are more than 10% absolute below the Schockley-Queisser limit. Single junction PSC were measured at 86 - 88% of implied FF. We attribute this difference to the bulk transport losses which were still present in the best cells, evidenced by voltage-dependent EQE (figure 4.28). This problem can be avoided by using a thinner perovskite (as in single junction) or by improving the bulk material quality. Reducing the thickness is restricted by the current matching requirement of monolithic tandems, unless some other optical solution can be found for selectively reflecting some light at the recombination junction. Otherwise, it will be necessary to further improve the bulk charge transport, whether that is a consequence of recombination in the bulk crystal or surface recombination at internal crystallite surfaces.

Second, the implied FF values of these cells line up with the measured FF and R_{OC}, of which the R_{OC} is unexpectedly high. Certain bottom-cells of this batch were finished into single junction SHJ using the same front and rear electrical connections, and contained the same recombination junction. These reference cells had R_{OC} values between 2.5 - 2.7 Ωcm^2, much

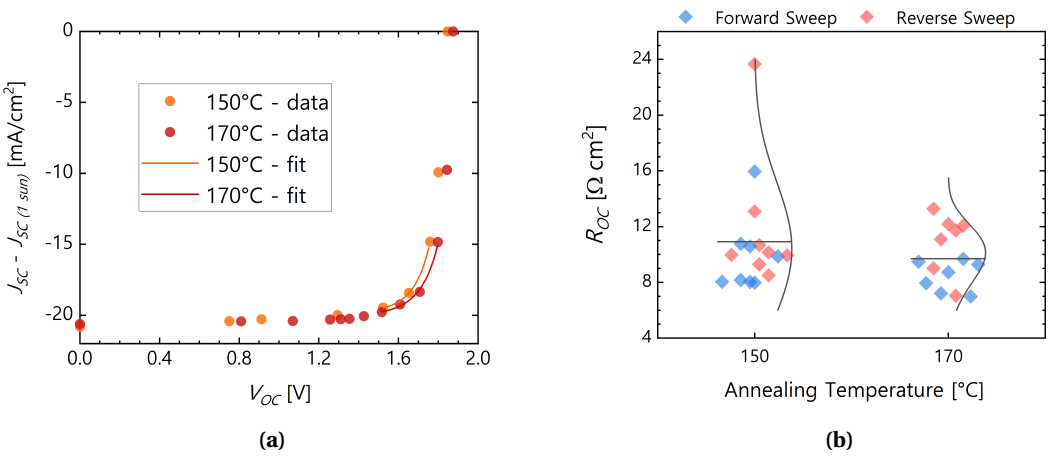

Figure 4.30 – Implied JV curves and measured R_{OC} values for tandems made with different perovskite annealing temperatures. (a) Implied JV curves are reconstructed from the Suns-V_{OC} method of a tandem cell measured at different illumination intensities. The implied FF values for the 150°C and 170°C curves are 79.5% and 81.1%, respectively. (b) R_{OC} values measured for the same cells as in figure 4.29.

lower than the 7 - 11 Ωcm^2 values measured in the tandems. The additional resistance in the tandems must then come from something within the perovskite top-cell stack, such as the SnO_2. Finding and repairing this source of resistance, and achieving the same R_{OC} in tandems as in the bottom-cells, would already improve FF by 4 - 5% absolute. Thus another project that should be undertaken is that of identifying resistive losses, particularly in the C_{60}/SnO_2/IZO stack, which is the only segment of the full stack that hasn't been verified externally.

The final loss mechanism that is still present in our devices relates to the J_{SC} and V_{OC}, not FF. The C_{60} layer brings both parasitic absorption (figure 4.4) and interfacial recombination (figure 2.15), while also being expensive. These are significant loss mechanisms that have so far avoided being addressed due to the high carrier mobility, ease of processing, and few quality replacements for C_{60}. PSC of the n-i-p orientation have frequently used an SnO_2/perovskite interface with success, but this has yet to translate to p-i-n configurations due to deposition methods that are incompatible with perovskite. Large-area deposition of SnO_2 by ALD is feasible, as we already use it in our cells, but work remains towards developing new growth mechanisms, seeding layers, or a non-C_{60} interlayer which would allow SnO_2 to be grown on perovskite with the same quality of interface and charge selective transport. Together, if realized, these improvements could lead to tandems with potentially over 21.0 mA/cm^2 of J_{SC}, 2.0 V of V_{OC}, 80% FF, and a total efficiency over 33%.

Concluding Remarks

This thesis sought to improve the performance of perovskite/c-Si tandem solar cells via characterization and understanding of the underlying material. We specifically focused on perovskites fabricated via a hybrid evaporation/spin-coating technique, as this enables the deposition of perovskite layers on pyramidal c-Si surfaces with features an order of magnitude taller than the perovskite layer thickness. We chose to constrain the thesis work to perovskites as deposited from this method, as the ability to deposit on such surfaces makes the full tandem architecture potentially compatible with industrial standards for c-Si PV.

The first segment of research focused on single junction PSC, to develop material and interface quality within this structure. We examined each of the individual steps in the hybrid deposition process and determined how they affected the end material. Many steps had overlapping effects, which we were able to unify by measuring the bulk material quality. This was minimized, giving an optimum recipe. Next, we showed the effect of different charge-transport materials on interfacial recombination, via relative PL measurements. A molecule (fluorinated benzene phosphonic acid, FBPA) was introduced and resulted higher cell voltages, which we attributed to surface passivation and reduced of interfacial losses with the charge transport layers. We further linked interface recombination and the annealing environment, finding that oxygen passivation via a heat-activated process is crucial to cell performance. The losses could be recovered via a Lewis base additive (ethanethiol), but ultimately its chemical role was not identical to that of oxygen. A new hole-transporting layer was applied, which formed a non-damaging interface and functional cells without reliance on oxygen. The final research on the isolated perovskite material pertained to the morphology and charge-transport ability of the layer. Both improved with annealing temperature, but an upper limit was set by heat-induced formation of damaging PbI_2. The onset threshold of this degradation pushed to higher temperatures with the addition of FBPA. This enabled better morphology and charge-transport, resulting in lower series resistance and higher fill-factor.

The second part of this thesis centered on optical improvements of the cell stack via texturing the absorber layer. We chose to use ZnO as the source of texture due to its multifunctionality and industrially-viability. We started by performing simulations which confirmed the possibility of optical enhancement. ZnO layers were then deposited by low-pressure chemical vapor deposition, and parameters were tuned to balance the scattering and absorption. Perovskite cells were fabricated on these scattering substrates using the hybrid method previously optimized. There was a relationship between the substrate morphology and how the perovskite layer formed, causing the recipes for both to be modified. This led to an optimized recipe, but still with lower current output than the flat reference. We thus pivoted to a solution-processed perovskite layer, with a recipe thick enough to cover the ZnO texture. This resulted in better optics, current gain, and an overall improvement of device efficiency of 1.1% absolute.

The third and final subject of this thesis was that of full perovskite/silicon tandem cells. We started from the results attained in previous thesis, which reached 25.1% stabilized efficiencies. From that baseline, we separately approached the current, voltage, and fill-factor of our tandems. First, we increased the top-cell thickness by 50% and tuned the front transparent contact. This in turn raised the perovskite absorption and allowed a higher bandgap to be used in the top-cell. Tandems with these developments reached over 20.2 mA/cm^2 in short-circuit current. This result is 90.2% of the radiative limit, and 0.6 mA/cm^2 higher than any other reported perovskite/c-Si tandem J_{SC} reported to date. For the voltage, we applied the same advancements as in single junction cells. FBPA and better hole-transport layers were introduced, and tandem cell voltages surpassed 1.9 V. Finally, we improved the fill-factor by separately optimizing each sub-cell. The silicon bottom-cells were found to suffer from mechanical damages during processing. These were resolved with a robust rear SiO_X protection layer, and bottom-cells surpassed 75% fill-factor. The top-cells were improved via the same FBPA-enabled higher temperature annealing as in single junctions. Together with the improved bottom-cells, this resulted in tandems with stabilized efficiency of 27.3%. This is higher than any single junction silicon cell, and shows the viability of high efficiencies using hybrid deposited perovskite/silicon tandems.

Outlook for Perovskite/Silicon Tandem Photovoltaics

The central goal of this thesis was develop technologies that could someday bring higher efficiency PV systems to industry. I hope that the work presented here did meaningfully contribute to this effort, but the overall goal is far bigger than any one person or lab could accomplish. Perovskite/silicon tandems are not commercially available as of writing, and do not look to enter the market in a significant way for still some years. So, I conclude this thesis by looking forward to how that might happen, and giving my personal interpretation, opinions, and expectations for this technology.

The remaining barriers between perovskite/c-Si tandems and industrial relevance come from both science and engineering. On the engineering side, it is rather simple questions of upscaling both cell size and production volume. It is reasonable to expect some sort of slot-die coating method will produce sufficiently large area and uniform perovskites. This could be deposited from solvents which dissolve Pb, but the volatility of such solvents is off-putting for industrial safety reasons. An option which I expect to be more successful, though I admit I am biased, would be to sputter a Pb or Pb-halide template and subsequently deposit organohalide salts (similar to our in-house method). Sputtering is advantageous over evaporation due to the small vacuum-chamber volume, and is already an industrial method. The second deposition could be from a gentler solvent via slot-die coating, or via vapor-phase close space sublimation methods. But whatever the process, I expect the remaining engineering problems to be solvable with extant methods, and producing large volumes of wafer-scale perovskite/c-Si tandems to be feasible.

The scientific challenges that remain are more difficult. The main question is on the long-term stability of perovskites, both intrinsically and in the presence of external factors. The instability of perovskites is well documented, and they will have to show improved durability in order to be a viable product. Much of this development will depend on fundamental research into perovskite materials and the atomic-level dynamics that make up the degradation processes. Perhaps this will solve the problems, but it is highly uncertain. Many sources of degradation can simply be avoided by good encapsulation. But this would rely on using an edge sealant

in modules, which is generally taboo for c-Si manufacturers due to an added process step (though perhaps feasible when adding all the other top-cell steps). Regardless, this does not solve the problem, but only prevents it. Still it might be sufficient (to end customers) to just have a robust encapsulation scheme, which is a likely solvable engineering problem.

As for the intrinsic degradation of perovskite materials, nearly all problems are linked to the mobility of ions within the perovskite crystal lattice. I believe that long-term stable perovskites will only be realized if the motion of ions within the material and between the perovskite and adjacent layers is reduced to near zero. This is conceivable, if the population of halide vacancies in the bulk is negligible and the surface lattice terminations are fully passivated. Achieving this in practice is the work of fundamental material research and lab-scale process development. If this type of material is realized, and if the resulting perovskite is high-efficiency, and if the methods are scalable to industry, then the goal of producing commercially-viable perovskite/c-Si tandems will be reality. Thus it is possible, but relies on a lot of unproven solutions.

Still, I expect many start-ups to attempt bringing this technology to industry. The leading company is Oxford PV. They are far ahead of any other group in terms of publicly demonstrated results, but do not yet have a product. Their success is so far made possible by hundreds of millions of dollars in venture capital and government grants. This is a good sign of enthusiasm for the technology, but the volume of funding needed to get this far and the even larger sums that they will need to raise in order to continue operations is only a deterrent for new players. Contrary to battery technologies, which have the weight of auto-industry capital supporting them, PV must rely on their own profits, private investors, and the will of world governments. Beyond the acquisition of capital, new start-ups will need to compete with Oxford PV in both product quality and market share, the whole time dependent on academic research for the very viability of their product. Thus I perceive the risk of such a venture to be extremely high. That is not to say it is impossible. A clear example is First Solar, which lasted over 10 years as a start-up before offering their first product. For perovskites, it remains true that no amount of hard work at a start-up will overcome a product that breaks itself. But if the physics is on our side and the cells do someday work, then we'll be glad to have started now.

A more realistic route for this technology is that of established c-Si manufacturers slowly transitioning their production after the concept proves itself viable. This could equally come from their own research or acquisition of a start-up. Such companies will have the capital to invest and the foundation of an extant product/income source. This transition will be slow, but also low enough risk to tolerate the volatility of emerging markets. It may not be necessary if we scale c-Si well enough, but if it does work then it will certainly help. It's also possible that perovskite/c-Si tandems will be an irreplaceable key to deploying enough PV for decarbonization. Only the future will tell, and it won't happen without tireless work from every team involved.

A List of Abbreviations

AFM	Atomic Force Microscopy
ALD	Atomic Layer Deposition
a-Si:H	Hydrogenated Amorphous Silicon
BA	Butylammonium
BOS	Balance of Systems
capex	Capital Expenditure
CIGS	Copper Indium Gallium Selenide, $Cu(InGa)Se_2$
c-Si	Crystalline Silicon
CTL	Charge Transport Layer
DEZ	DiEthyl-Zinc
DMA	Dimethylammonium
DP	Dew Point
E_g	Bandgap Energy
EQE	External Quantum Efficiency
ET	EthaneThiol
ETL	Electron Transport Layer
FA	Formamidinium
FABr	Formamidinium Bromide
FAI	Formamidinium Iodide

FBPA	2,3,4,5,6-Pentafluorobenzylphosphonic acid
FF	Fill-Factor
GA	Guanadinium
GIWAXS	Grazing-Incidence Wide-Angle X-ray Scattering
HTL	Hole Transport Layer
ITO	Indium Tin Oxide
J_{ph}	Photogenerated Current Density
J_{SC}	Short-Circuit Current
LP-CVD	Low-Pressure Chemical Vapor Deposition
MA	Methylammonium
MPP	Maximum Power Point
nc-Si	Nano-Crystalline Silicon
PDS	Photothermal Deflection Spectroscopy
PEA	Phenethylammonium
PE-CVD	Plasma-Enhanced Chemical Vapor Deposition
PL	Photoluminescence
PLQY	Photo-Luminescence Quantum Yield
PSC	Perovskite Solar Cell
PV	Photovoltaic
PVD	Physical Vapor Deposition
QFLS	Quasi-Fermi-Level Splitting
RF	Radio Frequency
RH	Relative Humidity
RMS	Root Mean Squared
SAM	Self-Assembled Monolayer
SCAPS	Solar cell CAPacitance Simulator
SEM	Scanning Electron Microscopy

SHJ	Silicon HeteroJunction
SP	Solution Process
SRH	Shockley-Read-Hall
ST	Semi-Transparent
TCO	Transparent Conductive Oxide
TEM	Transmission Electron Microscopy
V_{OC}	Open-Circuit Voltage
XPS	X-ray Photoelectron Spectroscopy
XRD	X-Ray Diffraction

B Supplementary Tests and Figures

This section includes data and discussions of work performed during this thesis which was not included in the main text for one reason or another. In certain cases, this is because the subject was too far outside the scope of this thesis and was therefore not investigated deeply enough to form a confident understanding. In other cases, the information shown here is related to a main subject, but does not directly contribute to the result and is therefore left out of the main story for clarity. Overall, the information in this section falls short of the relevance or quality necessary to be included in the main text, but is still valid experimentation that may be useful to anyone who tries to follow or replicate these results in the future.

B.1 PVD/SP Bilayer Conversion Viewed Step by Step

For the sake of confirming our expectations for the various processes in the PVD/SP method, we performed side-view SEM on a sample after each step in the deposition. These are shown in figure B.1. Past results had attributed the ability to successfully convert thick PbI_2 templates on texture to the porosity of those templates [62], [149]. This had not been observed in some years, and since before the addition of the pre-anneal. We therefore wished to confirm that this was still the case while also observing the pre-anneal process more directly. We observed that the template is indeed porous when following the "new" recipe established in section 4.2.1. This porosity gives it a similar thickness on flat substrates where it is compact (inset in figure B.1) as when measured normal to the c-Si pyramid surface. After the SP step, the same template morphology is not visible. Though the abundant bright regions along the bottom of the layer suggest significant remaining PbI_2. Upon pre-annealing, the density of these bright regions drops, though not to zero. The film does not appear to be a crystalline perovskite as there are no visible domains or boundaries. Thus the pre-anneal is behaving as expected from previous measurements (figures 2.9 and B.35), in that it causes intermixing of the bilayer with minimal crystallization. Finally, with the main annealing the perovskite morphology becomes visible with large, smooth, domains and boundaries.

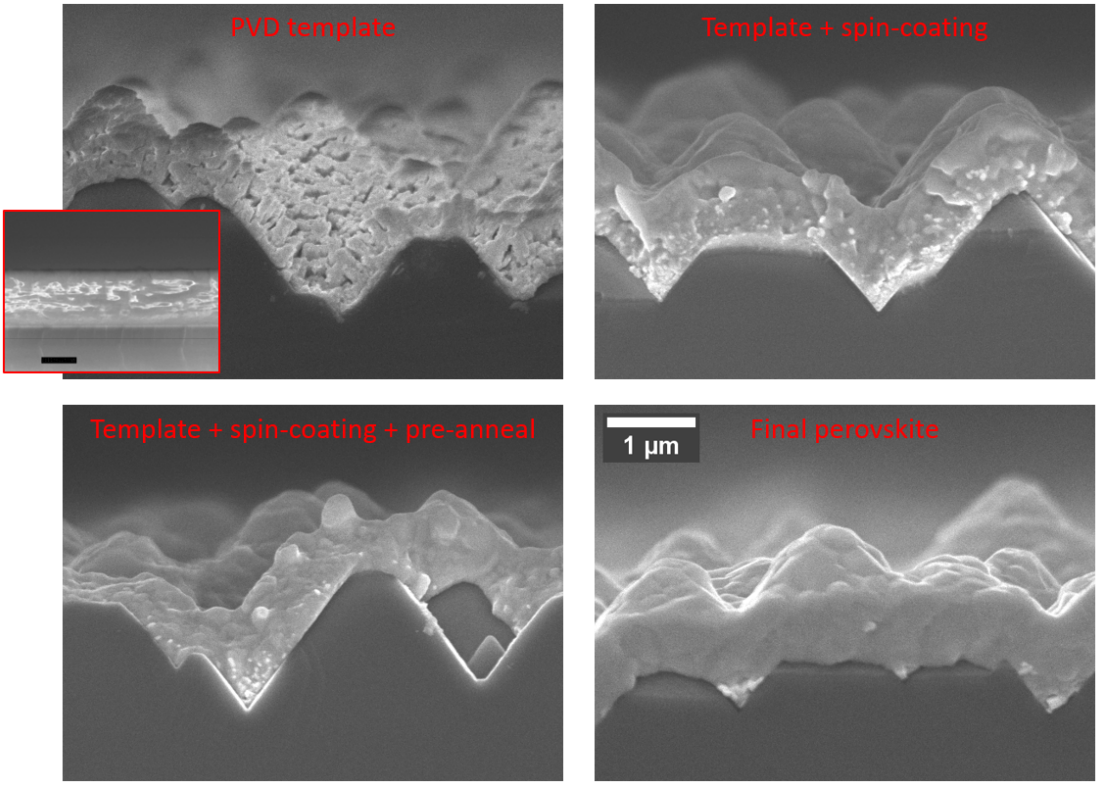

Figure B.1 – SEM of each step in the PVD/SP process. The inset of the top left image is a template from the same deposition, only on a flat substrate. All images are to the same scale. The template contains the standard 10%vol CsBr relative to PbI_2. The spin-coating was at 2000 rpm with a 730 mM solution of 1:2 FAI:FABr. The pre-anneal was 90 seconds at 80°C in N_2. The main annealing was 20 minutes at 150°C in air with 15°C DP. We note that there appears to be residual PbI_2 in the valleys of the final perovskite film. In this particular test, the optimum solution concentration was found to be 750 mM.

B.2 Structural Modification with Large Ammonium Cations

As discussed in section 1.2.2, an active sub-area of PSC research during the beginning of this thesis was centered on using large ammonium cations to modify the perovskite surface and crystalline properties. Here, "large" referred to the the tolerance factor defined by Goldschmidt [31]. These ions are too large to form a normal 3D perovskite lattice, and rather sat on the crystal surface. The resulting perovskite surfaces were favorably terminated, since the ammonium moiety could occupy its natural place while the rest of the molecule was neutral, and did not require a subsequent crystal plane. In the case that multiple parallel surfaces formed, this resulted in sheets of perovskite, referred to as 2D perovskite [72]. Examples of these cations includes guanadinium (GA), butlyammonium (BA), octylammonium, and phenethylammonium (PEA). In practice, these were used either intermixed within a bulk 3D absorber, or deposited separately to form an interfacial layer of the large cations. In our work, we tested BA, GA, and PEA, using both intermixed and separate-layer strategies. Below we will show the results of optimization for various strategies, and discuss the successes and problems encountered during this research.

When mixed directly into the main spin-coating solution, these molecules affect the perovskite crystallization. This can be seen in the top-down SEM images of figure B.2. The grains stayed the same size and slightly increased in roughness with 14%mol GA inclusion, going from 12.2 to 15.0 nm RMS roughness. Including 9%mol BA had a larger effect, increasing grain size and also the roughness up to 25.3 nm. Based on these measurements, we interpret the 2D SEM image as large round crystal domains. This is supported by the JV and EQE data in figure B.3. The BA cells have a flat-topped EQE curve, indicative of an optically rough surface, and the JV curve is very round, as would happen if the CTLs could not properly contact the surface. The

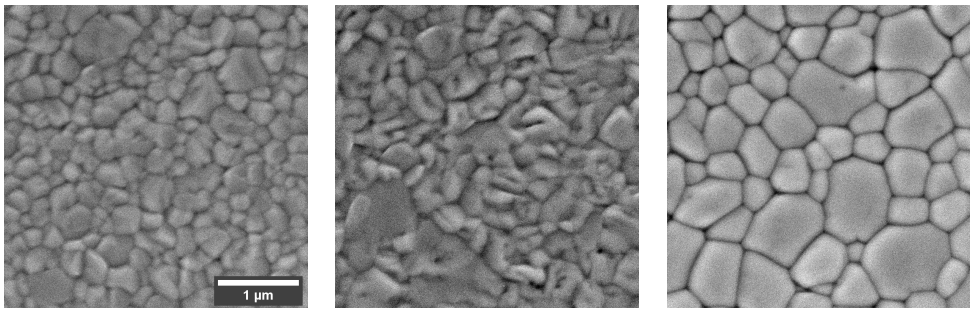

(a) Pure FA **(b)** 14%mol GA **(c)** 9%mol BA

Figure B.2 – SEM images of perovskites made with GA and BA. Perovskites were made on glass/ITO/Spiro-TTB substrates. The template used 15%vol CsI relative to PbI_2. The spin solution either included (a) pure FA, (b) 15%mol GA relative to FA, or (c) 9%mol BA relative to FA. Then the same spin-coating and annealing steps were used. The RMS roughness values of these films extracted from AFM data are: (a) 12.2 nm, (b) 15.0 nm, and (c) 25.3 nm.

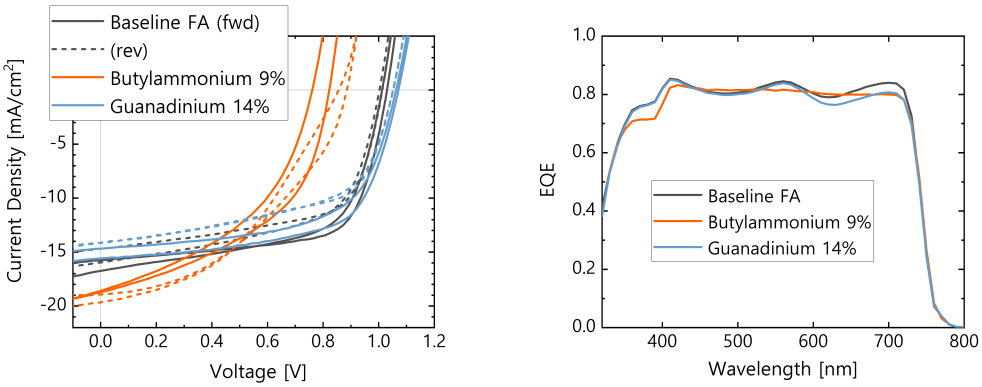

(a) **(b)**

Figure B.3 – Cell performance for perovskites made with GA and BA. The layers shown in figure B.2 were made into complete PSC. (a) shows the JV for two cells of each condition and (b) shows the EQE for each condition's champion cell.

GA cells are similar to the reference, but with slightly higher V_{OC}. This does not translate to efficiency, as the GA cells are also slightly more shunted, and thus the reference has the overall best efficiency. All compositions show the same E_g in the EQE measurement.

We continued to work with GA, as it had the closest to the reference efficiency. We found that perovskites with GA incorporated required different annealing conditions than the baseline without GA. An example of this is shown in figure B.4. During this phase of research, we were exploring 2-step annealing, with first a high temperature step for a short period of time, and second a low temperature step for longer. It was thought that this could force a quick interdiffusion, then allow the crystal quality to improve without being hot enough to evaporate components. This was not the case, and all cell metrics dropped with increased anneal time at 90°C. But we show these results as they are the only instance in which a cell with a large ammonium cation mixed into the main SP solution (in this case GA) reached the same efficiency or slightly better than the baseline.

The next strategy with the large ammonium cations was to form a base layer below the main perovskite absorber. This followed from demonstrations of 2D perovskites being exploited as an electron-blocking layer due to their high E_g relative to standard perovskites, which elevated the conduction band minimum energy [92], [93]. We first tried this on flat NiO_X-based PSC, by spinning low concentrations of stoichiometric PEA_2PbI_4 and BA_2PbI_4 onto the HTL before continuing with the main perovskite deposition. The best results of this structure are shown in figure B.5. The cells with a BA-terminated 2D base layer performed the best due to FF and J_{SC}. We also tried depositing just the cations on the substrate before the perovskite deposition, in the hopes that they would form a well-terminated bottom surface. The best results from this strategy are shown in figure B.6. Too much PEA on the bottom surface made the cell resistive, dropping the FF and J_{SC}. But reliably, the best result came with no PEA in the solution at all.

Thus pure ethanol was spun according to the same recipe. The fact that this gave the best performance, and higher V_{OC} than the baseline, indicated that the PEA was not active, and the benefits came more from cleaning the substrates. Overall, we concluded that it was not realistic to form a layer of 2D perovskite below the bulk absorber in a way that is compatible with textured c-Si surfaces.

This project was largely motivated by good results in the literature (discussed in section 1.2.2), but we were unable to reproduce this success in house. We attribute this discrepancy primarily to the difference in fabrication methods between our lab and those which produced successful results. Many results relied on a thin layer of 2D perovskites on top of the main 3D perovskite absorber, deposited in a second step. This functioned as an electron-blocking layer between the absorber and the HTL [92], [93]. But since we use p-i-n cells, we would need to deposit the 2D perovskite below. This is not demonstrated in literature. Other groups had success with the large ammonium cations deposited on the top surface while in p-i-n configuration [91], [95], but did so with solution-based methods and not a 2-step deposition as we use. Other successful demonstrations were either in the n-i-p configuration [98]–[101] or relied

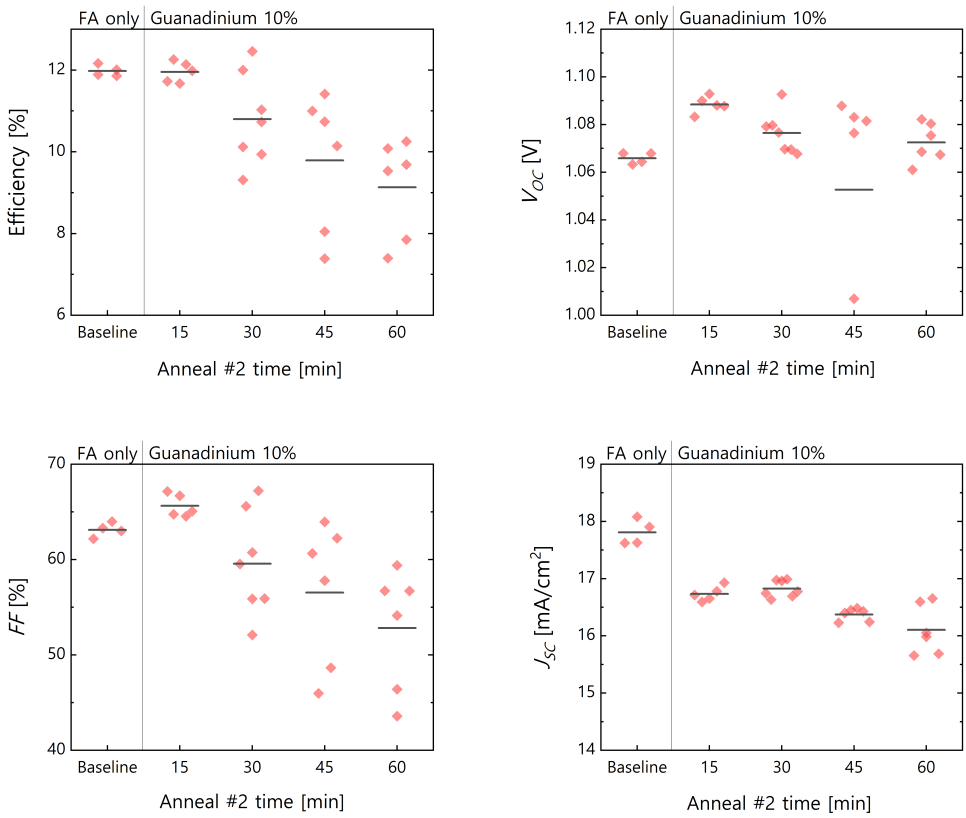

Figure B.4 – *JV* performance for PSC with GA and annealed for different times. GA cells were annealed for 30 sec at 150°C in air, then were annealed for varied times at 90°C in air. The GA was included at 10%mol relative to FA in the SP solution.

on the large cations to be mixed in a single-step spin-coating solution [96], [97]. Thus we conclude that these fabrication techniques are critical to the success of the method. The PVD/SP method is likely limited in that the larger ions are unable to diffuse through the template in the same way that they could in the liquid phase before crystallization. Regardless of why, we were unable to replicate the good results in literature using our method.

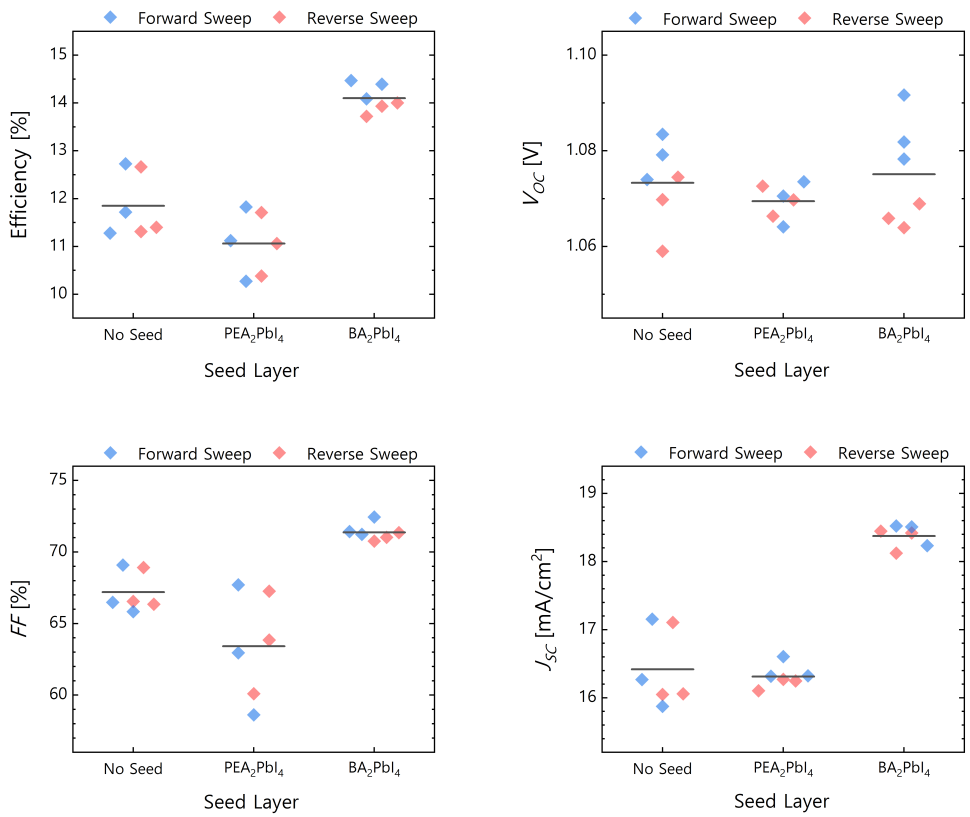

Figure B.5 – Cell performance for PSC with different 2D perovskites deposited below the main absorber. 25 mM of the indicated perovskite stoichiometry were deposited at 7000 rpm from a 4:1 mixture of dimethylformamide and dimethylsulfoxide. Then the substrates were annealed for 2 minutes at 60°C and the PVD/SP process was performed as normal.

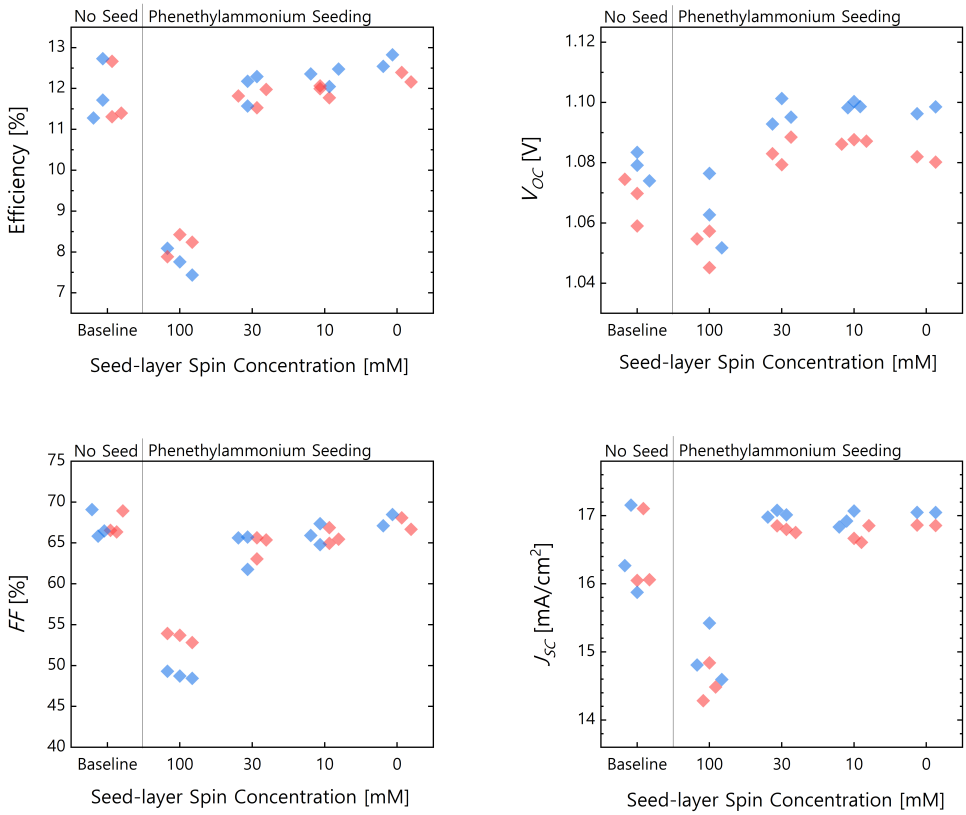

Figure B.6 – Cell performance for PSC with different amounts of PEA-I deposited below the main absorber. Solutions of PEA-I were spin coated from ethanol at 7000 rpm, and the samples were subsequently annealed for 2 minutes at 60°C. From there, the normal PVD/SP process was applied to form the main absorber layer. In the case of 0 concentration, pure ethanol was deposited according to the same recipe, as a control.

B.3 Dimethylammonium as A-site Cation

Due to reports in the literature about stable high-E_g perovskites being achieved via the use of dimethylammonium (DMA) as the A-site cation [57], we attempted to replicate these results with the PVD/SP method. Part of the replication was to increase the CsBr content in the template to 16%vol, in order to have the correct Cs:FA:DMA ratio. This CsBr content is held constant through the experiments shown here.

The first tests were to observe the PL emission for E_g stability of perovskite on glass, as had been reported. The results of this are shown in figure B.7. The E_g was not stabilized, and the peak position followed the same trend in time as the reference sample. We note here that the color scale progresses linearly from blue to pink over time, and the pink is concentrated at the ending position because the PL rapidly moved to this state and stabilized there. But still, despite the failure to mimic the reported E_g stability (from [57]), the intensity did increase relative to the reference, so we chose to extend the tests to full cells. The results of this are

shown in figure B.8. At the time of these tests, ET was being used regularly in the perovskite. Thus, we intermixed DMA at a reduced rate from the best PL result, and similarly reduced the ET concentration, due to the expectation that multiple ions with size slightly larger than FA would lead to structural disorder. Overall, the DMA was found to improve FF but reduce J_{SC} and V_{OC}. This did not accomplish the goal of stabilizing the E_g or increasing the V_{OC} due to eliminating halide segregation, and thus the project was dropped. The difference between literature and our practice likely comes from the differences between our hybrid method and the fully SP method used in the original demonstration [57].

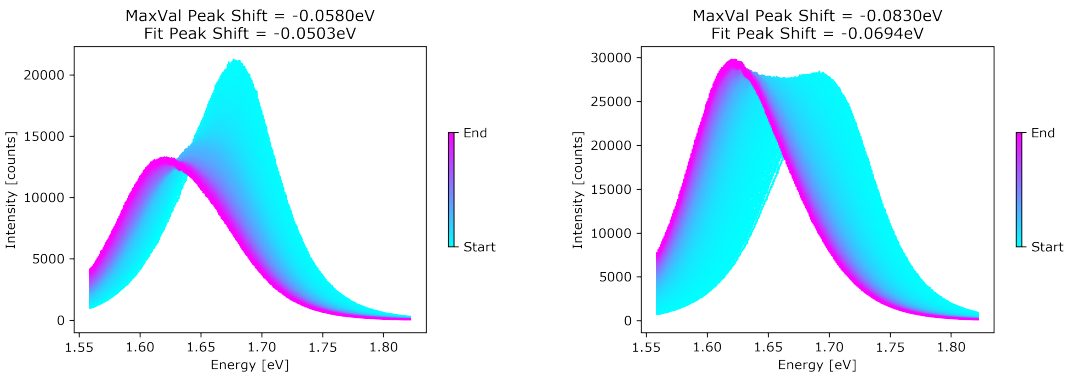

(a) baseline FACs perovskite

(b) 16%mol DMA relative to FA

Figure B.7 – PL measurements over 1 minute for perovskites with/out DMA as A-site ion. Samples were continuously illuminated with a 514 nm laser at 1-sun intensity, through a microscope objective over 1 minute. The spectrum was integrated each 100 ms, and the spectra are overlain from start to finish.

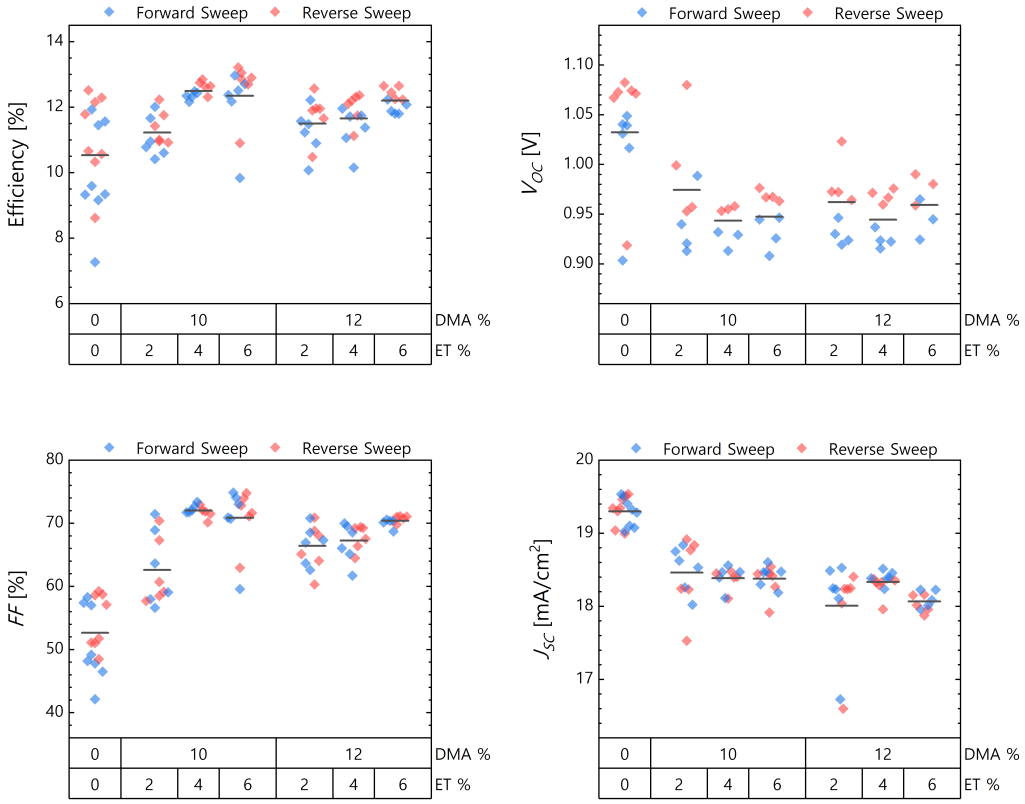

Figure B.8 – Cell performance for PSC with ET and DMA included in the perovskite. Cells were made with different amounts of DMA and ET in the main spin solution. The % refers to the molar ratio of each ingredient relative to FA.

B.4 Control Measurements for Spatially Varied CTL Experiment

Here we show a control measurements for the experimental design discussed in figure 2.14. We spatially masked the HTL and ETL depositions, so that different interfaces could be compared with the same perovskite. However, this requires the measurement of PL emission through the C_{60} layer. C_{60} is highly absorptive, as discussed in figure 4.4. Thus we wanted to confirm that the measured intensity was actually representative of the recombination rates in the perovskite, and not an artifact of C_{60} absorption. To do this, we measured the same samples, deposited on glass, from both sides. The results are shown in figure B.9. While the intensity of the overall image changes due to the optics of passing through an additional glass layer, the intensity of the C_{60} region remains similarly low in all cases. Regardless of if the C_{60} is above or below the perovskite, or if the excitation comes from above or below, the PL losses are similar.

This also serves as evidence that our perovskite has a charge diffusion length greater than the layer thickness. These measurements used a 514 nm excitation laser. Based on the absorption coefficient as measured by PDS in section 2.2.3, this excitation should be almost entirely absorbed in the first tens of nanometers of depth. Thus, most carriers are created closer to one surface than the other. Seeing the same interfacial effect regardless of which side the carriers are created on tells us that the carriers are able to diffuse across the layer thickness with minimal losses. This reasoning also supports the passivation ability of TaTm. Relative to the bare perovskite, the TaTm/perovskite interface gives brighter PL when excited from the side with TaTm than when excited from the other side of the perovskite thickness. This further supports the results of section 2.3.1.

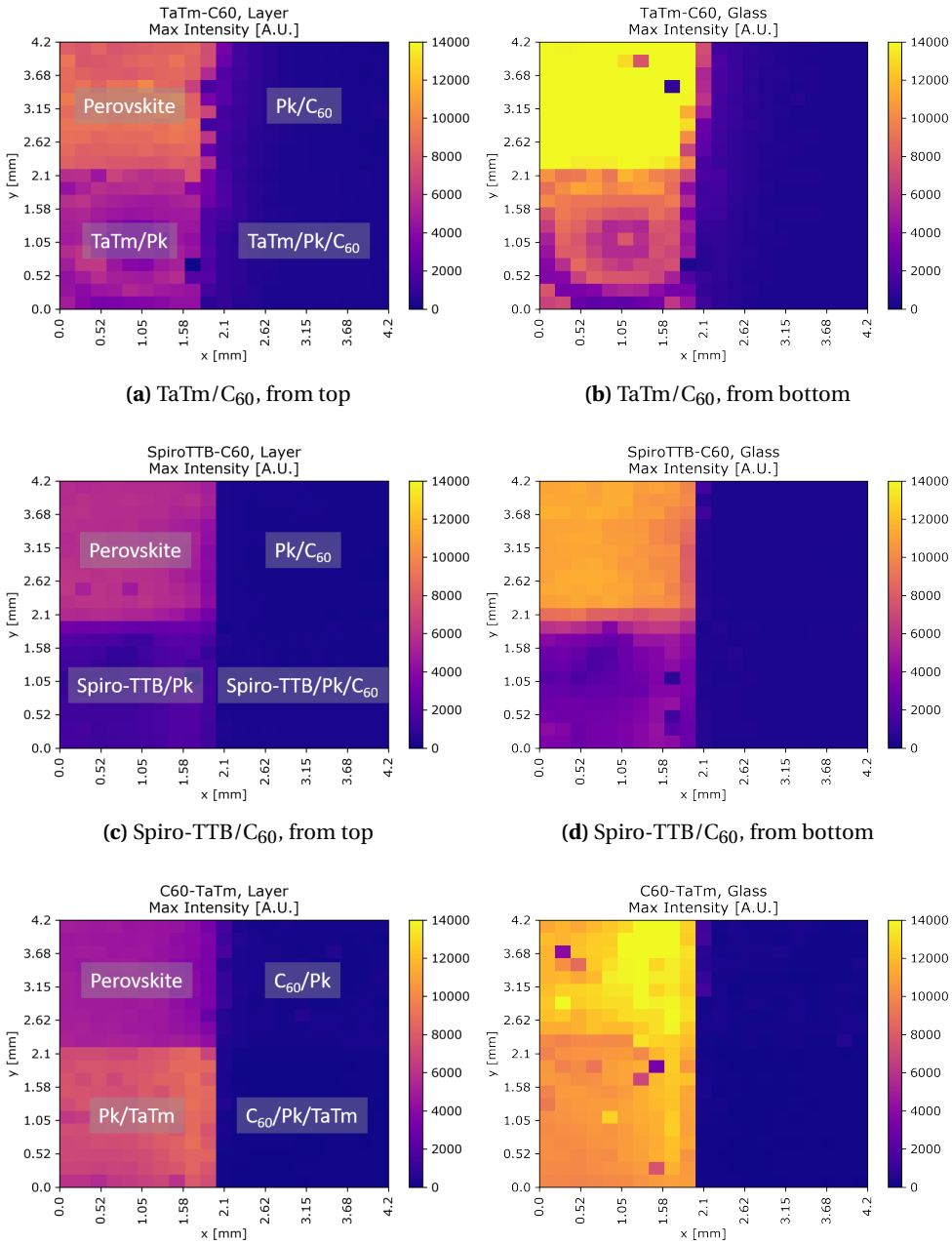

(a) TaTm/C_{60}, from top

(b) TaTm/C_{60}, from bottom

(c) Spiro-TTB/C_{60}, from top

(d) Spiro-TTB/C_{60}, from bottom

(e) C_{60}/TaTm, from top

(f) C_{60}/TaTm, from bottom

Figure B.9 – Spatial maps of PL intensity for perovskite on varied CTL stacks, measured from top and bottom sides. (a-b) has TaTm on the bottom half below the perovskite, and C_{60} on the right half above the perovskite. (c-d) has Spiro-TTB on the bottom half below the perovskite, and C_{60} on the right half above the perovskite. (e-f) has C_{60} on the right half below the perovskite, and TaTm on the bottom half above the perovskite. In all cases, the top left quadrant is bare perovskite. The step size is 200 µm and the illumination spot is 80 µm in diameter. All images are scaled to the same intensity.

B.5 Further Characterization of N_2 Annealing and ET

In section 2.3.2 we observed unexpected and severe consequences to cells annealed in a N_2 environment, and partially corrected these problems with the addition of ET. There was much characterization to try and understand the underlying mechanism. Here we show measurements that were interesting and informative, but fell outside of the main story line. We also show explanatory sample preparation images for the XPS measurements on TEM grids.

First, XRD and AFM measurements were performed on the initial ET concentration sweep of figures 2.24 and 2.25, to observe secondary effects of the molecule on perovskite formation. The XRD results in figure B.10 show that low-level ET addition does not cause crystalline PbI_2 to form, but that it does appear at higher ET concentrations. Besides the PbI_2, we see a slight shift in the perovskite peak location (for 0, 4, and 20%mol: 14.294°, 14.246°, and 14.293°). This suggests either partial ET inclusion in the lattice or different stresses on the lattice due to modified crystallization. For the AFM data (figure B.11), we see that indeed the microstructure is modified with only 4%mol ET. There is no change to average grain size, although parallel ridges appear along the grain tops. These may be due to grain twinning, from ET inclusion in the lattice or different crystallization dynamics [248]. But while the XRD showed the 4%mol ET perovskite to be closer to the 0% reference, the AFM shows the 4%mol to be closer to the 20%mol case. This supports the idea that the presence of a Lewis base can modify the crystallization kinetics due to formation of an adduct with the PbI_2 [210], but that there is an upper level to the benefits of this, set by the appearance of excess crystalline PbI_2. We cannot say precisely the ET concentration that causes these effects, since ET has a boiling point of only 35°C and thus may entirely leave the layer upon annealing. The concentrations in the final perovskite were too low to detect the presence of sulfur with measurement techniques

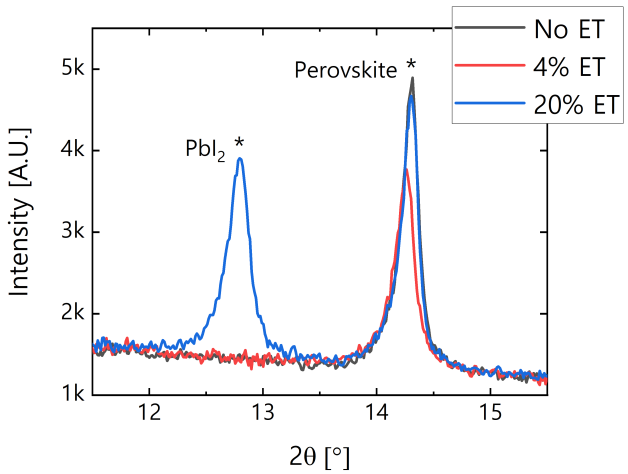

Figure B.10 – XRD patterns for perovskites with varied ET doping rates. The percentage refers to the molar ratio with respect to FA, measured in the spin-coating solution. To encourage ET adoption within the crystal, the FA concentration was reduced in parallel with the ET increasing. The patterns are shifted to align the diffraction peak of ITO at 30.25°.

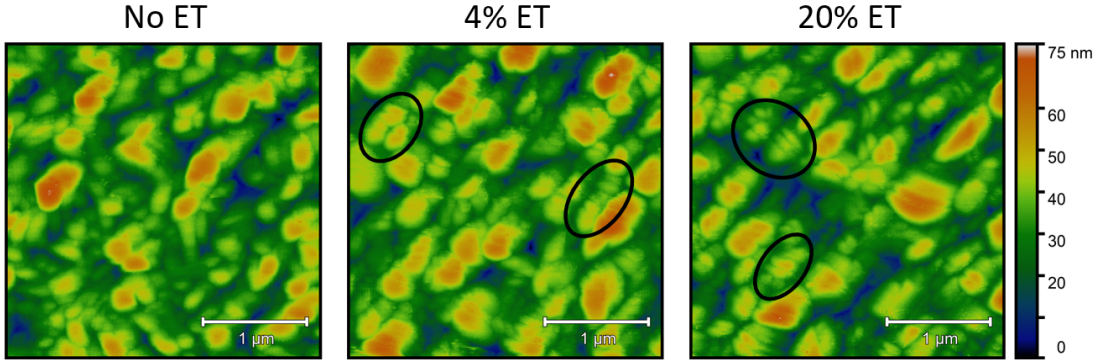

Figure B.11 – AFM height profiles for perovskite films with varied ET doping rates. The percentage refers to the molar ratio with respect to FA, measured in the spin-coating solution. To encourage ET adoption within the crystal, the FA concentration was reduced in parallel with the ET increasing. Measurements were taken on full PSC stacks, so a 20 nm layer of C_{60} is on top of all samples, but assumed to be conformal.

such as XPS or SEM energy dispersive X-ray spectroscopy, so we are left to imply the ET %mol based on the experimental conditions. Regardless, these measurements show that ET modifies the perovskite crystallization and morphology.

We further distinguish the role of ET by controlling if it is present during crystallization and using it in N_2 annealed perovskite. The results, shown in figure B.12, tell us that ET's improvements mostly come from the modified crystallization and that ET and oxygen do not fulfill the same role chemically. First, figure B.12a compares air annealed perovskites with ET either used in the spin solution as previously, or treated to the already formed perovskite via enclosing samples in an environment saturated in ET vapor[1]. This maintains ET exposure without modifying the crystallization dynamics. The samples with ET during crystallization have brighter PL, in line with previous results. The fact that ET improves PL in addition to oxygen tells us that the roles of oxygen and ET do not fully overlap (similar to the conclusion with FBPA). The vapor post-treatment does not give the same PL enhancement, but does increase the PL of some pixels outside the range of the reference case. This is evidence that indeed it has a chemical passivation effect, but that the top surface (where the vapor treatment is expected to have the most effect) is not the site where the ET in the SP solution is primarily active. Whether it is because of ET being present at the bottom surface or inducing better crystallization, it is most effective when included in the SP solution.

Next, figure B.12b shows the same experiment for perovskite annealed in N_2, on glass. Again, the PL for N_2-perovskite is very poor (notice the different x-axis), but the ET no longer improves the PL. The main result of this test is the confirmation that ET and oxygen do not serve the same role, and that PL and JV performance are not always correlated. Despite ET enabling working N_2 annealed PSC (figure 2.24b), the PL does not follow. This further demonstrates the complexity of perovskite materials, in that the defects which caused low J_{SC} could be repaired

[1] According to a method demonstrated for a similar molecule, 1-butanethiol, [127]

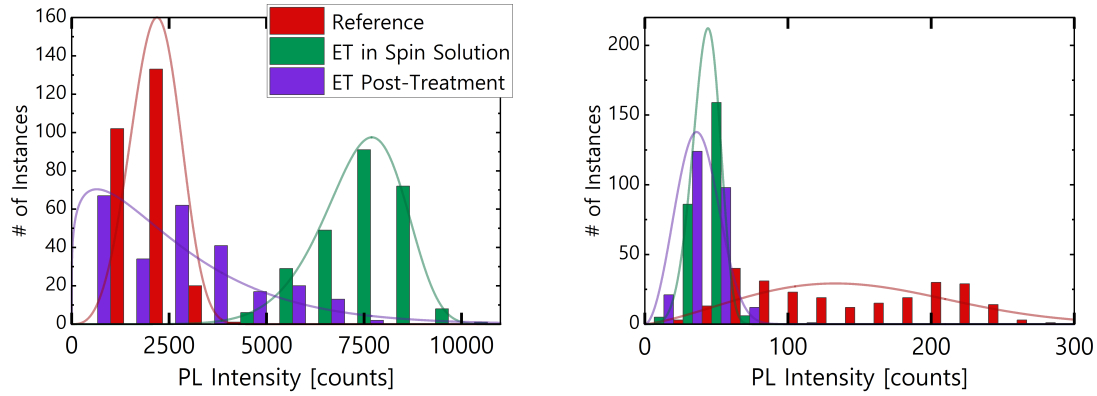

(a) Samples annealed in air

(b) Samples annealed in N_2

Figure B.12 – Histograms of PL intensity measurements from perovskite layers with ET included in the spin-coating solution or treated on the surface. Samples were prepared on glass and PL measurements were taken according to the method in figure 2.14, across the whole substrate with 1 mm spacing between points (322 data points per sample, 2 samples per condition). ET was included either at 6%mol in the spin-coating solution or treated to the surface of fully-formed perovskite via a vapor-based method [127]. (a) shows the intensities measured for samples with the standard 150°C anneal in air, and (b) shows the same data for samples annealed in N_2. Note the different intensity bins on the x-axis. All samples used a template with 16%vol CsBr.

by ET, but there remain other defects which can kill the PL output without affecting J_{SC}. We recall that the ET-repaired JV of figure 2.24b still had lower J_{SC}, FF, and V_{OC} than the air annealed reference. So there should be some PL loss in this case, but not worse than the PL of reference perovskite. A final note, the results of figure B.12b also tell us that the effect of ET on crystallization is not what "fixes" the performance of N_2 annealed PSC, as both the spin and vapor treatments had the same effect.

We further examine the relative behavior of ET and oxygen by taking PL images of the exact cells as shown in figure 2.24b (the working N_2 annealed cells). These are the same measurement as were featured in figure 2.26. The images were not only done for baseline and ET doped samples, but also for air and N_2 annealing. These are shown in figure B.13. When annealed in N_2, the normal inhomogeneity observed in the baseline perovskite is magnified. The same distribution of spots is visible, but in the PL-quenched N_2-perovskite, the spots are instead incredibly bright among a dark background. All images were taken with the same image capture settings (max intensity of $65,536 = 2^{16}$). From this, the baseline in air had an average of 4,440 counts with a maximum of 11,468 counts. The baseline in N_2 had an average of 414 counts and 12 pixels saturating the detector, and 2,431 pixels (of 2,250,000) greater than 11,500 counts. This inhomogeneity was eliminated with the addition of 12% ET, both in the air and N_2 annealed samples. Despite overall lower PL, the air annealed had an average of 1,442 and max of 10,311 counts, while the N_2 annealed had an average of 1,319 and max of 3,778 counts.

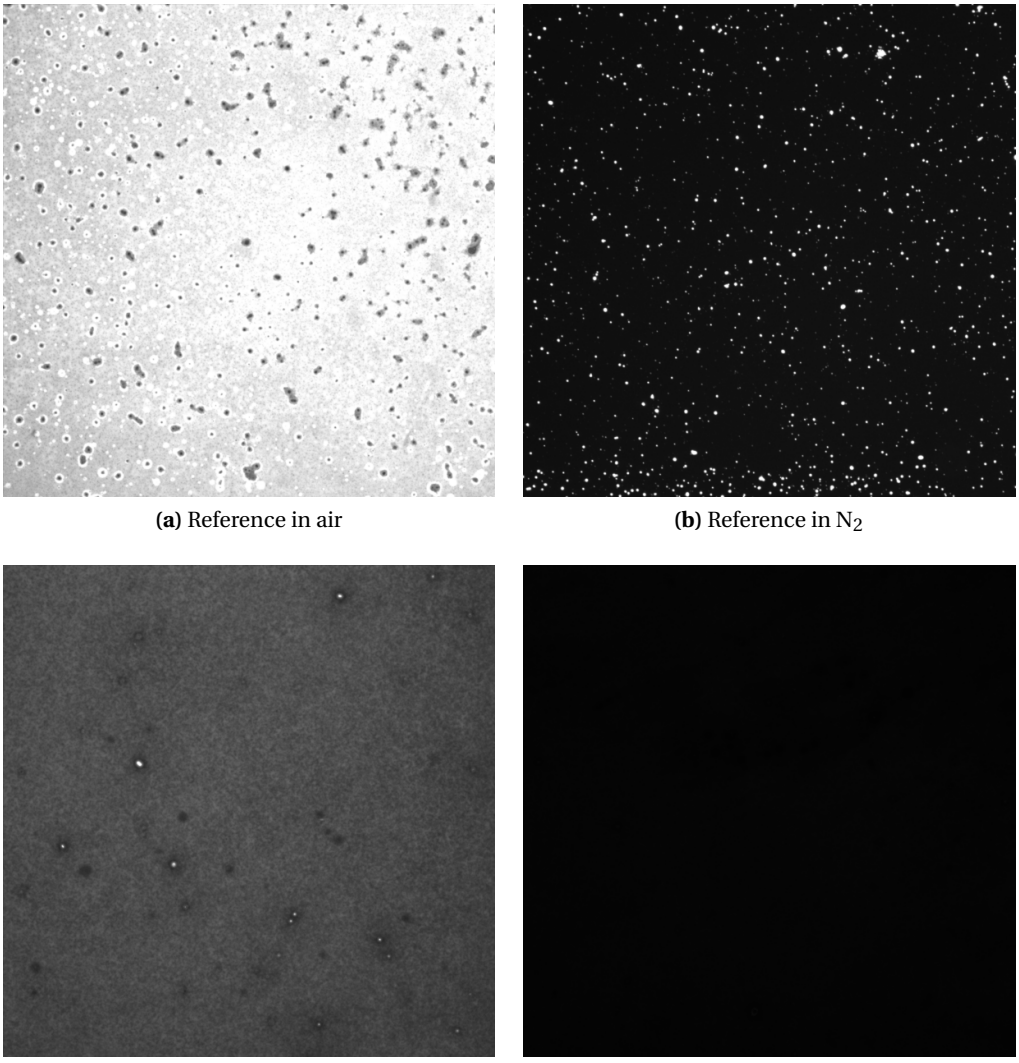

(a) Reference in air

(b) Reference in N_2

(c) 12% ET in air

(d) 12% ET in N_2

Figure B.13 – PL images of samples annealed in air and N_2, without or with ET inclusion. Images are all scaled to the same brightness. Images were taken through the glass substrate, imaging a region within the metalized cell area. Excitation was with a red LED that was filtered to pass only below 670 nm. Their PL was imaged with a Nikon camera through a 670-715 nm bandpass filter to only take the high-energy emission tail. The median PL counts for each image are (a): 41416 (b): 2708 (c): 13005 (d): 1284 counts out of 65536 (2^{16}).

The inhomogeneity was not only spacial, but temporal. This is illustrated in figure B.14. PL spectra were measured each second for one minute, and the peak location and intensity are plotted for the same samples as above. It can be seen that again the ET doped samples are stable in both intensity and emission energy, while the baseline samples are not. In the case of air annealing, the E_g shifty by over 20 meV during the minute, while the intensity remains relatively constant. The N_2 annealed, however, has a 30 second period in which a very bright and low-E_g peak appears and disappears (60x brighter and 38 meV lower). After this, the intensity and E_g return to how they were prior, although the E_g is remains slightly shifted from its initial value. We attribute both the temporal and spatial PL intensity variation to the formation and breakdown of highly-emissive low-E_g states [76] due to un-bound mobile ions, which would normally be slowed by oxygen binding [124], [249].

There remain questions about ET and its role in the perovskite, but overall it is not a potential replacement for O_2 exposure. The remaining questions are diverse, such as why the PL improves but the V_{OC} drops, why the E_g shifts slightly (figure 2.24c), how the crystallization kinetics change to create the more uniform layer (figure 2.26), how much of the PL enhancement is due to better crystallization vs chemical passivation, how much ET remains in the material after annealing, and why the PL can stay low in N_2 while the cells work. These are interesting and answerable questions, but ultimately got left to the side due to the failure of ET in cells.

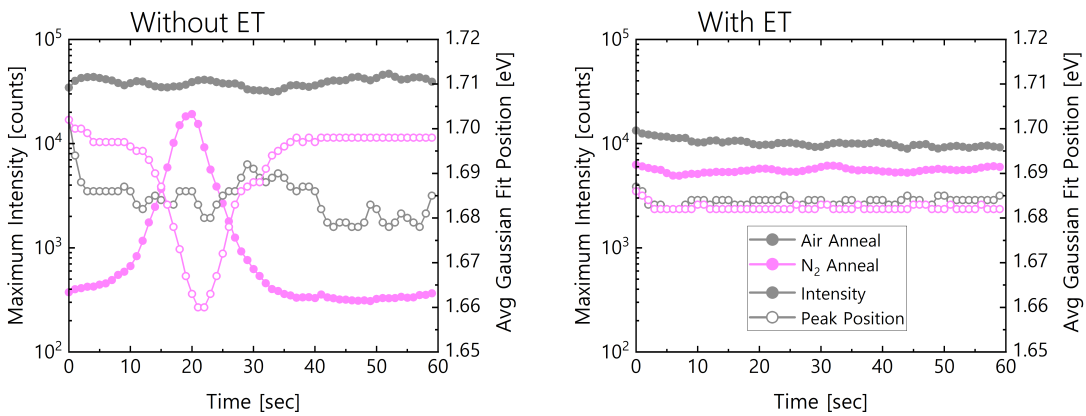

Figure B.14 – PL intensity and peak position over time, for perovskites annealed in air or N_2, with-/out ET doping. For the same samples as shown in figure B.13, PL spectra were measured through a microscope objective over time, using a 514 nm laser at 1-sun intensity. From these spectra, the intensity and peak emission energy were extracted. These plots show both, with the maximum intensity plotted on the left axis and the emission peak position plotted on the right axis. Measurements were taken on the metalized area of the cell.

B.5.1 Preparation of Samples for XPS Measurement

In section 2.3.2 we performed extensive characterization of air and N_2 annealed perovskite layers in order to determine what caused the difference in their performance. One of the techniques used was to deposit perovskite on TEM grids and try to measure XPS of the bottom surface. TEM grids are thin copper disks with a mesh, which then has a thin (8 nm) layer of carbon lain over the holes (from Plano). We hoped that this would hold the perovskite while also being thin enough for the X-ray beam and resulting released electrons to pass through. The measurements and interpretations are again in section 2.3.2, but here we show SEM images of a test deposition on this structure, for the sake of confirming the validity of the deposition and method. These images are in figure B.15. In (a), the full substrate shows the normal formation of the perovskite over the substrate area, but that the TEM grid is still visibly copper-colored. This would indicate the lack of perovskite covering it, but the inconsistency of this color leaves open the possibility of some areas having normal perovskite. In (b), we see that there is indeed coverage of most of the disk. Some areas have the grid visible, while in other areas it is obscured by the covering perovskite. (c) and (d) show areas of bad and good coverage. Normally the perovskite does not have cracks or bright spots on the surface. But still the are of good coverage is in the minority, and less than the measurement beam's spot size of 1-3 mm^2. Zooming in further, (e) shows that the center of the individual squares is largely missing the atypical bright spots. Looking closer though, and (f) shows that indeed these spots remain, albeit smaller, over all of the perovskite area. These are predicted to be excess precursors, and their matching of the TEM grid pattern suggests that indeed the TEM grid did affect the perovskite formation. Overall, we still used these for measurement, as it was the only option for preserving the bottom surface for measurement without exposing to air.

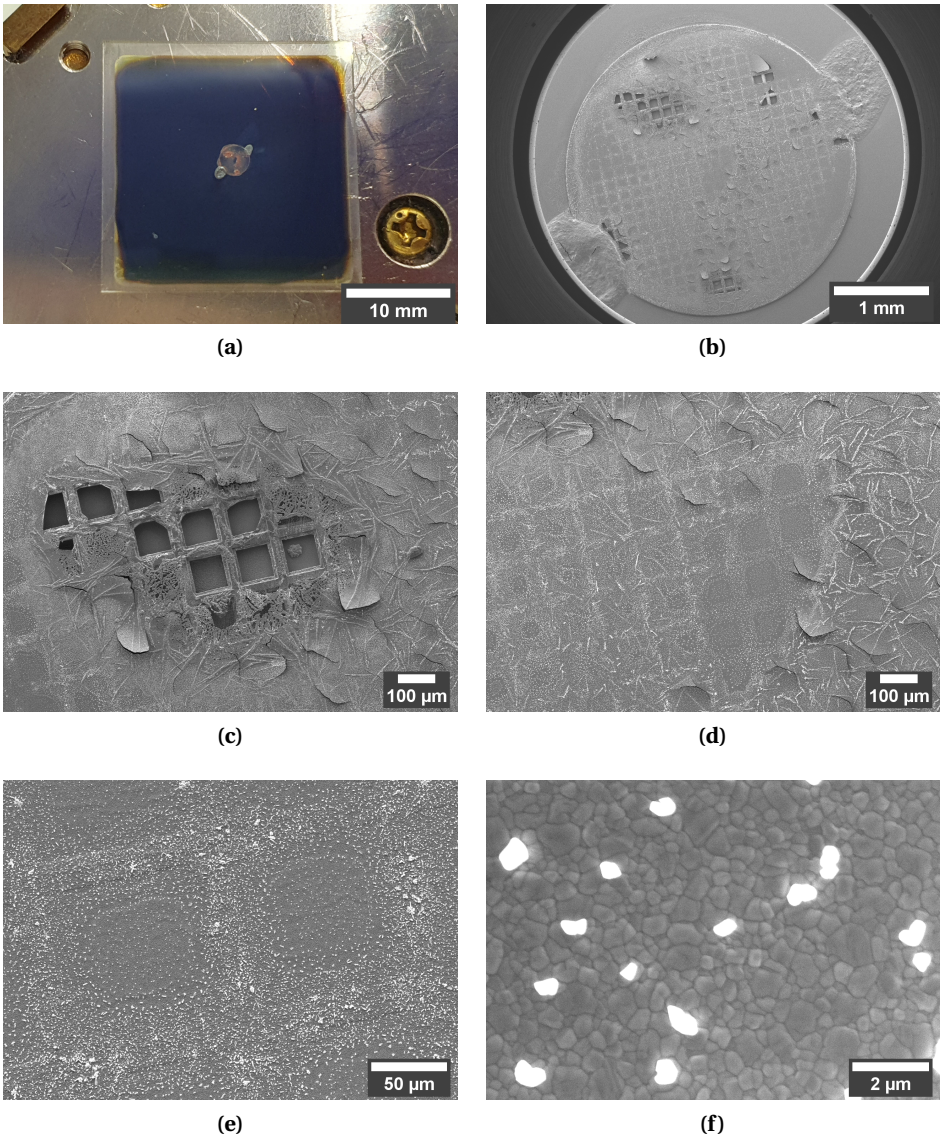

Figure B.15 – Images of perovskite deposited on a TEM grid for XPS measurement. (a) shows an image of the sample taken with an ordinary camera. The TEM grid is the central disk, and is secured in place with two dots of conductive carbon adhesive. (b) shows a low-magnification SEM image of the entire TEM grid. (c-d) show two regions of the grid at the same magnification. (e) shows a magnification of two grid squares, and (f) shows the center of one square, zoomed enough to see the perovskite domain structure.

B.6 Template Evaporation and Uniformity - Effects in Cells

Some checks were made to confirm the reliability of the PbI_2 PVD template. First we varied the deposition rate and composition for the single junction flat recipe (normally 180 nm PbI_2 thickness, 10%vol CsBr). First, we evaporated four template layers with different amounts of CsBr and at different rates. The SEM images of these templates and the resulting perovskite layers are shown in figure B.16. In the template, we observe that the condition closest to the baseline (13% in this case) was the most porous, and that others appear mostly compact. But once the perovskite is formed, there is little visible difference. These layers were then finished into cells, and the results are shown in figure B.17. Overall, the baseline appears to be the best, in line with its porous appearance. We theorize that there is a relationship between porosity and end perovskite material quality, as this would aid in the intermixing of the PVD and SP components. This has been credited with aiding interdiffusion in the past [149]. In the same test, we also tried to observe if there were differences in the template formation when forming on a layer of 2D perovskite, following the results of section B.2. There was a clear effect in the template with no CsBr, but the same was not observed in the templates which did include CsBr. The cell results did not show meaningful differences between these conditions, and the perovskite is visibly the same according to SEM. Overall, these observations show that the template formation does matter to the end perovskite behavior, but the number of relevant variables was so large that the project was deemed too time-consuming to fit into the plan for this thesis work.

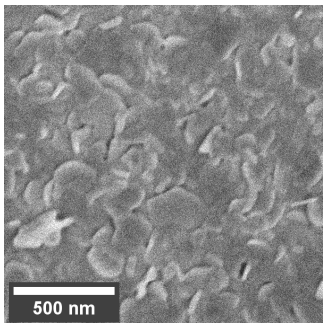

(a) Template with 0% CsBr

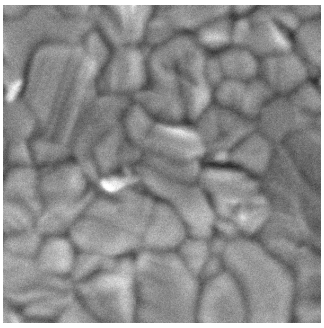

(b) Resulting perovskite

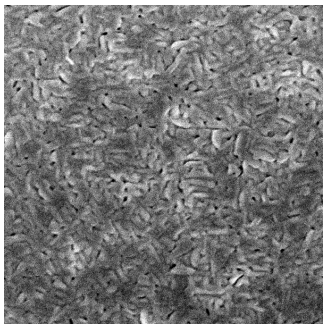

(c) Template with 13% CsBr

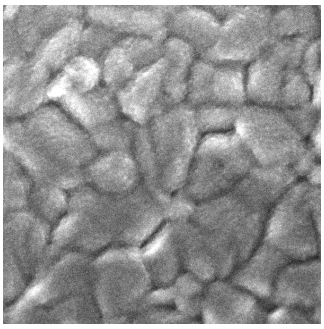

(d) Resulting perovskite

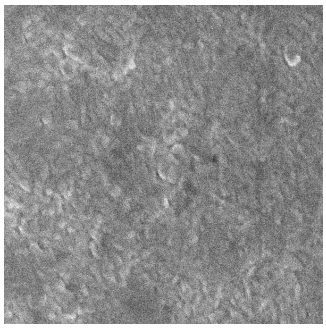

(e) Template with 25% CsBr

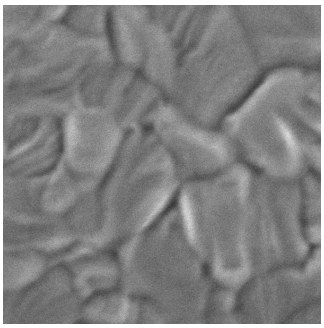

(f) Resulting perovskite

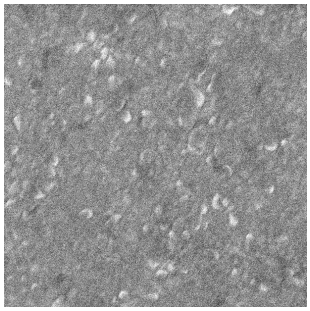

(g) Template with 13% CsBr, evaporated at 5.0 Å/s

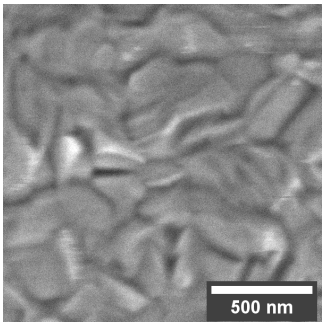

(h) Resulting perovskite

Figure B.16 – SEM images of various template layers and the resulting perovskite. Templates were deposited on NiO_X with 0, 13, or 25%vol CsBr relative to PbI_2, and at either 1.0 or 5.0 Å/s. All images are to the same scale. We note that only image (d) is taken with a C_{60} layer above the perovskite, all others are the bare film.

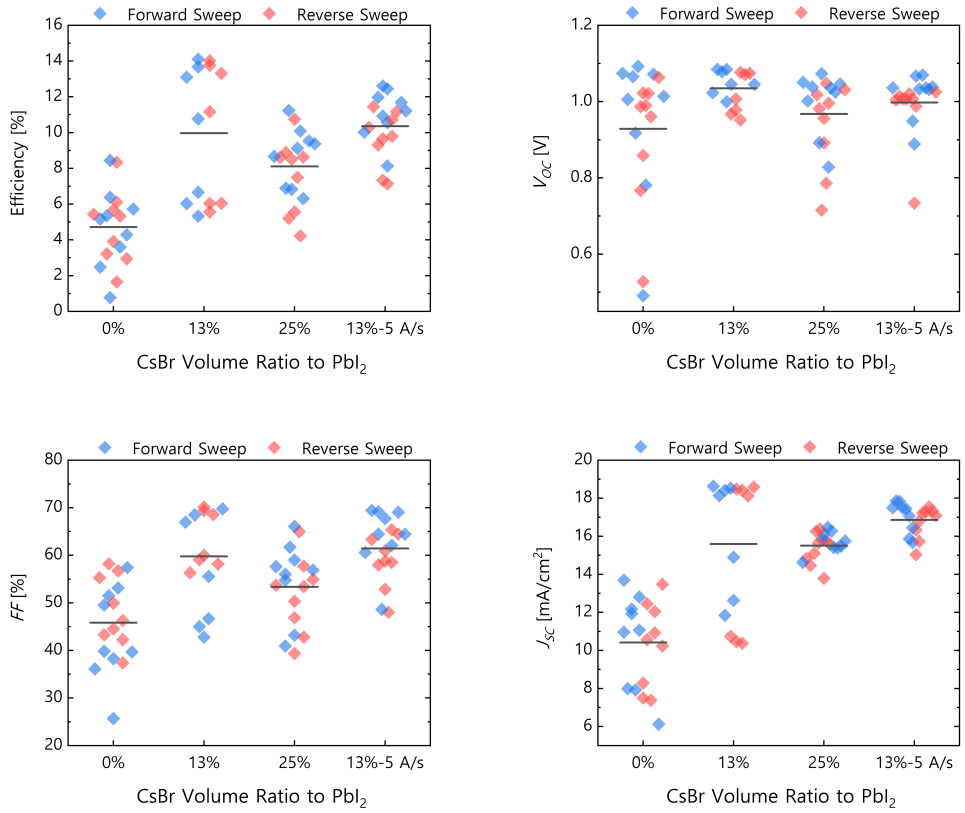

Figure B.17 – Cell performance for PSC made with differently deposited PVD template layers. The templates were the same as shown in figure B.16. They were all spin-coated at 4000 rpm with the same 445 mM solution of 1:2 FAI:FABr in ethanol, and annealed for 20 minutes at 150°C in ambient air.

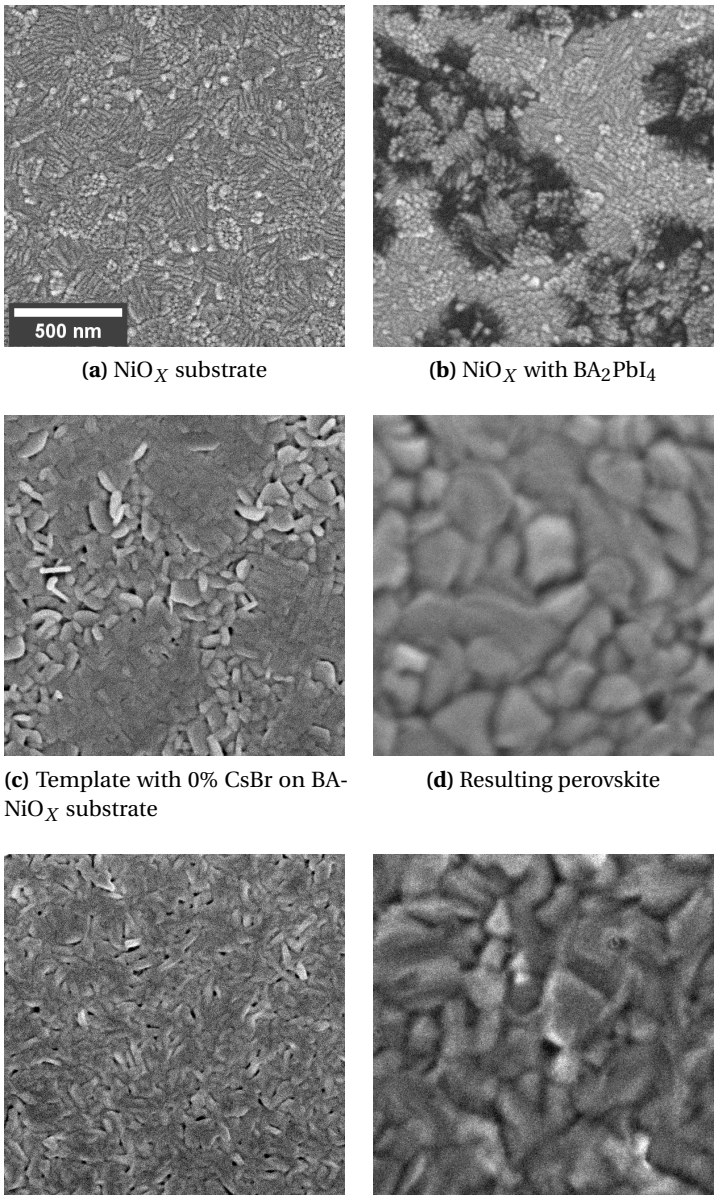

(a) NiO_X substrate

(b) NiO_X with BA_2PbI_4

(c) Template with 0% CsBr on BA-NiO_X substrate

(d) Resulting perovskite

(e) Template with 13% CsBr on BA-NiO_X substrate

(f) Resulting perovskite

Figure B.18 – SEM images of template and perovskite layers deposited on a substrate of NiO_X with 2D perovskite. BA_2PbI_4 was deposited on the NiO_X layer via spin-coating according to the same recipe as in figure B.5. Then a PVD template was deposited with 0, 13, or 25%vol CsBr relative to PbI_2, and at either 1.0 or 5.0 Å/s. All images are to the same scale.

The second test was to examine the uniformity of the evaporation, specifically with regards to c-Si texture. We wanted to know if the slight differences in thickness observed across substrate area and pyramid faces was relevant to cell performance. Examples of the observed inhomogeneity are shown in figure B.19. First, the perovskite does not visibly change from one pyramid face to the other. This does not mean that there is the same amount of template deposited on inward and outward (relative to the circular sample holder) facing sides of pyramids, but that after conversion there is not a visible difference in the material thickness. There may be different chemical balance between template and organo-halides on the opposite faces, which we test for below. Second, the C_{60} was observed to deposit more on the inward-facing pyramid face than the outer, by about 30%. This could affect cell performance across each individual pyramid, which again is tested for below. Finally, the lower row of images in figure B.19 shows the same template in cross-section SEM, measured at three points across the substrate. The outer/inner edge again refers to whether that side of the substrate was closer to the edge or center of the circular sample holder of the PVD step.

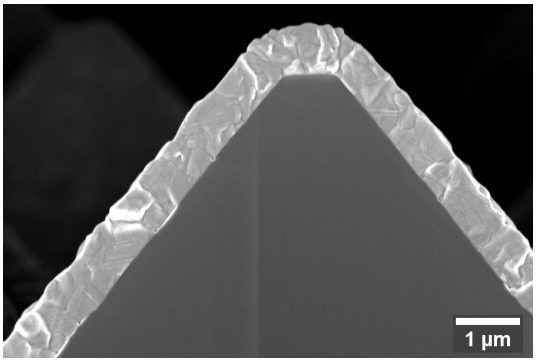

(a) Perovskite on c-Si

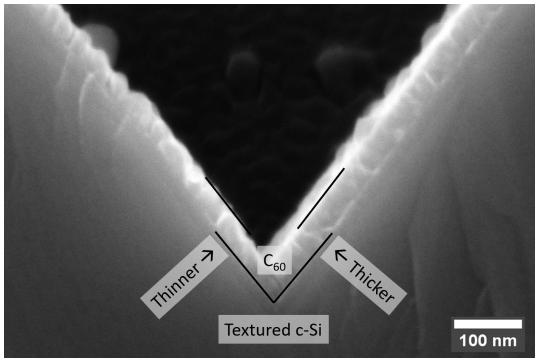

(b) C_{60} on c-Si

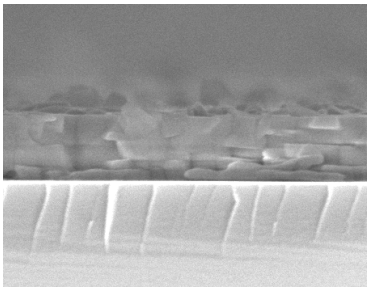

(c) Outer edge, 224 nm

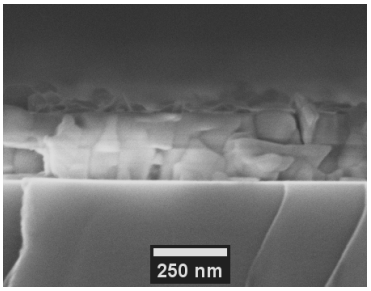

(d) Center, 227 nm

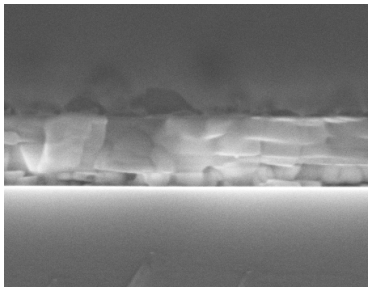

(e) Inner edge, 232 nm

Figure B.19 – Perovskite, C_{60}, and template layers as deposited on textured c-Si. The perovskite layer was formed according to the final recipe of section 4.2, with a 600 nm PbI_2 template, 150°C annealing, and no FBPA. The C_{60} layer measured 52 nm on a flat substrate, and was uniform across the substrate area. The thicknesses for the inward facing edge was 37.6 nm and for the outward facing edge 28.2 nm. The templates come from the same substrate, and were measured near the outer edge, center, and inner edge of the substrate. The scale is the same for all.

To test the effect of these non-uniformities in cells, we fabricated single junction cells on c-Si texture with the cell area aligned with the radius or tangent lines of the circular sample holder plate. The cells in question are shown in figure B.20. This way, the radial cells would have a thickness gradient along them and the tangental cells would not. The cells were measured in JV and EQE, and results are shown in figure B.21. The tangental cells to have higher current than the radial cells. We attribute this to the thickness gradient across the radial cells resulting in thinner perovskite towards one end of the cell area. This part of the cell would be thinner and absorb less, lowering the cell current. To quantify this loss, we measured EQE across the cell area. A diagram of how the EQE measurement beam was aligned to the samples is shown in figure B.20. The top two EQE plots in figure B.21 show the three measurements for each of the best radial and tangental cells. For the radial cell which has the thickness gradient, there is a slight EQE boost in the middle of the cell, and it is lower on either side. This supports the idea that perovskite conversion is finely tuned, and the outer/inner sides have either too little/much template for the organo-halide, while the center is well balanced. In contrast, the tangental cell does not have these variations, and all the curves align. So we conclude that there is some thickness gradient in the template across the substrate area, and that this is relevant to the perovskite formation and cell performance in these areas. Thus cells should be made with smaller dimensions to minimize these effects. An example of the typical 1.02 cm^2 square cell design is shown below the long cells in figure B.20.

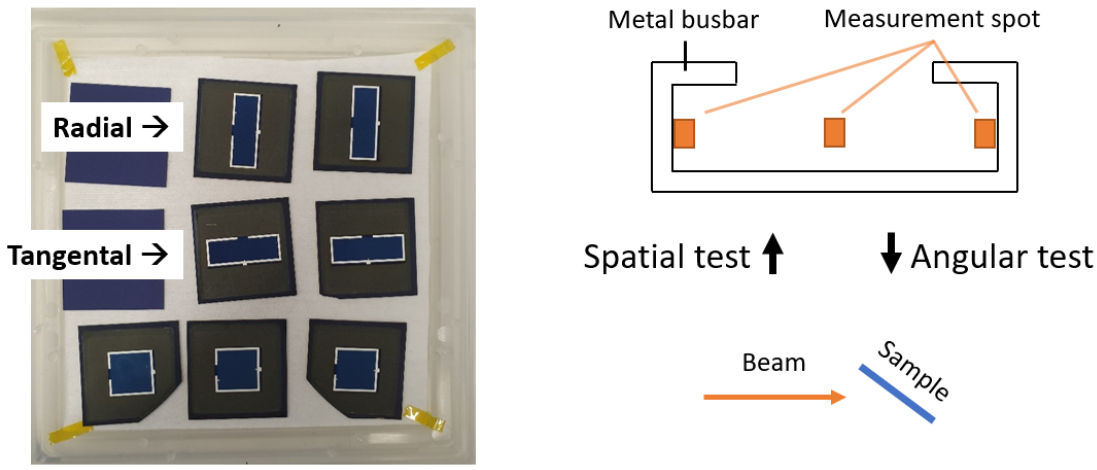

Figure B.20 – Diagram of the sample preparation and measurement to determine PVD uniformity. Single junction cells were fabricated on symmetric SHJ with a 1.03 cm^2 "long" cell design. They were positioned with the long axis either radial or tangental to the circular sample holder of the PVD deposition, on the outermost position on the circle. Once finished, the EQE of the cells was measured in three locations, illustrated relative to the metal busbar as the "spatial test". An "angular test" was also performed, where the sample was oriented so the illumination beam would primarily strike the pyramid faces which were pointed outward or inward (relative to the circular sample holder) during the PVD step.

The second part of the test was to examine the pyramid faces, due to inhomogeneity in the C_{60} and potentially the template. For this, we measured the EQE with the cell oriented according to the diagram in figure B.20. This way we could selectively irradiate the sample on the pyramid faces which were facing outward/inward during the PVD step. This was performed with the measurement location fixed on the outer edge of the radial sample, to maximize the effect. The results are in figure B.21, and show that in fact the outward face has the best EQE. Although we hesitate to draw strong conclusions from this single measurement, as it is likely more dependent than the others on optics and the exact angle of measurement, which was not precisely controlled. But overall, there is not a major loss on the outward face, which suggests that any effect of pyramidal inhomogeneity is minimal.

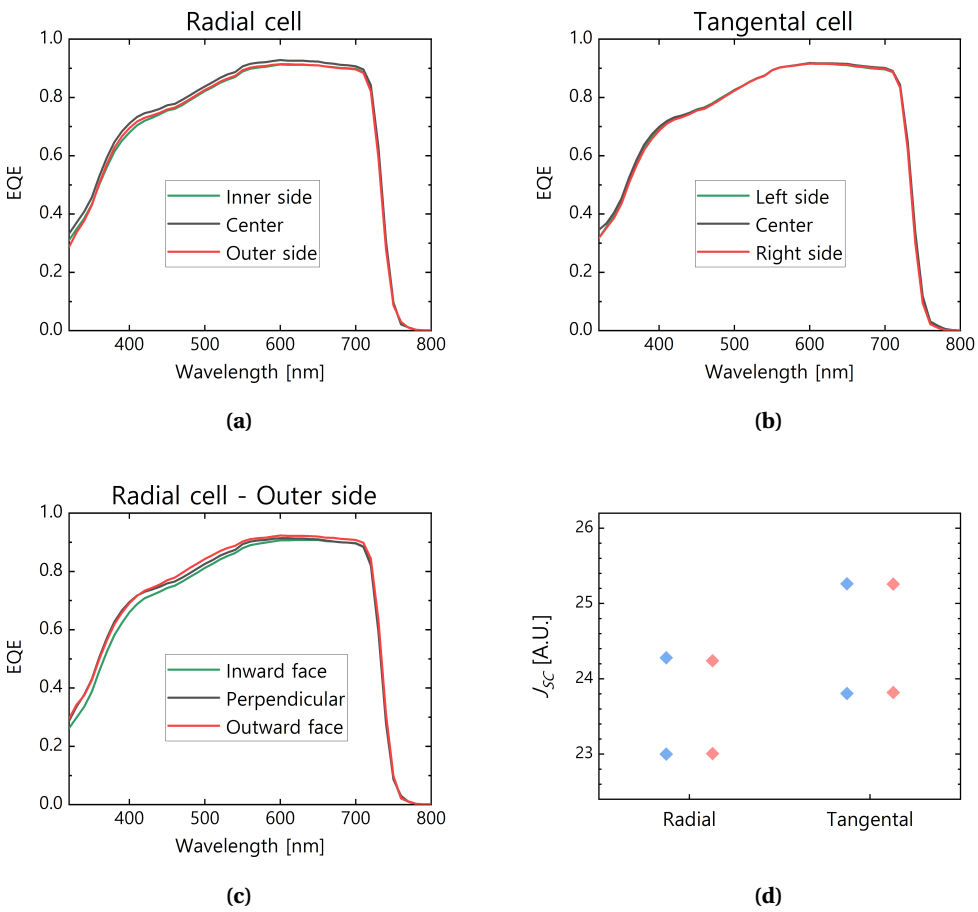

Figure B.21 – EQE and *JV* results for the cells described in figure B.20. EQE spectra were measured in three positions each for the radially and tangentally oriented cells. Inner/outer positions are in reference to the circular sample holder of the PVD step. The *JV* data were taken without a mask, and thus have higher current density than normally possible.

B.7 Further Tests of PSC on Textured ZnO

Here we show other tests that were performed in relation to putting perovskite absorbers on ZnO-textured substrates. The first is simple low-illumination JV measurements of the champion hybrid-method cells which were previously shown in figure 3.25. The low-illumination measurement serves to highlight the impact of shunts on the JV curve, and these results are shown in figure B.22. From this, we see that both the cells with and without an Ar-etch suffer from shunting, relative to the flat baseline case. In the full-illumination JV, the Ar-etched cells suffered less from shunting, but this measurement confirms that they did still have shunts, but that those were just less impactful than for the non-etched case.

A secondary test which deserves mention is that of covering up shunt paths in the textured PSC with a fully evaporated perovskite. We can evaporate a 1:1 molar ratio of CsBr and PbI_2 onto the perovskite after the main PVD/SP deposition is finished. In theory, this will form a perovskite and cover shunt paths. The results, shown in figure B.23, reveal this strategy to be largely unsuccessful. The whole batch suffered from an S-shape in the JV curve, but this does not confound the overall result that the inorganic evaporated perovskite did not convincingly reduce shunts. This is illustrated by the extracted R_{SC} values, which show that in all cases the ZnO-textured PSC were much more shunted than the flat references (R_{SC} should be maximized, and lower values indicate shunting). But also the 2-layer PSC performed worse than the baseline perovskite in R_{SC} and efficiency. This is likely due to significant crystalline disorder induced by having two perovskites with very different compositions in contact with eachother. The two layers likely exchange ions and create disorder within eachother.

The last test of ZnO-textured PSC that we will show is that of semi-transparent (ST) cells. These were discussed on the level of optical simulation in section 3.2.2. At that point, we expected from simulation that the texture of ZnO substrates would cause enough light scattering to compensate for the removal of the metallic rear reflector. However, this was not the case in practice. We see in the EQE spectra of figure B.24 that the same red-wavelength loss occurs in

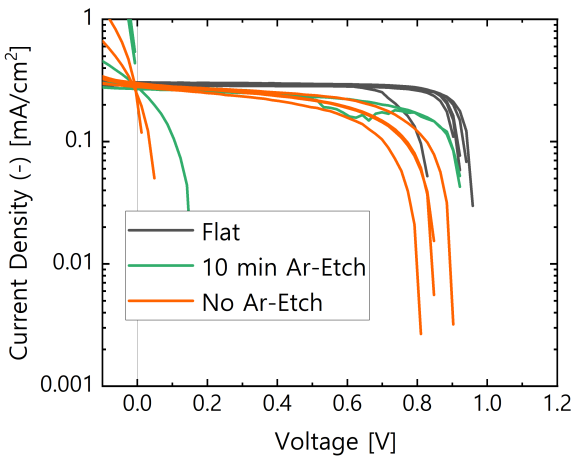

Figure B.22 – Low-illumination *JV* measurements for PSC on flat ITO or textured ZnO substrates. These cells are the same as were shown in figure 3.25. They were measured through a metallic mesh filter that passed about 1% of light.

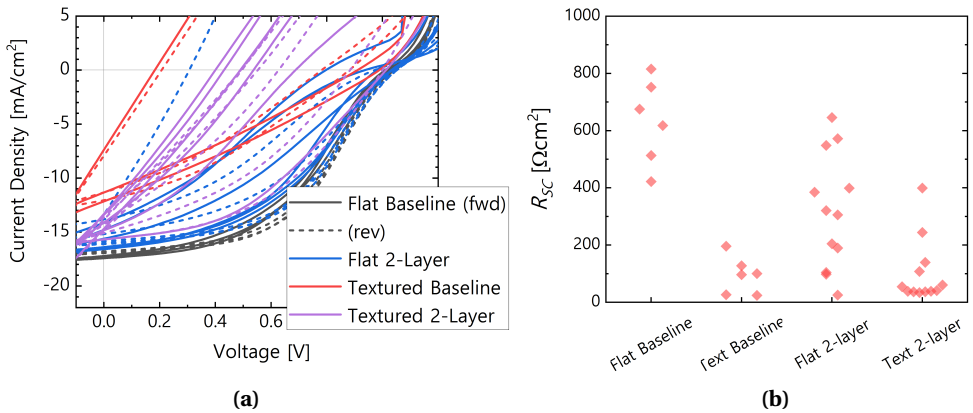

Figure B.23 – *JV* performance of PSC on ZnO substrates using a 2-layer perovskite. PSC were made on flat and textured substrates, and upon some samples were evaporated 30 nm of 1:1 molar ratio of CsBr and PbI_2. This was intended to form a perovskite layer which would protect against shunts. The resulting JV performance is shown in (a), and the extracted R_{SC} values are plotted for each case in (b).

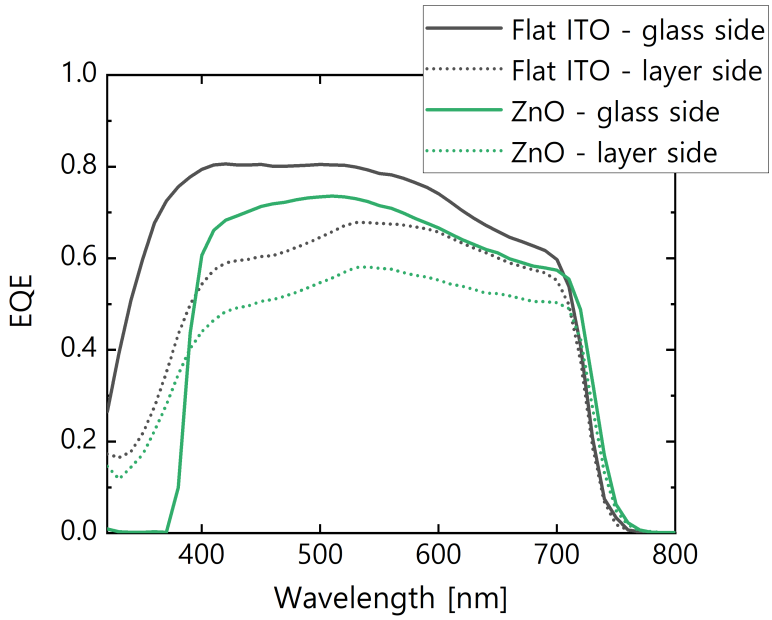

Figure B.24 – EQE spectra of flat and ZnO-textured PSC made with a transparent rear electrode. PSC were made on the standard flat glass/ITO and textured glass/ZnO/ITO substrates, and after the perovskite was deposited LiF/C_{60}/SnO_2/IZO/Ag fingers. EQE was measured with illumination coming from both sides.

textured cells as well as the flat ones. The difference between the simulation and experiment likely comes from the simulations assuming that all interfaces above the ZnO were conformal to the same morphology, which we found in experimentation to be false. Evidence of this can be seen in the side-view SEM of figure 3.18, where the top surface is considerably smoother than the ZnO surface beneath.

B.7.1 Other Limitations and Challenges of the PVD/SP Method on ZnO

Here we show other measurements that explain the difficulties of applying the hybrid PVD/SP method to textured ZnO substrates. A main issue was the full area conductive ZnO layer. This meant that electrically contacting the cell must be done with extreme care, as piercing through the cell stack with the measurement probes would connect both electrodes and instantly shunt the device. Attempts were made to electrically separate the regions where the positive and negative probes contact the substrate, by scribing either with a scalpel or diamond tipped pen. In practice, this increased shunting to nearly 100%. This was due to the thickness of the ZnO layer (around 2 µm) compared to the thickness of the cell (less than 500 nm). At the scribe line, a relatively huge cliff of ZnO was exposed to air. The perovskite failed to cover this, leaving the cliff face exposed to direct contact with the evaporated Ag top electrode. An example of this is shown in figure B.25, where a full PSC was scribed, to show the difference between the layer thicknesses.

Eventually a solution was found, via an HCl etch of the ZnO. This produced a ramp instead of a cliff face. The HCl acid etch was an aqueous solution that we dripped onto the area of the ZnO layers which would later be contacted by the measurement probes (roughly 5 mm at the edge of the substrate). This removed the ZnO from that area, and created a ramp up to the main layer height instead of the cliff obtained from scribing. Evidence of this is the lack of

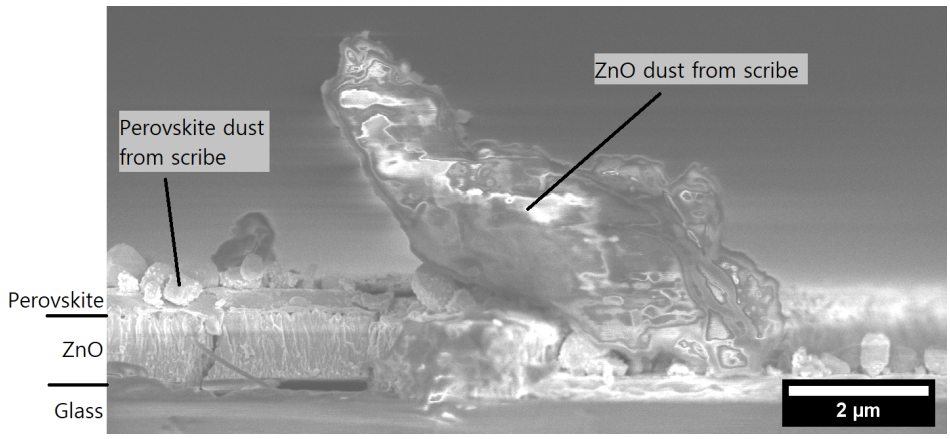

Figure B.25 – SEM image of a scribe line through a ZnO cell. ZnO layers were scribed with both a diamond pen and a scalpel in attempts to isolate the front and rear contacts of the cell. This image shows a cell scribed after production, to highlight the difference in scale between the cell, electrode, and ZnO layer thicknesses.

shunt formation around the ZnO edge in figure 3.29. However, both of these advancements came over a year after the champion cells of figure 3.25 were made. Thus, for most of the development, the best known strategy was to be careful not to apply enough force to scrape through the sub-micrometer PSC when placing the measurement pins, and be lucky.

The ALD AlO_X layer (discussed in figure 3.29) which electrically decoupled the ZnO had other benefits as well. The chemical stability of the cells improved, which we attribute to the AlO_X layer blocking the diffusion of Zn ions from the ZnO into the perovskite layer or vice versa. ZnO exposure can otherwise damage perovskites [231]. We previously relied on the ITO layer to act as a buffer, but the AlO_X was an improvement off of that. Evidence of this is shown in figure B.26, where cells without the buffer layer have localized degradation immediately. Still, after some time, the ZnO-textured cells all degraded faster than the flat cells, regardless of the AlO_X protection. This is shown on the right side of figure B.26, where all cells have the AlO_X buffer.

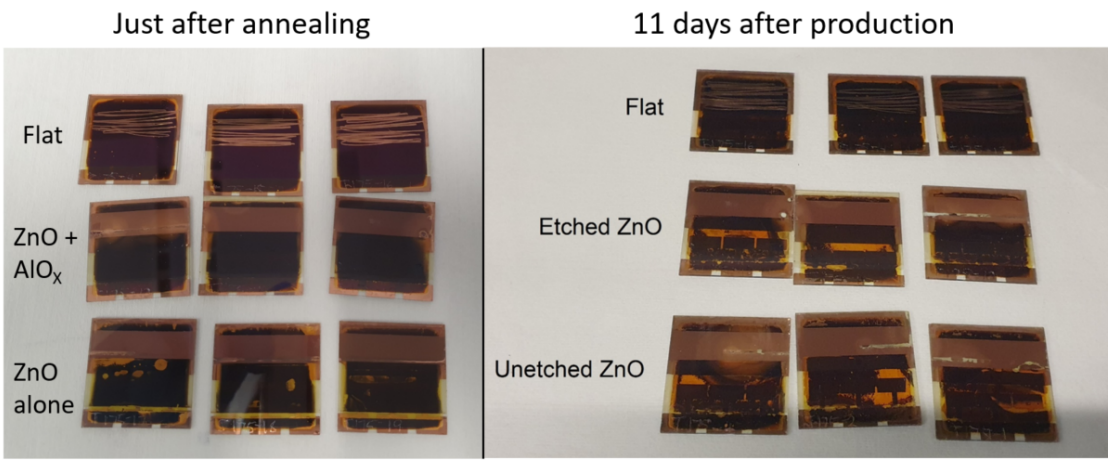

Figure B.26 – Images of PSC with or without ZnO degrading over time, viewed through the glass substrate. All samples were produced as part of the same PVD/SP batch. Most samples included the ALD AlO_X buffer layer atop the ZnO, but three samples were left without as a reference. These developed yellow spots during annealing, while none were visible on the samples with a protective layer. Over one week after production (storage in N_2), the flat cells remained dark while all ZnO-textured cells are visibly degraded. In the right-hand image, all cells have the AlO_X buffer layer.

B.8 Other Measurements of ITO/SAM as HTL

In sections 2.3.1, 2.4.2, and 4.3 we discussed the use of SAM molecules as HTL, their effect on interface quality, and how this manifests in PSC performance. Other measurements were carried out beyond the discussed topics, but were not always conclusive or thorough enough for a confident conclusion to be reached. Nevertheless, the measurements contain useful information, and are thus reported here.

The first of these is related to the higher-temperature annealing discussed in section 2.4. In this section, we showed that perovskite layers annealed at 170°C instead of 150°C had better PLQY, and cells using these layers had lower R_{OC} and better FF. We attributed this to better transport in the perovskite, but this is not the whole story. We did not directly measure charge transport, only the full stack resistance. Therefore we must control that the other layers are not responsible for the reduced resistance. The first test was to the ITO, which we found to not change with annealing in this temperature range (figure B.27). It is known that annealing of ITO layers can improve their conductivity, but that going above a few hundred °C will damage them [243], [250]. Regardless, figure B.27 confirms that the 130°C - 170°C range does not affect the ITO.

Transport in the SAM layer did improve with annealing, enough to explain most of the effect observed in the PSC FF. To test this, we subjected glass/ITO/MeO-2PACz samples to 150°C and 170°C annealing for 20 minutes in N_2, to mimic what they would normally experience during the main perovskite annealing. Then, the deposition of PVD/SP perovskite continued as normal, but using a 130°C main annealing step to form the perovskite layer, to avoid exposing the un-annealed SAM to higher temperatures. We found that this similarly improved the FF and R_{OC} of the PSC. This is shown in figure B.28. As expected, the 130°C annealed perovskite produced poor FF, but this was improved in the cells with an annealed SAM layer. The FF improved by 10% absolute, and the R_{OC} reduced by one third. This mimics the improvements

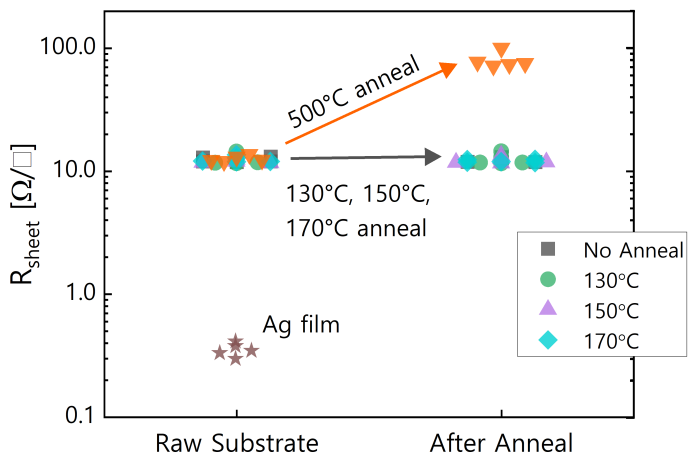

Figure B.27 – Sheet resistance measured for ITO substrates before and after annealing. Standard glass/ITO substrates are obtained from Kintec, and rated at 15 $\Omega/\square$. The sheet resistance was measured at five points across each substrate, then they were annealed in an N_2 environment, and measured again. The values were obtained on a 4-point probe measurement setup, using a Keithley 2601 Sourcemeter and Keithley 2700 Multimeter.

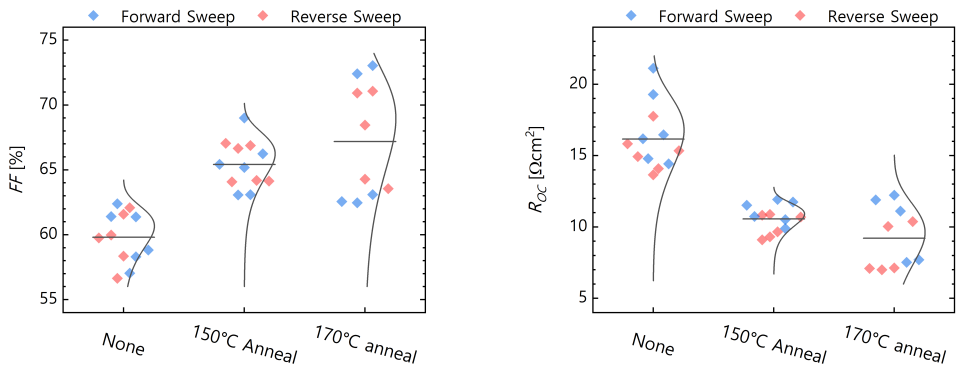

Figure B.28 – Effect of annealing the SAM layer on cell performance. All cells were annealed at 130°C for the interdiffusion and crystallization of the perovskite. Before that, The glass/ITO/MeO-2PACz substrates were annealed alone at 150°C, 170°C, or not at all. Normally, the samples are annealed at this stage for 10 minutes at 100°C, but here certain samples received a second annealing in N_2 for 20 minutes, before the perovskite deposition.

seen in the main text (figure 2.33), largely invalidating the claims of section 2.4.2. Still though, the R_{OC} values do not reach as low and the FF values not as high as the cell results of figure 2.33. This, combined with the knowledge that i) the perovskite quality alone is better when annealed at higher temperature (PLQY of figure 2.32) and ii) the HTL and perovskite layer formation are not independent variables; lead us to conclude that the improved FF of PSC with 170°C annealing are partially caused by both SAM and perovskite layers improving their charge transport.

The second effect we discuss here is that of different SAM molecules. There are multiple options for SAM materials [56], [111]. These include MeO-2PACz, 2PACz, and Me-4PACz. Each of these is a slightly different molecule with different energy levels and performance in cells [56]. We too compared their effectiveness, and the results are shown here. First, we show the difference between the three molecules MeO-2PACz, 2PACz, and Me-4PACz when deposited on ITO, as well as one condition of MeO-2PACz deposited on 5 nm of NiO_X. In each case, the ITO or NiO_X was deposited directly on the nc-Si recombination junction of symmetric SHJ substrates, as were described in section 4.1. The cell results of these, as measured both 1 and 13 days after cell fabrication, are shown in figure B.29. Initially, the Me-4PACz outperforms the other SAMs, but after some aging, the MeO-2PACz improves to the same level. Also notable, is that the Me-4PACz cells develop a FF hysteresis after aging, which is not present in the other cells or the initial measure of Me-4PACz cells. But overall, the performance of Me-4PACz and MeO-2PACz arrives to about the same point, and therefore we do not conclude that either is significantly better. Another difference between the SAMs is shown in figure B.30. In this measurement, the cells were exposed to light and the V_{OC} measured each 20 ms. The

Me-4PACz voltage reaches a stabilized value in roughly 1 second, while the 2PACz takes about 10 seconds, and the MeO-2PACz close to 100 seconds (except for one outlier). This indicates that the molecules behave differently, despite their similar efficiency numbers.

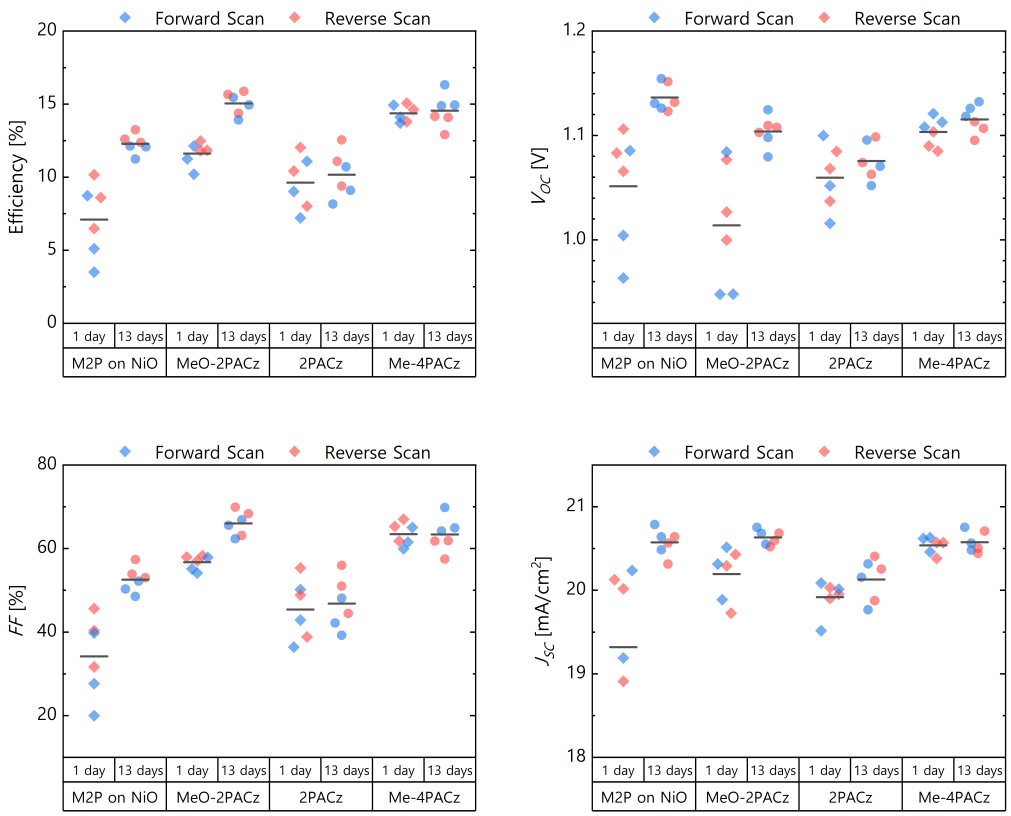

Figure B.29 – Cell performance for PSC made with different SAM molecules, with and without aging. Cells were fabricated on symmetric SHJ substrates, and thus are single junction devices on c-Si texture. The 1.02 cm^2 cell design was used. The only difference between them is the SAM molecule used, along with one case of a 5 nm NiO_X layer being used instead of ITO. The cells were measured 1 day after fabrication, and remeasured 13 days after fabrication.

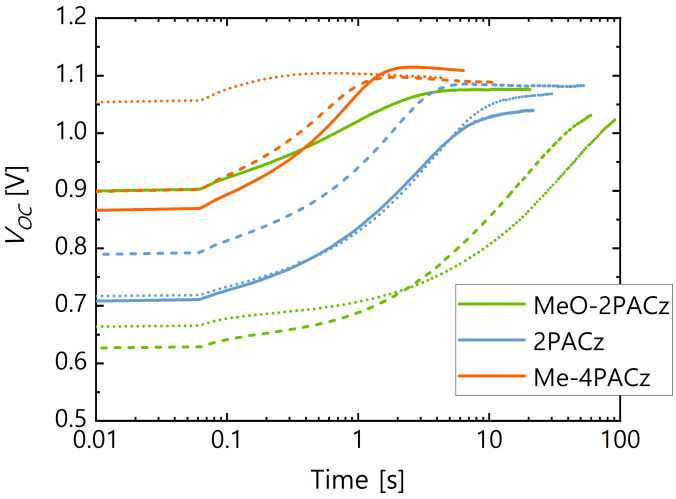

Figure B.30 – V_{OC} tracking measurements for PSC with different SAM materials. The same cells as shown in figure B.29 were measured by exposing to 1-sun AM1.5G light and holding at open-circuit. The voltage was then recorded each 20 ms until the value stabilized. Each line represents a unique cell.

B.9 Observations of Perovskite Degradation

It was typical for perovskite samples to degrade into yellow PbI_2 in the weeks to months after they were formed. Typically such samples were discarded at this point, but occasionally we observed variations in the degradation behavior of samples. Here we present three examples of this phenomenon.

The first is in figure B.31. CTL quadrants were prepared to spatially vary the interfaces of the perovskite. The top left quarter is always glass/perovskite, and all other sections have a CTL above or below the perovskite. The degradation is inconsistent from sample to sample, but there is a discernible trend. The glass/perovskite is the most often yellowed, while the bottom half is the least yellowed. In all cases, the bottom half has TaTm below the perovskite, suggesting that this interface is more stable than that of glass/perovskite. The lower right quarter is more degraded in the second row than the top row. The difference between these groups is that the CTL above the perovskite and only on the right half is TaTm for the top row of samples and C_{60} for the middle row. Thus we believe the perovskite/C_{60} interface to be worse than perovskite/TaTm. This is in agreement with the PL results of figure 2.15 which showed much worse recombination at the C_{60} interface. Contrary to this, the samples annealed in N_2 do not have noticably more degradation despite their significantly worse recombination (section 2.3.2). There is no explanation for why the sample on the bottom right is so well preserved.

The second example is in figure B.32. These are all the same standard PVD/SP perovskite with no additives. The substrate, however, is varied. Most samples are similarly yellowed, except for the glass/ITO/TaTm/perovskite, which is distinctly much darker. This is not to say that the perovskite is perfectly preserved, but it is certainly much less degraded than its counterparts on other substrates. It is unknown why this interface is beneficial, but we can

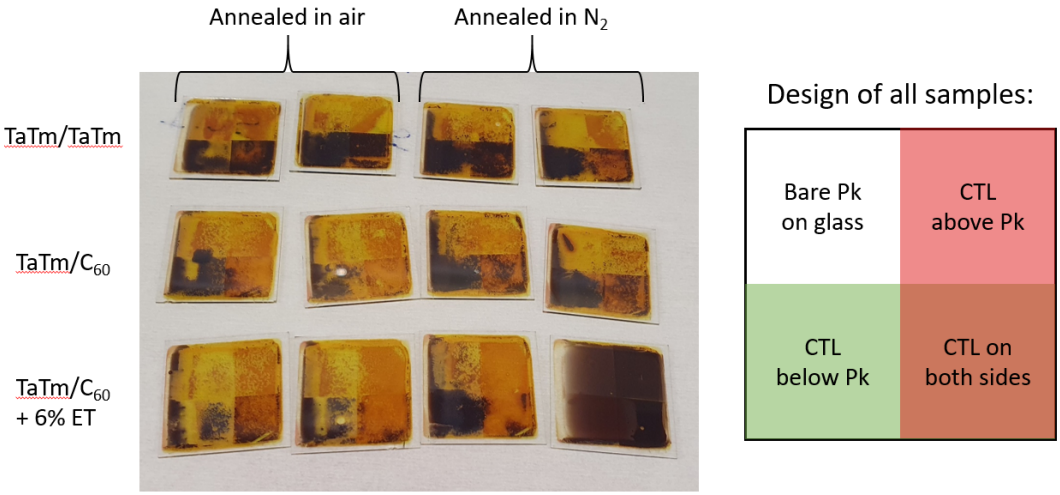

Figure B.31 – Degradation of perovskite on spatially varied substrates after 122 days. Perovskites were formed on CTL quadrants as described in figure 2.14a and diagrammed on the right side here. Two samples each were prepared with the CTLs indicated on the left edge, with the first one below the perovskite and the second one above. The bottom row of samples was made with 6%mol ET relative to FA. No samples have FBPA. Samples were stored together in a regularly opened N_2 flushed box.

theorize that it is either due to the morphology of the ITO being ideal for perovskite growth or the band alignment / band bending that occurs at this interface impedes the formation of degradation-inducing defects.

The last example is in figure B.33. These samples were annealed over a series of temperatures from 100°C to 180°C. These are the same samples as were measured in section 2.4.1, thus they have been through SEM, XRD, and PLQY measurements. We observe that most samples are yellowed, though the lower-temperature samples more than others. But most interestingly, the temperature at which degredation onsets is higher for the samples with FBPA. The without-FBPA perovskite is degraded already at 120°C, but the with-FBPA perovskite remains brown up until 150°C. This is in line with the observations of figure 2.30, which showed that PbI_2 as a degradation product increases with annealing temperature. We predicted that the FBPA-passivated perovskite would be more stable because it had less PbI_2, but did not directly test it. This is a rough confirmation of that idea, and supports the theory that FBPA allows higher temperature annealing and the better perovskite performance that comes with it.

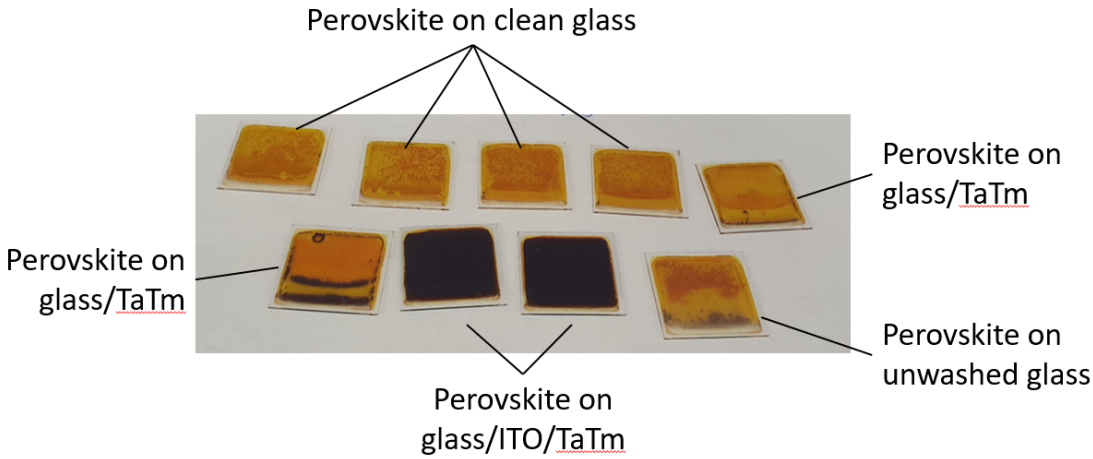

Figure B.32 – Degradation of perovskite with different bottom interfaces after 109 days. Perovskites were deposited on differently prepared substrates and used for PL measurements. No samples have FBPA or other additives. Samples were stored together in a regularly opened N_2 flushed box.

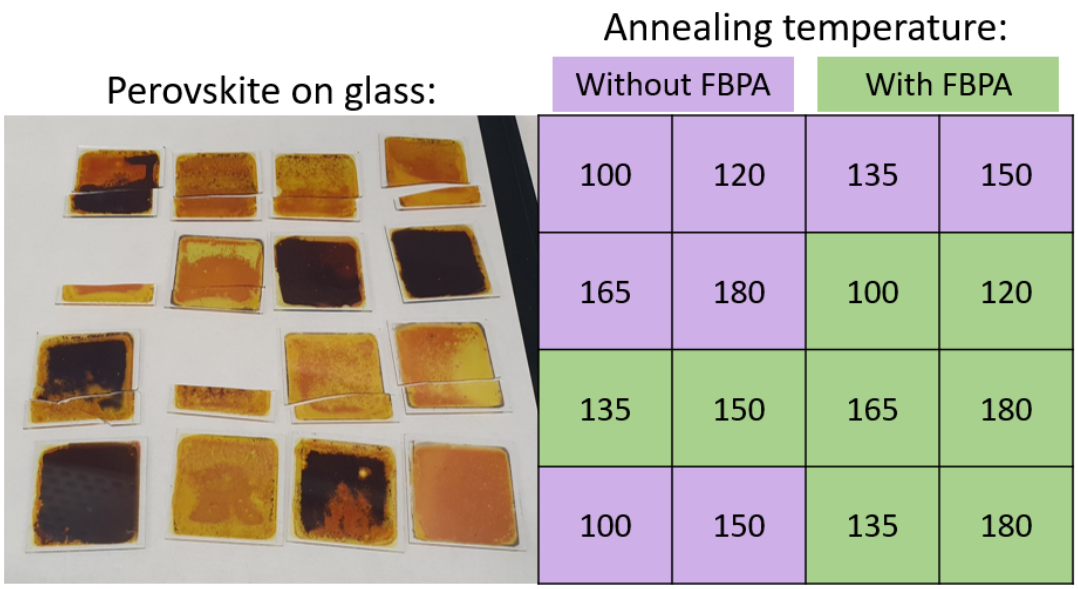

Figure B.33 – Degradation of perovskites with or without FBPA after 109 days. An annealing temperature sweep was performed for perovskites with and without FBPA. The conditions of each sample are given in the adjacent table. These are the same samples as measured in figures 2.29, 2.30, and 2.32. Samples were stored together in a regularly opened N_2 flushed box.

B.10 Optimization of Thick Perovskite Top-Cells

In section 4.2.1 we discussed the development of thicker perovskite layers for the purpose of increasing top-cell J_{SC}. Here we show the finer details of the optimization which were left out of the main text for brevity. We streamline the process by viewing the films from side-view in the SEM instead of making full cells. This removes the convolution of the other layers' quality on cell performance and reduces the experimental time. From these measurements we are able to visually observe the presence or lack of residual PbI_2 at the bottom of the perovskite and in the valleys. This method can later be supplemented with measurements more sensitive to PbI_2 excess (such as XRD) or FA halide excess (such as PSC fabrication). We first investigated the spin speed of the SP step. The results are shown in figure B.34. Excess template is visible as regions of PbI_2 on the bottom surface of the perovskite and particularly in the valleys. PbI_2 is non-conductive, and thus charges quickly in the SEM and appears brighter than the surrounding conductive materials. There is the no PbI_2 visible in the image from 1000 rpm spin speed, but this does not guarantee its absence.

The next processing parameter visited was the pre-anneal. This was previously optimized in section 2.2.2, where we found it to benefit perovskite due to evaporation of residual solvent. Given the increased thickness of the perovskite on c-Si, we tested longer pre-anneal times. The SEM images in figure B.35 show that all layers appear fully converted, with no residual PbI_2 excess visible at the bottom surfaces. However, there are significantly more visible domain boundaries in the sample without a pre-anneal. We attribute the improved morphology to a better mixing of the PVD/SP bilayer prior to the main crystallization. As discussed in section 2.4.2, increased domain boundary density is detrimental to cell performance. This effect is reproduced here, and shown in figure B.36. The shorter pre-anneal was better, and we continued with this optimum. In general this experiment suffered from human error external to the tested variable, as the reference is notably poor, but still there are observed differences between conditions. The sample without pre-anneal performed worse in all cell metrics, and this aligned with visible morphological changes in SEM.

The final parameter considered was the dew point (DP) of the air during the main annealing step. Again, this was previously discussed in section 2.2.2, but likely changes for the case of a thicker perovskite. We tested the standard condition used for flat/thin perovskites (16°C DP) against higher and lower values (figure B.37). This experiment was run in parallel with that of figure B.36, and thus suffers from the same external error which limited the batch performance, but still the differences between conditions is enough to tell us about the effect of the annealing DP. We observe that it is possible to have excessive H_2O interaction during annealing, and a lower DP of about 11°C is best.

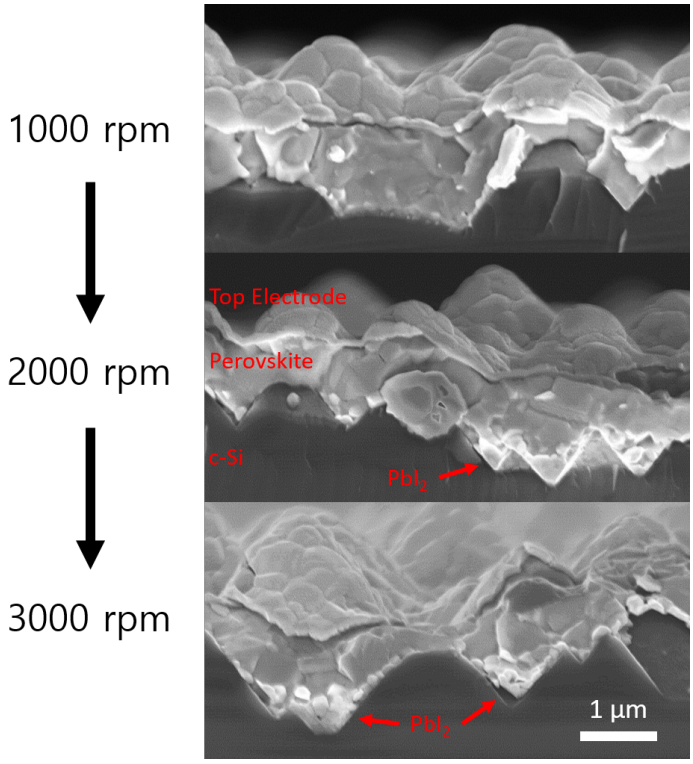

Figure B.34 – SEM side-view images for perovskite on c-Si made with varied spin speeds in the SP step. The solution concentration, annealing, and template thickness were constant between samples. For comparison, in the single junction flat case a 180 nm template is spun at 4000 rpm.

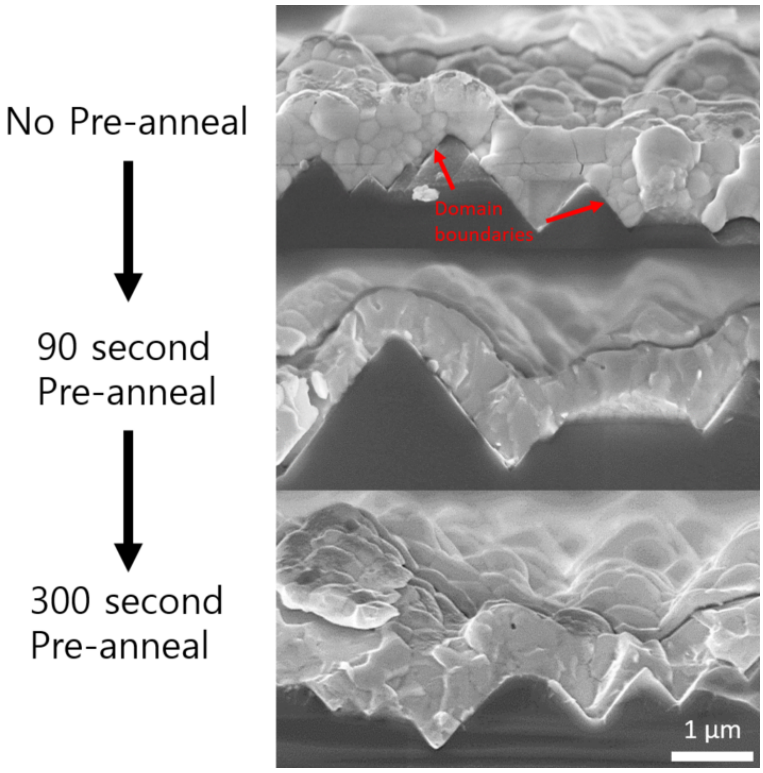

Figure B.35 – SEM side-view images for perovskite on c-Si made with varied pre-anneal durations. The solution concentration, spin speed, and template thickness were constant between samples. For comparison, in the single junction flat case a 15 second pre-anneal is used. The square region in the top image near the bottom middle is due to electron beam damage, and is not a natural feature of the perovskite.

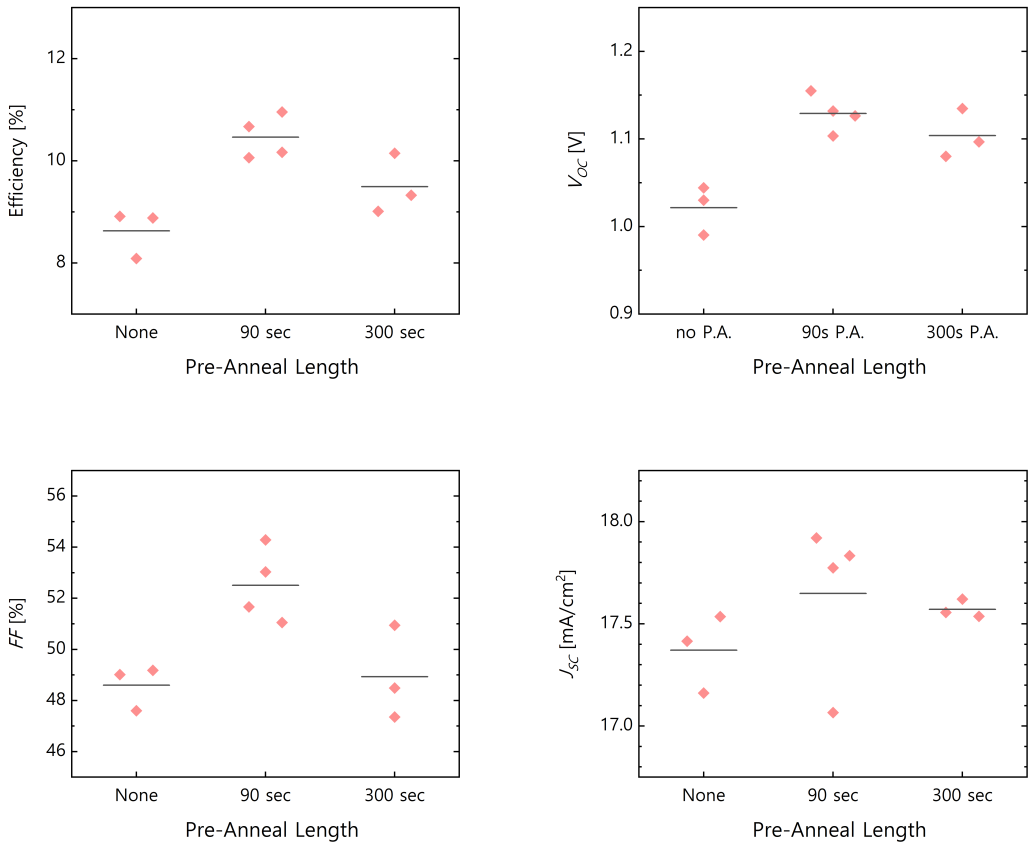

Figure B.36 – Cell performance for perovskite on c-Si made with different pre-anneal lengths. PSC were made on symmetric SHJ, and used the 1.43 cm^2 design. The 80°C pre-anneal takes place immediately after the end of spin-coating, and cells are removed to air for the main annealing only after all were spun and pre-annealed. Only reverse-scan measurements are shown, each point represents a unique sample.

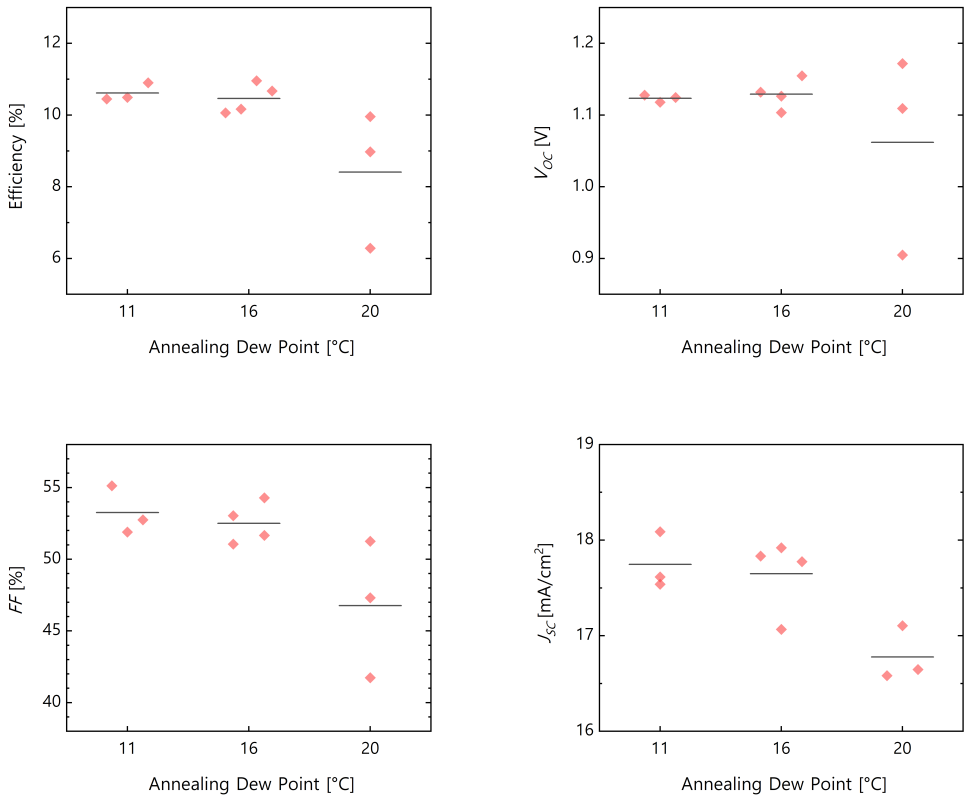

Figure B.37 – Cell performance for perovskite on c-Si made with different DP during the main annealing. PSC were made on symmetric SHJ, using the 1.43 cm^2 design. The main anneal was at 150°C, and DP was controlled by varying the humidity in the chamber in response to the measured air temperature. Only reverse-scan measurements are shown, each point represents a unique sample.

B.11 Parameters of SCAPS Simulations

Here we give the basic parameters of the SCAPS [247] simulations used in section 4.4.2 and figure 4.27 in particular. The cell stack was left contact - SAM - interface - perovskite - C_{60} - right contact - illumination. The main parameters of each layer and their defects are given below:

left contact	work function [eV]	5.3
	majority carrier barrier height [eV] relative to EF relative to EV or EC	 0.05 -0.2484
	optical filter	data of figure 4.7
SAM	thickness [nm]	1.0
	bandgap [eV] electron affinity [eV]	3.0 2.35
	density of states (both) [/cm^3]	1.0E20
	mobility [cm^2/(Vs)] electrons holes	 1.0E-7 20
	defect charge capture cross section (both) [cm^2] energy level below EC [eV] density [/cm^3]	 neutral 1.0E-14 1.5 1.0E15
interface	capture cross section [cm^2] electrons holes	 1.0E-16 1.0E-12
	energy level above highest EV [eV]	0.2
	density [/cm^3]	1.0E13
perovskite	thickness [nm]	700
	bandgap [eV] electron affinity [eV]	1.67 3.9
	density of states (both) [/cm^3]	2.2E18
	mobility [cm^2/(Vs)] electrons holes	 5.0 5.0
	defect charge capture cross section (both) [cm^2] energy level below EC [eV] density [/cm^3]	 single acceptor 2.0E-13 0.9 1.0E13

interface	capture cross section [cm^2] electrons holes	 1.0E-11 1.0E-16
	energy level below lowest EC [eV]	0.05
	density [$/cm^3$]	1.0E10
C_{60}	thickness [nm]	3.0
	bandgap [eV] electron affinity [eV]	2.00 3.9
	density of states (both) [$/cm^3$]	1.0E20
	mobility [$cm^2/(Vs)$] electrons holes	 .01 1.0E-7
	defect charge capture cross section (both) [cm^2] energy level below EC [eV] density [$/cm^3$]	 neutral 1.0E-14 0.7 1.0E16
right contact	work function [eV]	4.2
	majority carrier barrier height [eV] relative to EF relative to EV or EC	 0.3 0.0614
	optical filter	data of figure 4.7

B.12 High-Temperature Tandems with TaTm as HTL

For the sake of combining the best V_{OC} design with the best FF perovskite, we produced tandems with TaTm as HTL and 170°C annealing. This HTL had previously given the highest observed V_{OC}, but had lower FF than cells with SAM as HTL. So it would be the ideal case to achieve high FF on this material, but this was not possible in practice. JV measurements are shown in figure B.38, where the 170°C cells all had a pronounced S-shape and reduced FF. We attribute this to the dewetting of TaTm from the pyramidal surface of the bottom-cell, as shown in figure 4.13. This would choke extraction to a smaller surface area of thicker TaTm, doubly affecting the hole extraction. Thus, in the end it was not possible to combine the best V_{OC} design with the best FF perovskite.

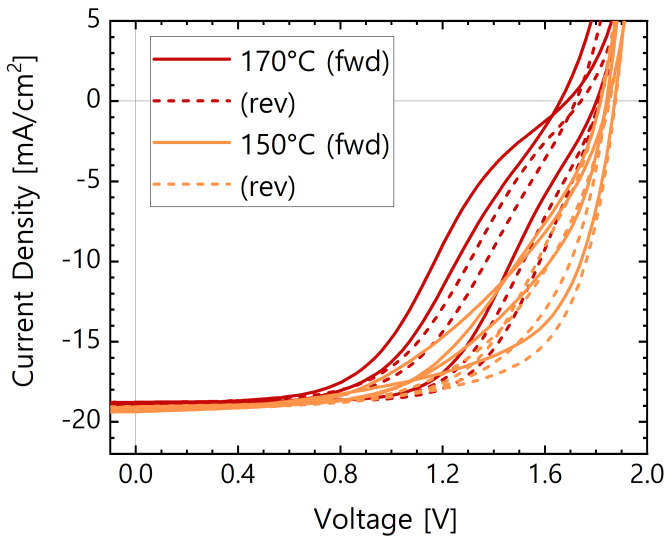

Figure B.38 – *JV* measurements of tandem cells made with different annealing temperatures, and TaTm as HTL. Cells were made in parallel, with only the perovskite annealing temperature changed. 5 nm (measured normal to the c-Si pyramid face) of TaTm was evaporated as HTL. It is expected that the S-shape in the 170°C JV curves is induced by dewetting of the TaTm, which is already known to be present as low as 150°C, shown in figure 4.13. These cells used the 1.02 cm^2 front electrode design.

Bibliography

[1] Working Group 1, "AR6 Climate Change 2021: The Physical Science Basis", The Intergovernmental Panel on Climate Change, Research Report, 2021.

[2] International Energy Agency. (2021). "Total energy supply (TES) by source, World 1990-2019", [Online]. Available: iea.org/data-and-statistics/data-products.

[3] ——, (2021). "Net Zero by 2050: A Roadmap for the Global Energy Sector", [Online]. Available: iea.li/nzedata.

[4] British Petroleum. (2020). "bp Statistical Review of World Energy 2020", [Online]. Available: bp.com/en/global/corporate/energy-economics/statistical-review-of-world-energy.html.

[5] ACS Climate Science Toolkit. (2012). "Energy from the Sun", [Online]. Available: https://www.acs.org/content/acs/en/climatescience/energybalance/energyfromsun.html.

[6] Fraunhofer Institute for Solar Energy Systems. (2021). "Photovoltaics Report", [Online]. Available: ise.fraunhofer.de/en/publications/studies/photovoltaics-report.html.

[7] International Renewable Energy Agency. (2021). "Renewable Power Generation Costs in 2020", [Online]. Available: irena.org/publications/2021/Jun/Renewable-Power-Costs-in-2020.

[8] U.S. Energy Information Administration. (2021). "Electric Power Monthly", [Online]. Available: https://www.eia.gov/electricity/monthly/index.php.

[9] L. T. Murphy and N. Elimä, "In Broad Daylight: Uyghur Forced Labour and Global Solar Supply Chains", Sheffield Hallam University Helena Kennedy Centre for International Justice, Research Report, 2021.

[10] W. Shockley and H. J. Queisser, "Detailed balance limit of efficiency of p-n junction solar cells", *Journal of Applied Physics*, vol. 32, no. 3, pp. 510–519, 1961. DOI: 10.1063/1.1736034.

[11] R. Swanson, "Approaching the 29% limit efficiency of silicon solar cells", in *Conference Record of the Thirty-first IEEE Photovoltaic Specialists Conference, 2005.*, 2005, pp. 889–894. DOI: 10.1109/PVSC.2005.1488274.

[12] NREL, *NREL research cell efficiencies chart*, Nov. 2021. [Online]. Available: nrel.gov/pv/cell-efficiency.html.

[13] M. Green, E. Dunlop, J. Hohl-Ebinger, M. Yoshita, N. Kopidakis, and X. Hao, "Solar cell efficiency tables (version 57)", *Progress in Photovoltaics: Research and Applications*, vol. 29, no. 1, pp. 3–15, 2021. DOI: 10.1002/pip.3371.

[14] S. Sofia, J. Mailoa, D. Weiss, B. Stanbery, T. Buonassisi, and I. M. Peters, "Economic viability of thin-film tandem solar modules in the United States", *Nature Energy*, vol. 3, May 2018. DOI: 10.1038/s41560-018-0126-z.

[15] A. D. Vos, "Detailed balance limit of the efficiency of tandem solar cells", *Journal of Physics D: Applied Physics*, vol. 13, no. 5, pp. 839–846, May 1980. DOI: 10.1088/0022-3727/13/5/018.

[16] L. C. Hirst and N. J. Ekins-Daukes, "Fundamental losses in solar cells", *Progress in Photovoltaics: Research and Applications*, vol. 19, no. 3, pp. 286–293, 2011. DOI: 10.1002/pip.1024.

[17] C. H. Henry, "Limiting efficiencies of ideal single and multiple energy gap terrestrial solar cells", *Journal of Applied Physics*, vol. 51, no. 8, pp. 4494–4500, 1980. DOI: 10.1063/1.328272.

[18] B. Chen, X. Zheng, Y. Bai, N. P. Padture, and J. Huang, "Progress in tandem solar cells based on hybrid organic–inorganic perovskites", *Advanced Energy Materials*, vol. 7, no. 14, p. 1 602 400, 2017. DOI: 10.1002/aenm.201602400.

[19] K. A. W. Horowitz, T. Remo, B. Smith, and A. Ptak, "A techno-economic analysis and cost reduction roadmap for III-V solar cells", National Renewable Energy Laboratory, Technical Report, 2018.

[20] J. Li, A. Aierken, Y. Liu, Y. Zhuang, X. Yang, J. H. Mo, R. K. Fan, Q. Y. Chen, S. Y. Zhang, Y. M. Huang, and Q. Zhang, "A brief review of high efficiency iii-v solar cells for space application", *Frontiers in Physics*, vol. 8, p. 657, 2021. DOI: 10.3389/fphy.2020.631925.

[21] S. Essig, C. Allebé, T. Remo, J. Geisz, M. Steiner, K. Horowitz, L. Barraud, J. Ward, M. Schnabel, A. Descoeudres, D. Young, M. Woodhouse, M. Despeisse, C. Ballif, and A. Tamboli, "Raising the one-sun conversion efficiency of III–V/Si solar cells to 32.8% for two junctions and 35.9% for three junctions", *Nature Energy*, vol. 6, Aug. 2017. DOI: 10.1038/nenergy.2017.144.

[22] J. Werner, B. Niesen, and C. Ballif, "Perovskite/silicon tandem solar cells: marriage of convenience or true love story? – an overview", *Advanced Materials Interfaces*, vol. 5, no. 1, p. 1 700 731, 2018. DOI: 10.1002/admi.201700731.

[23] Y. Rong, Y. Hu, A. Mei, H. Tan, M. I. Saidaminov, S. I. Seok, M. D. McGehee, E. H. Sargent, and H. Han, "Challenges for commercializing perovskite solar cells", *Science*, vol. 361, no. 6408, eaat8235, 2018. DOI: 10.1126/science.aat8235.

[24] C. Liu, Y. Yang, K. Rakstys, A. Mahata, M. Franckevicius, E. Mosconi, R. Skackauskaite, B. Ding, K. G. Brooks, O. J. Usiobo, J.-N. Audinot, H. Kanda, S. Driukas, G. Kavaliauskaite, V. Gulbinas, M. Dessimoz, V. Getautis, F. De Angelis, Y. Ding, S. Dai, P. J. Dyson, and M. K. Nazeeruddin, "Tuning structural isomers of phenylenediammonium to afford efficient and stable perovskite solar cells and modules", *Nature Communications*, vol. 12, no. 1, p. 6394, Nov. 2021. DOI: 10.1038/s41467-021-26754-2.

[25] M. Khenkin, E. Katz, A. Abate, G. Bardizza, J. Berry, C. Brabec, F. Brunetti, V. Bulovic, Q. Burlingame, A. Di Carlo, R. Cheacharoen, C. Bing, A. Colsmann, S. Cros, K. Domanski, M. Dusza, C. Fell, S. Forrest, Y. Galagan, and M. Lira-Cantu, "Consensus statement for stability assessment and reporting for perovskite photovoltaics based on isos procedures", *Nature Energy*, vol. 5, pp. 35–49, Jan. 2020. DOI: 10.1038/s41560-019-0529-5.

[26] J. Qian, M. Ernst, N. Wu, and A. Blakers, "Impact of perovskite solar cell degradation on the lifetime energy yield and economic viability of perovskite/silicon tandem modules", *Sustainable Energy Fuels*, vol. 3, pp. 1439–1447, 6 2019. DOI: 10.1039/C9SE00143C.

[27] A. Urbina, "The balance between efficiency, stability and environmental impacts in perovskite solar cells: a review", *Journal of Physics: Energy*, vol. 2, no. 2, p. 022 001, Feb. 2020. DOI: 10.1088/2515-7655/ab5eee.

[28] P. Roy, N. Kumar Sinha, S. Tiwari, and A. Khare, "A review on perovskite solar cells: evolution of architecture, fabrication techniques, commercialization issues and status", *Solar Energy*, vol. 198, pp. 665–688, 2020, ISSN: 0038-092X. DOI: 10.1016/j.solener.2020.01.080.

[29] Oxford PV. (2020). "Oxford PV hits new world record for solar cell", [Online]. Available: oxfordpv.com/news/oxford-pv-hits-new-world-record-solar-cell.

[30] NREL, *NREL module efficiencies chart*, Nov. 2021. [Online]. Available: nrel.gov/pv/module-efficiency.html.

[31] V. M. Goldschmidt, "Die gesetze der krystallochemie", *Naturwissenschaften*, vol. 14, no. 21, pp. 477–485, May 1926. DOI: 10.1007/BF01507527.

[32] F. Wagner, S. Ferrer, and G. Somorjai, "Surface aspects of hydrogen photogeneration of titanium oxides", 1980.

[33] T. Jesper Jacobsson, J.-P. Correa-Baena, M. Pazoki, M. Saliba, K. Schenk, M. Grätzel, and A. Hagfeldt, "Exploration of the compositional space for mixed lead halogen perovskites for high efficiency solar cells", *Energy Environ. Sci.*, vol. 9, pp. 1706–1724, 5 2016. DOI: 10.1039/C6EE00030D.

[34] M. Saliba, T. Matsui, K. Domanski, J.-Y. Seo, A. Ummadisingu, S. M. Zakeeruddin, J.-P. Correa-Baena, W. R. Tress, A. Abate, A. Hagfeldt, and M. Grätzel, "Incorporation of rubidium cations into perovskite solar cells improves photovoltaic performance", *Science*, vol. 354, no. 6309, pp. 206–209, 2016. DOI: 10.1126/science.aah5557.

[35] T. J. Jacobsson, S. Svanström, V. Andrei, J. P. H. Rivett, N. Kornienko, B. Philippe, U. B. Cappel, H. Rensmo, F. Deschler, and G. Boschloo, "Extending the compositional space of mixed lead halide perovskites by cs, rb, k, and na doping", *The Journal of Physical Chemistry C*, vol. 122, no. 25, pp. 13 548–13 557, 2018. DOI: 10.1021/acs.jpcc.7b12464.

[36] L. Zhang, X. Liu, J. Li, and S. McKechnie, "Interactions between molecules and perovskites in halide perovskite solar cells", *Solar Energy Materials and Solar Cells*, vol. 175, pp. 1–19, 2018, ISSN: 0927-0248. DOI: 10.1016/j.solmat.2017.09.038.

[37] A. Kojima, K. Teshima, Y. Shirai, and T. Miyasaka, "Organometal halide perovskites as visible-light sensitizers for photovoltaic cells", *Journal of the American Chemical Society*, vol. 131, no. 17, pp. 6050–6051, 2009. DOI: 10.1021/ja809598r.

[38] K. X. Steirer, P. Schulz, G. Teeter, V. Stevanovic, M. Yang, K. Zhu, and J. J. Berry, "Defect tolerance in methylammonium lead triiodide perovskite", *ACS Energy Letters*, vol. 1, no. 2, pp. 360–366, 2016. DOI: 10.1021/acsenergylett.6b00196.

[39] Q. Wali, N. K. Elumalai, Y. Iqbal, A. Uddin, and R. Jose, "Tandem perovskite solar cells", *Renewable and Sustainable Energy Reviews*, vol. 84, pp. 89–110, 2018, ISSN: 1364-0321. DOI: 10.1016/j.rser.2018.01.005.

[40] M. M. Stylianakis, T. Maksudov, A. Panagiotopoulos, G. Kakavelakis, and K. Petridis, "Inorganic and hybrid perovskite based laser devices: a review", *Materials*, vol. 12, no. 6, 2019, ISSN: 1996-1944. DOI: 10.3390/ma12060859.

[41] Q. Van Le, H. W. Jang, and S. Y. Kim, "Recent advances toward high-efficiency halide perovskite light-emitting diodes: review and perspective", *Small Methods*, vol. 2, no. 10, p. 1 700 419, 2018. DOI: 10.1002/smtd.201700419.

[42] C. Gu and J.-S. Lee, "Flexible hybrid organic–inorganic perovskite memory", *ACS Nano*, vol. 10, no. 5, pp. 5413–5418, 2016. DOI: 10.1021/acsnano.6b01643.

[43] D. Liu, Q. Lin, Z. Zang, M. Wang, P. Wangyang, X. Tang, M. Zhou, and W. Hu, "Flexible all-inorganic perovskite cspbbr3 nonvolatile memory device", *ACS Applied Materials & Interfaces*, vol. 9, no. 7, pp. 6171–6176, 2017. DOI: 10.1021/acsami.6b15149.

[44] B. Sutherland and E. Sargent, "Perovskite photonic sources", *Nature Photonics*, vol. 10, Apr. 2016. DOI: 10.1038/NPHOTON.2016.62.

[45] W. Yu, F. Li, L. Yu, M. Khan niazi, Y. Zou, D. Corzo, A. Basu, C. Ma, S. Dey, M. Tietze, U. Buttner, X. Wang, Z. Wang, M. Hedhili, C. Guo, T. Wu, and A. Amassian, "Single crystal hybrid perovskite field-effect transistors", *Nature Communications*, vol. 9, Dec. 2018. DOI: 10.1038/s41467-018-07706-9.

[46] J. H. Noh, S. H. Im, J. H. Heo, T. N. Mandal, and S. I. Seok, "Chemical management for colorful, efficient, and stable inorganic–organic hybrid nanostructured solar cells", *Nano Letters*, vol. 13, no. 4, pp. 1764–1769, 2013. DOI: 10.1021/nl400349b.

[47] M. T. Hörantner and H. J. Snaith, "Predicting and optimising the energy yield of perovskite-on-silicon tandem solar cells under real world conditions", *Energy Environ. Sci.*, vol. 10, pp. 1983–1993, 9 2017. DOI: 10.1039/C7EE01232B.

[48] S. De Wolf, J. Holovský, S.-J. Moon, P. Löper, B. Niesen, M. Ledinsky, F.-J. Haug, J.-H. Yum, and C. Ballif, "Organometallic halide perovskites: sharp optical absorption edge and its relation to photovoltaic performance", *The Journal of Physical Chemistry Letters*, vol. 5, no. 6, pp. 1035–1039, 2014. DOI: 10.1021/jz500279b.

[49] J. Gong, J. Liang, and K. Sumathy, "Review on dye-sensitized solar cells (DSSCs): fundamental concepts and novel materials", *Renewable and Sustainable Energy Reviews*, vol. 16, no. 8, pp. 5848–5860, 2012, ISSN: 1364-0321. DOI: 10.1016/j.rser.2012.04.044.

[50] M. M. Lee, J. Teuscher, T. Miyasaka, T. N. Murakami, and H. J. Snaith, "Efficient hybrid solar cells based on meso-superstructured organometal halide perovskites", *Science*, vol. 338, no. 6107, pp. 643–647, 2012. DOI: 10.1126/science.1228604.

[51] M. Xiao, F. Huang, W. Huang, Y. Dkhissi, Y. Zhu, J. Etheridge, A. Gray-Weale, U. Bach, Y.-B. Cheng, and L. Spiccia, "A fast deposition-crystallization procedure for highly efficient lead iodide perovskite thin-film solar cells", *Angewandte Chemie International Edition*, vol. 53, no. 37, pp. 9898–9903, 2014. DOI: 10.1002/anie.201405334.

[52] N. Jeon, J. Noh, Y. Kim, W. Yang, S. Ryu, and S. Seok, "Solvent engineering for high-performance inorganic-organic hybrid perovskite solar cells", *Nature Materials*, vol. 13, no. 9, pp. 897–903, Jan. 2014, ISSN: 1476-1122. DOI: 10.1038/nmat4014.

[53] L. Krückemeier, U. Rau, M. Stolterfoht, and T. Kirchartz, "How to report record open-circuit voltages in lead-halide perovskite solar cells", *Advanced Energy Materials*, vol. 10, no. 1, p. 1 902 573, 2020. DOI: 10.1002/aenm.201902573.

[54] J.-W. Lee, D.-H. Kim, H.-S. Kim, S.-W. Seo, S. M. Cho, and N.-G. Park, "Formamidinium and cesium hybridization for photo- and moisture-stable perovskite solar cell", *Advanced Energy Materials*, vol. 5, no. 20, p. 1 501 310, 2015. DOI: 10.1002/aenm.201501310.

[55] J. Xu, C. C. Boyd, Z. J. Yu, A. F. Palmstrom, D. J. Witter, B. W. Larson, R. M. France, J. Werner, S. P. Harvey, E. J. Wolf, W. Weigand, S. Manzoor, M. F. A. M. van Hest, J. J. Berry, J. M. Luther, Z. C. Holman, and M. D. McGehee, "Triple-halide wide-band gap perovskites with suppressed phase segregation for efficient tandems", *Science*, vol. 367, no. 6482, pp. 1097–1104, 2020. DOI: 10.1126/science.aaz5074.

[56] A. Al-Ashouri, A. Magomedov, M. Roß, M. Jošt, M. Talaikis, G. Chistiakova, T. Bertram, J. Marquez-Prieto, E. Köhnen, E. Kasparavičius, S. Levcenco, L. Gil-Escrig, C. Hages, R. Schlatmann, B. Rech, T. Malinauskas, T. Unold, C. A. Kaufmann, L. Korte, and S. Albrecht, "Conformal monolayer contacts with lossless interfaces for perovskite single junction and monolithic tandem solar cells", *Energy & Environmental Science*, vol. 12, Oct. 2019. DOI: 10.1039/C9EE02268F.

[57] A. F. Palmstrom, G. E. Eperon, T. Leijtens, R. Prasanna, S. N. Habisreutinger, W. Nemeth, E. A. Gaulding, S. P. Dunfield, M. Reese, S. Nanayakkara, T. Moot, J. Werner, J. Liu, B. To, S. T. Christensen, M. D. McGehee, M. F. van Hest, J. M. Luther, J. J. Berry, and D. T. Moore, "Enabling flexible all-perovskite tandem solar cells", *Joule*, vol. 3, no. 9, pp. 2193–2204, 2019, ISSN: 2542-4351. DOI: 10.1016/j.joule.2019.05.009.

[58] J.-P. Correa-Baena, M. Saliba, T. Buonassisi, M. Grätzel, A. Abate, W. Tress, and A. Hagfeldt, "Promises and challenges of perovskite solar cells", *Science*, vol. 358, no. 6364, pp. 739–744, 2017. DOI: 10.1126/science.aam6323.

[59] F. Fu, S. Pisoni, Q. Jeangros, J. Sastre-Pellicer, M. Kawecki, A. Paracchino, T. Moser, J. Werner, C. Andres, L. Duchêne, P. Fiala, M. Rawlence, S. Nicolay, C. Ballif, A. N. Tiwari, and S. Buecheler, "I2 vapor-induced degradation of formamidinium lead iodide based perovskite solar cells under heat-light soaking conditions", *Energy Environ. Sci.*, vol. 12, pp. 3074–3088, 10 2019. DOI: 10.1039/C9EE02043H.

[60] W. Qiu, A. Ray, M. Jaysankar, T. Merckx, J. P. Bastos, D. Cheyns, R. Gehlhaar, J. Poortmans, and P. Heremans, "An interdiffusion method for highly performing cesium/-formamidinium double cation perovskites", *Advanced Functional Materials*, vol. 27, no. 28, p. 1 700 920, 2017. DOI: 10.1002/adfm.201700920.

[61] I. L. Braly, R. J. Stoddard, A. Rajagopal, A. R. Uhl, J. K. Katahara, A. K.-Y. Jen, and H. W. Hillhouse, "Current-induced phase segregation in mixed halide hybrid perovskites and its impact on two-terminal tandem solar cell design", *ACS Energy Letters*, vol. 2, no. 8, pp. 1841–1847, 2017. DOI: 10.1021/acsenergylett.7b00525.

[62] F. Sahli, Q. Jeangros, and C. Ballif, "Development of highly efficient perovskite-on-silicon tandem solar cells", Ph.D. dissertation, EPFL, 2020.

[63] J. Werner, B. Niesen, and C. Ballif, "Perovskite / silicon tandem solar cells : toward affordable ultra-high efficiency photovoltaics ?", Ph.D. dissertation, Lausanne, 2018.

[64] D. Bi, W. Tress, M. I. Dar, P. Gao, J. Luo, C. Renevier, K. Schenk, A. Abate, F. Giordano, J.-P. Correa Baena, J.-D. Decoppet, S. M. Zakeeruddin, M. K. Nazeeruddin, M. Grätzel, and A. Hagfeldt, "Efficient luminescent solar cells based on tailored mixed-cation perovskites", *Science Advances*, vol. 2, no. 1, 2016. DOI: 10.1126/sciadv.1501170.

[65] Y. C. Kim, N. J. Jeon, J. H. Noh, W. S. Yang, J. Seo, J. S. Yun, A. Ho-Baillie, S. Huang, M. A. Green, J. Seidel, T. K. Ahn, and S. I. Seok, "Beneficial effects of PbI2 incorporated in organo-lead halide perovskite solar cells", *Advanced Energy Materials*, vol. 6, no. 4, p. 1 502 104, 2016. DOI: 10.1002/aenm.201502104.

[66] T. J. Jacobsson, J.-P. Correa-Baena, E. Halvani Anaraki, B. Philippe, S. D. Stranks, M. E. F. Bouduban, W. Tress, K. Schenk, J. Teuscher, J.-E. Moser, H. Rensmo, and A. Hagfeldt, "Unreacted PbI2 as a double-edged sword for enhancing the performance of perovskite solar cells", *Journal of the American Chemical Society*, vol. 138, no. 32, pp. 10 331–10 343, 2016. DOI: 10.1021/jacs.6b06320.

[67] S. Shukla, S. Shukla, L. J. Haur, S. S. H. Dintakurti, G. Han, A. Priyadarshi, T. Baikie, S. G. Mhaisalkar, and N. Mathews, "Effect of formamidinium/cesium substitution and PbI2 on the long-term stability of triple-cation perovskites", *ChemSusChem*, vol. 10, no. 19, pp. 3804–3809, 2017. DOI: 10.1002/cssc.201701203.

[68] E. T. Hoke, D. J. Slotcavage, E. R. Dohner, A. R. Bowring, H. I. Karunadasa, and M. D. McGehee, "Reversible photo-induced trap formation in mixed-halide hybrid perovskites for photovoltaics", *Chem. Sci.*, vol. 6, pp. 613–617, 1 2015. DOI: 10.1039/C4SC03141E.

[69] C. G. Bischak, C. L. Hetherington, H. Wu, S. Aloni, D. F. Ogletree, D. T. Limmer, and N. S. Ginsberg, "Origin of reversible photoinduced phase separation in hybrid perovskites", *Nano Letters*, vol. 17, no. 2, pp. 1028–1033, 2017. DOI: 10.1021/acs.nanolett.6b04453.

[70] A. J. Barker, A. Sadhanala, F. Deschler, M. Gandini, S. P. Senanayak, P. M. Pearce, E. Mosconi, A. J. Pearson, Y. Wu, A. R. Srimath Kandada, T. Leijtens, F. De Angelis, S. E. Dutton, A. Petrozza, and R. H. Friend, "Defect-assisted photoinduced halide segregation in mixed-halide perovskite thin films", *ACS Energy Letters*, vol. 2, no. 6, pp. 1416–1424, 2017. DOI: 10.1021/acsenergylett.7b00282.

[71] E. L. Unger, L. Kegelmann, K. Suchan, D. Sörell, L. Korte, and S. Albrecht, "Roadmap and roadblocks for the band gap tunability of metal halide perovskites", *J. Mater. Chem. A*, vol. 5, pp. 11 401–11 409, 23 2017. DOI: 10.1039/C7TA00404D.

[72] T. C.-J. Yang, P. Fiala, Q. Jeangros, and C. Ballif, "High-bandgap perovskite materials for multijunction solar cells", *Joule*, vol. 2, no. 8, pp. 1421–1436, 2018, ISSN: 2542-4351. DOI: 10.1016/j.joule.2018.05.008.

[73] K. Domanski, B. Roose, T. Matsui, M. Saliba, S.-H. Turren-Cruz, J.-P. Correa-Baena, C. R. Carmona, G. Richardson, J. M. Foster, F. De Angelis, J. M. Ball, A. Petrozza, N. Mine, M. K. Nazeeruddin, W. Tress, M. Grätzel, U. Steiner, A. Hagfeldt, and A. Abate, "Migration of cations induces reversible performance losses over day/night cycling in perovskite solar cells", *Energy Environ. Sci.*, vol. 10, pp. 604–613, 2 2017. DOI: 10.1039/C6EE03352K.

[74] M. De Bastiani, E. Aydin, T. Allen, D. Walter, A. Fell, J. Peng, N. Gasparini, J. Troughton, D. Baran, K. Weber, T. P. White, and S. De Wolf, "Interfacial dynamics and contact passivation in perovskite solar cells", *Advanced Electronic Materials*, vol. 5, no. 1, p. 1 800 500, 2019. DOI: 10.1002/aelm.201800500.

[75] D. A. Jacobs, Y. Wu, H. Shen, C. Barugkin, F. J. Beck, T. P. White, K. Weber, and K. R. Catchpole, "Hysteresis phenomena in perovskite solar cells: the many and varied effects of ionic accumulation", *Phys. Chem. Chem. Phys.*, vol. 19, pp. 3094–3103, 4 2017. DOI: 10.1039/C6CP06989D.

[76] P. Caprioglio, S. Caicedo-Dávila, T. C.-J. Yang, C. M. Wolff, F. Peña-Camargo, P. Fiala, B. Rech, C. Ballif, D. Abou-Ras, M. Stolterfoht, S. Albrecht, Q. Jeangros, and D. Neher, "Nano-emitting heterostructures violate optical reciprocity and enable efficient photoluminescence in halide-segregated methylammonium-free wide bandgap perovskites", *ACS Energy Letters*, vol. 6, no. 2, pp. 419–428, 2021. DOI: 10.1021/acsenergylett.0c02270.

[77] R. A. Z. Razera, D. A. Jacobs, F. Fu, P. Fiala, M. Dussouillez, F. Sahli, T. C. J. Yang, L. Ding, A. Walter, A. F. Feil, H. I. Boudinov, S. Nicolay, C. Ballif, and Q. Jeangros, "Instability of p–i–n perovskite solar cells under reverse bias", *J. Mater. Chem. A*, vol. 8, pp. 242–250, 1 2020. DOI: 10.1039/C9TA12032G.

[78] A. R. Bowring, L. Bertoluzzi, B. C. O'Regan, and M. D. McGehee, "Reverse bias behavior of halide perovskite solar cells", *Advanced Energy Materials*, vol. 8, no. 8, p. 1 702 365, 2018. DOI: 10.1002/aenm.201702365.

[79] T. Duong, Y. Wu, H. Shen, J. Peng, X. Fu, D. Jacobs, E.-C. Wang, T. C. Kho, K. C. Fong, M. Stocks, E. Franklin, A. Blakers, N. Zin, K. McIntosh, W. Li, Y.-B. Cheng, T. P. White, K. Weber, and K. Catchpole, "Rubidium multication perovskite with optimized bandgap for perovskite-silicon tandem with over 26% efficiency", *Advanced Energy Materials*, vol. 7, no. 14, p. 1 700 228, 2017. DOI: 10.1002/aenm.201700228.

[80] Z. Tang, T. Bessho, F. Awai, T. Kinoshita, M. Maitani, R. Jono, T. Murakami, H. Wang, T. Kubo, S. Uchida, and H. Segawa, "Hysteresis-free perovskite solar cells made of potassium-doped organometal halide perovskite", *Scientific Reports*, vol. 7, Sep. 2017. DOI: 10.1038/s41598-017-12436-x.

[81] M. Abdi-Jalebi, Z. Andaji Garmaroudi, S. Cacovich, C. Stavrakas, B. Philippe, J. Richter, M. Alsari, E. Booker, E. Hutter, A. Pearson, S. Lilliu, T. Savenije, H. Rensmo, G. Divitini, C. Ducati, R. Friend, and S. Stranks, "Maximizing and stabilizing luminescence from halide perovskites with potassium passivation", *Nature*, vol. 555, pp. 497–501, Feb. 2018. DOI: 10.1038/nature25989.

[82] W. Fan, Y. Shi, T. Shi, S. Chu, W. Chen, K. O. Ighodalo, J. Zhao, X. Li, and Z. Xiao, "Suppression and reversion of light-induced phase separation in mixed-halide perovskites by oxygen passivation", *ACS Energy Letters*, vol. 4, no. 9, pp. 2052–2058, 2019. DOI: 10.1021/acsenergylett.9b01383.

[83] N. Tessler and Y. Vaynzof, "Preventing hysteresis in perovskite solar cells by undoped charge blocking layers", *ACS Applied Energy Materials*, vol. 1, no. 2, pp. 676–683, 2018. DOI: 10.1021/acsaem.7b00176.

[84] R. A. Belisle, K. A. Bush, L. Bertoluzzi, A. Gold-Parker, M. F. Toney, and M. D. McGehee, "Impact of surfaces on photoinduced halide segregation in mixed-halide perovskites", *ACS Energy Letters*, vol. 3, no. 11, pp. 2694–2700, 2018. DOI: 10.1021/acsenergylett.8b01562.

[85] W. S. Yang, B.-W. Park, E. H. Jung, N. J. Jeon, Y. C. Kim, D. U. Lee, S. S. Shin, J. Seo, E. K. Kim, J. H. Noh, and S. I. Seok, "Iodide management in formamidinium-lead-halide–based perovskite layers for efficient solar cells", *Science*, vol. 356, no. 6345, pp. 1376–1379, 2017. DOI: 10.1126/science.aan2301.

[86] T. Duong, Y. Wu, H. Shen, J. Peng, X. Fu, D. Jacobs, E.-C. Wang, T. C. Kho, K. C. Fong, M. Stocks, E. Franklin, A. Blakers, N. Zin, K. McIntosh, W. Li, Y.-B. Cheng, T. P. White, K. Weber, and K. Catchpole, "Rubidium multication perovskite with optimized bandgap for perovskite-silicon tandem with over 26% efficiency", *Advanced Energy Materials*, vol. 7, no. 14, p. 1 700 228, 2017. DOI: 10.1002/aenm.201700228.

[87] S. Mahesh, J. M. Ball, R. D. J. Oliver, D. P. McMeekin, P. K. Nayak, M. B. Johnston, and H. J. Snaith, "Revealing the origin of voltage loss in mixed-halide perovskite solar cells", *Energy Environ. Sci.*, vol. 13, pp. 258–267, 1 2020. DOI: 10.1039/C9EE02162K.

[88] Y. Zhou, F. Wang, Y. Cao, J.-P. Wang, H.-H. Fang, M. Loi, N. Zhao, and C.-P. Wong, "Benzylamine-treated wide-bandgap perovskite with high thermal-photostability and photovoltaic performance", *Advanced Energy Materials*, vol. 7, p. 1 701 048, Sep. 2017.

[89] Z. Xiao, L. Zhao, N. L. Tran, Y. L. Lin, S. H. Silver, R. A. Kerner, N. Yao, A. Kahn, G. D. Scholes, and B. P. Rand, "Mixed-halide perovskites with stabilized bandgaps", *Nano Letters*, vol. 17, no. 11, pp. 6863–6869, 2017. DOI: 10.1021/acs.nanolett.7b03179.

[90] D. Luo, W. Yang, Z. Wang, A. Sadhanala, Q. Hu, R. Su, R. Shivanna, G. F. Trindade, J. F. Watts, Z. Xu, T. Liu, K. Chen, F. Ye, P. Wu, L. Zhao, J. Wu, Y. Tu, Y. Zhang, X. Yang, W. Zhang, R. H. Friend, Q. Gong, H. J. Snaith, and R. Zhu, "Enhanced photovoltage for inverted planar heterojunction perovskite solar cells", *Science*, vol. 360, no. 6396, pp. 1442–1446, 2018. DOI: 10.1126/science.aap9282.

[91] Y. Bai, S. Xiao, C. Hu, T. Zhang, X. Meng, H. Lin, Y. Yang, and S. Yang, "Dimensional engineering of a graded 3d–2d halide perovskite interface enables ultrahigh voc enhanced stability in the p-i-n photovoltaics", *Advanced Energy Materials*, vol. 7, no. 20, p. 1 701 038, 2017. DOI: 10.1002/aenm.201701038.

[92] K. T. Cho, G. Grancini, Y. Lee, E. Oveisi, J. Ryu, O. Almora, M. Tschumi, P. A. Schouwink, G. Seo, S. Heo, J. Park, J. Jang, S. Paek, G. Garcia-Belmonte, and M. K. Nazeeruddin, "Selective growth of layered perovskites for stable and efficient photovoltaics", *Energy Environ. Sci.*, vol. 11, pp. 952–959, 4 2018. DOI: 10.1039/C7EE03513F.

[93] K. Lee, J. Kim, H. Yu, J. W. Lee, C.-M. Yoon, S. K. Kim, and J. Jang, "A highly stable and efficient carbon electrode-based perovskite solar cell achieved via interfacial growth of 2D PEA2PbI4 perovskite", *J. Mater. Chem. A*, vol. 6, pp. 24 560–24 568, 47 2018. DOI: 10.1039/C8TA09433K.

[94] Y. Zhou, F. Wang, Y. Cao, J.-P. Wang, H.-H. Fang, M. A. Loi, N. Zhao, and C.-P. Wong, "Benzylamine-treated wide-bandgap perovskite with high thermal-photostability and photovoltaic performance", *Advanced Energy Materials*, vol. 7, no. 22, p. 1 701 048, 2017. DOI: 10.1002/aenm.201701048.

[95] H. Dong, J. Xi, L. Zuo, J. Li, Y. Yang, D. Wang, Y. Yu, L. Ma, C. Ran, W. Gao, B. Jiao, J. Xu, T. Lei, F. Wei, F. Yuan, L. Zhang, Y. Shi, X. Hou, and Z. Wu, "Conjugated molecules "bridge": functional ligand toward highly efficient and long-term stable perovskite solar cell", *Advanced Functional Materials*, vol. 29, no. 17, p. 1 808 119, 2019. DOI: 10.1002/adfm.201808119.

[96] X. Zheng, Y. Hou, C. Bao, J. Yin, F. Yuan, Z. Huang, K. Song, J. Liu, J. Troughton, N. Gasparini, C. Zhou, Y. Lin, D.-J. Xue, B. Chen, A. K. Johnston, N. Wei, M. N. Hedhili, M. Wei, A. Y. Alsalloum, P. Maity, B. Turedi, C. Yang, D. Baran, T. D. Anthopoulos, Y. Han, Z.-H. Lu, O. F. Mohammed, F. Gao, E. H. Sargent, and O. M. Bakr, "Managing grains and interfaces via ligand anchoring enables 22.3%-efficiency inverted perovskite solar cells", *Nature Energy*, vol. 5, pp. 131–140, 2 Feb. 2020, ISSN: 2058-7546. DOI: 10.1038/s41560-019-0538-4.

[97] D. Kim, H. J. Jung, I. J. Park, B. W. Larson, S. P. Dunfield, C. Xiao, J. Kim, J. Tong, P. Boonmongkolras, S. G. Ji, F. Zhang, S. R. Pae, M. Kim, S. B. Kang, V. Dravid, J. J. Berry, J. Y. Kim, K. Zhu, D. H. Kim, and B. Shin, "Efficient, stable silicon tandem cells enabled by anion-engineered wide-bandgap perovskites", *Science*, vol. 368, no. 6487, pp. 155–160, 2020. DOI: 10.1126/science.aba3433.

[98] G. Yang, Z. Ren, K. Liu, M. Qin, W. Deng, H. Zhang, H. Wang, J. Liang, F. Ye, Q. Liang, H. Yin, Y. Chen, Y. Zhuang, S. Li, B. Gao, J. Wang, T. Shi, X. Wang, X. Lu, H. Wu, J. Hou, D. ei, S. K. So, Y. Yang, G. Fang, and G. Li, "Stable and low-photovoltage-loss perovskite solar cells by multifunctional passivation", *Nature Photonics*, Jul. 2021. DOI: 10.1038/s41566-021-00829-4.

[99] C. M. Wolff, L. Canil, C. Rehermann, N. Ngoc Linh, F. Zu, M. Ralaiarisoa, P. Caprioglio, L. Fiedler, M. Stolterfoht, S. Kogikoski, I. Bald, N. Koch, E. L. Unger, T. Dittrich, A. Abate, and D. Neher, "Perfluorinated self-assembled monolayers enhance the stability and efficiency of inverted perovskite solar cells", *ACS Nano*, vol. 14, no. 2, pp. 1445–1456, 2020. DOI: 10.1021/acsnano.9b03268.

[100] S. Gharibzadeh, B. Abdollahi Nejand, M. Jakoby, T. Abzieher, D. Hauschild, S. Moghadamzadeh, J. A. Schwenzer, P. Brenner, R. Schmager, A. A. Haghighirad, L. Weinhardt, U. Lemmer, B. S. Richards, I. A. Howard, and U. W. Paetzold, "Record open-circuit voltage wide-bandgap perovskite solar cells utilizing 2D/3D perovskite heterostructure", *Advanced Energy Materials*, vol. 9, no. 21, p. 1 803 699, 2019. DOI: 10.1002/aenm.201803699.

[101] M. A. Mahmud, T. Duong, Y. Yin, H. T. Pham, D. Walter, J. Peng, Y. Wu, L. Li, H. Shen, N. Wu, N. Mozaffari, G. Andersson, K. R. Catchpole, K. J. Weber, and T. P. White, "Double-sided surface passivation of 3d perovskite film for high-efficiency mixed-dimensional perovskite solar cells", *Advanced Functional Materials*, vol. 30, no. 7, p. 1 907 962, 2020. DOI: 10.1002/adfm.201907962.

[102] P. Schulz, "Interface design for metal halide perovskite solar cells", *ACS Energy Letters*, vol. 3, no. 6, pp. 1287–1293, 2018. DOI: 10.1021/acsenergylett.8b00404.

[103] T. Sherkar, C. Momblona, L. Gil-Escrig, J. Ávila, M. Sessolo, H. Bolink, and L. Koster, "Recombination in perovskite solar cells: significance of grain boundaries, interface traps and defect ions", *ACS Energy Letters*, vol. 2, May 2017. DOI: 10.1021/acsenergylett.7b00236.

[104] M. Stolterfoht, P. Caprioglio, C. M. Wolff, J. A. Márquez, J. Nordmann, S. Zhang, D. Rothhardt, U. Hörmann, Y. Amir, A. Redinger, L. Kegelmann, F. Zu, S. Albrecht, N. Koch, T. Kirchartz, M. Saliba, T. Unold, and D. Neher, "The impact of energy alignment and interfacial recombination on the internal and external open-circuit voltage of perovskite solar cells", *Energy Environ. Sci.*, vol. 12, pp. 2778–2788, 9 2019. DOI: 10.1039/C9EE02020A.

[105] B. Chen, P. N. Rudd, S. Yang, Y. Yuan, and J. Huang, "Imperfections and their passivation in halide perovskite solar cells", *Chem. Soc. Rev.*, vol. 48, pp. 3842–3867, 14 2019. DOI: 10.1039/C8CS00853A.

[106] S. Yang, J. Dai, Z. Yu, Y. Shao, Y. Zhou, X. Xiao, X. C. Zeng, and J. Huang, "Tailoring passivation molecular structures for extremely small open-circuit voltage loss in perovskite solar cells", *Journal of the American Chemical Society*, vol. 141, no. 14, pp. 5781–5787, 2019. DOI: 10.1021/jacs.8b13091.

[107] M. Long, T. Zhang, M. Liu, Z. Chen, C. Wang, W. Xie, F. Xie, J. Chen, G. Li, and J. Xu, "Abnormal synergetic effect of organic and halide ions on the stability and optoelectronic properties of a mixed perovskite via in situ characterizations", *Advanced Materials*, vol. 30, no. 28, p. 1 801 562, 2018. DOI: 10.1002/adma.201801562.

[108] L. Liu, W.-H. Fang, R. Long, and O. V. Prezhdo, "Lewis base passivation of hybrid halide perovskites slows electron–hole recombination: time-domain ab initio analysis", *The Journal of Physical Chemistry Letters*, vol. 9, no. 5, pp. 1164–1171, 2018. DOI: 10.1021/acs.jpclett.8b00177.

[109] D. Meggiolaro, E. Mosconi, and F. De Angelis, "Formation of surface defects dominates ion migration in lead-halide perovskites", *ACS Energy Letters*, vol. 4, no. 3, pp. 779–785, 2019. DOI: 10.1021/acsenergylett.9b00247.

[110] M. Stolterfoht, C. M. Wolff, J. A. Márquez, S. Zhang, C. J. Hages, D. Rothhardt, S. Albrecht, P. L. Burn, P. Meredith, T. Unold, and D. Neher, "Visualization and suppression of interfacial recombination for high-efficiency large-area pin perovskite solar cells", *Nature Energy*, vol. 3, pp. 847–854, 10 Oct. 2018. DOI: 10.1038/s41560-018-0219-8.

[111] A. Al-Ashouri, E. Köhnen, B. Li, A. Magomedov, H. Hempel, P. Caprioglio, J. A. Márquez, A. B. Morales Vilches, E. Kasparavicius, J. A. Smith, N. Phung, D. Menzel, M. Grischek, L. Kegelmann, D. Skroblin, C. Gollwitzer, T. Malinauskas, M. Jošt, G. Matič, B. Rech, R. Schlatmann, M. Topič, L. Korte, A. Abate, B. Stannowski, D. Neher, M. Stolterfoht, T. Unold, V. Getautis, and S. Albrecht, "Monolithic perovskite/silicon tandem solar cell with >29% efficiency by enhanced hole extraction", *Science*, vol. 370, no. 6522, pp. 1300–1309, 2020. DOI: 10.1126/science.abd4016.

[112] S. Yang, S. Chen, E. Mosconi, Y. Fang, X. Xiao, C. Wang, Y. Zhou, Z. Yu, J. Zhao, Y. Gao, F. De Angelis, and J. Huang, "Stabilizing halide perovskite surfaces for solar cell operation with wide-bandgap lead oxysalts", *Science*, vol. 365, no. 6452, pp. 473–478, 2019. DOI: 10.1126/science.aax3294.

[113] D. H. Kim, C. P. Muzzillo, J. Tong, A. F. Palmstrom, B. W. Larson, C. Choi, S. P. Harvey, S. Glynn, J. B. Whitaker, F. Zhang, Z. Li, H. Lu, M. F. van Hest, J. J. Berry, L. M. Mansfield, Y. Huang, Y. Yan, and K. Zhu, "Bimolecular additives improve wide-band-gap perovskites for efficient tandem solar cells with CIGS", *Joule*, vol. 3, no. 7, pp. 1734–1745, 2019, ISSN: 2542-4351. DOI: 10.1016/j.joule.2019.04.012.

[114] Z. Liu, L. Krückemeier, B. Krogmeier, B. Klingebiel, J. A. Márquez, S. Levcenko, S. Öz, S. Mathur, U. Rau, T. Unold, and T. Kirchartz, "Open-circuit voltages exceeding 1.26 V in planar methylammonium lead iodide perovskite solar cells", *ACS Energy Letters*, vol. 4, no. 1, pp. 110–117, 2019. DOI: 10.1021/acsenergylett.8b01906.

[115] Y. Gao, Y. Wu, Y. Liu, C. Chen, X. Bai, L. Yang, Z. Shi, W. W. Yu, Q. Dai, and Y. Zhang, "Dual functions of crystallization control and defect passivation enabled by an ionic compensation strategy for stable and high-efficient perovskite solar cells", *ACS Applied Materials & Interfaces*, vol. 12, no. 3, pp. 3631–3641, 2020. DOI: 10.1021/acsami.9b19538.

[116] B. Liu, H. Bi, D. He, L. Bai, W. Wang, H. Yuan, Q. Song, P. Su, Z. Zang, T. Zhou, and J. Chen, "Interfacial defect passivation and stress release via multi-active-site ligand anchoring enables efficient and stable methylammonium-free perovskite solar cells", *ACS Energy Letters*, vol. 6, no. 7, pp. 2526–2538, 2021. DOI: 10.1021/acsenergylett.1c00794.

[117] J. Peng, J. I. Khan, W. Liu, E. Ugur, T. Duong, Y. Wu, H. Shen, K. Wang, H. Dang, E. Aydin, X. Yang, Y. Wan, K. J. Weber, K. R. Catchpole, F. Laquai, S. De Wolf, and T. P. White, "A universal double-side passivation for high open-circuit voltage in perovskite solar cells: role of carbonyl groups in poly(methyl methacrylate)", *Advanced Energy Materials*, vol. 8, no. 30, p. 1 801 208, 2018. DOI: 10.1002/aenm.201801208.

[118] J. S. Godding, A. J. Ramadan, Y.-H. Lin, K. Schutt, H. J. Snaith, and B. Wenger, "Oxidative passivation of metal halide perovskites", *Joule*, vol. 3, no. 11, pp. 2716–2731, 2019, ISSN: 2542-4351. DOI: 10.1016/j.joule.2019.08.006.

[119] Z. Yang, J. Dou, S. Kou, J. Dang, Y. Ji, G. Yang, W.-Q. Wu, D.-B. Kuang, and M. Wang, "Multifunctional phosphorus-containing Lewis acid and base passivation enabling efficient and moisture-stable perovskite solar cells", *Advanced Functional Materials*, vol. 30, no. 15, p. 1 910 710, 2020. DOI: 10.1002/adfm.201910710.

[120] M. Jeong, I. W. Choi, E. M. Go, Y. Cho, M. Kim, B. Lee, S. Jeong, Y. Jo, H. W. Choi, J. Lee, J.-H. Bae, S. K. Kwak, D. S. Kim, and C. Yang, "Stable perovskite solar cells with efficiency exceeding 24.8% and 0.3-v voltage loss", *Science*, vol. 369, no. 6511, pp. 1615–1620, 2020. DOI: 10.1126/science.abb7167.

[121] S.-C. Liu, Z. Li, Y. Yang, X. Wang, Y.-X. Chen, D.-J. Xue, and J.-S. Hu, "Investigation of oxygen passivation for high-performance all-inorganic perovskite solar cells", *Journal of the American Chemical Society*, vol. 141, no. 45, pp. 18 075–18 082, 2019. DOI: 10.1021/jacs.9b07182.

[122] A. Szemjonov, K. Galkowski, M. Anaya, Z. Andaji-Garmaroudi, T. K. Baikie, S. Mackowski, I. D. Baikie, S. D. Stranks, and M. S. Islam, "Impact of oxygen on the electronic structure of triple-cation halide perovskites", *ACS Materials Letters*, vol. 1, no. 5, pp. 506–510, 2019. DOI: 10.1021/acsmaterialslett.9b00294.

[123] R. Brenes, D. Guo, A. Osherov, N. K. Noel, C. Eames, E. M. Hutter, S. K. Pathak, F. Niroui, R. H. Friend, M. S. Islam, H. J. Snaith, V. Bulović, T. J. Savenije, and S. D. Stranks, "Metal halide perovskite polycrystalline films exhibiting properties of single crystals", *Joule*, vol. 1, no. 1, pp. 155–167, 2017, ISSN: 2542-4351. DOI: 10.1016/j.joule.2017.08.006.

[124] D. Meggiolaro, E. Mosconi, and F. De Angelis, "Mechanism of reversible trap passivation by molecular oxygen in lead-halide perovskites", *ACS Energy Letters*, vol. 2, no. 12, pp. 2794–2798, 2017. DOI: 10.1021/acsenergylett.7b00955.

[125] J. Xu, A. Buin, A. H. Ip, W. Li, O. Voznyy, R. Comin, M. Yuan, S. Jeon, Z. Ning, J. J. McDowell, P. Kanjanaboos, J.-P. Sun, X. Lan, L. N. Quan, D. H. Kim, I. G. Hill, P. Maksymovych, and E. H. Sargent, "Perovskite-fullerene hybrid materials suppress hysteresis in planar diodes", *Nature communications*, vol. 6, pp. 1–8, 1 May 2015, ISSN: 2041-1723. DOI: 10.1038/ncomms8081.

[126] N. K. Noel, A. Abate, S. D. Stranks, E. S. Parrott, V. M. Burlakov, A. Goriely, and H. J. Snaith, "Enhanced photoluminescence and solar cell performance via Lewis base passivation of organic–inorganic lead halide perovskites", *ACS Nano*, vol. 8, no. 10, pp. 9815–9821, 2014. DOI: 10.1021/nn5036476.

[127] Y. Hou, E. Aydin, M. De Bastiani, C. Xiao, F. H. Isikgor, D.-J. Xue, B. Chen, H. Chen, B. Bahrami, A. H. Chowdhury, A. Johnston, S.-W. Baek, Z. Huang, M. Wei, Y. Dong, J. Troughton, R. Jalmood, A. J. Mirabelli, T. G. Allen, E. Van Kerschaver, M. I. Saidaminov, D. Baran, Q. Qiao, K. Zhu, S. De Wolf, and E. H. Sargent, "Efficient tandem solar cells with solution-processed perovskite on textured crystalline silicon", *Science*, vol. 367, no. 6482, pp. 1135–1140, 2020, ISSN: 0036-8075. DOI: 10.1126/science.aaz3691.

[128] E. Akman, A. E. Shalan, F. Sadegh, and S. Akin, "Moisture-resistant FAPbI3 perovskite solar cell with 22.25% power conversion efficiency through pentafluorobenzyl phosphonic acid passivation", *ChemSusChem*, vol. 14, no. 4, pp. 1176–1183, 2021. DOI: 10.1002/cssc.202002707.

[129] S. D. Stranks, G. E. Eperon, G. Grancini, C. Menelaou, M. J. P. Alcocer, T. Leijtens, L. M. Herz, A. Petrozza, and H. J. Snaith, "Electron-hole diffusion lengths exceeding 1 micrometer in an organometal trihalide perovskite absorber", *Science*, vol. 342, no. 6156, pp. 341–344, 2013. DOI: 10.1126/science.1243982.

[130] G. W. P. Adhyaksa, L. W. Veldhuizen, Y. Kuang, S. Brittman, R. E. I. Schropp, and E. C. Garnett, "Carrier diffusion lengths in hybrid perovskites: processing, composition, aging, and surface passivation effects", *Chemistry of Materials*, vol. 28, no. 15, pp. 5259–5263, 2016. DOI: 10.1021/acs.chemmater.6b00466.

[131] G. D. Tainter, M. T. Hörantner, L. M. Pazos-Outón, R. D. Lamboll, H. Ābolinš, T. Leijtens, S. Mahesh, R. H. Friend, H. J. Snaith, H. J. Joyce, and F. Deschler, "Long-range charge extraction in back-contact perovskite architectures via suppressed recombination", *Joule*, vol. 3, no. 5, pp. 1301–1313, 2019, ISSN: 2542-4351. DOI: 10.1016/j.joule.2019.03.010.

[132] A. A. Zhumekenov, M. I. Saidaminov, M. A. Haque, E. Alarousu, S. P. Sarmah, B. Murali, I. Dursun, X.-H. Miao, A. L. Abdelhady, T. Wu, O. F. Mohammed, and O. M. Bakr, "Formamidinium lead halide perovskite crystals with unprecedented long carrier dynamics and diffusion length", *ACS Energy Letters*, vol. 1, no. 1, pp. 32–37, 2016. DOI: 10.1021/acsenergylett.6b00002.

[133] J. Xu, C. C. Boyd, Z. J. Yu, A. F. Palmstrom, D. J. Witter, B. W. Larson, R. M. France, J. Werner, S. P. Harvey, E. J. Wolf, W. Weigand, S. Manzoor, M. F. A. M. van Hest, J. J. Berry, J. M. Luther, Z. C. Holman, and M. D. McGehee, "Triple-halide wide-band gap perovskites with suppressed phase segregation for efficient tandems", *Science*, vol. 367, no. 6482, pp. 1097–1104, 2020. DOI: 10.1126/science.aaz5074.

[134] D. A. Jacobs, M. Langenhorst, F. Sahli, B. S. Richards, T. P. White, C. Ballif, K. R. Catchpole, and U. W. Paetzold, "Light management: a key concept in high-efficiency perovskite/silicon tandem photovoltaics", *The Journal of Physical Chemistry Letters*, vol. 10, no. 11, pp. 3159–3170, 2019. DOI: 10.1021/acs.jpclett.8b03721.

[135] J. Lehr, M. Langenhorst, R. Schmager, S. Kirner, U. Lemmer, B. S. Richards, C. Case, and U. W. Paetzold, "Energy yield modelling of perovskite/silicon two-terminal tandem pv modules with flat and textured interfaces", *Sustainable Energy Fuels*, vol. 2, pp. 2754–2761, 12 2018. DOI: 10.1039/C8SE00465J.

[136] J. Lehr, M. Langenhorst, R. Schmager, F. Gota, S. Kirner, U. Lemmer, B. S. Richards, C. Case, and U. W. Paetzold, "Energy yield of bifacial textured perovskite/silicon tandem photovoltaic modules", *Solar Energy Materials and Solar Cells*, vol. 208, p. 110 367, 2020, ISSN: 0927-0248. DOI: 10.1016/j.solmat.2019.110367.

[137] F. Wang, Y. Zhang, M. Yang, L. Fan, L. Yang, Y. Sui, J. Yang, and X. Zhang, "Toward ultra-thin and omnidirectional perovskite solar cells: concurrent improvement in conversion efficiency by employing light-trapping and recrystallizing treatment", *Nano Energy*, vol. 60, Mar. 2019. DOI: 10.1016/j.nanoen.2019.03.059.

[138] M. Boccard, T. Söderström, P. Cuony, C. Battaglia, S. Hänni, S. Nicolay, L. Ding, M. Benkhaira, G. Bugnon, A. Billet, M. Charrière, F. Meillaud, M. Despeisse, and C. Ballif, "Optimization of ZnO front electrodes for high-efficiency micromorph thin-film Si solar cells", *IEEE Journal of Photovoltaics*, vol. 2, no. 3, pp. 229–235, 2012. DOI: 10.1109/JPHOTOV.2011.2180514.

[139] S. Benagli, D. Borrello, E. Vallat, J. Meier, U. Kroll, J. Hoetzel, J. Bailat, J. Steinhauser, M. Marmelo, and G. Monteduro, "High efficiency amorphous silicon devices on LP-CVD TCO prepared in industrial Kai-M R&D reactor", *24th European Photovoltaic Solar Energy Conference, Hamburg*, pp. 344–349, Jan. 2009.

[140] S. Bose, A. Rayarfrancis, P. Bhargav, G. Ahmad, S. Mukhopadhyay, S. Mandal, and A. K. Barua, "Optimization of the texturization of ZnO:Al surface using HCl + HNO3 for application in thin film silicon solar cells", *J Mater Sci: Mater Electron*, vol. 29, pp. 3210–3218, 2018. DOI: 10.1007/s10854-017-8256-9.

[141] W. L. Bailey, M. G. Coleman, C. B. Harris, and I. A. Lesk, *United states patent: 4137123 - texture etching of silicon: method*, 1979. [Online]. Available: http://patft.uspto.gov/netacgi/nph-Parser?Sect1=PTO2%5C&Sect2=HITOFF%5C&p=1%5C&u=%5C%2Fnetahtml%5C%2FPTO%5C%2Fsearch-bool.html%5C&r=32%5C&f=G%5C&l=50%5C&co1=AND%5C&d=PTXT%5C&s1=4,137,123%5C&OS=4,137,123%5C&RS=4,137,123.

[142] P. Tockhorn, J. Sutter, R. Colom, L. Kegelmann, A. Al-Ashouri, M. Roß, K. Jäger, T. Unold, S. Burger, S. Albrecht, and C. Becker, "Improved quantum efficiency by advanced light management in nanotextured solution-processed perovskite solar cells", *ACS Photonics*, vol. 7, no. 9, pp. 2589–2600, 2020. DOI: 10.1021/acsphotonics.0c00935.

[143] M. Soldera, Q. Wang, F. Soldera, V. Lang, A. Abate, and A. F. Lasagni, "Toward high-throughput texturing of polymer foils for enhanced light trapping in flexible perovskite solar cells using roll-to-roll hot embossing", *Advanced Engineering Materials*, vol. 22, no. 4, p. 1 901 217, 2020. DOI: 10.1002/adem.201901217.

[144] C. Y. Xu, W. Hu, G. Wang, L. Niu, A. M. Elseman, L. Liao, Y. Yao, G. Xu, L. Luo, D. Liu, G. Zhou, P. Li, and Q. Song, "Coordinated optical matching of a texture interface made from demixing blended polymers for high-performance inverted perovskite solar cells", *ACS Nano*, vol. 14, no. 1, pp. 196–203, 2020. DOI: 10.1021/acsnano.9b07594.

[145] K. Deng, Z. Liu, M. Wang, and L. Li, "Nanoimprinted grating-embedded perovskite solar cells with improved light management", *Advanced Functional Materials*, vol. 29, no. 19, p. 1 900 830, 2019. DOI: 10.1002/adfm.201900830.

[146] J. F. Li, H. Y. Hao, J. B. Hao, L. Shi, J. J. Dong, H. Liu, and J. Xing, "Light trapping effect of textured FTO in perovskite solar cells", *IOP Conference Series: Materials Science and Engineering*, vol. 479, p. 012 046, Mar. 2019. DOI: 10.1088/1757-899x/479/1/012046.

[147] O. Dupré, B. Niesen, S. De Wolf, and C. Ballif, "Field performance versus standard test condition efficiency of tandem solar cells and the singular case of perovskites/silicon devices", *The Journal of Physical Chemistry Letters*, vol. 9, no. 2, pp. 446–458, 2018. DOI: 10.1021/acs.jpclett.7b02277.

[148] M. Lokanc, R. Eggert, and M. Redlinger, "The availability of indium: the present, medium term, and long term", Oct. 2015. DOI: 10.2172/1327212. [Online]. Available: https://www.osti.gov/biblio/1327212.

[149] F. Sahli, J. Werner, B. Kamino, M. Bräuninger, R. Monnard, B. Paviet-Salomon, L. Barraud, L. Ding, J. J. Díaz León, D. Sacchetto, G. Cattaneo, M. Despeisse, M. Boccard, S. Nicolay, Q. Jeangros, B. Niesen, and C. Ballif, "Fully textured monolithic perovskite/silicon tandem solar cells with 25.2% power conversion efficiency", *Nature Materials*, vol. 17, Sep. 2018. DOI: 10.1038/s41563-018-0115-4.

[150] J. P. Mailoa, C. D. Bailie, E. C. Johlin, E. T. Hoke, A. J. Akey, W. H. Nguyen, M. D. McGehee, and T. Buonassisi, "A 2-terminal perovskite/silicon multijunction solar cell enabled by a silicon tunnel junction", *Applied Physics Letters*, vol. 106, no. 12, p. 121 105, 2015. DOI: 10.1063/1.4914179.

[151] J. Werner, L. Barraud, A. Walter, M. Bräuninger, F. Sahli, D. Sacchetto, N. Tétreault, B. Paviet-Salomon, S.-J. Moon, C. Allebé, M. Despeisse, S. Nicolay, S. De Wolf, B. Niesen, and C. Ballif, "Efficient near-infrared-transparent perovskite solar cells enabling direct comparison of 4-terminal and monolithic perovskite/silicon tandem cells", *ACS Energy Letters*, vol. 1, no. 2, pp. 474–480, 2016. DOI: 10.1021/acsenergylett.6b00254.

[152] M. Boccard and C. Ballif, "Influence of the subcell properties on the fill factor of two-terminal perovskite–silicon tandem solar cells", *ACS Energy Letters*, vol. 5, no. 4, pp. 1077–1082, 2020. DOI: 10.1021/acsenergylett.0c00156.

[153] G. Nogay, F. Sahli, J. Werner, R. Monnard, M. Boccard, M. Despeisse, F.-J. Haug, Q. Jeangros, A. Ingenito, and C. Ballif, "25.1%-efficient monolithic perovskite/silicon tandem solar cell based on a p-type monocrystalline textured silicon wafer and high-temperature passivating contacts", *ACS Energy Letters*, vol. 4, no. 4, pp. 844–845, 2019. DOI: 10.1021/acsenergylett.9b00377.

[154] P. Tockhorn, P. Wagner, L. Kegelmann, J.-C. Stang, M. Mews, S. Albrecht, and L. Korte, "Three-terminal perovskite/silicon tandem solar cells with top and interdigitated rear contacts", *ACS Applied Energy Materials*, vol. 3, no. 2, pp. 1381–1392, 2020. DOI: 10.1021/acsaem.9b01800.

[155] B. Chen, Z. J. Yu, S. Manzoor, S. Wang, W. Weigand, Z. Yu, G. Yang, Z. Ni, X. Dai, Z. C. Holman, and J. Huang, "Blade-coated perovskites on textured silicon for 26%-efficient monolithic perovskite/silicon tandem solar cells", *Joule*, vol. 4, no. 4, pp. 850–864, 2020, ISSN: 2542-4351. DOI: 10.1016/j.joule.2020.01.008.

[156] F. H. Isikgor, F. Furlan, J. Liu, E. Ugur, M. K. Eswaran, A. S. Subbiah, E. Yengel, M. De Bastiani, G. T. Harrison, S. Zhumagali, C. T. Howells, E. Aydin, M. Wang, N. Gasparini, T. G. Allen, A. ur Rehman, E. Van Kerschaver, D. Baran, I. McCulloch, T. D. Anthopoulos, U. Schwingenschlögl, F. Laquai, and S. De Wolf, "Concurrent cationic and anionic perovskite defect passivation enables 27.4% perovskite/silicon tandems with suppression of halide segregation", *Joule*, vol. 5, no. 6, pp. 1566–1586, 2021, ISSN: 2542-4351. DOI: 10.1016/j.joule.2021.05.013.

[157] S. D. Wolf, A. Descoeudres, Z. C. Holman, and C. Ballif, "High-efficiency silicon heterojunction solar cells: a review", *Green*, vol. 2, no. 1, pp. 7–24, 2012. DOI: 10.1515/green-2011-0018.

[158] S. De Wolf and M. Kondo, "Nature of doped a-si:h/c-si interface recombination", *Journal of Applied Physics*, vol. 105, no. 10, p. 103 707, 2009. DOI: 10.1063/1.3129578.

[159] M. Roß, S. Severin, M. B. Stutz, P. Wagner, H. Köbler, M. Favin-Lévêque, A. Al-Ashouri, P. Korb, P. Tockhorn, A. Abate, B. Stannowski, B. Rech, and S. Albrecht, "Co-evaporated formamidinium lead iodide based perovskites with 1000 h constant stability for fully textured monolithic perovskite/silicon tandem solar cells", *Advanced Energy Materials*, vol. 11, no. 35, p. 2 101 460, 2021. DOI: 10.1002/aenm.202101460.

[160] K. Bush, A. Palmstrom, Z. Yu, M. Boccard, R. Cheacharoen, J. Mailoa, D. McMeekin, R. Hoye, C. Bailie, T. Leijtens, I. Peters, M. Minichetti, N. Rolston, R. Prasanna, S. Sofia, D. Harwood, W. Ma, F. Moghadam, H. Snaith, T. Buonassisi, Z. Holman, S. Bent, and M. McGehee, "23.6%-efficient monolithic perovskite/silicon tandem solar cells with improved stability", English (US), *Nature Energy*, vol. 2, no. 4, Mar. 2017, ISSN: 2058-7546. DOI: 10.1038/nenergy.2017.9.

[161] J. Sutter, P. Tockhorn, P. Wagner, K. Jäger, A. Al-Ashouri, B. Stannowski, S. Albrecht, and C. Becker, "Periodically nanostructured perovskite/silicon tandem solar cells with power conversion efficiency exceeding 26%", in *2021 IEEE 48th Photovoltaic Specialists Conference (PVSC)*, 2021, pp. 1034–1036. DOI: 10.1109/PVSC43889.2021.9518715.

[162] F. Sahli, B. A. Kamino, J. Werner, M. Bräuninger, B. Paviet-Salomon, L. Barraud, R. Monnard, J. P. Seif, A. Tomasi, Q. Jeangros, A. Hessler-Wyser, S. De Wolf, M. Despeisse, S. Nicolay, B. Niesen, and C. Ballif, "Improved optics in monolithic perovskite/silicon tandem solar cells with a nanocrystalline silicon recombination junction", *Advanced Energy Materials*, vol. 8, no. 6, p. 1 701 609, 2018. DOI: 10.1002/aenm.201701609.

[163] C. Momblona, L. Gil-Escrig, E. Bandiello, E. M. Hutter, M. Sessolo, K. Lederer, J. Blochwitz-Nimoth, and H. J. Bolink, "Efficient vacuum deposited p-i-n and n-i-p perovskite solar cells employing doped charge transport layers", *Energy Environ. Sci.*, vol. 9, pp. 3456–3463, 11 2016. DOI: 10.1039/C6EE02100J.

[164] D. P. McMeekin, G. Sadoughi, W. Rehman, G. E. Eperon, M. Saliba, M. T. Hörantner, A. Haghighirad, N. Sakai, L. Korte, B. Rech, M. B. Johnston, L. M. Herz, and H. J. Snaith, "A mixed-cation lead mixed-halide perovskite absorber for tandem solar cells", *Science*, vol. 351, no. 6269, pp. 151–155, 2016, ISSN: 0036-8075. DOI: 10.1126/science.aad5845.

[165] F. Fu, T. Feurer, T. P. Weiss, S. Pisoni, E. Avancini, C. Andres, S. Buecheler, and A. N. Tiwari, "High-efficiency inverted semi-transparent planar perovskite solar cells in substrate configuration", *Nature Energy*, vol. 2, p. 16 190, 1 Dec. 2016. DOI: 10.1038/nenergy.2016.190.

[166] C. Ma and N.-G. Park, "A realistic methodology for 30% efficient perovskite solar cells", *Chem*, vol. 6, no. 6, pp. 1254–1264, 2020, ISSN: 2451-9294. DOI: 10.1016/j.chempr.2020.04.013.

[167] J. Werner, G. Dubuis, A. Walter, P. L oper, S.-J. Moon, S. Nicolay, M. Morales-Masis, S. De Wolf, B. Niesen, and C. Ballif, "Sputtered rear electrode with broadband transparency for perovskite solar cells", *Solar Energy Materials and Solar Cells*, vol. 141, pp. 7. 407–413, 2015. DOI: 10.1016/j.solmat.2015.06.024.

[168] J. Diekmann, P. Caprioglio, M. H. Futscher, V. M. Le Corre, S. Reichert, F. Jaiser, M. Arvind, L. Perdigón Toro, E. Gutierrez-Partida, F. Peña-Camargo, C. Deibel, B. Ehrler, T. Unold, T. Kirchartz, D. Neher, and M. Stolterfoht, "Pathways towards 30% efficient single-junction perovskite solar cells and the role of mobile ions", *Solar RRL*, DOI: 10.1002/solr.202100219.

[169] V. M. Le Corre, M. Stolterfoht, L. Perdigón Toro, M. Feuerstein, C. Wolff, L. Gil-Escrig, H. J. Bolink, D. Neher, and L. J. A. Koster, "Charge transport layers limiting the efficiency of perovskite solar cells: how to optimize conductivity, doping, and thickness", *ACS Applied Energy Materials*, vol. 2, no. 9, pp. 6280–6287, 2019. DOI: 10.1021/acsaem.9b00856.

[170] E. Katz, "Chapter 13 - fullerene thin films as photovoltaic material", in *Nanostructured Materials for Solar Energy Conversion*, T. Soga, Ed., Amsterdam: Elsevier, 2006, pp. 361–443, ISBN: 978-0-444-52844-5. DOI: 10.1016/B978-044452844-5/50014-7.

[171] D. Shi, X. Qin, Y. Li, Y. He, C. Zhong, J. Pan, H. Dong, W. Xu, T. Li, W. Hu, J.-L. Brédas, and O. M. Bakr, "Spiro-ometad single crystals: remarkably enhanced charge-carrier transport via mesoscale ordering", *Science Advances*, vol. 2, no. 4, 2016. DOI: 10.1126/sciadv.1501491.

[172] J. Sutter, P. Tockhorn, P. Wagner, K. Jäger, A. Al-Ashouri, B. Stannowski, S. Albrecht, and C. Becker, "Periodically nanostructured perovskite/silicon tandem solar cells with power conversion efficiency exceeding 26%", in *2021 IEEE 48th Photovoltaic Specialists Conference (PVSC)*, 2021, pp. 1034–1036. DOI: 10.1109/PVSC43889.2021.9518715.

[173] Y. Wu, D. Yan, J. Peng, T. Duong, Y. Wan, S. P. Phang, H. Shen, N. Wu, C. Barugkin, X. Fu, S. Surve, D. Grant, D. Walter, T. P. White, K. R. Catchpole, and K. J. Weber, "Monolithic perovskite/silicon-homojunction tandem solar cell with over 22% efficiency", *Energy Environ. Sci.*, vol. 10, pp. 2472–2479, 11 2017. DOI: 10.1039/C7EE02288C.

[174] M. A. Green, Y. Hishikawa, E. D. Dunlop, D. H. Levi, J. Hohl-Ebinger, M. Yoshita, and A. W. Ho-Baillie, "Solar cell efficiency tables (version 53)", *Progress in Photovoltaics: Research and Applications*, vol. 27, no. 1, pp. 3–12, 2019. DOI: 10.1002/pip.3102.

[175] J. Zheng, H. Mehrvarz, F.-J. Ma, C. F. J. Lau, M. A. Green, S. Huang, and A. W. Y. Ho-Baillie, "21.8% efficient monolithic perovskite/homo-junction-silicon tandem solar cell on 16 cm2", *ACS Energy Letters*, vol. 3, no. 9, pp. 2299–2300, 2018. DOI: 10.1021/acsenergylett.8b01382.

[176] H. Shen, S. T. Omelchenko, D. A. Jacobs, S. Yalamanchili, Y. Wan, D. Yan, P. Phang, T. Duong, Y. Wu, Y. Yin, C. Samundsett, J. Peng, N. Wu, T. P. White, G. G. Andersson, N. S. Lewis, and K. R. Catchpole, "In situ recombination junction between p-si and tio₂ enables high-efficiency monolithic perovskite/si tandem cells", *Science Advances*, vol. 4, no. 12, p. 9711, 2018. DOI: 10.1126/sciadv.aau9711.

[177] M. A. Green, E. D. Dunlop, J. Hohl-Ebinger, M. Yoshita, N. Kopidakis, and X. Hao, "Solar cell efficiency tables (version 56)", *Progress in Photovoltaics: Research and Applications*, vol. 28, no. 7, pp. 629–638, 2020. DOI: 10.1002/pip.3303.

[178] L. Mazzarella, Y.-H. Lin, S. Kirner, A. B. Morales-Vilches, L. Korte, S. Albrecht, E. Crossland, B. Stannowski, C. Case, H. J. Snaith, and R. Schlatmann, "Infrared light management using a nanocrystalline silicon oxide interlayer in monolithic perovskite/silicon heterojunction tandem solar cells with efficiency above 25%", *Advanced Energy Materials*, vol. 9, no. 14, p. 1 803 241, 2019. DOI: 10.1002/aenm.201803241.

[179] B. A. Kamino, B. Paviet-Salomon, S.-J. Moon, N. Badel, J. Levrat, G. Christmann, A. Walter, A. Faes, L. Ding, J. J. Diaz Leon, A. Paracchino, M. Despeisse, C. Ballif, and S. Nicolay, "Low-temperature screen-printed metallization for the scale-up of two-terminal perovskite–silicon tandems", *ACS Applied Energy Materials*, vol. 2, no. 5, pp. 3815–3821, 2019. DOI: 10.1021/acsaem.9b00502.

[180] E. Lamanna, F. Matteocci, E. Calabrò, L. Serenelli, E. Salza, L. Martini, F. Menchini, M. Izzi, A. Agresti, S. Pescetelli, S. Bellani, A. E. Del Río Castillo, F. Bonaccorso, M. Tucci, and A. Di Carlo, "Mechanically stacked, two-terminal graphene-based perovskite/silicon tandem solar cell with efficiency over 26%", *Joule*, vol. 4, no. 4, pp. 865–881, 2020, ISSN: 2542-4351. DOI: 10.1016/j.joule.2020.01.015.

[181] D. Kim, H. J. Jung, I. J. Park, B. W. Larson, S. P. Dunfield, C. Xiao, J. Kim, J. Tong, P. Boonmongkolras, S. G. Ji, F. Zhang, S. R. Pae, M. Kim, S. B. Kang, V. Dravid, J. J. Berry, J. Y. Kim, K. Zhu, D. H. Kim, and B. Shin, "Efficient, stable silicon tandem cells enabled by anion-engineered wide-bandgap perovskites", *Science*, vol. 368, no. 6487, pp. 155–160, 2020. DOI: 10.1126/science.aba3433.

[182] M. Saliba, J.-P. Correa-Baena, C. M. Wolff, M. Stolterfoht, N. Phung, S. Albrecht, D. Neher, and A. Abate, "How to make over 20% efficient perovskite solar cells in regular (n–i–p) and inverted (p–i–n) architectures", *Chemistry of Materials*, vol. 30, no. 13, pp. 4193–4201, 2018. DOI: 10.1021/acs.chemmater.8b00136.

[183] "Physical vapor deposition market size, share & trends analysis report by category, by application (medical equipment, solar products, data storage) by region, and segment forecasts, 2020 - 2027", Grand View Research, Market Analysis Report, 2020.

[184] F. Sahli, N. Miaz, N. Salsi, C. Bucher, A. Schafflützel, Q. Guesnay, L. Duchêne, B. Niesen, C. Ballif, and Q. Jeangros, "Vapor transport deposition of methylammonium iodide for perovskite solar cells", *ACS Applied Energy Materials*, vol. 4, no. 5, pp. 4333–4343, 2021. DOI: 10.1021/acsaem.0c02999.

[185] R. Vidal, J.-A. Alberola-Borràs, S. N. Habisreutinger, J.-L. Gimeno-Molina, D. T. Moore, T. H. Schloemer, I. Mora-Seró, J. J. Berry, and J. M. Luther, "Assessing health and environmental impacts of solvents for producing perovskite solar cells", *Nature Sustainability*, vol. 4, no. 3, pp. 277–285, 2021. DOI: 10.1038/s41893-020-00645-8.

[186] M. Liu, M. Johnston, and H. Snaith, "Efficient planar heterojunction perovskite solar cells by vapour deposition", *Nature*, vol. 501, pp. 395–398, Sep. 2013. DOI: 10.1038/nature12509.

[187] L. K. Ono, S. Wang, Y. Kato, S. R. Raga, and Y. Qi, "Fabrication of semi-transparent perovskite films with centimeter-scale superior uniformity by the hybrid deposition method", *Energy Environ. Sci.*, vol. 7, pp. 3989–3993, 12 2014. DOI: 10.1039/C4EE02539C.

[188] K. B. Lohmann, J. B. Patel, M. U. Rothmann, C. Q. Xia, R. D. J. Oliver, L. M. Herz, H. J. Snaith, and M. B. Johnston, "Control over crystal size in vapor deposited metal-halide perovskite films", *ACS Energy Letters*, vol. 5, no. 3, pp. 710–717, 2020. DOI: 10.1021/acsenergylett.0c00183.

[189] J. Borchert, I. Levchuk, L. C. Snoek, M. U. Rothmann, R. Haver, H. J. Snaith, C. J. Brabec, L. M. Herz, and M. B. Johnston, "Impurity tracking enables enhanced control and reproducibility of hybrid perovskite vapor deposition", *ACS Applied Materials & Interfaces*, vol. 11, no. 32, pp. 28 851–28 857, 2019. DOI: 10.1021/acsami.9b07619.

[190] E. J. Juarez-Perez, L. K. Ono, and Y. Qi, "Thermal degradation of formamidinium based lead halide perovskites into sym-triazine and hydrogen cyanide observed by coupled thermogravimetry-mass spectrometry analysis", *J. Mater. Chem. A*, vol. 7, pp. 16 912–16 919, 28 2019. DOI: 10.1039/C9TA06058H.

[191] R. Quintero-Bermudez, J. Kirman, D. Ma, E. H. Sargent, and R. Quintero-Torres, "Mechanisms of LiF interlayer enhancements of perovskite light-emitting diodes", *The Journal of Physical Chemistry Letters*, vol. 11, no. 10, pp. 4213–4220, 2020. DOI: 10.1021/acs.jpclett.0c00757.

[192] J. Werner, G. Nogay, F. Sahli, T. C.-J. Yang, M. Bräuninger, G. Christmann, A. Walter, B. A. Kamino, P. Fiala, P. Löper, S. Nicolay, Q. Jeangros, B. Niesen, and C. Ballif, "Complex refractive indices of cesium–formamidinium-based mixed-halide perovskites with optical band gaps from 1.5 to 1.8 eV", *ACS Energy Letters*, vol. 3, no. 3, pp. 742–747, 2018. DOI: 10.1021/acsenergylett.8b00089.

[193] C.-H. Chiang, M. K. Nazeeruddin, M. Grätzel, and C.-G. Wu, "The synergistic effect of h2o and dmf towards stable and 20% efficiency inverted perovskite solar cells", *Energy Environ. Sci.*, vol. 10, pp. 808–817, 3 2017. DOI: 10.1039/C6EE03586H.

[194] J. Hidalgo, C. A. R. Perini, A.-F. Castro-Mendez, D. Jones, H. Köbler, B. Lai, R. Li, S. Sun, A. Abate, and J.-P. Correa-Baena, "Moisture-induced crystallographic reorientations and effects on charge carrier extraction in metal halide perovskite solar cells", *ACS Energy Letters*, vol. 5, no. 11, pp. 3526–3534, 2020. DOI: 10.1021/acsenergylett.0c01964.

[195] M. L. Petrus, Y. Hu, D. Moia, P. Calado, A. M. A. Leguy, P. R. F. Barnes, and P. Docampo, "The influence of water vapor on the stability and processing of hybrid perovskite solar cells made from non-stoichiometric precursor mixtures", *ChemSusChem*, vol. 9, no. 18, pp. 2699–2707, 2016. DOI: 10.1002/cssc.201600999.

[196] Y. Ko, C. Lee, Y. Kim, Y. Kim, Y. J. Yun, and Y. Jun, "Dew point temperature as an invariant replacement for relative humidity for advanced perovskite solar cell fabrication systems", *J. Mater. Chem. A*, vol. 6, pp. 20 695–20 701, 42 2018. DOI: 10.1039/C8TA06689B.

[197] H. Tsai, R. Asadpour, J.-C. Blancon, C. C. Stoumpos, O. Durand, J. W. Strzalka, B. Chen, R. Verduzco, P. M. Ajayan, S. Tretiak, J. Even, M. A. Alam, M. G. Kanatzidis, W. Nie, and A. D. Mohite, "Light-induced lattice expansion leads to high-efficiency perovskite solar cells", *Science*, vol. 360, no. 6384, pp. 67–70, 2018. DOI: 10.1126/science.aap8671.

[198] D. P. Stadelmann. (2020). "JEMS", [Online]. Available: https://www.jems-swiss.ch/.

[199] U. Rau, "Reciprocity relation between photovoltaic quantum efficiency and electroluminescent emission of solar cells", *Phys. Rev. B*, vol. 76, p. 085 303, 8 Aug. 2007. DOI: 10.1103/PhysRevB.76.085303.

[200] M. Ledinsky, T. Schönfeldová, J. Holovský, E. Aydin, Z. Hájková, L. Landová, N. Neyková, A. Fejfar, and S. De Wolf, "Temperature dependence of the urbach energy in lead iodide perovskites", *The Journal of Physical Chemistry Letters*, vol. 10, no. 6, pp. 1368–1373, 2019. DOI: 10.1021/acs.jpclett.9b00138.

[201] J. Chantana, Y. Kawano, T. Nishimura, A. Mavlonov, and T. Minemoto, "Impact of urbach energy on open-circuit voltage deficit of thin-film solar cells", *Solar Energy Materials and Solar Cells*, vol. 210, p. 110 502, 2020, ISSN: 0927-0248. DOI: 10.1016/j.solmat.2020.110502.

[202] N. N. Udalova, A. S. Tutantsev, Q. Chen, A. Kraskov, E. A. Goodilin, and A. B. Tarasov, "New features of photochemical decomposition of hybrid lead halide perovskites by laser irradiation", *ACS Applied Materials & Interfaces*, vol. 12, no. 11, pp. 12 755–12 762, 2020. DOI: 10.1021/acsami.9b21689.

[203] W. Chen, W. Li, Z. Gan, Y.-B. Cheng, B. Jia, and X. Wen, "Long-distance ionic diffusion in cesium lead mixed halide perovskite induced by focused illumination", *Chemistry of Materials*, vol. 31, no. 21, pp. 9049–9056, 2019. DOI: 10.1021/acs.chemmater.9b03320.

[204] J. Ball and A. Petrozza, "Defects in perovskite-halides and their effects in solar cells", *Nature Energy*, vol. 1, p. 16 149, Oct. 2016. DOI: 10.1038/nenergy.2016.149.

[205] S. Lin, B. Yang, X. Qiu, J. Yan, J. Shi, Y. Yuan, W. Tan, X. Liu, H. Huang, Y. Gao, and C. Zhou, "Efficient and stable planar hole-transport-material-free perovskite solar cells using low temperature processed SnO2 as electron transport material", *Organic Electronics*, vol. 53, pp. 235–241, 2018, ISSN: 1566-1199. DOI: 10.1016/j.orgel.2017.12.002.

[206] M. Stolterfoht, C. M. Wolff, Y. Amir, A. Paulke, L. Perdigón-Toro, P. Caprioglio, and D. Neher, "Approaching the fill factor Shockley–Queisser limit in stable, dopant-free triple cation perovskite solar cells", *Energy Environ. Sci.*, vol. 10, pp. 1530–1539, 6 2017. DOI: 10.1039/C7EE00899F.

[207] C. C. Boyd, R. C. Shallcross, T. Moot, R. Kerner, L. Bertoluzzi, A. Onno, S. Kavadiya, C. Chosy, E. J. Wolf, J. Werner, J. A. Raiford, C. de Paula, A. F. Palmstrom, Z. J. Yu, J. J. Berry, S. F. Bent, Z. C. Holman, J. M. Luther, E. L. Ratcliff, N. R. Armstrong, and M. D. McGehee, "Overcoming redox reactions at perovskite-nickel oxide interfaces to boost voltages in perovskite solar cells", *Joule*, vol. 4, no. 8, pp. 1759–1775, 2020, ISSN: 2542-4351. DOI: 10.1016/j.joule.2020.06.004.

[208] D. Liu, Q. Wang, C. J. Traverse, C. Yang, M. Young, P. S. Kuttipillai, S. Y. Lunt, T. W. Hamann, and R. R. Lunt, "Impact of ultrathin C_{60} on perovskite photovoltaic devices", *ACS Nano*, vol. 12, no. 1, pp. 876–883, 2018. DOI: 10.1021/acsnano.7b08561.

[209] B. Chen, P. N. Rudd, S. Yang, Y. Yuan, and J. Huang, "Imperfections and their passivation in halide perovskite solar cells", *Chem. Soc. Rev.*, vol. 48, pp. 3842–3867, 14 2019. DOI: 10.1039/C8CS00853A.

[210] N. Ahn, D.-Y. Son, I.-H. Jang, S. M. Kang, M. Choi, and N.-G. Park, "Highly reproducible perovskite solar cells with average efficiency of 18.3% and best efficiency of 19.7% fabricated via Lewis base adduct of lead(II) iodide", *Journal of the American Chemical Society*, vol. 137, no. 27, pp. 8696–8699, 2015. DOI: 10.1021/jacs.5b04930.

[211] A.-F. Castro-Méndez, J. Hidalgo, and J.-P. Correa-Baena, "The role of grain boundaries in perovskite solar cells", *Advanced Energy Materials*, vol. 9, no. 38, p. 1 901 489, 2019. DOI: 10.1002/aenm.201901489.

[212] J. Holovsky, A. Peter Amalathas, L. Landová, B. Dzurnak, B. Conrad, M. Ledinský, Z. Hajkova, O. Pop-Georgievski, J. Svoboda, T. Yang, and Q. Jeangros, "Lead halide residue as a source of light-induced reversible defects in hybrid perovskite layers and solar cells", *ACS Energy Letters*, Nov. 2019. DOI: 10.1021/acsenergylett.9b02080.

[213] National Institute of Standards and Technology, NIST Standard Reference Database Number 20, *NIST x-ray photoelectron spectroscopy database*, Gaithersburg MD, 20899, Aug. 2021. DOI: 10.18434/T4T88K.

[214] M. Uller Rothmann, W. Li, Y. Zhu, U. Bach, L. Spiccia, J. Etheridge, and C. Bing, "Direct observation of intrinsic twin domains in tetragonal CH3NH3PbI3", *Nature Communications*, vol. 8, p. 14 547, Feb. 2017. DOI: 10.1038/ncomms14547.

[215] M. Avrami, "Kinetics of Phase Change. I: General Theory", *The Journal of Chemical Physics*, vol. 7, no. 12, pp. 1103–1112, 1939. DOI: 10.1063/1.1750380.

[216] T. P. I. Saragi, T. Fuhrmann-Lieker, and J. Salbeck, "Comparison of charge-carrier transport in thin films of spiro-linked compounds and their corresponding parent compounds", *Advanced Functional Materials*, vol. 16, no. 7, pp. 966–974, 2006. DOI: 10.1002/adfm.200500361.

[217] M. Stolterfoht, M. Grischek, P. Caprioglio, C. M. Wolff, E. Gutierrez-Partida, F. Peña-Camargo, D. Rothhardt, S. Zhang, M. Raoufi, J. Wolansky, M. Abdi-Jalebi, S. D. Stranks, S. Albrecht, T. Kirchartz, and D. Neher, "How to quantify the efficiency potential of neat perovskite films: perovskite semiconductors with an implied efficiency exceeding 28%", *Advanced Materials*, vol. 32, no. 17, p. 2 000 080, 2020. DOI: 10.1002/adma.202000080.

[218] J. Werner, C. C. Boyd, T. Moot, E. J. Wolf, R. M. France, S. A. Johnson, M. F. A. M. van Hest, J. M. Luther, K. Zhu, J. J. Berry, and M. D. McGehee, "Learning from existing photovoltaic technologies to identify alternative perovskite module designs", *Energy Environ. Sci.*, vol. 13, pp. 3393–3403, 10 2020. DOI: 10.1039/D0EE01923B.

[219] A. Crossay, S. Buecheler, L. Kranz, J. Perrenoud, C. Fella, Y. Romanyuk, and A. Tiwari, "Spray-deposited Al-doped ZnO transparent contacts for CdTe solar cells", *Solar Energy Materials and Solar Cells*, vol. 101, pp. 283–288, 2012, ISSN: 0927-0248. DOI: 10.1016/j.solmat.2012.02.008.

[220] S. Faÿ and A. Shah, "Zinc oxide grown by CVD process as transparent contact for thin film solar cell applications", in *Transparent Conductive Zinc Oxide: Basics and Applications in Thin Film Solar Cells*, K. Ellmer, A. Klein, and B. Rech, Eds. Berlin, Heidelberg: Springer Berlin Heidelberg, 2008, pp. 235–302, ISBN: 978-3-540-73612-7. DOI: 10.1007/978-3-540-73612-7_6.

[221] M. Boccard, P. Cuony, C. Battaglia, S. Hänni, S. Nicolay, L. Ding, M. Benkhaira, G. Bugnon, A. Billet, M. Charrière, K. Söderström, J. Escarré, F. Sculati-Meillaud, M. Despeisse, and C. Ballif, "Nanometer- and micrometer-scale texturing for high-efficiency micromorph thin-film silicon solar cells", *IEEE Journal of Photovoltaics*, vol. 2, no. 2, pp. 83–87, 2012. DOI: 10.1109/JPHOTOV.2011.2179414.

[222] K. Bittkau, M. Schulte, T. Beckers, and R. Carius, "Fourier analysis for the study of light scattering properties of randomly textured ZnO films", in *Photonics for Solar Energy Systems III*, R. B. Wehrspohn and A. Gombert, Eds., International Society for Optics and Photonics, vol. 7725, SPIE, 2010, pp. 141–148. DOI: 10.1117/12.854337.

[223] B. R. Lee, J. S. Goo, Y. W. Kim, Y.-J. You, H. Kim, S.-K. Lee, J. W. Shim, and T. G. Kim, "Highly efficient flexible organic photovoltaics using quasi-amorphous ZnO/Ag/ZnO transparent electrodes for indoor applications", *Journal of Power Sources*, vol. 417, pp. 61–69, 2019, ISSN: 0378-7753. DOI: 10.1016/j.jpowsour.2019.02.015.

[224] S. Faÿ, U. Kroll, C. Bucher, E. Vallat, and A. Shah, "Low pressure chemical vapour deposition of ZnO layers for thin-film solar cells: temperature-induced morphological changes", *Solar Energy Materials and Solar Cells*, vol. 86, pp. 385–397, Mar. 2005. DOI: 10.1016/j.solmat.2004.08.002.

[225] L. Fanni, C. Ballif, and S. Nicolay, "Explaining morphological and electrical features of boron-doped zinc oxide to tailor new electrodes for photovoltaics", Ph.D. dissertation, EPFL, 2016.

[226] L. Ding, C. Ballif, and S. Nicolay, "Low-pressure chemical vapor deposited zinc oxide films toward decoupled opto-electrical and morphological properties for more efficient electrodes", Ph.D. dissertation, EPFL, 2013.

[227] L. Fanni, A. B. Aebersold, D. Alexander, L. Ding, M. Morales Masis, S. Nicolay, and C. Ballif, "c-texture versus a-texture low pressure metalorganic chemical vapor deposition ZnO films: lower resistivity despite smaller grain size", *Thin Solid Films*, vol. 565, pp. 1–6, 2014, ISSN: 0040-6090. DOI: 10.1016/j.tsf.2014.06.033.

[228] Fluxim AG, Katharina-Sulzer-Platz 2, 8400 Winterthur, Switzerland.

[229] S. Nicolay, S. Faÿ, and C. Ballif, "Growth model of MOCVD polycrystalline ZnO", *Crystal Growth & Design*, vol. 9, no. 11, pp. 4957–4962, 2009. DOI: 10.1021/cg900732h.

[230] A. B. Aebersold, L. Fanni, A. Hessler-Wyser, S. Nicolay, C. Ballif, C. Hébert, and D. T. Alexander, "Quantifying competitive grain overgrowth in polycrystalline zno thin films", *Acta Materialia*, vol. 173, pp. 74–86, 2019, ISSN: 1359-6454. DOI: 10.1016/j.actamat.2019.04.049.

[231] K. Schutt, P. K. Nayak, A. J. Ramadan, B. Wenger, Y.-H. Lin, and H. J. Snaith, "Overcoming zinc oxide interface instability with a methylammonium-free perovskite for high-performance solar cells", *Advanced Functional Materials*, vol. 29, no. 47, p. 1 900 466, DOI: 10.1002/adfm.201900466.

[232] J. Jeong, M. Kim, J. Seo, H. Lu, P. Ahlawat, A. Mishra, Y. Yang, M. A. Hope, F. T. Eickemeyer, M. Kim, Y. J. Yoon, I. W. Choi, B. P. Darwich, S. J. Choi, Y. Jo, J. H. Lee, B. Walker, S. M. Zakeeruddin, L. Emsley, U. Rothlisberger, A. Hagfeldt, D. S. Kim, M. Grätzel, and J. Y. Kim, "Pseudo-halide anion engineering for a-FAPbI3 perovskite solar cells", *Nature*, vol. 592, pp. 381–385, 7854 2021. DOI: 10.1038/s41586-021-03406-5.

[233] PV Lighthouse. (2021). "Refractive index library", [Online]. Available: https://pvlighthouse.com.au/refractive-index-library.

[234] M. Boccard, L. Antognini, V. Paratte, J. Haschke, M. Truong, J. Cattin, J. Dréon, W. Lin, L.-L. Senaud, B. Paviet-Salomon, S. Nicolay, M. Despeisse, and C. Ballif, "Hole-selective front contact stack enabling 24.1%-efficient silicon heterojunction solar cells", *IEEE Journal of Photovoltaics*, vol. 11, no. 1, pp. 9–15, 2021. DOI: 10.1109/JPHOTOV.2020.3028262.

[235] L. Antognini, V. Paratte, J. Haschke, J. Cattin, J. Dréon, M. Lehmann, L.-L. Senaud, Q. Jeangros, C. Ballif, and M. Boccard, "Influence of the dopant gas precursor in p-type nanocrystalline silicon layers on the performance of front junction heterojunction solar cells", *IEEE Journal of Photovoltaics*, vol. 11, no. 4, pp. 944–956, 2021. DOI: 10.1109/JPHOTOV.2021.3074072.

[236] S. Manzoor, J. Häusele, K. A. Bush, A. F. Palmstrom, J. Carpenter, Z. J. Yu, S. F. Bent, M. D. Mcgehee, and Z. C. Holman, "Optical modeling of wide-bandgap perovskite and perovskite/silicon tandem solar cells using complex refractive indices for arbitrary-bandgap perovskite absorbers", *Opt. Express*, vol. 26, no. 21, pp. 27 441–27 460, Oct. 2018. DOI: 10.1364/OE.26.027441.

[237] M. A. Green, "Self-consistent optical parameters of intrinsic silicon at 300k including temperature coefficients", *Solar Energy Materials and Solar Cells*, vol. 92, no. 11, pp. 1305–1310, 2008, ISSN: 0927-0248. DOI: 10.1016/j.solmat.2008.06.009.

[238] PV-Tech. (2014). "Griddler: the handy 2D solar cell calculator", [Online]. Available: pv-tech.org/technical-papers/griddler-the-handy-2d-solar-cell-calculator/.

[239] Dyenamo. (2021). "Hole Transport Materials and Dopants", [Online]. Available: dyenamo.se/dyenamo_hole_transport_materials.php.

[240] V. Torrisi and F. Ruffino, "Metal-polymer nanocomposites: (co-)evaporation/(co)sputtering approaches and electrical properties", *Coatings*, vol. 5, no. 3, pp. 378–424, 2015. DOI: 10.3390/coatings5030378.

[241] J. Schmidt and K. Bothe, "Structure and transformation of the metastable boron- and oxygen-related defect center in crystalline silicon", *Phys. Rev. B*, vol. 69, p. 024 107, 2 Jan. 2004. DOI: 10.1103/PhysRevB.69.024107.

[242] B. Demaurex, S. De Wolf, A. Descoeudres, Z. Charles Holman, and C. Ballif, "Damage at hydrogenated amorphous/crystalline silicon interfaces by indium tin oxide overlayer sputtering", *Applied Physics Letters*, vol. 101, no. 17, p. 171 604, 2012. DOI: 10.1063/1.4764529.

[243] J. Haschke, R. Lemerle, B. Aïssa, A. A. Abdallah, M. M. Kivambe, M. Boccard, and C. Ballif, "Annealing of silicon heterojunction solar cells: interplay of solar cell and indium tin oxide properties", *IEEE Journal of Photovoltaics*, vol. 9, no. 5, pp. 1202–1207, 2019. DOI: 10.1109/JPHOTOV.2019.2924389.

[244] C. Luderer, C. Messmer, M. Hermle, and M. Bivour, "Transport losses at the TCO/a-Si:H/c-Si heterojunction: influence of different layers and annealing", *IEEE Journal of Photovoltaics*, vol. PP, pp. 1–7, Apr. 2020. DOI: 10.1109/JPHOTOV.2020.2983989.

[245] K.-U. Ritzau, T. Behrendt, D. Palaferri, M. Bivour, and M. Hermle, "Hydrogen doping of indium tin oxide due to thermal treatment of hetero-junction solar cells", *Thin Solid Films*, vol. 599, pp. 161–165, 2016, ISSN: 0040-6090. DOI: 10.1016/j.tsf.2015.12.027.

[246] J. Schmidt, A. Merkle, R. Brendel, B. Hoex, M. C. M. van de Sanden, and W. M. M. Kessels, "Surface passivation of high-efficiency silicon solar cells by atomic-layer-deposited Al2O3", *Progress in Photovoltaics: Research and Applications*, vol. 16, no. 6, pp. 461–466, 2008. DOI: 10.1002/pip.823.

[247] ELIS, University of Gent. (2020). "Simulation programme SCAPS-1D for thin film solar cells", [Online]. Available: https://scaps.elis.ugent.be/.

[248] W. Liu, Y. Liu, J. Wang, C. Wu, C. Liu, L. Xiao, Z. Chen, S. Wang, and Q. Gong, "Twin domains in organometallic halide perovskite thin-films", *Crystals*, vol. 8, no. 5, 2018. DOI: 10.3390/cryst8050216.

[249] W. Fan, Y. Shi, T. Shi, S. Chu, W. Chen, K. O. Ighodalo, J. Zhao, X. Li, and Z. Xiao, "Suppression and reversion of light-induced phase separation in mixed-halide perovskites by oxygen passivation", *ACS Energy Letters*, vol. 4, no. 9, pp. 2052–2058, 2019. DOI: 10.1021/acsenergylett.9b01383.

[250] P. Troyan, Y. Zhidik, and E. Zhidik, "Investigation of temperature stability of ITO films characteristics", *MATEC Web Conf.*, vol. 143, p. 03 010, 2018. DOI: 10.1051/matecconf/201714303010.

PETER FIALA

Semiconductor Engineer

PROFILE

A natural engineer, with diverse experience in the domain of materials science. Peter has spent years in the lab researching photovoltaic materials, laser and lens systems, nano-scale communication technology, and more. Outside the lab, he continues to seek out challenges, from climbing Alps to sailing to building cars.

CONTACT

Email:
PeterFiala@pm.me

Phone:
+41 78 684 81 54

Profile:
linkedin.com/in/PeterFiala

LANGUAGES

American (mother tongue)
French (C1)
German (B1)
Arabic (B1)

Coding: Python, Matlab, Labview

HOBBIES

Backpacking & alpinism
Travel & culture
Language learning
Gardening
Music

WORK EXPERIENCE

Ecole Polytechnique Fédéral de Lausanne – Ph.D. Researcher
Sept. 2017 – Dec. 2021
Ph.D. in Materials Science. Research and development of high-efficiency perovskite/silicon tandem solar cells. Focus on processing and characterization of various semiconductors. Extensive lab experience and multiple publications.

NASA Student Airborne Research Program – Researcher
Summer 2016
Design and execution of an independent research project. Processing of large data sets to uncover links between land use and air pollution. Main results published.

Univ. of Rochester Department of Chemistry – Research Assistant
Sept. 2015 – May 2017
Various projects assisting Ph.D. students in their sample preparation and measurement. Research focused on semiconductor quantum dots.

Laboratory for Laser Energetics – Undergraduate Assistant
Feb. 2014 – Sept. 2015, Summer 2017
Multiple diverse projects related to improving power transmission and uniformity on one of the world's largest laser systems. Multiple publications and application of my results in the main laser line.

EDUCATION

University of Rochester
Bachelors of Science in Optical Engineering – May 2017
3.92 GPA (of 4) in bachelors optics courses. Minor in Chemical Engineering. Certificate in Nanoscience and Nanoengineering. Recipient of the Wilder Trustee Leadership Scholarship and Take Five Scholarship. Active member of Mini-Baja engineering team.